VERA Virtual Environment for Reactor Applications

ORNL/SPR-2023/3125

CTF Theory Manual: Version 4.4

Sept 30, 2023

R. Salko[1], M. Avramova[2], A. Wysocki[1], B. Hizoum[1], J. Hu[1], and A. Abarca[2]

[1]Oak Ridge National Laboratory
[2]North Carolina State University

OAK RIDGE National Laboratory

U.S. DEPARTMENT OF ENERGY

ORNL is managed by UT-Battelle LLC for the US Department of Energy.

ORNL/SPR-2023/3125

CTF THEORY MANUAL: VERSION 4.4

R. Salko[1], M. Avramova[2], A. Wysocki[1], B. Hizoum[1], J. Hu[1], and A. Abarca[2]

[1]Oak Ridge National Laboratory
[2]North Carolina State University

Date Published: Sept 30, 2023

Prepared by
OAK RIDGE NATIONAL LABORATORY
Oak Ridge, TN 37831-6283
managed by
UT-Battelle, LLC
for the
US DEPARTMENT OF ENERGY
under contract DE-AC05-00OR22725

CTF Theory Manual: Version 4.4

Revision Log

Revision	Date	Affected Pages	Revision Description
0	06/29/2022	All	Converted document to new template; this version supersedes document number ORNL/TM-2020/1721
1	9/30/2023	Chapters 3, 4, 6, 7, 9, and 12	Changes to better organize the document, fix consistency issues with flow regime naming, and update models to reflect what is currently in CTF

Document pages that are:

Export Controlled:	None
IP/Proprietary/NDA Controlled:	None
Sensitive Controlled:	None
Unlimited:	All

THE NORTH CAROLINA STATE UNIVERSITY

DEPARTMENT OF NUCLEAR ENGINEERING

REACTOR DYNAMICS AND FUEL MODELING GROUP

NC STATE UNIVERSITY

CTF Theory Manual: Version 4.4

Sept 30, 2023

CONTRIBUTORS

CTF has been developed by many individuals at various institutions over the course many years. While the title page author list provides authors of the current version of this document or significant contributors to past versions, it does not consider every person that has contributed to this document or CTF in some way. The following list, which is presented in alphabetical order, summarizes all past contributors to this document who have not already been acknowledged on the title page.

- Taylor Blyth
- Chris Dances
- Ana Jambrina
- Caleb Jernigan
- Joseph Kelly
- Nathan Porter
- Aysenur Toptan

CTF Theory Manual: Version 4.4

Approvals:

Robert Salko, CTF Product Software Manager	**Date**
Marc-Oliver Delchini, Independent Reviewer	**Date**

CONTENTS

LIST OF FIGURES

LIST OF TABLES

ABBREVIATIONS

ANTS	Alternative Nonlinear Two-Phase Subchannel
BFBT	BWR Full-size Fine-mesh Bundle Tests
BWR	boiling water reactor
CASL	Consortium for Advanced Simulation of Light Water Reactors
CFL	Courant Friedrichs Lewy
CHF	critical heat flux
COBRA-TF	Coolant-Boiling in Rod Arrays – Two Fluids
CTF	PSU RDFMG version of COBRA-TF
DFFB	dispersed flow film boiling
DNB	departure from nucleate boiling
HTC	heat transfer coefficient
IAFB	inverted annular film boiling
IAPWS	International Association for the Properties of Water and Steam
ICE	implicit continuous Euler
LBLOCA	large-break loss-of-coolant accident
LHS	left-hand side
LOCA	loss-of-coolant accident
LWR	light-water reactor
MFB	minimum film boiling
NFI	Nuclear Fuel Industries
NPP	nuclear power plant
NRC	US Nuclear Regulatory Commission
ONB	onset of nucleate boiling
ORNL	Oak Ridge National Laboratory
PSU	Pennsylvania State University
PWR	pressurized water reactor
RDFMG	Reactor Dynamics and Fuel Modeling Group
RHS	right-hand side
SIFGRS	Simple Integrated Fission Gas Release and Swelling
SIMPLE	Semi-Implicit Method for Pressure-Linked Equations
T/H	thermal/hydraulic
TD	theoretical density
TRACE	TRAC/RELAP Advanced Computational Engine
TRACG	Transient Reactor Analysis Code GE
V&V	validation & verification

ABSTRACT

Coolant-Boiling in Rod Arrays – Two Fluids (COBRA-TF) is a thermal/hydraulic (T/H) simulation code designed for light-water reactor (LWR) vessel analysis. It uses a two-fluid, three-field (i.e., fluid film, fluid drops, and vapor) modeling approach. Both subchannel and 3D Cartesian forms of its governing equations are available for the solution. The code was originally developed by Pacific Northwest Laboratory in 1980 and has been used and modified by several institutions over the last few decades.

COBRA-TF also found use at the Pennsylvania State University (PSU) by the Reactor Dynamics and Fuel Modeling Group (RDFMG) and has been improved, updated, and subsequently rebranded as CTF. CTF was later adopted in the early 2010s by Oak Ridge National Laboratory (ORNL) for use in the Consortium for Advanced Simulation of Light Water Reactors (CASL) program, which led to a significant advancement of the code's software quality, modeling accuracy, testing systems, and capabilities for improved support in modeling common LWR nominal and transient behavior. As part of the improvement process, it was necessary to generate sufficient documentation for the public domain code which had lacked such material upon being adopted by RDFMG. This document serves as a theory manual for CTF, detailing the many two-phase heat transfer, drag, and important accident scenario models contained in the code, as well as the numerical solution process utilized. Additional documents available in the CTF documentation suite include the user manual and the verification and validation manual.

1. INTRODUCTION

The most important aspect of the civilian use of nuclear power is ensuring public safety from radiological releases despite any number of postulated risks to the integrity of nuclear power plant (NPP) systems. Such insurance is obtained through rigorous testing and re-testing of plant safety systems for any and all likely accident scenarios that can threaten NPP stability. Accident behavior is best assessed through a combination of experimental and computational simulations of postulated reactor accident scenarios. With 1988 revisions to US Nuclear Regulatory Commission (NRC) safety analysis requirements (10CFR.50.46), great gains in plant economy and safety can be made with the use of computational best-estimate models in plant design and operation.

COBRA-TF is one such computational tool for assessing NPP behavior. The code, developed originally in 1980 by Pacific Northwest Laboratory under sponsorship of the NRC [1], began as a T/H rod-bundle analysis code but has been continually updated and expanded over the past several decades. The code uses a two-fluid modeling approach with consideration for three separate, independent flow fields; fluid film, vapor, and liquid droplets. COBRA-TF includes a wide range of T/H models crucial to accurate LWR safety analysis, including but not limited toflow regime–dependent two-phase heat transfer, interphase heat transfer and drag, droplet breakup, and quench-front tracking. Because of its full 3D capabilities and extensive array of reactor T/H modeling capabilities, COBRA-TF has found much use in modeling LWR rod-bundle transient analysis and pressurized water reactor (PWR) whole-vessel loss-of-coolant accident (LOCA) analysis.

CTF is an improved version of COBRA-TF and is developed and maintained by the RDFMG at the PSU. Improvements include:

- Transition to FORTRAN 90 source code
- Enhanced user-friendliness with improved error checking and free-format input deck
- Quality assurance utilizing an extensive validation & verification (V&V) matrix
- Turbulent mixing, void drift, and direct heating model improvements
- Enhanced computational efficiency by implementation of new numerical solution schemes
- Better code physical model and user modeling documentation

This document discusses the numerical solution and physical phenomena modeling capabilities of CTF in detail. In essence, it is a theory manual for the code. The two-fluid modeling approach, along with the associated conservation equations and numerical solution process, is discussed in Chapter 2. This is the foundation for modeling flow—setting up the transport equations for each unique fluid, discretizing them, applying them to a mesh of the volume, and solving them by a numerical iterative approach.

Setting up the conservation equations is only the first step, and the equations cannot be solved until they are completely defined. The equations will contain several terms that link similar conservation equations located in different spatial locations (i.e., mesh cells) resulting from physical phenomena like void drift and turbulent mixing. Likewise, the equations will include terms that link them in the same spatial location because of interphase effects like phase change and entrainment. These terms are dubbed “closure” terms because they define the remaining conservation equation terms and allow them to be solved for the independent variables.

Before modeling these closure terms, it is necessary to determine the general behavior of the two-phase flow in the mesh cell being modeled. This is accomplished by using a flow regime map to categorize the flow behavior into one of several classifications of flow. This allows for accurate determination of

the interphase contact area, which is necessary to determine interphase heat transfer and drag, as well as the correct selection of closure-term models. The CTF flow regime maps and interphase area calculation process are described in Chapter 4.

The different models used to close the equations are discussed in Chapters 5, 6, 7, 8, and 9.

The only remaining unknown parameters at this point are the thermophysical fluid and solid properties. These properties are available to CTF via intrinsic fluid property data tables and are discussed in Chapters 14 and 15.

With this information and through adequate user-provided boundary conditions, CTF is capable of deriving a solution for fluid behavior; however, it may be desirable to also model the behavior of fuel rods or reactor decay heat because of their importance in safety analysis. CTF also includes models for heated and unheated conductors, including nuclear fuel rod models, which are discussed in Chapter 10.

The primary purpose of this manual is the discussion of the theory behind CTF and models that have been implemented into the code. It is noted, however, that during CTF development for boiling water reactor (BWR) applications, a new solver was developed, called Alternative Nonlinear Two-Phase Subchannel (ANTS). This solver was tightly integrated into CTF to take advantage of the infrastructure, which includes the input/output user interfaces, the coupling interface, and the CTF fuel rod solver. However, the solution methodology is significantly different than the one in CTF because ANTS aims to provide a very fast solution at the expense of model fidelity. Therefore, no discussion of the ANTS solver is included in this manual; instead, the reader is pointed to the publication on ANTS theory [2].

Additional documentation outside of this manual is also available that describes instructions for modeling T/H problems using CTF and provides details on modules and global variables in CTF source code.

2. GOVERNING EQUATIONS

2.1 INTRODUCTION

This section establishes the foundation to describe the CTF flow modeling approach through discussion of the code conservation equations. The equations are presented in their most basic forms and are gradually manipulated into the forms used to create COBRA-TF.

A two-fluid model is employed in CTF with consideration for three separate fluid fields—liquid film, liquid droplets, and vapor. Each of the three fields is modeled with its own set of conservation equations, with the exception being that the liquid and droplet fields are assumed to be in thermal equilibrium, so they share an energy equation. The sets of conservation equations are formulated using a Cartesian coordinate system (3D solution) or a simplified subchannel approach. The user may choose which approach to use when modeling a system with CTF.

In this section, the general conservation equations of mass, momentum, and energy are presented in Section 2.2. Assumptions are listed, and the equations are reduced where necessary. They are then expanded out for each field and for each spatial direction.

To be useful in a T/H code environment, the conservation equations must be put into finite-difference form and then applied and solved over a mesh of finite volumes. The computational mesh structure and the discretized forms of the conservation equations are discussed in Section 2.3. Once the governing conservation equations are set up for a computational cell mesh of the flow geometry, they must be solved simultaneously using a numerical approach. The numerical approach is discussed in Section 3.

2.2 CONSERVATION EQUATIONS

2.2.1 Introduction

The generalized form of the conservation equations of mass, momentum, and energy are given first with a description of each term in the equations in Section 2.2.2. After each conservation equation is presented, the assumptions used to implement the equations into CTF are defined. Next, the Cartesian forms of the CTF conservation equations are shown in Section 2.2.3, and the subchannel forms of the CTF conservation equations are shown in Section 2.2.4.

2.2.2 Generalized Conservation Equations

For a given computational cell, mass, momentum, and energy are conserved. This behavior is captured for each field using three conservation equations, except the liquid and droplet fields share an energy equation. This is the heart of the two-fluid model—modeling each phase with its own set of mass, momentum, and energy equations. The conservation equations, of course, are dependent on one another and are linked by interaction terms that account for factors such as mass and heat transfer between phases (e.g., evaporation/condensation or entrainment/de-entrainment). Each of the conservation equations is presented and discussed in succession, along with a description of each term in the equations.

2.2.2.1 Generalized Phasic Mass Conservation Equation

The general mass conservation equation is presented in Eq. (1).

$$\frac{\partial}{\partial t}\left(\alpha_k \rho_k\right) + \nabla \cdot \left(\alpha_k \rho_k \vec{V}_k\right) = L_k + M_e^T \tag{1}$$

The k subscript denotes the field under consideration; it can be l for the liquid film field, v for the vapor field, or e for the entrained droplet field. On the left-hand side (LHS) of Eq. (1), the first term is the change of mass with time, and the second term is the advection of the field mass into or out of the volume ($\vec{V}$ is the field velocity). On the right-hand side (RHS), the L_k term represents the mass transfer into or out of phase k—interphase mass transfer can occur by either evaporation/condensation or by entrainment/de-entrainment. The L term is expanded for each field as follows:

$$L_v = \Gamma''', \tag{2a}$$

$$L_l = -(1-\eta)\Gamma''' - S''', \text{ and} \tag{2b}$$

$$L_e = -\eta\Gamma''' + S''' \tag{2c}$$

The Γ''' term represents the volumetric mass transfer resulting from phase change. Note that the Γ''' term is additive for the vapor field, whereas it is subtractive for the liquid and droplet fields: if the sign of Γ''' is positive, then evaporation adds mass to the vapor and subtracts it from the liquid fields (the reverse is true for condensation). For the liquid and droplet fields, Γ''' is multiplied by $1-\eta$ and η, respectively. The η term represents the fraction of phase change occurring between vapor and entrained droplets. Eq. (3) shows the definition of η for the case of evaporation, and Eq. (4) shows the definition of η for the case of condensation.

$$\eta_{\text{evap}} = \min \begin{cases} 1 - \dfrac{Q'''_{wl}}{\Gamma''' H_{fg}} \\ \dfrac{\alpha_e}{1-\alpha_v} \end{cases} \tag{3}$$

$$\eta_{\text{cond}} = \frac{\alpha_e}{1-\alpha_v} \tag{4}$$

In Eqs. (3) and (4), Q'''_{wl} is the volumetric heat transfer from the wall to liquid phase, and H_{fg} is the latent heat of vaporization. The phase change model used to calculate Γ and the entrainment/de-entrainment models are described in Section 9.

The final term of the general mass conservation equation is the mass transfer in the mesh cell resulting from turbulent mixing and void drift. Advanced turbulence models are not included in CTF, and because axially dominated subchannel flow is assumed, a simple turbulent diffusion model is used to calculated turbulent transfer of axial momentum through subchannel gaps. Note that turbulent mixing only occurs in the lateral direction. The turbulent diffusion approximation and void drift models are discussed further in Section 8.

2.2.2.2 Generalized Phasic Momentum Conservation Equation

The momentum conservation equation is given in Eq. (5).

$$\begin{aligned} &\frac{\partial}{\partial t}\left(\alpha_k \rho_k \vec{V}_k\right) + \frac{\partial}{\partial x}\left(\alpha_k \rho_k u_k \vec{V}_k\right) + \frac{\partial}{\partial y}\left(\alpha_k \rho_k v_k \vec{V}_k\right) + \frac{\partial}{\partial z}\left(\alpha_k \rho_k w_k \vec{V}_k\right) \\ &= \alpha_k \rho_k \vec{g} - \alpha_k \nabla P + \nabla \cdot \left[\alpha_k \left(\boldsymbol{\tau}_k^{ij} + \boldsymbol{T}_k^{ij}\right)\right] + \vec{M}_k^L + \vec{M}_k^d + \vec{M}_k^T \end{aligned} \tag{5}$$

On the LHS, the terms are change of volume momentum with time and advection of momentum. Note that the LHS terms multiply by the vector velocity $\vec{V}_k$, so each term will have three components ($u_k\vec{i} + v_k\vec{j} + w_k\vec{k}$) and will result in three separate momentum equations for each of the three directions (if using Cartesian

coordinates). On the RHS, the terms are gravitational force, pressure force, viscous and turbulent shear stress, momentum source/sink resulting from phase change and entrainment, interfacial drag forces, and momentum transfer resulting from turbulent mixing. The pressure has no phase dependency because it is assumed to be equal in all phases, and gravity is assumed to be the only body force.

Because the turbulent shear stress term is not actually modeled in CTF, it is eliminated in future forms of the momentum equation. Turbulent mixing is captured using a simple turbulent diffusion approximation.

The viscous stress term can be expanded into wall shear and fluid-fluid shear components as follows:

$$\nabla \cdot \left(\alpha_e \boldsymbol{\tau}_e^{ij}\right) = \vec{\tau}'''_{\text{we}} \tag{6}$$

$$\nabla \cdot \left(\alpha_v \boldsymbol{\tau}_v^{ij}\right) = \vec{\tau}'''_{\text{wv}} + \nabla \cdot \left(\alpha_v \boldsymbol{\sigma}_v^{ij}\right) \tag{7}$$

$$\nabla \cdot \left(\alpha_l \boldsymbol{\tau}_l^{ij}\right) = \vec{\tau}'''_{\text{wl}} + \nabla \cdot \left(\alpha_l \boldsymbol{\sigma}_l^{ij}\right) \tag{8}$$

The $\vec{\tau}'''_{\text{we}}$, $\vec{\tau}'''_{\text{wv}}$, and $\vec{\tau}'''_{\text{wl}}$ terms are the volumetric wall drag and form losses of the entrained, vapor, and liquid phases, respectively. Note that it is assumed that the entrained droplet field does not to contact the wall, so there is no wall drag. However, the $\vec{\tau}'''_{\text{we}}$ term does account for form loss effects experienced by the droplet field. The liquid-liquid viscous shear stresses actually are not modeled by CTF, so they are eliminated in future derivations of the momentum equations.

The $\vec{M}_k^L$ term is the momentum source/sink from phase change and entrainment/de-entrainment—it is expanded as follows:

$$\vec{M}_v^L = \Gamma'''\vec{V} \tag{9a}$$

$$\vec{M}_l^L = -\Gamma'''(1-\eta)\vec{V} - S'''\vec{V} \tag{9b}$$

$$\vec{M}_e^L = -\Gamma'''\eta\vec{V} + S'''\vec{V} \tag{9c}$$

The $\vec{V}$ term is the velocity of the phase from which mass originates. For example, if evaporation is occurring from the droplet field, then the momentum, $\Gamma'''\eta\vec{V}_e$, will leave the entrained field and be subtracted from the droplet field momentum conservation equation. Conversely, that same amount of momentum will enter the vapor field.

The interfacial drag term, $\vec{M}^d$, can simply be expanded for each of the three fields as follows:

$$\vec{M}_v^d = -\vec{\tau}'''_{\text{i,vl}} - \vec{\tau}'''_{\text{i,ve}} \tag{10a}$$

$$\vec{M}_l^d = \vec{\tau}'''_{\text{i,vl}} \tag{10b}$$

$$\vec{M}_e^d = \vec{\tau}'''_{\text{i,ve}} \tag{10c}$$

The $\vec{\tau}'''_{\text{i,vl}}$ and $\vec{\tau}'''_{\text{i,ve}}$ terms are the volumetric interphase drag forces for the vapor-liquid and vapor-droplet interfaces, respectively. Note that the drag terms are subtractive for the vapor field and additive for the droplet and liquid fields. This is because the CTF convention allows the vapor phase to move faster than the liquid and droplet phases, which means that interfacial friction would act against the vapor phase, but it would act with the liquid and droplet phases. If the opposite were true and the vapor phase were somehow moving slower than the liquid and droplet phases, then the signs of the terms would simply be reversed in CTF. The interfacial shear is a flow regime–dependent value, and its calculation is further discussed in Section 6,

The final term of Eq. (5) is the momentum source caused by turbulent mixing and void drift, $\vec{M}_k^T$. Note that only axial momentum is convected by turbulent mixing and void drift.

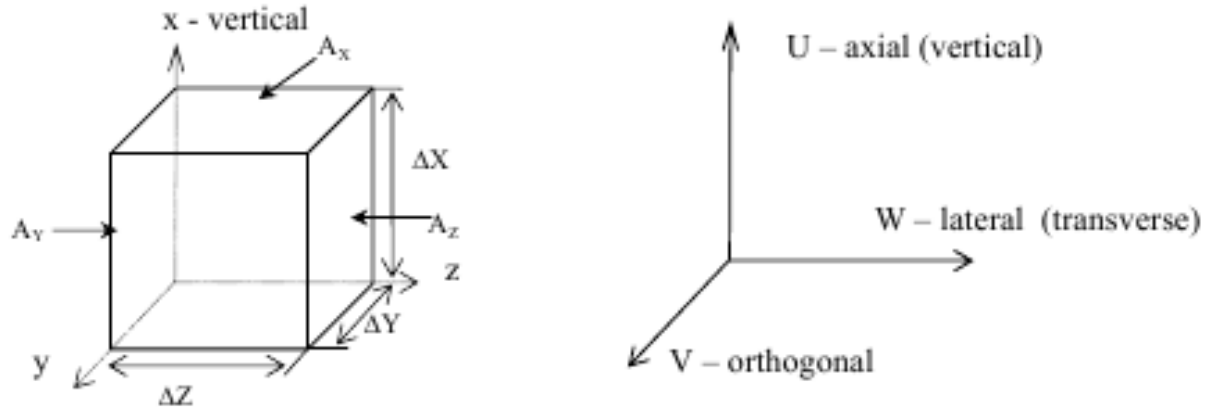

Figure 1. Control volume defined in Cartesian coordinates.

2.2.2.3 Generalized Phasic Energy Conservation Equation

The generalized energy equation is presented in Eq. (11).

$$\frac{\partial}{\partial t}\left(\alpha_k \rho_k h_k\right) + \nabla \cdot \left(\alpha_k \rho_k h_k \vec{V}_k\right) = -\nabla \cdot \left[\alpha_k \left(\vec{Q}_k + \vec{q}_k^{T}\right)\right] + \Gamma_k h_k^i + q_{wk}''' + \alpha_k \frac{\partial P}{\partial t} \tag{11}$$

The LHS terms are change of phase energy with respect to time, and advection of phase energy into or out of the cell. The RHS terms are k-phase conduction and turbulence heat flux, energy transfer caused by phase-change, volumetric wall heat transfer, and the pressure work term. It is assumed that there is no volumetric heat generation occurring in the fluid. Radiative heat transfer only occurs between solid surfaces and the vapor/droplet fields. Internal dissipation is negligible, and once again, pressure is uniform throughout the phases.

There is no modeling of heat conduction in the fluids, so $\vec{Q}_k$ is zero in CTF. The $\vec{q}_k^{T}$ term represents energy exchange by turbulent mixing and by void drift; however, it is only considered in the lateral and orthogonal directions.

2.2.3 CTF Expanded Conservation Equations in Cartesian Form

The generalized conservation equations are presented in their expanded form in this section, with consideration for the aforementioned assumptions. Each field conservation equation is explicitly written out. Figure 1 shows a control volume defined for the Cartesian geometry[3].

2.2.3.1 Mass Continuity Conservation Equation in Cartesian Coordinates

Vapor conservation of mass is shown in Eq. (12).

$$\frac{\partial}{\partial t}\left(\alpha_v \rho_v\right) + \frac{\partial}{\partial x}\left(\alpha_v \rho_v u_v\right) + \frac{\partial}{\partial y}\left(\alpha_v \rho_v v_v\right) + \frac{\partial}{\partial z}\left(\alpha_v \rho_v w_v\right) = \Gamma''' + M_v^{T'''} \tag{12}$$

Liquid conservation of mass is shown in Eq. (13).

$$\frac{\partial}{\partial t}(\alpha_l \rho_l) + \frac{\partial}{\partial x}(\alpha_l \rho_l u_l) + \frac{\partial}{\partial y}(\alpha_l \rho_l v_l) + \frac{\partial}{\partial z}(\alpha_l \rho_l w_l) = -\Gamma'''(1-\eta) - S''' + M_l^{T'''} \tag{13}$$

Droplet conservation of mass is shown in Eq. (14).

$$\frac{\partial}{\partial t}(\alpha_e \rho_l) + \frac{\partial}{\partial x}(\alpha_e \rho_l u_e) + \frac{\partial}{\partial y}(\alpha_e \rho_l v_e) + \frac{\partial}{\partial z}(\alpha_e \rho_l w_e) = -\Gamma'''\eta + S''' + M_e^{T'''} \tag{14}$$

2.2.3.2 Momentum Conservation Equation in Cartesian Coordinates

Each field can move in three separate directions in Cartesian coordinates, so there is an x-, y-, and z-component of each field's momentum conservation equation. The vapor conservation equation for the x-direction is given in Eq. (15).

$$\begin{aligned}&\frac{\partial}{\partial t}(\alpha_v \rho_v u_v) + \frac{\partial}{\partial x}(\alpha_v \rho_v u_v u_v) + \frac{\partial}{\partial y}(\alpha_v \rho_v u_v v_v) + \frac{\partial}{\partial z}(\alpha_v \rho_v u_v w_v) \\ &= -\alpha_v \frac{\partial P}{\partial x} - \alpha_v \rho_v g - \tau'''_{\mathrm{wx,v}} - \tau'''_{\mathrm{ix,vl}} - \tau'''_{\mathrm{ix,ve}} + \Gamma''' u + \sum_{k=1}^{\mathrm{nk}} (M_v^T)_k'''\end{aligned} \tag{15}$$

The axial component of momentum can be convected into the mesh cell from any of three directions, which accounts for the three advection terms on the LHS of Eq. (15). The three shear terms only include shear forces acting on the vapor phase in the x-direction. The momentum source from mass transfer, $\Gamma''' u$, will have components of phase change from both the droplet and liquid fields, and the phase velocity that multiplies by Γ''' will be dependent on the direction of phase change (i.e. evaporation or condensation). The final term accounts for turbulent mixing of axial momentum—it is summed over all transverse connections to the mesh cell.

The y- and z- components of vapor momentum conservation are shown in Eqs. (16) and (17), respectively. Note that there are no gravitational body force terms in the y- and z- component equations and no turbulent mixing of transverse momentum.

$$\frac{\partial}{\partial t}(\alpha_v \rho_v v_v) + \frac{\partial}{\partial x}(\alpha_v \rho_v v_v u_v) + \frac{\partial}{\partial y}(\alpha_v \rho_v v_v v_v) + \frac{\partial}{\partial z}(\alpha_v \rho_v v_v w_v) = -\alpha_v \frac{\partial P}{\partial y} - \tau'''_{\mathrm{wy,v}} - \tau'''_{\mathrm{iy,vl}} - \tau'''_{\mathrm{iy,ve}} + \Gamma''' v \tag{16}$$

$$\frac{\partial}{\partial t}(\alpha_v \rho_v w_v) + \frac{\partial}{\partial x}(\alpha_v \rho_v w_v u_v) + \frac{\partial}{\partial y}(\alpha_v \rho_v w_v v_v) + \frac{\partial}{\partial z}(\alpha_v \rho_v w_v w_v) = -\alpha_v \frac{\partial P}{\partial z} - \tau'''_{\mathrm{wz,v}} - \tau'''_{\mathrm{iz,vl}} - \tau'''_{\mathrm{iz,ve}} + \Gamma''' w \tag{17}$$

The liquid conservation equations are given in Eqs. (18), (19), and (20).

$$\begin{aligned}&\frac{\partial}{\partial t}(\alpha_l \rho_l u_l) + \frac{\partial}{\partial x}(\alpha_l \rho_l u_l u_l) + \frac{\partial}{\partial y}(\alpha_l \rho_l u_l v_l) + \frac{\partial}{\partial z}(\alpha_l \rho_l u_l w_l) \\ &= -\alpha_l \frac{\partial P}{\partial x} - \alpha_l \rho_l g - \tau'''_{\mathrm{wx,l}} + \tau'''_{\mathrm{ix,vl}} - \Gamma'''(1-\eta) u + \sum_{k=1}^{\mathrm{nk}} (M_l^T)_k'''\end{aligned} \tag{18}$$

$$\frac{\partial}{\partial t}(\alpha_l \rho_l v_l) + \frac{\partial}{\partial x}(\alpha_l \rho_l v_l u_l) + \frac{\partial}{\partial y}(\alpha_l \rho_l v_l v_l) + \frac{\partial}{\partial z}(\alpha_l \rho_l v_l w_l) = -\alpha_l \frac{\partial P}{\partial y} - \tau'''_{\mathrm{wy,l}} + \tau'''_{\mathrm{iy,vl}} - \Gamma'''(1-\eta)v \quad (19)$$

$$\frac{\partial}{\partial t}(\alpha_l \rho_l w_l) + \frac{\partial}{\partial x}(\alpha_l \rho_l w_l u_l) + \frac{\partial}{\partial y}(\alpha_l \rho_l w_l v_l) + \frac{\partial}{\partial z}(\alpha_l \rho_l w_l w_l) = -\alpha_l \frac{\partial P}{\partial z} - \tau'''_{\mathrm{wz,l}} + \tau'''_{\mathrm{iz,vl}} - \Gamma'''(1-\eta)w \quad (20)$$

Note that in the liquid momentum equations, the interfacial shear components became additive, whereas the momentum source from mass transfer became subtractive.

Equations (21)–(23) show the x-, y- and z- components of momentum conservation for the entrained field.

$$\begin{aligned}\frac{\partial}{\partial t}(\alpha_e \rho_l u_e) + \frac{\partial}{\partial x}(\alpha_e \rho_l u_e u_e) + \frac{\partial}{\partial y}(\alpha_e \rho_l u_e v_e) + \frac{\partial}{\partial z}(\alpha_e \rho_l u_e w_e) \\ = -\alpha_e \frac{\partial P}{\partial x} - \alpha_e \rho_l g - \tau'''_{\mathrm{wx,e}} + \tau'''_{\mathrm{ix,ve}} - \Gamma''' \eta u + \sum_{k=1}^{\mathrm{nk}} (M_e^T)'''_k\end{aligned} \quad (21)$$

$$\frac{\partial}{\partial t}(\alpha_e \rho_l v_e) + \frac{\partial}{\partial x}(\alpha_e \rho_l v_e u_e) + \frac{\partial}{\partial y}(\alpha_e \rho_l v_e v_e) + \frac{\partial}{\partial z}(\alpha_e \rho_l v_e w_e) = -\alpha_e \frac{\partial P}{\partial y} - \tau'''_{\mathrm{wy,e}} + \tau'''_{\mathrm{iy,ve}} - \Gamma''' \eta v \quad (22)$$

$$\frac{\partial}{\partial t}(\alpha_e \rho_l w_e) + \frac{\partial}{\partial x}(\alpha_e \rho_l w_e u_e) + \frac{\partial}{\partial y}(\alpha_e \rho_l w_e v_e) + \frac{\partial}{\partial z}(\alpha_e \rho_l w_e w_e) = -\alpha_e \frac{\partial P}{\partial z} - \tau'''_{\mathrm{wz,e}} + \tau'''_{\mathrm{iz,ve}} - \Gamma''' \eta w \quad (23)$$

2.2.3.3 Energy Equation in Cartesian Coordinates

Only two energy equations are required: one for vapor phase, and one for the entrained and liquid fields. Equation (24) provides the vapor energy equation in Cartesian coordinates.

$$\frac{\partial}{\partial t}(\alpha_v \rho_v h_v) + \frac{\partial}{\partial x}(\alpha_v \rho_v h_v u_v) + \frac{\partial}{\partial y}(\alpha_v \rho_v h_v v_v) + \frac{\partial}{\partial z}(\alpha_v \rho_v h_v w_v) = \frac{\partial}{\partial y} q^T_{v,y} + \frac{\partial}{\partial z} q^T_{v,z} + \Gamma''' h + q'''_{wv} + \alpha_v \frac{\partial P}{\partial t} \quad (24)$$

The q_v^T term is the transfer of energy into or out of the mesh cell as a result of turbulent exchange; it is calculated using a turbulent diffusion approximation. Enthalpy will be carried into or out of the mesh cell in the lateral directions only—hence the absence of the x-direction term. The $\Gamma''' h$ term is the implicit heat transfer term which accounts for evaporation and condensation effects. The enthalpy in the term will either be the saturation liquid or vapor enthalpy; however, no subscript has been provided in Eq. (24) for h because the implicit heat transfer model is slightly more complicated than it is depicted here, because it accounts for contributions of mass transfer from subcooled liquid, subcooled vapor, super-heated liquid, and super-heated vapor. The enthalpy carried with Γ''' will depend on the evaporating and condensing sources. The implicit heat transfer model is discussed in greater detail in Section 7.

Equation (25) presents the liquid energy equation.

$$\begin{aligned}\frac{\partial}{\partial t}((\alpha_l + \alpha_e)\rho_l h_l) + \frac{\partial}{\partial x}(\alpha_l \rho_l h_l u_l) + \frac{\partial}{\partial x}(\alpha_e \rho_l h_l u_e) + \frac{\partial}{\partial y}(\alpha_l \rho_l h_l v_l) + \frac{\partial}{\partial y}(\alpha_e \rho_l h_l v_e) \\ + \frac{\partial}{\partial z}(\alpha_l \rho_l h_l w_l) + \frac{\partial}{\partial z}(\alpha_e \rho_l h_l w_e) = \frac{\partial}{\partial y} q^T_{l,y} + \frac{\partial}{\partial z} q^T_{l,z} - \Gamma''' h + q'''_{wv} + (\alpha_l + \alpha_e)\frac{\partial P}{\partial t}\end{aligned} \quad (25)$$

Equation (25) includes six advection terms because both droplet and liquid fields are modeled. However, turbulent mixing and void drift only cause mixing of the liquid field.

2.2.4 CTF Conservation Equations in Subchannel Form

The subchannel approach is a simplification of the conservation equations that only considers two flow directions—axial flow and lateral flow. The lateral flow directions are not a set of fixed coordinates; instead, the term, "lateral flow" covers any orthogonal direction to the vertical axis. Because fixed coordinates are not defined for the lateral direction in the subchannel approach, lateral flow has no direction once it leaves a gap. Lateral flow enters a subchannel volume through "gaps" between the volume and other adjacent subchannel volumes. This is a suitable assumption for the axially dominated flow of a reactor fuel bundle because the relatively minuscule lateral flows transfer little momentum across subchannel mesh cell elements. The result of this assumption is one less momentum equation for each of the three fields.

2.2.4.1 Mass Conservation Equations in Subchannel Coordinates

The vapor, liquid, and entrained droplet mass conservation equations are presented in Eqs. (26)–(28). The gap velocity is now represented by w_k. The gap mass transfer terms are summed over all the gaps connecting to the mesh cell.

$$\frac{\partial}{\partial t}\left(\alpha_v \rho_v\right) + \frac{\partial}{\partial x}\left(\alpha_v \rho_v u_v\right) + \sum_{k=1}^{\mathrm{nk}} \left(\alpha_v \rho_v w_v\right)_k = \Gamma''' + \sum_{k=1}^{\mathrm{nk}} \left(M_v^{T'''}\right)_k \tag{26}$$

$$\frac{\partial}{\partial t}\left(\alpha_l \rho_l\right) + \frac{\partial}{\partial x}\left(\alpha_l \rho_l u_l\right) + \sum_{k=1}^{\mathrm{nk}} \left(\alpha_l \rho_l w_l\right)_k = -\Gamma'''(1-\eta) - S''' + \sum_{k=1}^{\mathrm{nk}} \left(M_l^{T'''}\right)_k \tag{27}$$

$$\frac{\partial}{\partial t}\left(\alpha_e \rho_l\right) + \frac{\partial}{\partial x}\left(\alpha_e \rho_l u_e\right) + \sum_{k=1}^{\mathrm{nk}} \left(\alpha_e \rho_l w_e\right)_k = -\Gamma'''\eta + S''' + \sum_{k=1}^{\mathrm{nk}} \left(M_e^{T'''}\right)_k \tag{28}$$

2.2.4.2 Momentum Conservation Equations in Subchannel Coordinates

Momentum equations are only needed for the axial and lateral directions for each field. The axial momentum equations for vapor, liquid, and entrained droplets are presented in Eqs. (29)–(31). The additional terms, A, A_k, and S_k, are the axial cross-sectional area, gap cross-sectional area, and gap width, respectively. The axial momentum equations have an advection term dedicated to the axial direction and a second advection term that handles transverse convection of axial momentum from all existing volume gaps. All gaps connected to the axial momentum cell are considered for the transverse advection term in the axial momentum equation.

$$\begin{aligned}\frac{\partial}{\partial t}\left(\alpha_v \rho_v u_v A\right) + \frac{\partial}{\partial x}\left(\alpha_v \rho_v u_v u_v A\right) + \sum_{k=1}^{\mathrm{nk}} \left(\alpha_v \rho_v u_v w_v S\right)_k = -\alpha_v A \frac{\partial P}{\partial x} - \alpha_v \rho_v g A - \tau'''_{\mathrm{wx,v}} A - \tau'''_{\mathrm{ix,vl}} A \\ - \tau'''_{\mathrm{ix,ve}} A + \Gamma''' u A + \sum_{k=1}^{\mathrm{nk}} \left(M_v^{T'''} A\right)_k\end{aligned} \tag{29}$$

$$\frac{\partial}{\partial t}(\alpha_l \rho_l u_l A) + \frac{\partial}{\partial x}(\alpha_l \rho_l u_l u_l A) + \sum_{k=1}^{\mathrm{nk}} (\alpha_l \rho_l u_l w_l S)_k = -\alpha_l A \frac{\partial P}{\partial x} - \alpha_l \rho_l g A - \tau'''_{\mathrm{wx,l}} A + \tau'''_{\mathrm{ix,vl}} A - \Gamma'''(1-\eta) u A - S''' u A + \sum_{k=1}^{\mathrm{nk}} \left(M_l^{T'''} A\right)_k \tag{30}$$

$$\frac{\partial}{\partial t}(\alpha_e \rho_l u_e A) + \frac{\partial}{\partial x}(\alpha_e \rho_l u_e u_e A) + \sum_{k=1}^{\mathrm{nk}} (\alpha_e \rho_l u_e w_e S)_k = -\alpha_e A \frac{\partial P}{\partial x} - \alpha_e \rho_l g A - \tau'''_{\mathrm{wx,e}} A + \tau'''_{\mathrm{ix,ve}} A - \Gamma''' \eta u A + S''' u A + \sum_{k=1}^{\mathrm{nk}} \left(M_e^{T'''} A\right)_k \tag{31}$$

The transverse momentum equations, which are solved for transverse momentum cells (discussed in Section 2.3), have advection terms for the axial direction and the direction of the gap being modeled. The transverse directions orthogonal to the gap direction are not considered in the subchannel approach. Furthermore, gaps cannot convect transverse momentum from and to one another because they do not know of each other's existence. Instead, transverse momentum simply "disappears" when it leaves a gap and goes into a channel. The lateral advection term in the equations will be convecting zero transverse momentum into the gap if fluid velocity is going into the gap, whereas it will convect the gap momentum out of the gap if fluid velocity is going out of the gap.

Lateral momentum equations are shown in Eqs. (32)–(34). Axial velocity can still convect lateral momentum in and out of the transverse momentum cells because gap cells are aware of other gaps above and below them. The subchannel momentum equations are described further after the CTF mesh and finite-differenced conservation equations are described in Section 2.3.

$$\frac{\partial}{\partial t}(\alpha_v \rho_v w_v) + \frac{\partial}{\partial z}(\alpha_v \rho_v w_v w_v) + \frac{\partial}{\partial x}(\alpha_v \rho_v w_v u_v) = -\alpha_v \frac{\partial P}{\partial z} - \tau'''_{\mathrm{wx,v}} - \tau'''_{\mathrm{ix,vl}} - \tau'''_{\mathrm{ix,ve}} + \Gamma''' w \tag{32}$$

$$\frac{\partial}{\partial t}(\alpha_l \rho_l w_l) + \frac{\partial}{\partial z}(\alpha_l \rho_l w_l w_l) + \frac{\partial}{\partial x}(\alpha_l \rho_l w_l u_l) = -\alpha_l \frac{\partial P}{\partial z} - \tau'''_{\mathrm{wx,l}} + \tau'''_{\mathrm{ix,vl}} - \Gamma'''(1-\eta) w - S''' w \tag{33}$$

$$\frac{\partial}{\partial t}(\alpha_e \rho_l w_e) + \frac{\partial}{\partial z}(\alpha_e \rho_l w_e w_e) + \frac{\partial}{\partial x}(\alpha_e \rho_l w_e u_e) = -\alpha_e \frac{\partial P}{\partial z} - \tau'''_{\mathrm{wx,l}} + \tau'''_{\mathrm{ix,ve}} - \Gamma''' \eta w + S''' w \tag{34}$$

2.2.4.3 Energy Conservation Equations in Subchannel Coordinates

The vapor and liquid energy conservation equations are given in Eqs. (35) and (36).

$$\frac{\partial}{\partial t}(\alpha_v \rho_v h_v) + \frac{\partial}{\partial x}(\alpha_v \rho_v h_v u_v) + \sum_{k=1}^{\mathrm{nk}} (\alpha_v \rho_v h_v w_v)_k = -\sum_{k=1}^{\mathrm{nk}} q_v^{T'''} + \Gamma''' h + q'''_{wv} + \alpha_v \frac{\partial P}{\partial t} \tag{35}$$

$$\frac{\partial}{\partial t}(\alpha_l \rho_l h_l) + \frac{\partial}{\partial x}(\alpha_l \rho_l h_l u_l) + \frac{\partial}{\partial x}(\alpha_e \rho_l h_l u_e) + \sum_{k=1}^{\mathrm{nk}} (\alpha_l \rho_l h_l w_l)_k + \sum_{k=1}^{\mathrm{nk}} (\alpha_e \rho_l h_l w_e)_k = -\sum_{k=1}^{\mathrm{nk}} q_l^{T'''} - \Gamma''' h + q'''_{wl} + (\alpha_l + \alpha_e) \frac{\partial P}{\partial t} \tag{36}$$

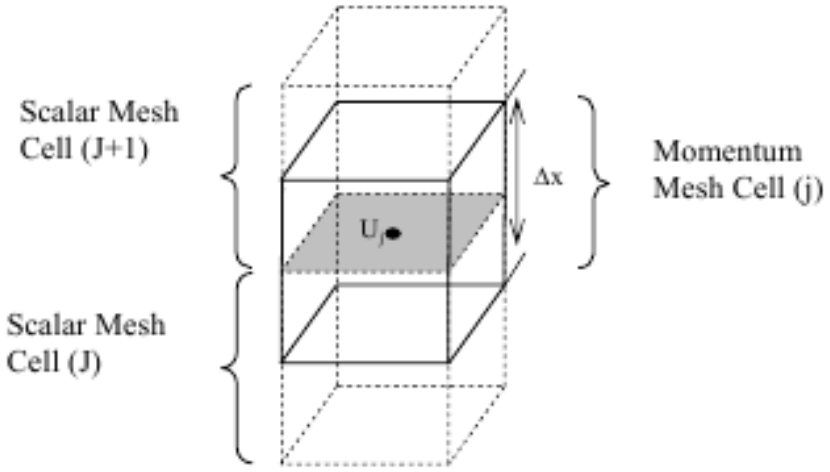

Figure 2. Scalar mesh cell and axial momentum mesh cell configuration.

2.3 DISCRETIZED CONSERVATION EQUATIONS AND COMPUTATIONAL MESH

2.3.1 CTF Flow Volume Meshing Approach

For the aforementioned conservation equations to be of practical use, they must be applied in some way to the modeling geometry. This is achieved by generating a mesh (grid) of volumes and then setting up the collection of mass, momentum, and energy equations for each field in each of the mesh cells. Actually, two meshes are utilized which are staggered from one another. One mesh—known as the *scalar mesh*—is used to define the scalar variables (e.g., α, P, h, and fluid properties). The second mesh—known as the itmomentum mesh—is used to define the fluid velocity field. The choice for a staggered mesh comes down to numerical stability and accuracy issues, which are discussed in more detail in Patankar [4].

Technically speaking, there are actually three different meshes; the momentum mesh is comprised of transverse momentum cells and axial momentum cells because both transverse and axial velocities must be determined. Figure 2 [5] shows how scalar mesh cells and axial momentum mesh cells overlap. Note that the scalar mesh cell and the axial momentum mesh cell just above it have the same index identifier. In the figure and this document, they are differentiated by capital and lowercase letters, but in the actual CTF source code, the cases are the same.

The scalar quantities are defined at the center of the scalar mesh cells, and the velocities are defined at the center of the momentum cells. As a result of this and the staggered mesh approach, the axial velocities will be available at the top and bottom faces of the scalar mesh cell. In a similar fashion, the transverse velocities will be available on the side faces of the scalar mesh cells because the transverse momentum cells overlap the scalar mesh cell sides, as shown in Figure 3 [5]. Note that in Figure 3, the adjacent lower and higher numbered scalar mesh cells are labeled with indices *ii* and *jj*.

The mesh generation process is handled by CTF after the user provides basic model information, including the number of model sections, the number of channels per section, the number of scalar mesh cells per channel, and channel connection information. A *section* is a grouping of channels all of the same total length. Sections communicate with one another via mass, energy, and momentum transport, but only in the axial direction (i.e., there are no gaps between sections). The user defines the number of channels located within each section and then specifies how the channels communicate with channels above or below the section they reside in, or the user specifies whether they do not communicate with any channels for cases in which they are next to a boundary.

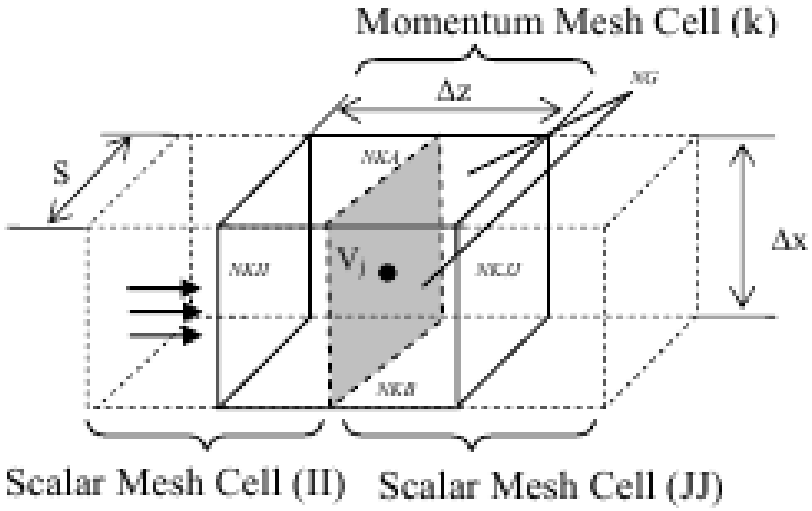

Figure 3. Scalar mesh cell and transverse momentum mesh cell configuration.

Inside the section, the user declares which subchannels communicate laterally via gaps, the channel geometry information, and the number of scalar mesh cells within the channels. It is also possible to have variable scalar mesh cell lengths in a section if it is necessary to obtain greater flow field detail in a certain model location. An example of a model mesh is presented in Figure 4 [6].

The features presented above comprise the extent of user control over the model meshing procedure. CTF will use that information to make a structured scalar mesh grid and will then connect the scalar mesh cells with axial momentum cells. A transverse momentum cell is created for each scalar cell in channels defined as having gaps, but if no gaps are defined, then no transverse momentum cells will be created.

Finite-difference forms of the conservation equations which can be solved by numerical method are then defined for the solution mesh. The discretized forms, like the previous forms, can be in Cartesian or subchannel forms, but as will be shown, actual transverse direction is not important for the mass and energy equations. The user must choose which form of the conservation equations should be used. If the Cartesian form is chosen, then the user must enter extra information, such as specification of the other gaps that each gap faces and which gaps convect momentum in the orthogonal direction.

2.3.2 Finite-Difference Conservation Equations

Once the basic flow modeling equations have been laid out and the flow volume meshing approach is defined, the conservation equations must be put into finite-difference form. The derivation begins with the mass conservation equation.

2.3.2.1 Finite-Difference Mass Conservation Equation

The process begins with the expanded mass conservation equations of Section 2.2.3.1. Equation (12) is repeated here, which is the expanded vapor mass conservation equation in Cartesian coordinates.

$$\frac{\partial}{\partial t}(\alpha_v \rho_v) + \frac{\partial}{\partial x}(\alpha_v \rho_v u_v) + \frac{\partial}{\partial y}(\alpha_v \rho_v v_v) + \frac{\partial}{\partial z}(\alpha_v \rho_v w_v) = \Gamma''' + \sum_{k=1}^{\mathrm{nk}} \left(M_v^{T'''}\right)_k$$

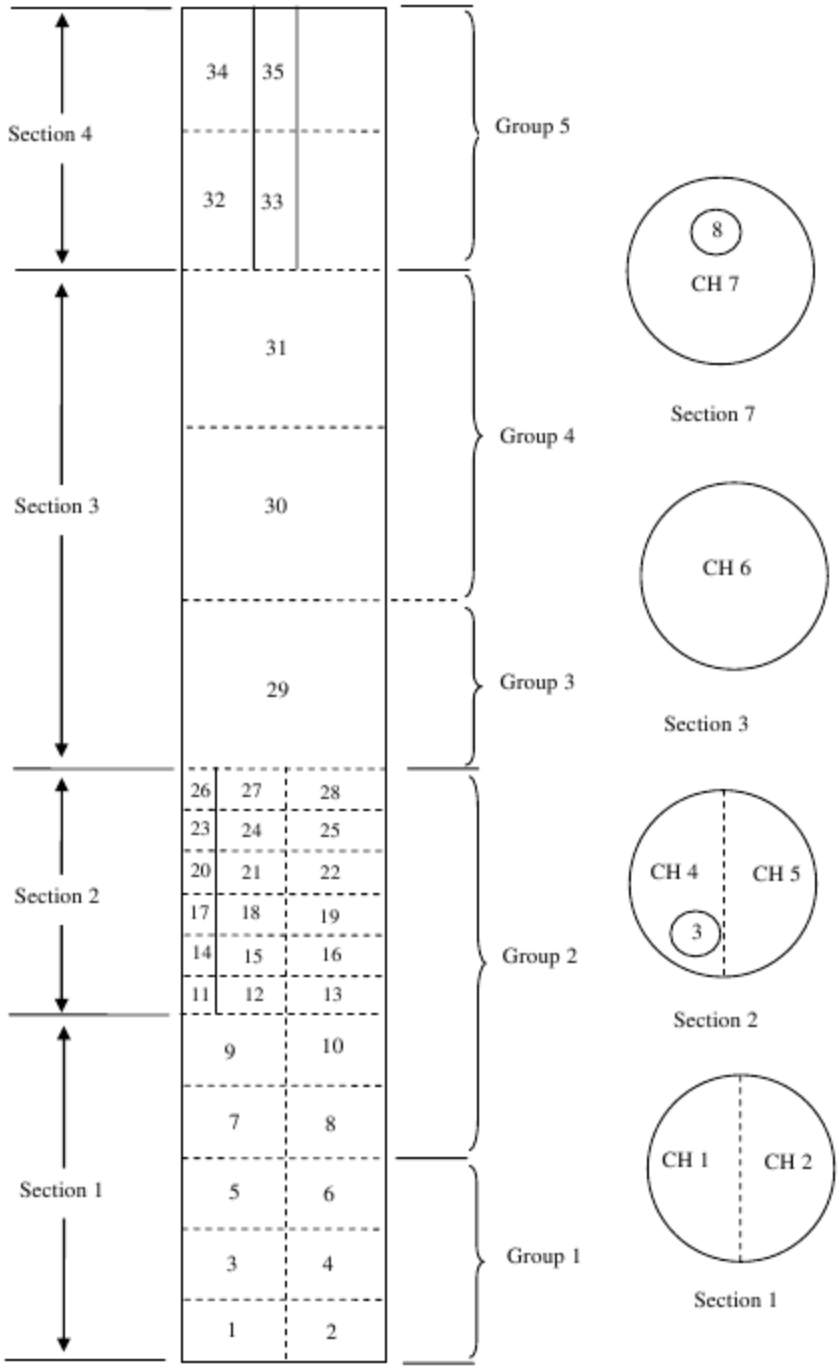

Figure 4. Example of a CTF mesh.

First, the volumetric mass creation term is transformed into a total mass creation term by multiplying through by cell volume.

$$\frac{\partial}{\partial t}\left(\alpha_v\rho_v\right)\Delta X\Delta Y\Delta Z+\frac{\partial}{\partial x}\left(\alpha_v\rho_v u_v\right)\Delta X\Delta Y\Delta Z+\frac{\partial}{\partial y}\left(\alpha_v\rho_v v_v\right)\Delta X\Delta Y\Delta Z+\frac{\partial}{\partial z}\left(\alpha_v\rho_v w_v\right)\Delta X\Delta Y\Delta Z=\Gamma+\sum_{k=1}^{\mathrm{nk}}\left(M_v^T\right)_k \tag{37}$$

The partial derivatives are expanded by taking the difference in mass change over time and over the control volume spatial directions in the specified directions.

$$\begin{aligned}&\frac{\left[\left(\alpha_v\rho_v\right)_J^{n+1}-\left(\alpha_v\rho_v\right)_J^n\right]}{\Delta t}\Delta X\Delta Y\Delta Z+\frac{\sum_{ia=1}^{na}\left[\left(\alpha_v\rho_v\right)^{\tilde{n}}u_{v,j}^{n+1}\Delta Y\Delta Z\right]_{ia}-\sum_{ib=1}^{nb}\left[\left(\alpha_v\rho_v\right)^{\tilde{n}}u_{v,j-1}^{n+1}\Delta Y\Delta Z\right]_{ib}}{\Delta X}\Delta X\\&+\frac{\sum_{k_{y+\Delta y}=1}^{nk_{y+\Delta y}}\left[\left(\alpha_v\rho_v\right)^{\tilde{n}}v_{v,J}^{n+1}\Delta Z\Delta X\right]_{k_{y+\Delta y}}-\sum_{k_y=1}^{nk_y}\left[\left(\alpha_v\rho_v\right)^{\tilde{n}}v_{v,J}^{n+1}\Delta Z\Delta X\right]_{k_y}}{\Delta Y}\Delta Y\\&+\frac{\sum_{k_{z+\Delta z}=1}^{nk_{z+\Delta z}}\left[\left(\alpha_v\rho_v\right)^{\tilde{n}}v_{v,J}^{n+1}\Delta Y\Delta X\right]_{k_{z+\Delta z}}-\sum_{k_z=1}^{nk_z}\left[\left(\alpha_v\rho_v\right)^{\tilde{n}}v_{v,J}^{n+1}\Delta Y\Delta X\right]_{k_z}}{\Delta Z}\Delta Z=\Gamma+\sum_{k=1}^{\mathrm{nk}}\left(M_v^T\right)_k\end{aligned} \tag{38}$$

Starting with the first term on the LHS, the temporal change in mesh cell mass is represented by subtracting the old timestep mass from the new timestep mass. The old timestep values are represented with an n superscript.

The next three fractions are the advection terms in the x-, y- and z-directions. The reason summation operators are shown in these terms is because each side of the scalar mesh may have multiple connections to other cells. The first term subtracts all the scalar cell top face (na) flow rates from all the bottom face (nb) flow rates. The positive direction for axial flow is defined moving from the cell bottom to cell top. The CTF convention is that flow moves from bottom to top; hence the given formulation.

A new superscript, $\tilde{n}$, appears in the advection terms. This superscript indicates that the scalar cell from which the term originates is dependent on the flow direction. For example, if in the axial advection term $u_{v,j-1}$ is positive, then $(\alpha_v\rho_v)_{J-1}$ will be used, and mass will be taken from cell $J-1$ and deposited into cell J. However, if $u_{v,j-1}$ is negative, then mass will be removed from cell J and put into cell $J-1$, and $(\alpha_v\rho_v)_J$ will be used.

The second advection term subtracts all the $y+\Delta y$ face flow rates from the y face flow rates. The z-direction advection term is similarly derived. In the next derivation, the actual orthogonal direction is collapsed into one term because the direction has no impact on the mass conservation equation. Furthermore, the correct geometry terms are used. Note that in this modification, the removal of the directional dependence in the advection terms converts the equation into a form that would be arrived at using the subchannel approach.

$$\begin{aligned}&\frac{\left[\left(\alpha_v\rho_v\right)_J^{n+1}-\left(\alpha_v\rho_v\right)_J^n\right]}{\Delta t}\Delta X_J A_{c,J}+\sum_{ia=1}^{na}\left[\left(\alpha_v\rho_v\right)^{\tilde{n}}u_{v,j}^{n+1}A_{m,ia}\right]_{ia}-\sum_{ib=1}^{nb}\left[\left(\alpha_v\rho_v\right)^{\tilde{n}}u_{v,j-1}^{n+1}A_{m,ib}\right]_{ib}\\&+\sum_{k=1}^{\mathrm{nk}}\left[\left(\alpha_v\rho_v\right)^{\tilde{n}}w_{k,v}^{n+1}L_k\right]_J\Delta X_J=\Gamma+\sum_{k=1}^{\mathrm{nk}}\left(M_v^T\right)_k+\text{Source}\end{aligned} \tag{39}$$

Here, the $\Delta X/\Delta X$, $\Delta Y/\Delta Y$, and $\Delta Z/\Delta Z$ terms in the advection terms have been cancelled. The scalar cell cross-sectional area has replaced the $\Delta Y \Delta Z$ term in the temporal term. The gap width, L_k, has been substituted for ΔY in the transverse advection term; $L_k \Delta X_J$ is the cross-sectional area in the transverse direction through which mass is convected. As for the axial advection term, $\Delta Y \Delta Z$ has been replaced with the cross-sectional area of the axial momentum cell that carries mass into or out of the scalar mesh cell. The transverse velocity of the gap under consideration is more simply notated with w_k. Finally, a source term has been added on the RHS.

The liquid and entrained field mass conservation equations are similarly derived. The final results are shown in Eq. (40) for liquid and Eq. (41) for droplets. These equations represent the finite-differenced forms of the mass conservation equations used in CTF which are used for either the Cartesian or subchannel modeling approach.

$$\begin{aligned}\frac{\left[(\alpha_l\rho_l)_J^{n+1} - (\alpha_l\rho_l)_J^n\right]}{\Delta t}\Delta X_J A_{c,J} + \sum_{ib=1}^{nb}\left[(\alpha_l\rho_l)^{\tilde{n}} u_{l,j-1}^{n+1} A_{m,ib}\right]_{ib} - \sum_{ia=1}^{na}\left[(\alpha_l\rho_l)^{\tilde{n}} u_{l,j}^{n+1} A_{m,ia}\right]_{ia} \\ + \sum_{k=1}^{\mathrm{nk}}\left[(\alpha_l\rho_l)^{\tilde{n}} w_{k,l}^{n+1}\right]_J L_k \Delta X_J = -\Gamma(1-\eta) - S + \text{Source}\end{aligned} \tag{40}$$

$$\begin{aligned}\frac{\left[(\alpha_e\rho_l)_J^{n+1} - (\alpha_e\rho_l)_J^n\right]}{\Delta t}\Delta X_J A_{c,J} + \sum_{ib=1}^{nb}\left[(\alpha_e\rho_l)^{\tilde{n}} u_{l,j-1}^{n+1} A_{m,ib}\right]_{ib} \\ - \sum_{ia=1}^{na}\left[(\alpha_e\rho_l)^{\tilde{n}} u_{l,j}^{n+1} A_{m,ia}\right]_{ia} + \sum_{k=1}^{\mathrm{nk}}\left[(\alpha_e\rho_l)^{\tilde{n}} w_{k,l}^{n+1}\right]_J L_k \Delta X_J = -\Gamma\eta - S + \text{Source}\end{aligned} \tag{41}$$

2.3.2.2 Finite-Differenced Momentum Conservation Equation

The finite-differenced momentum equation derivation for the vapor field in the axial direction begins using the Cartesian form. For this, Eq. (15) is used, which is restated below for convenience.

$$\begin{aligned}&\frac{\partial}{\partial t}(\alpha_v\rho_v u_v) + \frac{\partial}{\partial x}(\alpha_v\rho_v u_v u_v) + \frac{\partial}{\partial y}(\alpha_v\rho_v u_v v_v) + \frac{\partial}{\partial z}(\alpha_v\rho_v u_v w_v) \\ &= -\alpha_v\frac{\partial P}{\partial x} - \alpha_v\rho_v g - \tau'''_{\mathrm{wx,v}} - \tau'''_{\mathrm{ix,vl}} - \tau'''_{\mathrm{ix,ve}} + \Gamma''' u + \sum_{k=1}^{\mathrm{nk}}\left(M_v^T\right)_k'''\end{aligned}$$

Like for the finite-differenced mass conservation equation, the cell volume is multiplied through the equation, and discrete forms of the advection terms are expanded, subtracting momentum outflows from inflows. The advection terms are moved to the RHS so that only the temporal term remains on the left.

$$
\begin{aligned}
\frac{\left[(\alpha_v\rho_v u_v)_j^{n+1} - (\alpha_v\rho_v u_v)_j^n\right]}{\Delta t}\Delta X\Delta Y\Delta Z = &\left\{\sum_{ib=1}^{nb}\left[(\alpha_v\rho_v u_v)^{\tilde{n}}\bar{u}_v^n\right]_{ib}\Delta Y\Delta Z - \sum_{ia=1}^{na}\left[(\alpha_v\rho_v u_v)^{\tilde{n}}\bar{u}_v^n\right]_{ia}\Delta Y\Delta Z\right\} \\
&+\left\{\left(\sum_{kb_y=1}^{nkb_y}\left[(\alpha_v\rho_v u_v)^{\tilde{n}}v_v^n\right]_{kb_y}\Delta X\Delta Z + \sum_{ka_y=1}^{nka_y}\left[(\alpha_v\rho_v u_v)^{\tilde{n}}v_v^n\right]_{ka_y}\Delta X\Delta Z\right)\right. \\
&\qquad -\left(\sum_{kb_{y+\Delta y}=1}^{nkb_{y+\Delta y}}\left[(\alpha_v\rho_v u_v)^{\tilde{n}}v_v^n\right]_{(kb_y+\Delta y)}\Delta X\Delta Z\right. \\
&\qquad\left.\left. + \sum_{ka_{y+\Delta y}=1}^{nka_{y+\Delta y}}\left[(\alpha_v\rho_v u_v)^{\tilde{n}}v_v^n\right]_{(ka_y+\Delta y)}\Delta X\Delta Z\right)\right\} \\
&+\left\{\left(\sum_{kb_z=1}^{nkb_z}\left[(\alpha_v\rho_v u_v)^{\tilde{n}}w_v^n\right]_{kb_z}\Delta X\Delta Y + \sum_{ka_z=1}^{nka_z}\left[(\alpha_v\rho_v u_v)^{\tilde{n}}w_v^n\right]_{ka_z}\Delta X\Delta Y\right)\right. \\
&\qquad -\left(\sum_{kb_{z+\Delta z}=1}^{nkb_{z+\Delta z}}\left[(\alpha_v\rho_v u_v)^{\tilde{n}}w_v^n\right]_{(kb_z+\Delta z)}\Delta X\Delta Y\right. \\
&\qquad\left.\left. + \sum_{ka_{z+\Delta z}=1}^{nka_{z+\Delta z}}\left[(\alpha_v\rho_v u_v)^{\tilde{n}}w_v^n\right]_{(ka_z+\Delta z)}\Delta X\Delta Y\right)\right\} \\
&- (\overline{\alpha_v\rho_v})_j^n\, g\Delta X\Delta Y\Delta Z - \left(P_{J+1}^{n+1} - P_J^{n+1}\right)\bar{\alpha}_{v,j}^n\Delta Y\Delta Z - \tau_{w,v,j} \\
&- \tau_{i,vl,j} - \tau_{i,ve,j} + \Gamma u^n + \text{Source}_{v,j} + \sum_{kb=1}^{nkb}\left(M_v^T\right)_k + \sum_{ka=1}^{nka}\left(M_v^T\right)_k
\end{aligned}
\tag{42}
$$

The y- and z-direction advection terms have four terms. Because of the staggered mesh approach, gaps can bring momentum into the axial momentum cell on each face from the scalar cell above or below. In the equation, the terms k_y and $k_{y+\Delta y}$ denote the side faces of the mesh cell in the y-direction. Similarly, the k_z and $k_{z+\Delta z}$ terms denote the side faces of the mesh cell in the z-direction.

In the advection terms, terms with bars over them denote that the value is calculated. For example, in the x-direction advection term, the convecting velocity term has a bar over it because the velocity is not defined at the axial momentum cell faces where it is needed. Instead, the velocities of axial momentum cell j and $j-1$ must be averaged (for the lower face velocity). This is not necessary for the side faces because velocities are defined on the faces. For the pressure term, however, it is necessary to average scalar cells J and $J+1$ void fractions to obtain the value for momentum cell j.

The shear terms contain an implicit portion. The wall shear is defined as a coefficient times mass flow rate, and the interfacial shear is defined as a coefficient times velocity. The coefficient is calculated using all old-time values, while it multiplies by a new time velocity, meaning there is both old and new-time velocity in the shear terms.

$$
\tau_{w,x} = k_{w,x}\dot{m}\Delta X \tag{43}
$$

$$
\tau_{i,x} = k_{i,x}u\Delta X \tag{44}
$$

The wall drag model is further described in Section 6, and the interfacial drag model is further described in Section 5. It was necessary to present Eqs. (43) and (44) to inform the numerical solution discussion below.

One final substitution is made in the vapor axial momentum conservation equation—the cell geometry terms (e.g., ΔX, ΔY, and ΔZ) are replaced with the appropriate CTF geometry terms.

$$
\begin{aligned}
\frac{\left[(\alpha_v\rho_v u_v)_j^{n+1} - (\alpha_v\rho_v u_v)_j^n\right]}{\Delta t}\Delta X_j A_{m,j} = &\left\{\sum_{ib=1}^{nb}\left[(\alpha_v\rho_v u_v)^{\tilde{n}}\bar{u}_{v,J}^n\right]_{ib}A_{c,J} - \sum_{ia=1}^{na}\left[(\alpha_v\rho_v u_v)^{\tilde{n}}\bar{u}_{v,J+1}^n\right]_{ia}A_{c,J+1}\right\} \\
&+\left\{\left(\sum_{kb_y=1}^{nkb_y}\left[(\alpha_v\rho_v u_v)^{\tilde{n}}v_v^n\right]_{kb_y}\frac{\Delta X_J}{2}L_{kb_y} + \sum_{ka_y=1}^{nka_y}\left[(\alpha_v\rho_v u_v)^{\tilde{n}}v_v^n\right]_{ka_y}\frac{\Delta X_{J+1}}{2}L_{ka_y}\right)\right. \\
&\qquad -\left(\sum_{kb_{y+\Delta y}=1}^{nkb_{(y+\Delta y)}}\left[(\alpha_v\rho_v u_v)^{\tilde{n}}v_v^n\right]_{(kb_{y+\Delta y})}\frac{\Delta X_J}{2}L_{kb_{y+\Delta y}}\right. \\
&\qquad\left.\left. + \sum_{ka_{(y+\Delta y)}=1}^{nka_{y+\Delta y}}\left[(\alpha_v\rho_v u_v)^{\tilde{n}}v_v^n\right]_{(ka_{y+\Delta y})}\frac{\Delta X_{J+1}}{2}L_{ka_{y+\Delta y}}\right)\right\} \\
&+\left\{\left(\sum_{kb_z=1}^{nkb_z}\left[(\alpha_v\rho_v u_v)^{\tilde{n}}w_v^n\right]_{kb_z}\frac{\Delta X_J}{2}L_{kb_z}\right.\right. \\
&\qquad\left. + \sum_{ka_z=1}^{nka_z}\left[(\alpha_v\rho_v u_v)^{\tilde{n}}w_v^n\right]_{ka_z}\frac{\Delta X_{J+1}}{2}L_{ka_z}\right) \\
&\qquad -\left(\sum_{kb_{z+\Delta z}=1}^{nkb_{z+\Delta z}}\left[(\alpha_v\rho_v u_v)^{\tilde{n}}w_v^n\right]_{(kb_{z+\Delta z})}\frac{\Delta X_J}{2}L_{kb_{z+\Delta z}}\right. \\
&\qquad\left.\left. + \sum_{ka_{z+\Delta z}=1}^{nka_{z+\Delta z}}\left[(\alpha_v\rho_v u_v)^{\tilde{n}}w_v^n\right]_{(ka_{z+\Delta z})}\frac{\Delta X_{J+1}}{2}L_{ka_{z+\Delta z}}\right)\right\} \\
&- (\overline{\alpha_v\rho_v})_j^n\, g\Delta X_j A_{m,j} - \left(P_{J+1}^{n+1} - P_J^{n+1}\right)\bar{\alpha}_{v,j}^n A_{m,j} - \tau_{w,v,j} - \tau_{i,vl,j} \\
&- \tau_{i,ve,j} + \Gamma u^n + \text{Source}_{v,j} + \sum_{kb=1}^{nkb}\left(M_v^T\right)_k + \sum_{ka=1}^{nka}\left(M_v^T\right)_k
\end{aligned}
\tag{45}
$$

Recall that L is the width of the gap under consideration. Some of the ΔX terms are divided by 2; because of the staggered mesh approach, gaps that cause transverse momentum advection into the axial momentum cell only do so though half of the side face cross-sectional area.

The axial liquid and entrained momentum equations are similarly derived and are presented in Eqs. (46) and (47).

$$
\begin{aligned}
\frac{\left[(\alpha_l\rho_l u_l)_j^{n+1} - (\alpha_l\rho_l u_l)_j^{n}\right]}{\Delta t}\Delta X_j A_{m,j} = & \left\{\sum_{ib=1}^{nb}\left[(\alpha_l\rho_l u_l)^{\tilde{n}}\bar{u}_l^n\right]_{ib} A_{c,J} - \sum_{ia=1}^{na}\left[(\alpha_l\rho_l u_l)^{\tilde{n}}\bar{u}_l^n\right]_{ia} A_{c,J+1}\right\} \\
& + \left\{\left(\sum_{kb_y=1}^{nkb_y}\left[(\alpha_l\rho_l u_l)^{\tilde{n}}v_l^n\right]_{kb_y}\frac{\Delta X_J}{2}L_{kb_y} + \sum_{ka_y=1}^{nka_y}\left[(\alpha_l\rho_l u_l)^{\tilde{n}}v_l^n\right]_{ka_y}\frac{\Delta X_{J+1}}{2}L_{ka_y}\right)\right. \\
& \qquad - \left(\sum_{kb_{y+\Delta y}=1}^{nkb_{y+\Delta y}}\left[(\alpha_l\rho_l u_l)^{\tilde{n}}v_l^n\right]_{(kb_{y+\Delta y})}\frac{\Delta X_J}{2}L_{kb_{y+\Delta y}}\right. \\
& \qquad \left.\left. + \sum_{ka_{y+\Delta y}=1}^{nka_{y+\Delta y}}\left[(\alpha_l\rho_l u_l)^{\tilde{n}}v_l^n\right]_{(ka_{y+\Delta y})}\frac{\Delta X_{J+1}}{2}L_{kay+\Delta y}\right)\right\} \\
& + \left\{\left(\sum_{kb_z=1}^{nkb_z}\left[(\alpha_l\rho_l u_l)^{\tilde{n}}w_l^n\right]_{kb_z}\frac{\Delta X_J}{2}L_{kb_z} + \sum_{ka_z=1}^{nka_z}\left[(\alpha_l\rho_l u_l)^{\tilde{n}}w_l^n\right]_{ka_z}\frac{\Delta X_{J+1}}{2}L_{ka_z}\right)\right. \\
& \qquad - \left(\sum_{kb_{z+\Delta z}=1}^{nkb_{z+\Delta z}}\left[(\alpha_l\rho_l u_l)^{\tilde{n}}w_l^n\right]_{kb_{z+\Delta z}}\frac{\Delta X_J}{2}L_{kb_{z+\Delta z}}\right. \\
& \qquad \left.\left. + \sum_{ka_{z+\Delta z}=1}^{nka_{z+\Delta z}}\left[(\alpha_l\rho_l u_l)^{\tilde{n}}w_l^n\right]_{ka_{z+\Delta z}}\frac{\Delta X_{J+1}}{2}L_{ka_{z+\Delta z}}\right)\right\} \\
& - (\overline{\alpha_l\rho_l})_j^n\, g\Delta X_j A_{m,j} - \left(P_{J+1}^{n+1} - P_J^{n+1}\right)\bar{\alpha}_{l,j}^n A_{m,j} - \tau_{w,l,j} \\
& + \tau_{i,vl,j} - \Gamma(1-\eta)u^n + \text{Source}_{l,j} + \sum_{kb=1}^{nkb}\left(M_l^T\right)_k + \sum_{ka=1}^{nka}\left(M_l^T\right)_k
\end{aligned}
\tag{46}
$$

$$
\begin{aligned}
\frac{\left[(\alpha_e\rho_l u_e)_j^{n+1} - (\alpha_e\rho_l u_e)_j^n\right]}{\Delta t}\Delta X_j A_{m,j} = & \left\{\sum_{ib=1}^{nb}\left[(\alpha_e\rho_l u_e)^{\tilde{n}}\bar{u}_e^n\right]_{ib}A_{c,J} - \sum_{ia=1}^{na}\left[(\alpha_e\rho_l u_e)^{\tilde{n}}\bar{u}_e^n\right]_{ia}A_{c,J+1}\right\} \\
& + \left\{\left(\sum_{kb_y=1}^{nkb_y}\left[(\alpha_e\rho_l u_e)^{\tilde{n}}v_e^n\right]_{kb_y}\frac{\Delta X_J}{2}L_{kb_y} + \sum_{ka_y=1}^{nka_y}\left[(\alpha_e\rho_l u_e)^{\tilde{n}}v_e^n\right]_{ka_y}\frac{\Delta X_{J+1}}{2}L_{ka_y}\right)\right. \\
& \qquad - \left(\sum_{kb_{y+\Delta y}=1}^{nkb_{y+\Delta y}}\left[(\alpha_e\rho_l u_e)^{\tilde{n}}v_e^n\right]_{(kb_{y+\Delta y})}\frac{\Delta X_J}{2}L_{kb_{y+\Delta y}}\right. \\
& \qquad \left.\left. + \sum_{ka_{y+\Delta y}=1}^{nka_{y+\Delta y}}\left[(\alpha_e\rho_l u_e)^{\tilde{n}}v_e^n\right]_{(ka_{y+\Delta y})}\frac{\Delta X_{J+1}}{2}L_{ka_{y+\Delta y}}\right)\right\} \\
& + \left\{\left(\sum_{kb_z=1}^{nkb_z}\left[(\alpha_e\rho_l u_e)^{\tilde{n}}w_e^n\right]_{kb_z}\frac{\Delta X_J}{2}L_{kb_z} + \sum_{ka_z=1}^{nka_z}\left[(\alpha_e\rho_l u_e)^{\tilde{n}}w_e^n\right]_{ka_z}\frac{\Delta X_{J+1}}{2}L_{ka_z}\right)\right. \\
& \qquad - \left(\sum_{kb_{z+\Delta z}=1}^{nkb_{z+\Delta z}}\left[(\alpha_e\rho_l u_e)^{\tilde{n}}w_e^n\right]_{(kb_{z+\Delta z})}\frac{\Delta X_J}{2}L_{kb_{z+\Delta z}}\right. \\
& \qquad \left.\left. + \sum_{ka_{z+\Delta z}=1}^{nka_{z+\Delta z}}\left[(\alpha_e\rho_l u_e)^{\tilde{n}}w_e^n\right]_{(ka_{z+\Delta z})}\frac{\Delta X_{J+1}}{2}L_{ka_{z+\Delta z}}\right)\right\} \\
& - (\overline{\alpha_e\rho_l})_j^n\, g\Delta X_j A_{m,j} - \left(P_{J+1}^{n+1} - P_J^{n+1}\right)\bar{\alpha}_{e,j}^n A_{m,j} - \tau_{w,e,j} \\
& + \tau_{i,ve,j} - \Gamma\eta u^n + \text{Source}_{e,j} + \sum_{kb=1}^{nkb}\left(M_e^T\right)_k + \sum_{ka=1}^{nka}\left(M_e^T\right)_k
\end{aligned}
\tag{47}
$$

Now that the axial direction has been addressed, the remaining directions are considered. For the y- and z-directions, the interest is on the transverse momentum cells. Actually, there is no need for a set of equations for both the y- and z-directions because CTF only solves for one transverse momentum cell (gap) at a time. It is only important that the transverse direction be distinguished (direction going from ii to jj) vs. the direction orthogonal to that (see Figure 3). From here, the transverse direction is denoted the y-direction, and the direction orthogonal to this is denoted as the z-direction.

The transverse momentum cells are in the same axial location, J as adjacent scalar mesh cells and may have axial momentum cells above, j, and below, $j-1$. There may also be multiple connections in the transverse and orthogonal direction. Note that the axial advection term no longer requires a calculated convection velocity because the axial velocity is defined at the transverse momentum cell's top and bottom faces. However, the transverse term requires $\bar{v}$ to be calculated. The vapor, liquid, and entrained momentum equations are presented in Eqs. (48), (49), and (50).

A few new parameters are introduced, defined as follows:

- *niib* — the number of scalar cells below transverse momentum cell k on the ii side that convect transverse momentum across the bottom face
- njjb — the number of scalar cells below transverse momentum cell k on the jj side that convect transverse momentum across the top face
- *niia* — the number of scalar cells above transverse momentum cell k on the ii side that convect transverse momentum across the bottom face

- njja — the number of scalar cells above transverse momentum cell k on the jj side that convect transverse momentum across the top face

$$
\begin{aligned}
\frac{\left[(\alpha_v\rho_v v_v)_k^{n+1} - (\alpha_v\rho_v v_v)_k^n\right]}{\Delta t}\Delta X_J \Delta Y_k \Delta Z_k = &\left\{\left(\sum_{iib=1}^{niib}\left[(\alpha_v\rho_v v_v)^{\tilde{n}} u_v^n\right]_{iib}\frac{A_{m,ii,j-1}}{2} + \sum_{\text{jjb}=1}^{\text{njjb}}\left[(\alpha_v\rho_v v_v)^{\tilde{n}} u_v^n\right]_{\text{jjb}}\frac{A_{m,jj,j-1}}{2}\right)\right. \\
&\left. - \left(\sum_{iia=1}^{niia}\left[(\alpha_v\rho_v v_v)^{\tilde{n}} u_v^n\right]_{iia}\frac{A_{m,ii,j}}{2} + \sum_{\text{jja}=1}^{\text{njja}}\left[(\alpha_v\rho_v v_v)^{\tilde{n}} u_v^n\right]_{\text{jja}}\frac{A_{m,jj,j}}{2}\right)\right\} \\
&+ \left\{\sum_{k_y=1}^{nk_y}\left[(\alpha_v\rho_v v_v)^{\tilde{n}} \bar{v}_v^n\right]_{k_y}\Delta X_J L_{k_y}\right. \\
&\left. - \sum_{k_{y+\Delta y}=1}^{nk_{y+\Delta y}}\left[(\alpha_v\rho_v v_v)^{\tilde{n}} \bar{v}_v^n\right]_{k_{y+\Delta y}}\Delta X_J L_{k_{y+\Delta y}}\right\} \\
&+ \left\{\left(\sum_{kii_z=1}^{nkii_z}\left[(\alpha_v\rho_v v_v)^{\tilde{n}} w_v^n\right]_{kii_z}\Delta X_J \frac{L_{kii_z}}{2}\right.\right. \\
&\left.\left. + \sum_{kjj_z=1}^{nkjj_z}\left[(\alpha_v\rho_v v_v)^{\tilde{n}} w_v^n\right]_{kjj_z}\Delta X_J \frac{L_{kjj_z}}{2}\right)\right. \\
&\left. - \left(\sum_{kii_{z+\Delta z}=1}^{nkii_{z+\Delta z}}\left[(\alpha_v\rho_v v_v)^{\tilde{n}} w_v^n\right]_{k_{z+\Delta z}}\Delta X_J \frac{L_{kii_{z+\Delta z}}}{2}\right.\right. \\
&\left.\left. + \sum_{kjj_{z+\Delta z}=1}^{nkjj_{z+\Delta z}}\left[(\alpha_v\rho_v v_v)^{\tilde{n}} w_v^n\right]_{k_{z+\Delta z}}\Delta X_J \frac{L_{kjj_{z+\Delta z}}}{2}\right)\right\} \\
&- \left(P_{ii}^{n+1} - P_{jj}^{n+1}\right)\bar{\alpha}_{v,k,J}^n \Delta X_J \Delta Z_k - \tau_{w,v,J} \\
&- \tau_{i,vl,J} - \tau_{i,ve,J} + \Gamma v^n + \text{Source}_{v,j}
\end{aligned}
\tag{48}
$$

$$\frac{\left[(\alpha_l\rho_l v_l)_k^{n+1} - (\alpha_l\rho_l v_l)_k^{n}\right]}{\Delta t}\Delta X_J \Delta Y_k \Delta Z_k = \left\{\left(\sum_{iib=1}^{niib}\left[(\alpha_l\rho_l v_l)^{\tilde{n}} u_l^n\right]_{iib}\frac{A_{m,ii,j-1}}{2} + \sum_{\mathrm{jjb}=1}^{\mathrm{njjb}}\left[(\alpha_l\rho_l v_l)^{\tilde{n}} u_l^n\right]_{\mathrm{jjb}}\frac{A_{m,jj,j-1}}{2}\right)\right.$$
$$\left. - \left(\sum_{iia=1}^{niia}\left[(\alpha_l\rho_l v_l)^{\tilde{n}} u_l^n\right]_{iia}\frac{A_{m,ii,j}}{2} + \sum_{\mathrm{jja}=1}^{\mathrm{njja}}\left[(\alpha_l\rho_l v_l)^{\tilde{n}} u_l^n\right]_{\mathrm{jja}}\frac{A_{m,jj,j}}{2}\right)\right\}$$
$$+ \left\{\sum_{k_y=1}^{nk_y}\left[(\alpha_l\rho_l v_l)^{\tilde{n}}\bar{v}_l^n\right]_{k_y}\Delta X_J L_{k_y} - \sum_{k_{y+\Delta y}=1}^{nk_{y+\Delta y}}\left[(\alpha_l\rho_l v_l)^{\tilde{n}}\bar{v}_l^n\right]_{k_{y+\Delta y}}\Delta X_J L_{k_{y+\Delta y}}\right\}$$
$$+ \left\{\left(\sum_{kii_z=1}^{nkii_z}\left[(\alpha_l\rho_l v_l)^{\tilde{n}} w_l^n\right]_{kii_z}\Delta X_J\frac{L_{kii_z}}{2}\right.\right.$$
$$\left. + \sum_{kjj_z=1}^{nkjj_z}\left[(\alpha_l\rho_l v_l)^{\tilde{n}} w_l^n\right]_{kjj_z}\Delta X_J\frac{L_{kjj_z}}{2}\right)$$
$$- \left(\sum_{kii_{z+\Delta z}=1}^{nkii_{z+\Delta z}}\left[(\alpha_l\rho_l v_l)^{\tilde{n}} w_l^n\right]_{kii_{z+\Delta z}}\Delta X_J\frac{L_{kii_{z+\Delta z}}}{2}\right.$$
$$\left.\left. + \sum_{kjj_{z+\Delta z}=1}^{nkjj_{z+\Delta z}}\left[(\alpha_l\rho_l v_l)^{\tilde{n}} w_l^n\right]_{kjj_{z+\Delta z}}\Delta X_J\frac{L_{kjj_{z+\Delta z}}}{2}\right)\right\}$$
$$- \left(P_{ii}^{n+1} - P_{jj}^{n+1}\right)\bar{\alpha}_{l,k,J}^n \Delta X_J \Delta Z_k - \tau_{w,l,J} + \tau_{i,vl,J} - \Gamma(1-\eta)v^n + \mathrm{Source}_{l,j} \tag{49}$$

$$\frac{\left[(\alpha_e\rho_l v_e)_k^{n+1} - (\alpha_e\rho_l v_e)_k^{n}\right]}{\Delta t}\Delta X_J \Delta Y_k \Delta Z_k = \left\{\left(\sum_{iib=1}^{\mathrm{niib}}\left[(\alpha_e\rho_l v_e)^{\tilde{n}} u_e^n\right]_{iib}\frac{A_{m,ii,j-1}}{2} + \sum_{\mathrm{jjb}=1}^{\mathrm{njjb}}\left[(\alpha_e\rho_l v_e)^{\tilde{n}} u_e^n\right]_{\mathrm{jjb}}\frac{A_{m,jj,j-1}}{2}\right)\right.$$
$$\left. - \left(\sum_{iia=1}^{\mathrm{niia}}\left[(\alpha_e\rho_l v_e)^{\tilde{n}} u_e^n\right]_{iia}\frac{A_{m,ii,j}}{2} + \sum_{\mathrm{jja}=1}^{\mathrm{njja}}\left[(\alpha_e\rho_l v_e)^{\tilde{n}} u_e^n\right]_{\mathrm{jja}}\frac{A_{m,jj,j}}{2}\right)\right\}$$
$$+ \left\{\sum_{k_y=1}^{nk_y}\left[(\alpha_e\rho_l v_e)^{\tilde{n}}\bar{v}_e^n\right]_{k_y}\Delta X_J L_{k_y} - \sum_{k_{y+\Delta y}=1}^{nk_{y+\Delta y}}\left[(\alpha_e\rho_l v_e)^{\tilde{n}}\bar{v}_e^n\right]_{k_{y+\Delta y}}\Delta X_J L_{k_{y+\Delta y}}\right\}$$
$$+ \left\{\left(\sum_{kii_z=1}^{\mathrm{nkii}_z}\left[(\alpha_e\rho_l v_e)^{\tilde{n}} w_e^n\right]_{kii_z}\Delta X_J\frac{L_{kii_z}}{2}\right.\right.$$
$$\left. + \sum_{kjj_z=1}^{\mathrm{nkjj}_z}\left[(\alpha_e\rho_l v_e)^{\tilde{n}} w_e^n\right]_{kjj_z}\Delta X_J\frac{L_{kjj_z}}{2}\right)$$
$$- \left(\sum_{kii_{z+\Delta z}=1}^{\mathrm{nkii}_{z+\Delta z}}\left[(\alpha_e\rho_l v_e)^{\tilde{n}} w_e^n\right]_{kii_{z+\Delta z}}\Delta X_J\frac{L_{kii_{z+\Delta z}}}{2}\right.$$
$$\left.\left. + \sum_{kjj_{z+\Delta z}=1}^{\mathrm{nkjj}_{z+\Delta z}}\left[(\alpha_e\rho_l v_e)^{\tilde{n}} w_e^n\right]_{kjj_{z+\Delta z}}\Delta X_J\frac{L_{kjj_{z+\Delta z}}}{2}\right)\right\}$$
$$- \left(P_{ii}^{n+1} - P_{jj}^{n+1}\right)\bar{\alpha}_{e,k,J}^n \Delta X_J \Delta Z_k - \tau_{w,e,J} + \tau_{i,ve,J} - \Gamma\eta v^n + \mathrm{Source}_{e,j} \tag{50}$$

The subchannel form of the finite-differenced momentum equations can easily be derived from the Cartesian forms by eliminating directional dependence in the transverse directions. The axial vapor momentum equation is transformed into subchannel form and shown in Eq. (51).

$$\begin{aligned}\frac{\left[(\alpha_v\rho_v u_v)_j^{n+1}-(\alpha_v\rho_v u_v)_j^n\right]}{\Delta t}\Delta X_j A_{m,j} = &\left\{\sum_{ib=1}^{nb}\left[(\alpha_v\rho_v u_v)^{\tilde{n}}\bar{u}_{v,J}^n\right]_{ib}A_{c,J}-\sum_{ia=1}^{na}\left[(\alpha_v\rho_v u_v)^{\tilde{n}}\bar{u}_{v,J+1}^n\right]_{ia}A_{c,J+1}\right\}\\ &+\left\{\sum_{kb=1}^{nkb}\left[(\alpha_v\rho_v u_v)^{\tilde{n}}w_v^n\right]_{kb}\frac{\Delta X_J}{2}L_{kb}+\sum_{ka=1}^{nka}\left[(\alpha_v\rho_v u_v)^{\tilde{n}}w_v^n\right]_{ka}\frac{\Delta X_{J+1}}{2}L_{ka}\right\}\\ &-(\overline{\alpha_v\rho_v})_j^n\, g\Delta X_j A_{m,j}-\left(P_{J+1}^{n+1}-P_J^{n+1}\right)\bar{\alpha}_{v,j}^n A_{m,j}-\tau_{w,v,j}\\ &-\tau_{i,vl,j}-\tau_{i,ve,j}+\Gamma u^n+\text{Source}_{v,j}+\sum_{kb=1}^{nkb}\left(M_v^T\right)_k+\sum_{ka=1}^{nka}\left(M_v^T\right)_k\end{aligned} \tag{51}$$

Again, all gap velocities are represented by w. Transverse velocities are summed over all the gaps that connect to axial momentum cell j from above and below. The liquid and entrained subchannel momentum conservation equations are shown in Eqs. (52) and (53).

$$\begin{aligned}\frac{\left[(\alpha_l\rho_l u_l)_j^{n+1}-(\alpha_l\rho_l u_l)_j^n\right]}{\Delta t}\Delta X_j A_{m,j} = &\left\{\sum_{ib=1}^{nb}\left[(\alpha_l\rho_l u_l)^{\tilde{n}}\bar{u}_l^n\right]_{ib}A_{c,J}-\sum_{ia=1}^{na}\left[(\alpha_l\rho_l u_l)^{\tilde{n}}\bar{u}_l^n\right]_{ia}A_{c,J+1}\right\}\\ &+\left\{\sum_{kb=1}^{nkb}\left[(\alpha_l\rho_l u_l)^{\tilde{n}}w_l^n\right]_{kb}\frac{\Delta X_J}{2}L_{kb}+\sum_{ka=1}^{nka}\left[(\alpha_l\rho_l u_l)^{\tilde{n}}w_l^n\right]_{ka}\frac{\Delta X_{J+1}}{2}L_{ka}\right\}\\ &-(\overline{\alpha_l\rho_l})_j^n\, g\Delta X_j A_{m,j}-\left(P_{J+1}^{n+1}-P_J^{n+1}\right)\bar{\alpha}_{l,j}^n A_{m,j}-\tau_{w,l,j}\\ &+\tau_{i,vl,j}-\Gamma(1-\eta)u^n+\text{Source}_{l,j}+\sum_{kb=1}^{nkb}\left(M_l^T\right)_k+\sum_{ka=1}^{nka}\left(M_l^T\right)_k\end{aligned} \tag{52}$$

$$\begin{aligned}\frac{\left[(\alpha_e\rho_l u_e)_j^{n+1}-(\alpha_e\rho_l u_e)_j^n\right]}{\Delta t}\Delta X_j A_{m,j} = &\left\{\sum_{ib=1}^{nb}\left[(\alpha_e\rho_l u_e)^{\tilde{n}}\bar{u}_e^n\right]_{ib}A_{c,J}-\sum_{ia=1}^{na}\left[(\alpha_e\rho_l u_e)^{\tilde{n}}\bar{u}_e^n\right]_{ia}A_{c,J+1}\right\}\\ &+\left\{\sum_{kb=1}^{nkb}\left[(\alpha_e\rho_l u_e)^{\tilde{n}}w_e^n\right]_{kb}\frac{\Delta X_J}{2}L_{kb}+\sum_{ka=1}^{nka}\left[(\alpha_e\rho_l u_e)^{\tilde{n}}w_e^n\right]_{ka}\frac{\Delta X_{J+1}}{2}L_{ka}\right\}\\ &-(\overline{\alpha_e\rho_l})_j^n\, g\Delta X_j A_{m,j}-\left(P_{J+1}^{n+1}-P_J^{n+1}\right)\bar{\alpha}_{e,j}^n A_{m,j}-\tau_{w,e,j}\\ &+\tau_{i,ve,j}-\Gamma\eta u^n+\text{Source}_{e,j}+\sum_{kb=1}^{nkb}\left(M_e^T\right)_k+\sum_{ka=1}^{nka}\left(M_e^T\right)_k\end{aligned} \tag{53}$$

The lateral momentum equation in subchannel form for vapor is shown in Eq. (54).

$$\frac{\left[(\alpha_v\rho_v w_v)_k^{n+1} - (\alpha_v\rho_v w_v)_k^n\right]}{\Delta t}\Delta X_J L_k \Delta Z_k = \left\{\sum_{ib=1}^{nb}\left[(\alpha_v\rho_v w_v)^{\tilde{n}}\bar{u}_v^n\right]_{ib} A_{c,J} - \sum_{ia=1}^{na}\left[(\alpha_v\rho_v w_v)^{\tilde{n}}\bar{u}_v^n\right]_{ia} A_{c,J+1}\right\}$$
$$+\left\{\sum_{k_y=1}^{nk_y}\left[(\alpha_v\rho_v w_v)^{\tilde{n}}\bar{w}_v^n\right]_{k_y}\Delta X_J L_{k_y} - \sum_{k_{y+\Delta y}=1}^{nk_{y+\Delta y}}\left[(\alpha_v\rho_v w_v)^{\tilde{n}}\bar{w}_v^n\right]_{k_{y+\Delta y}}\Delta X_J L_{k_{y+\Delta y}}\right\}$$
$$+\left(P_{ii}^{n+1} - P_{jj}^{n+1}\right)\bar{\alpha}_{v,k}^n \Delta X_J L_k - \tau_{w,v,k} - \tau_{i,vl,k} - \tau_{i,ve,k} + \Gamma w^n + \text{Source}_{v,k} \tag{54}$$

The subchannel form of the lateral momentum equation no longer has the z-direction. The y-direction represents any lateral flow path. The orthogonal transport of transverse momentum has been removed. The transverse transport of momentum is retained because CTF still knows about gaps behind and in front of the lateral momentum cell being solved. Note that it is possible that there is no gap in front of or behind any given gap. In this case, the lateral momentum will accelerate from zero if there is no gap behind the subject gap, or it will decelerate and dissipate if there is no gap in front of the subject gap.

In keeping with the CTF global coordinate system, positive transverse velocity moves from channel ii to channel jj. A positive gap k velocity will convect transverse momentum from channel ii into gap k and will convect transverse velocity in gap k out to channel jj. Just as was assumed for channel ii and jj transverse velocities, that channel ii and jj transverse momentums must also be assumed as zero. Therefore, a positive gap k velocity will convect zero transverse momentum into transverse momentum cell k, but it will convect the gap k transverse momentum out on the jj side. Conversely, a negative gap k velocity will convect the gap k transverse momentum out on the ii side, but it will convect nothing in from the jj side.

The liquid and entrained transverse momentum equations are similarly derived and are shown in Eqs. (55) and (56).

$$\frac{\left[(\alpha_l\rho_l w_l)_k^{n+1} - (\alpha_l\rho_l w_l)_k^n\right]}{\Delta t}\Delta X_J L_k \Delta Z_k = \left\{\sum_{ib=1}^{nb}\left[(\alpha_l\rho_l w_l)^{\tilde{n}}\bar{u}_l^n\right]_{ib} A_{c,J} - \sum_{ia=1}^{na}\left[(\alpha_l\rho_l w_l)^{\tilde{n}}\bar{u}_l^n\right]_{ia} A_{c,J+1}\right\}$$
$$+\left\{\sum_{k_y=1}^{nk_y}\left[(\alpha_l\rho_l w_l)^{\tilde{n}}\bar{w}_l^n\right]_{k_y}\Delta X_J L_{k_y} - \sum_{k_{y+\Delta y}=1}^{nk_{y+\Delta y}}\left[(\alpha_l\rho_l w_l)^{\tilde{n}}\bar{w}_l^n\right]_{k_{y+\Delta y}}\Delta X_J L_{k_{y+\Delta y}}\right\}$$
$$+\left(P_{ii}^{n+1} - P_{jj}^{n+1}\right)\bar{\alpha}_{l,k}^n \Delta X_J L_k - \tau_{w,l,k} + \tau_{i,vl,k} - \Gamma(1-\eta)w^n + \text{Source}_{l,k} \tag{55}$$

$$\frac{\left[(\alpha_e\rho_l w_e)_k^{n+1} - (\alpha_e\rho_l w_e)_k^n\right]}{\Delta t}\Delta X_J L_k \Delta Z_k = \left\{\sum_{ib=1}^{nb}\left[(\alpha_e\rho_l w_e)^{\tilde{n}}\bar{u}_e^n\right]_{ib} A_{c,J} - \sum_{ia=1}^{na}\left[(\alpha_e\rho_l w_e)^{\tilde{n}}\bar{u}_e^n\right]_{ia} A_{c,J+1}\right\}$$
$$+\left\{\sum_{k_y=1}^{nk_y}\left[(\alpha_e\rho_l w_e)^{\tilde{n}}\bar{w}_e^n\right]_{k_y}\Delta X_J L_{k_y} - \sum_{k_{y+\Delta y}=1}^{nk_{y+\Delta y}}\left[(\alpha_e\rho_l w_e)^{\tilde{n}}\bar{w}_e^n\right]_{k_{y+\Delta y}}\Delta X_J L_{k_{y+\Delta y}}\right\}$$
$$+\left(P_{ii}^{n+1} - P_{jj}^{n+1}\right)\bar{\alpha}_{e,k}^n \Delta X_J L_k - \tau_{w,e,k} + \tau_{i,ve,k} - \Gamma\eta w^n + \text{Source}_{e,k} \tag{56}$$

2.3.2.3 Finite-Differenced Energy Conservation Equations

First, the general-expanded vapor energy equation is restated in Cartesian form.

$$\frac{\partial}{\partial t}\left(\alpha_v\rho_v h_v\right)+\frac{\partial}{\partial x}\left(\alpha_v\rho_v h_v u_v\right)+\frac{\partial}{\partial y}\left(\alpha_v\rho_v h_v v_v\right)+\frac{\partial}{\partial z}\left(\alpha_v\rho_v h_v w_v\right)=+\frac{\partial}{\partial y}q_v^T+\frac{\partial}{\partial z}q_v^T+\Gamma'''h+q'''_{wv}+\alpha_v\frac{\partial P}{\partial t}$$

The energy equations are solved for the scalar mesh cells. The equation is multiplied by mesh cell volume, the temporal term is expanded in time, and the advection terms are expanded in their respective spatial directions.

$$\begin{aligned}&\frac{\left[(\alpha_v\rho_v h_v)_J^{n+1}-(\alpha_v\rho_v h_v)_J^{n}\right]}{\Delta t}\Delta X\Delta Y\Delta Z+\left\{\sum_{ib=1}^{nib}\left[(\alpha_v\rho_v h_v)^{\tilde{n}}u_v^{n+1}\right]_{ib}\Delta Y\Delta Z-\sum_{ia=1}^{nia}\left[(\alpha_v\rho_v h_v)^{\tilde{n}}u_v^{n+1}\right]_{ia}\Delta Y\Delta Z\right\}\\&+\left\{\sum_{k_y=1}^{nk_y}\left[(\alpha_v\rho_v h_v)^{\tilde{n}}v_v^{n+1}\right]_{k_y}\Delta X\Delta Z-\sum_{k_{y+\Delta y}=1}^{nk_{y+\Delta y}}\left[(\alpha_v\rho_v h_v)^{\tilde{n}}v_v^{n+1}\right]_{k_{y+\Delta y}}\Delta X\Delta Z\right\}\\&+\left\{\sum_{k_z=1}^{nk_z}\left[(\alpha_v\rho_v h_v)^{\tilde{n}}w_v^{n+1}\right]_{k_z}\Delta X\Delta Y-\sum_{k_{z+\Delta z}=1}^{nk_{z+\Delta z}}\left[(\alpha_v\rho_v h_v)^{\tilde{n}}w_v^{n+1}\right]_{k_{z+\Delta z}}\Delta X\Delta Y\right\}=q_{v,y}^T\Delta X\Delta Z\\&\quad+q_{v,z}\Delta X\Delta Y+\Gamma h+q_{w,v}+\frac{\alpha_v^n(P^{n+1}-P^n)_J}{\Delta t}\Delta Y\Delta Z\end{aligned}\tag{57}$$

The appropriate CTF geometry terms are substituted in Eq. (58). Also, as in the mass equations, the transverse direction, whether it is in the y- or z-direction, is immaterial for the energy equation. Therefore, the y- and z-advection terms are collapsed into one sum about the gaps connected to the scalar mesh cell.

$$\begin{aligned}&\frac{\left[(\alpha_v\rho_v h_v)_J^{n+1}-(\alpha_v\rho_v h_v)_J^{n}\right]}{\Delta t}\Delta X_J A_{c,J}+\left\{\sum_{ib=1}^{nib}\left[(\alpha_v\rho_v h_v)^{\tilde{n}}u_v^{n+1}\right]_{ib}A_{m,j-1}-\sum_{ia=1}^{nia}\left[(\alpha_v\rho_v h_v)^{\tilde{n}}u_v^{n+1}\right]_{ia}A_{m,j}\right\}\\&+\sum_{k=1}^{\mathrm{nk}}\left[(\alpha_v\rho_v h_v)^{\tilde{n}}w_v^{n+1}\right]_k\Delta X_J L_k=\sum_{k=1}^{\mathrm{nk}}\left[q_v^T\Delta X_J L_k\right]_k+\Gamma h+q_{w,v}+\frac{\alpha_v^n(P^{n+1}-P^n)_J}{\Delta t}\Delta Y_J\Delta Z_J\end{aligned}\tag{58}$$

The liquid energy equation is presented in Eq. (59).

$$\begin{aligned}&\frac{\left[((\alpha_l+\alpha_e)\rho_l h_l)_J^{n+1}-((\alpha_l+\alpha_e)\rho_l h_l)_J^{n}\right]}{\Delta t}\Delta X_J A_{c,J}\\&+\left\{\sum_{ib=1}^{nib}\left[(\alpha_l\rho_l h_l)^{\tilde{n}}u_l^{n+1}+(\alpha_e\rho_l h_l)^{\tilde{n}}u_e^{n+1}\right]_{ib}A_{m,j-1}-\sum_{ia=1}^{nia}\left[(\alpha_l\rho_l h_l)^{\tilde{n}}u_l^{n+1}+(\alpha_e\rho_l h_l)^{\tilde{n}}u_e^{n+1}\right]_{ia}A_{m,j}\right\}\\&+\sum_{k=1}^{\mathrm{nk}}\left[(\alpha_l\rho_l h_l)^{\tilde{n}}w_l^{n+1}+(\alpha_e\rho_l h_l)^{\tilde{n}}w_e^{n+1}\right]_k\Delta X_J L_k=\sum_{k=1}^{\mathrm{nk}}\left[q_l^T\Delta X_J L_k\right]_k\\&\quad-\Gamma h+q_{w,l}+\frac{(\alpha_l+\alpha_e)^n(P^{n+1}-P^n)_J}{\Delta t}\Delta Y_J\Delta Z_J\end{aligned}\tag{59}$$

Note that Eqs. (58) and (59) are applicable for both the Cartesian and subchannel forms of the finite-differenced energy equations.

2.4 INTERFACIAL AREA TRANSPORT EQUATION

The interfacial area transport equation tracks the interfacial area of the droplet field throughout the flow field. The equation is written as follows:

$$\frac{dA'''_{i,d}}{dt} + \nabla \cdot \left(A'''_{i,d}\vec{U}_e\right) = A'''_{i,E} + A'''_{i,\Gamma} \tag{60}$$

The terms on the LHS represent the rate of change in interfacial area with respect to time and the efflux of interfacial area through mesh cell connections. The RHS terms include the generation of interfacial area from entrainment and evaporation.

The interfacial area transport equation is performed after back-substitution is performed for the Jacobian matrices. Equation (60) is first multiplied through by the cell volume, and the efflux term is put into discrete form:

$$\frac{dA'''_{i,d}}{dt}V_c + \sum_j \left(A'''_{i,d}U_e A\right)_j = A_{i,E} + A_{i,\Gamma}. \tag{61}$$

The change in droplet volume resulting from evaporation is obtained from a mass balance:

$$N_d \frac{dV_d}{dt} = \frac{-\eta\Gamma}{\rho_l}. \tag{62}$$

N_d is the number of drops in the cell, V_d is the droplet volume, and $\eta\Gamma$ is the evaporation rate from droplets as discussed in Section 2.2.2. The total entrained field volume divided by a single droplet volume gives the number of droplets:

$$N_d = \frac{\alpha_e V_c}{V_d}. \tag{63}$$

Substituting this into Eq. (62) and putting the temporal term in discreet form gives

$$\frac{\alpha_e^{n+1}V_c^{n+1}}{V_d^{n+1}}\frac{V_d^{n+1} - V_d^n}{\Delta t} = -\frac{\eta^n\Gamma^n}{\rho_l^{n+1}}. \tag{64}$$

Simplifying this gives

$$\frac{V_d^{n+1}}{V_d^n} = 1 + \frac{\eta^n\Gamma^n\Delta t}{\rho_l^{n+1}\alpha_e^{n+1}V_c^{n+1}}. \tag{65}$$

The volume of a sphere can be equated to its surface area as follows:

$$\frac{V_d^{n+1}}{V_d^n} = \left(\frac{A_{i,d}^{n+1}}{A_{i,d}^n}\right)^{\frac{3}{2}}. \tag{66}$$

Substituting Eq. (66) into Eq. (65) yields

$$A_{i,d}^{n+1'''} = A_{i,d}^{n'''} \left(\frac{1}{1 + \frac{\eta^n \Gamma^n \Delta t}{\rho_l^{n+1} \alpha_e^{n+1} V_c^{n+1}}} \right)^{\frac{2}{3}} \tag{67}$$

or

$$A_{i,d}^{n+1'''} = A_{i,d}^{n'''} \left(\frac{\rho_l^{n+1} \alpha_e^{n+1} V_c^{n+1}}{\rho_l^{n+1} \alpha_e^{n+1} V_c^{n+1} + \eta^n \Gamma^n \Delta t} \right)^{\frac{2}{3}}. \tag{68}$$

Substituting Eq. (68) into Eq. (61) yields the following:

$$A_{i,d}^{n+1'''} = A_{i,d}^{n'''} \left(\frac{\rho_l^{n+1} \alpha_e^{n+1} V_c^{n+1}}{\rho_l^{n+1} \alpha_e^{n+1} V_c^{n+1} + \eta^n \Gamma^n \Delta t} \right)^{\frac{2}{3}} + \left\{ \sum_j \left(A_{i,d}^{n'''} u_e^{n+1} A \right)_j + A_{i,e} \right\} \frac{\Delta t}{V_c}. \tag{69}$$

Limits are placed on this final form of the equation when calculating the new time interfacial area:

$$A_{i,d}^{'''} = \min \left\{ \max \left\{ \begin{array}{c} A_{i,d}^{'''} \text{ from Eq. (69)} \\ \frac{10^{-5}}{A_x \Delta X} \end{array} \right. \right. \\ \left. \left. 12,000 \alpha_e \right. \right. \tag{70}$$

2.5 BORON TRACKING AND PRECIPITATION MODELING

2.5.1 Boron Tracking Model

The basic boron tracking algorithm is implemented in CTF such that after the fluid flow fields in each node are calculated, the boron solute flow rate is calculated at each node boundary. Based on the results of the solute flow rate, the boron mass and concentration are determined in each node.

The boron tracking model was later implemented in CTF by Ozdemir (2012) [7] with the addition of cross flow between subchannels. The importance of entrained droplet field boric acid transport was highlighted in both the Westinghouse Precipitation Modes PRT Report of Kliem et al. (2008) [8] and Tuunanen et al. (1988) [9], and the group experimental studies of Tuunanen et al. (1994) [10]. Therefore, the boron solute transient is calculated for both the continuous and entrained droplet fields (Freixa et al. 2007) [11]. The implemented boron tracking algorithm was verified using analytical and CFD solution and was subsequently validated using measured data [12] [13].

The boron tracking model performs a solution of the soluble boron conservation equation in track boron motion through the mesh. The advection term of the governing equation can be solved using one of two options: (1) the first-order upwind differencing scheme, or 2) the second-order modified Godunov scheme. In addition, the second-order modified Godunov scheme solves the diffusion term of the governing equation.

The following assumptions are used for the solute tracking model based on an Eulerian method:

1. Liquid (solvent) properties are not altered by the presence of the solute,
2. Solute is transported only in the liquid phase and at the velocity of the liquid phase,
3. Energy transported by the solute is negligible, and

4. Inertia of the solute is negligible.

According to these assumptions, the solute field is described separately from the rest of the flow fields using a 3D hyperbolic transport equation.

Based on the Eulerian approach, the solution domain of the flow region is defined by computational cells, and the fluid properties can be defined as time-dependent. Besides two-phase continuity, momentum, and energy equations, an additional 1D field equation for the conservation of the solute is included to identify the boron concentration.

The fundamental diffusion equation—the Burgers Equation—including the physical diffusion term D, which makes the equation nonlinear, can be written as follows:

$$\frac{\partial \rho_b}{\partial t} + \frac{v_p \cdot \partial \rho_b}{\partial x} = \frac{\partial}{\partial x}\left(D\frac{\partial \rho_b}{\partial x}\right) + S, \tag{71}$$

where ρ_b is the spatial boron density, v_p is the particle velocity, D is the physical diffusion coefficient, and S is the source term. The spatial boron density, ρ_b, is defined as

$$\rho_b = \alpha_f \rho_f C_b = \rho_m (1 - x) C_b, \tag{72}$$

where α_f represents the fluid void fraction, ρ_f is the fluid density, C_b is boron concentration, ρ_m represents the density of the mixture, and x is the quality. The nonlinear Burgers equation can be simplified by neglecting the diffusion coefficient. When applied to boron mass, the equation is written as follows:

$$\frac{\partial \rho_b}{\partial t} + \frac{1}{A}\frac{v_p \cdot \partial \rho_b \cdot A}{\partial x} = 0. \tag{73}$$

As discussed in the list of assumptions above, it is assumed that the particle velocity υ_p is equal to the fluid velocity υ_f.

2.5.1.1 First-Order Accurate Upward Difference Scheme

Eq. (73) can be rewritten with respect to the boron density term ρ_b and the speed υ;

$$\frac{\partial \rho_b}{\partial t} + \upsilon \frac{\rho_b}{\partial x} = 0. \tag{74}$$

Next, Eq. (74) can be discretized by applying a forward difference in time and a backward difference in space, as follows:

$$\frac{\rho_{b,i}^{n+1} - \rho_{b,i}^{n}}{\Delta t} + \frac{\upsilon}{\Delta x}(\rho_{b,i}^{n} - \rho_{b,i-1}^{n}) = 0. \tag{75}$$

A Taylor series expansion can be used to define $\rho_{b,i}^{n+1}$ and $\rho_{b,i-1}^{n}$ in terms of $\rho_{b,i}^{n}$ as follows:

$$\rho_{b,i}^{n+1} = \rho_{b,i}^{n} + \Delta t\left(\frac{\partial \rho_b}{\partial t}\right)_i^n + \frac{\Delta t^2}{2}\left(\frac{\partial^2 \rho_b}{\partial t^2}\right)_i^n + \frac{\Delta t^3}{6}\left(\frac{\partial^3 \rho_b}{\partial t^3}\right)_i^n \tag{76}$$

$$\rho^n_{b,i-1} = \rho^n_{b,i} - \Delta x \left(\frac{\partial \rho_b}{\partial x}\right)^n_i + \frac{\Delta x^2}{2}\left(\frac{\partial^2 \rho_b}{\partial x^2}\right)^n_i - \frac{\Delta x^3}{6}\left(\frac{\partial^3 \rho_b}{\partial x^3}\right)^n_i \tag{77}$$

The expression from Eq. (76) and Eq. (77) can be substituted in for the terms, $\frac{\rho^{n+1}_{b,i}}{\Delta t}$ and $\frac{\upsilon(\rho^n_{b,i} - \rho^n_{b,i-1})}{\Delta x}$ in Eq. (75). The relation between numerical scheme and the differential equation—the truncation error—ϵ_t is:

$$\left[\frac{\rho^{n+1}_{b,i} - \rho^n_{b,i}}{\Delta t} + \frac{\upsilon}{\Delta x}(\rho^n_{b,i} - \rho^n_{b,i-1})\right] - \left[\left(\frac{\partial \rho_b}{\partial t}\right)^n_i + \upsilon\left(\frac{\partial \rho_b}{\partial x}\right)^n_i\right] = \frac{\Delta t}{2}\left(\frac{\partial^2 \rho_b}{\partial t^2}\right)^n_i - \upsilon\frac{\Delta x}{2}\left(\frac{\partial^2 \rho_b}{\partial x^2}\right)^n_i + O(\Delta t^2, \Delta x^2) \tag{78}$$

$$\epsilon_t = \frac{\Delta t}{2}(\frac{\partial^2 \rho_b}{\partial t^2})^n_i - \frac{\upsilon \Delta x}{2}(\frac{\partial^2 \rho_b}{\partial x^2})^n_i + O(\Delta t^2, \Delta x^2) \tag{79}$$

Because $\lim_{\Delta t \to 0 \Delta x \to 0}(\epsilon_t) = 0$, the scheme can be defined as consistent. If the higher order terms ($O(\Delta t^2, \Delta x^2)$) are neglected, then Eq. (78) can be rewritten as

$$\begin{aligned}\left(\frac{\partial \rho_b}{\partial t}\right)^n_i + \upsilon\left(\frac{\partial \rho_b}{\partial x}\right)^n_i &= -\upsilon\frac{\delta x}{2}\left(1 - \frac{\upsilon \Delta t}{\Delta x}\right)\left(\frac{\partial^2 \rho_b}{\partial x^2}\right)^n_i \\ &= -D_{num}\left(\frac{\partial^2 \rho_b}{\partial x^2}\right)^n_i,\end{aligned} \tag{80}$$

where

$$D_{num} = \frac{\upsilon \Delta x}{2}\left(1 - \frac{\upsilon \Delta t}{\delta x}\right). \tag{81}$$

From Eq. (80) it can be concluded that discretization of the linear convection equation, Eq. (73), introduces numerical diffusion D_{num} (numerical viscosity) in its numerical solution, which is defined in Eq. (81).

The numerical diffusion term, D_{num} should be positive to obtain a solution damped in time. If D_{num} becomes negative, then numerical diffusion grows indefinitely in time, and the solution becomes unstable. Then, for the first-order upwind scheme stability, it should be

$$0 \leq \frac{\upsilon \Delta t}{\Delta x} \leq 1. \tag{82}$$

This relation is defined as the *Courant limit condition* (defined in Eq. (127)), which can be given as the stability requirement with respect to the ratio between the timestep (Δt) and the cell size (Δx). The Courant limit also controls the other CTF governing equations that use an upwind advection scheme. The benefit of the upwind differencing numerical scheme is that it provides a positive definite solution which increases its stability and robustness.

2.5.1.2 Second-Order Godunov Scheme

Investigations conducted by Freixa et al. (2007) [11] into the accuracy of the solution methods first concluded that the upward difference scheme suffers from numerical diffusion caused by numerical truncation. It was found that the second-order accurate Godunov scheme significantly reduces the numerical diffusion commonly observed in the upward difference scheme. However, an accounting for physical diffusion was still lacking in the original Godunov solution scheme. Based on the finite volume method, the volume integral of Eq. (73) can be taken over the total volume of the cell V as

$$\int_V \frac{\partial \rho_b}{\partial t} \partial V + \int_V \left(\frac{1}{A} \frac{\partial (\rho_b \cdot \upsilon_f \cdot A)}{\partial x} \right) \partial V = 0. \tag{83}$$

Using the divergence theorem, Eq. (83) can be rewritten in a control volume (V) and with a surface area (A):

$$\int_V \frac{\partial \rho_b}{\partial t} \partial V + \int_A \rho_b \cdot \upsilon_f \cdot \partial A = 0. \tag{84}$$

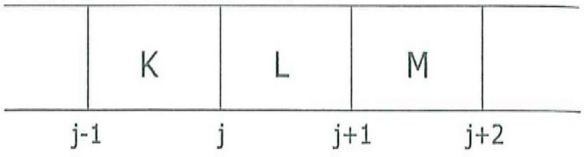

Figure 5. Spatial Notation Used to Demonstrate the Modified Godunov Scheme, by Ozdemir (2012) [7].

Based on Figure 5, the upward difference discretization of Eq. (84) gives the following solution with respect to mass flux G_j and G_{j+1}:

$$[\rho_{b,L}^{n+1} - \rho_{b,L}^{n}] + \left[\frac{\delta t}{V_L} (A_{j+1} G_{j+1}^{n} - A_j G_j^{n}) \right] = 0. \tag{85}$$

The above relation gives the first-order accurate Godunov scheme. Because the velocity (υ) is known in both old (n) and new ($n+1$) timesteps, it can be linearly interpolated to generate an approximation based on time-centered velocity ($\upsilon^{n+1/2)}$) as:

$$\upsilon_{f,j+1}^{n+1/2} = \upsilon = \frac{1}{2} (\upsilon_{f,j+1}^{n+1} + \upsilon_{f,j+1}^{n}). \tag{86}$$

Then the flux terms G_j and G_{j+1} in the old time domain n are defined as

$$G_{j+1}^{n} = \frac{1}{2} [\upsilon_{f,j+1}^{n+1/2} (\rho_{b,j+1}^{n,L} + \rho_{b,j+1}^{n,M}) + |\upsilon_{f,j+1}^{n+1/2} (\rho_{b,j+1}^{n,L} - \rho_{b,j+1}^{n,M})|] \tag{87}$$

$$G_{j}^{n} = \frac{1}{2} [\upsilon_{f,j}^{n+1/2} (\rho_{b,j}^{n,L} + \rho_{b,j}^{n,M}) + |\upsilon_{f,j}^{n+1/2} (\rho_{b,j}^{n,L} - \rho_{b,j}^{n,M})|] \tag{88}$$

Equations (89) and (90) represent the boron density in the neighboring cells at their common interface:

$$\rho_{b,j+1}^{n,L} = \rho_{b,L}^{n} + \left(\frac{1}{2}\Delta x_L\right)\left(1 - \frac{\upsilon\Delta t}{\Delta x_L}\right)\bar{S}_L \tag{89}$$

$$\rho_{b,j+1}^{n,M} = \rho_{b,M}^{n} + \left(\frac{1}{2}\Delta x_M\right)\left(1 - \frac{\upsilon\Delta t}{\Delta x_M}\right)\bar{S}_M \tag{90}$$

The cell-centered limited gradient $\bar{S}_L$ is defined as

$$\bar{S}_L = (1 + \theta_L\omega_L)\Phi(r,1)S_{j+1} = (1 + \theta_L\omega_L)\Phi(r,1)\left(\frac{\rho_{b,M}^{n} - \rho_{b,L}^{n}}{\Delta x_{j+1}}\right). \tag{91}$$

The cell-centered limited gradient $\bar{S}_L$ provides higher order accuracy in space and time interpolation for cell edge values of ρ_b with respect to the changes in the neighboring cells from the flux at their common interface, as seen in Eqs. (89) and (90). The superbee nonlinear flux limiter of Roe [14], Φ, is used to prevent flux oscillations between adjacent cells. The effect of the flux limiter is to smooth parts of the solution near a discontinuity in the solution. The limiter switches to a first-order upwind flux-conserved advection scheme to prevent numerical instability. The flux limiter is given as

$$\Phi(r,1) = \max[0, \min(2r,1), \min(r,2)], \tag{92}$$

where

$$r = \frac{S_j}{S_{j+1}}, \tag{93}$$

$$S_j = \frac{\rho_{b,L}^{n} - \rho_{b,K}^{n}}{\Delta x_j}, \textit{and} \tag{94}$$

$$S_{j+1} = \frac{\rho_{b,M}^{n} - \rho_{b,L}^{n}}{\Delta x_{j+1}}. \tag{95}$$

The artificial compression term of Yee [15] is introduced to ensure that the solution is continuous because the number of grid points tends to be relatively small, and the scheme introduces spurious oscillations into the solution where discontinuities and shocks are present. In the artificial compression term $(1 + \theta_L\omega_L)$, θ_L, is defined as

$$\theta_L = \frac{|1 - r|}{1 + |r|}, \tag{96}$$

and the parameter ω_L is partially defined by the local Courant number.

$$\omega_L = \min(C_{r,L}, 1 - C_{r,L}) \tag{97}$$

These modifications make the Godunov method second-order accurate. Using the second-order accurate Godunov solution scheme and introducing a diffusion term to consider physical diffusion, a modified Godunov solution scheme was devised by Freixa. An additional diffusion term has been defined within the Godunov solution by replacing the integrated boron field in Eq. (84).

$$\int_V \frac{\partial \rho_b}{\partial t} \partial V + \int_A \left(\rho_b \cdot \upsilon_f - D \frac{\partial \rho_b}{\partial x} \right) \cdot \partial A = 0 \tag{98}$$

Two physical diffusion terms (D) were defined based on the collision of the boron particles and turbulent phenomena, which are Brownian diffusion and Eddy diffusion. When a small particle is suspended in a fluid, it is subjected to the impact of the gas or liquid molecules. The instantaneous momentum given to the particle varies randomly and causes the particle to move on an erratic path known as *Brownian motion*. The Brownian diffusion coefficient given by Einstein [16] with the added Cunningham correlation factor [17] is

$$D_{Brownian} = \frac{k_b \cdot T \cdot C_c}{6\pi \cdot \rho \cdot \upsilon \cdot a}, \tag{99}$$

where k_b is the Boltzmann constant, T represents the temperature, ρ is the fluid density, υ is the velocity, and a represents the particle radius. The Cunningham correction factor is defined as a function of λ, which represents the mean free path, and a represents the particle radius.

$$C_c = 1 + \frac{\lambda}{a}[1.257 + 0.4e^{-1.1a/\lambda}] \tag{100}$$

Eddy diffusion appears with turbulent phenomena. Turbulence is characterized by the motion of the fluid particles, which is irregular with respect to both direction and time. Even though the dominant velocity direction is axial, there can be regions with a direction and modulus that are different from those of the mean velocity. The turbulent fluid is imagined to consist of lumps of fluids or eddies of different sizes. Eddy diffusion is slightly different from fluid turbulent diffusion, but in this case, because of the low weight of the particles, both diffusivities will be essentially equal.

Equation (101) was developed by Macian-Juan and Mahaffy [18] based on the dispersion model. The suggested value for G_0 was equal to 1.35.

$$D_{Eddy} = G_0 \upsilon R e^{7/8} \tag{101}$$

Although the range of values of the Brownian coefficient for boron acid particles oscillates between 10^{-6} and 10^{-7}, the Eddy coefficient has a scale order of 10^{-2} to 10^{-3}, depending on the fluid velocity. Consequently, Brownian diffusion is removed from the equation. Then, following a similar procedure, Eq. (89) and analogously, Eq. (90), are rewritten including the Eddy diffusion coefficient D_E.

$$\rho_{b,j+1}^{n,L} = \rho_{b,L}^{n} + \left[\left(\frac{1}{2} \Delta x_L \right) \left(1 - \frac{\upsilon \Delta t}{\Delta x_L} \right) - \varphi_L \right] \bar{S}_L, \tag{102}$$

where φ is the limited diffusion term:

$$\varphi_L = min\left(\frac{\Delta x}{2C_r}, \frac{D_{Eddy}}{\upsilon_L} \right). \tag{103}$$

2.5.2 Boron Precipitation Model

The boron precipitation model was added to predict the plated out solute concentration in CTF. The solubility of boron increases with the increase of coolant temperature. Thus, it is essential to account for the coolant temperature effect in maximum boron concentration calculations:

1. First the maximum solubility of the boric acid in $100g$ of water (maximum mass fraction, m_{max}) is calculated according to Kim et al.'s correlation [19] as

$$\frac{m_max}{100} = \psi \cdot \left(-\frac{2.68 \times 10^8}{2.73.15 + T_{liq}} + 6.04 \right), \tag{104}$$

   where the conversion parameter ψ is given as

$$\psi = 3.432 \times 10^2 (\lambda + 1.80 \times 10^3 \times T_{\text{liq}}). \tag{105}$$

   $\lambda = 0.1795$ and T_{liq} is the liquid temperature in °C.

2. Then, the maximum boron concentration is evaluated based on the amount of liquid mass (m_{liq}) both in continuous and entrained droplet liquid phases:

$$\rho_{b,max} = \frac{m_{b,max}}{m_{liq} + m_{b,max}}. \tag{106}$$

From Figure 6, Kim et al.'s solubility correlation is derived in a temperature range between 40−160°C (313−433K), including the effects of buffer agents like trisodium phosphate (TPT) which generate particulate oxide corrosion products and increase the risk of precipitation by chemical reactions with other dissolved materials [19].

In CTF, if the liquid temperature reaches a value outside the given range, then the value at 160°C is used (Figure 7). If the new solute density goes beyond the maximum value, then CTF assumes the excess is precipitated and the solute density reaches its maximum value. The maximum boron concentration profile used in CTF is given in Figure 7.

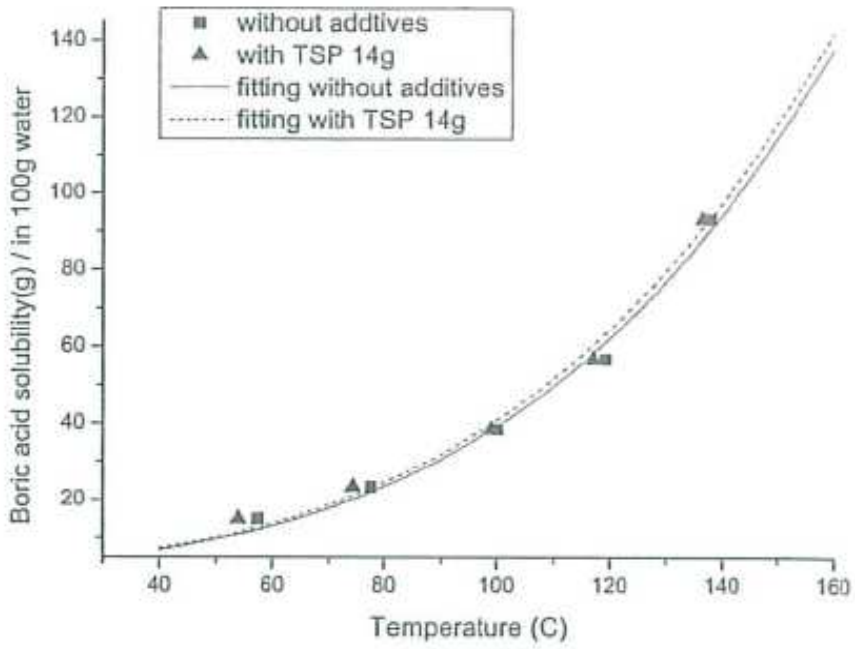

Figure 6. Boric acid solubility correlation w.r.t. $100g$ **water by Kim (2008) [19]**

.

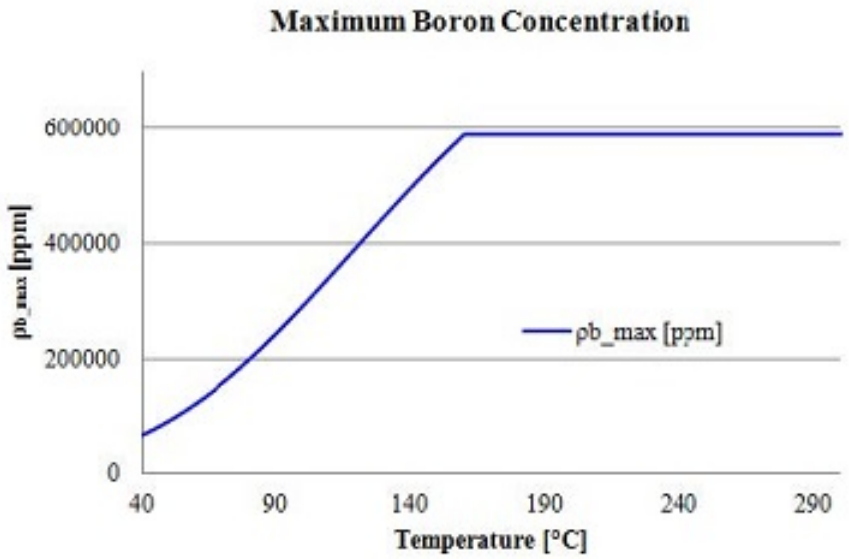

Figure 7. CTF Maximum boric acid concentration by correlation from Kim et al. [19]

.

3. NUMERICAL SOLUTION

CTF uses a form of the Semi-Implicit Method for Pressure-Linked Equations (SIMPLE) to solve the conservation equations that have been defined in Chapter 2. The steps of the Semi-Implicit Method for Pressure-Linked Equations (SIMPLE) algorithm, taken from Patankar [4], are:

1. Guess the pressure field p^*.
2. Solve the momentum equations to obtain fluid velocities u^*, v^*, and w^*.
3. Use the continuity equation to solve for the pressure field correction p'.
4. Calculate the corrected pressure field p by adding p' to p^*.
5. Calculate the corrected velocity field—u, v, and w—using the corrected pressure field.
6. Solve the remaining discretized equations that influence the flow field (i.e. energy equation).
7. Treat the corrected pressure p as the new guessed pressure p^*, and repeat steps 1–6 until convergence is reached.

Each step is discussed with regard to the CTF solution process, which differs in some respects. For Step 1, the user must provide a reference pressure to CTF. CTF will calculate the pressure field accounting for hydrostatic forces using this value and then use that as the initial guess. CTF performs a solution of the conservation equations for each time step in the modeled transient. Every timestep after the first will use the previous timestep's calculated pressure field as a guess for the new one.

For Step 2, the transverse momentum equations are solved first, followed by the axial momentum equations. As for Step 3, Patankar was considering an unheated case in which fluid energy was constant; however, for this case, it is necessary to use both the continuity and energy equations to determine the pressure correction. The independent scalar cell properties and momentum cell mass flow rates are solved for using the previous timestep values and the effect of the pressure correction. Step 3 forms what is known as the "inner iteration," which requires the solution of the pressure correction equations. Because there will be one pressure correction equation for each scalar cell in the mesh, this can be a very large matrix to solve. CTF is capable of solving this matrix by direct Gaussian elimination or by using one of the iterative Krylov methods.

With the corrections to the pressure field calculated, the current-iteration pressure field is then determined in Step 4. Additionally, back-substitution is performed to obtain the current-iteration values for the other dependent variables (e.g., void and enthalpy). Because the pressure field was changed, the velocities are updated accordingly in Step 5.

For Step 6, other equations solved by CTF include the interfacial area transport equation for tracking the interfacial area of the droplet field, and possibly fuel rod heat transfer and decay heat equations. Steps 1–6 form one cycle of what is known as an "outer iteration." CTF has a set of convergence criteria (see Section 3.6) that are checked upon the completion of Step 6. If they are not met, then the current iteration is attempted again with a smaller timestep. This is repeated up to a user-specified number of times for each outer iteration. If the outer iteration converges, CTF then moves onto the next timestep, repeating Steps 1–6 and marching through time until the simulation is completed.

Three main steps of this algorithm are described in greater detail below: solution of the momentum equations, solution of the mass and energy equations, and solution of the system pressure matrix. These steps are not mutually exclusive, because the momentum equations are initially solved and then later corrected after solution of the pressure matrix, and the derivation of the mass and energy equations are used for solution of the pressure matrix. However, it is sufficient for the purposes of this manual to lead the discussion in this manner while making note of these matters along the way.

3.1 LINEARIZATION AND SOLUTION OF THE MOMENTUM EQUATIONS

The purpose of he momentum equations is to solve for the field mass flow rates for the current timestep. In the momentum equations, the new-time mass flow rates appear in the temporal term and the shear terms. Everywhere else where the mass flow rate is needed (e.g., advection terms), the old-time value is used.

The solution process is to solve the transverse momentum equations first and the axial momentum equations second. Whether using the subchannel or Cartesian form of the momentum equations, CTF will solve the liquid, droplet, and vapor transverse momentum equations simultaneously for one gap at a time.

Before covering the solution process for the momentum equations, the finite-differenced transverse momentum equation will be reduced in Cartesian form. Returning to Eq. (48),

$$
\begin{aligned}
\frac{\left[(\alpha_v\rho_v v_v)_k^{n+1} - (\alpha_v\rho_v v_v)_k^n\right]}{\Delta t}\Delta X_J \Delta Y_k \Delta Z_k = &\left\{\left(\sum_{iib=1}^{niib}\left[(\alpha_v\rho_v v_v)^{\tilde{n}} u_v^n\right]_{iib}\frac{A_{m,ii,j-1}}{2} + \sum_{\mathrm{jjb}=1}^{\mathrm{njjb}}\left[(\alpha_v\rho_v v_v)^{\tilde{n}} u_v^n\right]_{\mathrm{jjb}}\frac{A_{m,jj,j-1}}{2}\right)\right.\\
&\left.-\left(\sum_{iia=1}^{niia}\left[(\alpha_v\rho_v v_v)^{\tilde{n}} u_v^n\right]_{iia}\frac{A_{m,ii,j}}{2} + \sum_{\mathrm{jja}=1}^{\mathrm{njja}}\left[(\alpha_v\rho_v v_v)^{\tilde{n}} u_v^n\right]_{\mathrm{jja}}\frac{A_{m,jj,j}}{2}\right)\right\}\\
&+\left\{\sum_{k_y=1}^{nk_y}\left[(\alpha_v\rho_v v_v)^{\tilde{n}}\bar{v}_v^n\right]_{k_y}\Delta X_J L_{k_y}\right.\\
&\left.-\sum_{k_{y+\Delta y}=1}^{nk_{y+\Delta y}}\left[(\alpha_v\rho_v v_v)^{\tilde{n}}\bar{v}_v^n\right]_{k_{y+\Delta y}}\Delta X_J L_{k_{y+\Delta y}}\right\}\\
&+\left\{\left(\sum_{kii_z=1}^{nkii_z}\left[(\alpha_v\rho_v v_v)^{\tilde{n}} w_v^n\right]_{kii_z}\Delta X_J\frac{L_{kii_z}}{2}\right.\right.\\
&\left.\left.+\sum_{kjj_z=1}^{nkjj_z}\left[(\alpha_v\rho_v v_v)^{\tilde{n}} w_v^n\right]_{kjj_z}\Delta X_J\frac{L_{kjj_z}}{2}\right)\right.\\
&\left.-\left(\sum_{kii_{z+\Delta z}=1}^{nkii_{z+\Delta z}}\left[(\alpha_v\rho_v v_v)^{\tilde{n}} w_v^n\right]_{k_{z+\Delta z}}\Delta X_J\frac{L_{kii_{z+\Delta z}}}{2}\right.\right.\\
&\left.\left.+\sum_{kjj_{z+\Delta z}=1}^{nkjj_{z+\Delta z}}\left[(\alpha_v\rho_v v_v)^{\tilde{n}} w_v^n\right]_{k_{z+\Delta z}}\Delta X_J\frac{L_{kjj_{z+\Delta z}}}{2}\right)\right\}\\
&-\left(P_{ii}^{n+1} - P_{jj}^{n+1}\right)\bar{\alpha}_{v,k,J}^n\Delta X_J\Delta Z_k - \tau_{w,v,J}\\
&-\tau_{i,vl,J} - \tau_{i,ve,J} + \Gamma v^n + \mathrm{Source}_{v,j}.
\end{aligned}
$$

Immediately, the transverse momentum equation can be collapsed into a greatly reduced form using the actual CTF source code variables:

- ufold$(2,k)$ — transverse vapor momentum convected into cell k by axial vapor velocity on the cell bottom
- uwgm — transverse vapor momentum convected out of the cell by axial vapor velocity on the cell top
- vwgm(k) — transverse vapor momentum convected into cell k by orthogonal vapor velocity

- vvfii — transverse vapor momentum convected into the cell by transverse vapor velocity on the *ii* side of the cell
- vvfjj — transverse vapor momentum convected out of the cell by transverse vapor velocity on the *jj* side of the cell
- vgamv — transverse vapor momentum convected into the cell by phase change

Also note that during the first momentum solve, the pressure terms are old time values. It is not until after the dependent variable update and back-substitution when the velocity field is updated using the new pressure values. In the following equations, which are for the first momentum solve, the pressure terms take on the old time superscripts.

$$\frac{\left[(\alpha_v\rho_v v_v)_k^{n+1} - (\alpha_v\rho_v v_v)_k^n\right]}{\Delta t}\Delta X_J\Delta Y_k\Delta Z_k = \{\text{ufold}(2,k) - \text{uwgm }\} + \{\text{vvfii } - \text{vvfjj }\} + \{\text{vwgm}(k)\} \\ -\left(P_{ii}^n - P_{jj}^n\right)\bar{\alpha}_{v,k,J}^n\Delta X_J\Delta Z_k - \tau_{w,v,J} - \tau_{i,vl,J} - \tau_{i,ve,J} + \text{vgamv} \tag{107}$$

Note that the source term was absorbed into one of the advection terms and no longer appears. Because we are solving for mass flow rates, the $\alpha\rho vA$ terms are collapsed to $\dot{m}$, and the shear terms are expanded.

$$\frac{\left[\dot{m}_v^{n+1} - \dot{m}_v^n\right]\Delta X_J}{\Delta t} = \{\text{ufold}(2,k) - \text{uwgm }\} + \{\text{vvfii } - \text{vvfjj }\} + \{\text{vwgm}(k)\} - \left(P_{ii}^n - P_{jj}^n\right)\bar{\alpha}_{v,k,J}^n\Delta X_J\Delta Z_k \\ - k_{w,x}^n\dot{m}_v^{n+1}\Delta X_J - k_{vl,x}^n(v_v^{n+1} - v_l^{n+1})\Delta X_J - k_{ve,x}^n(v_v^{n+1} - v_e^{n+1})\Delta X_J + \text{vgamv} \tag{108}$$

The new-time velocities are converted to new-time mass flow rates using the averaged old-time scalar variables.

$$\frac{\left[\dot{m}_v^{n+1} - \dot{m}_v^n\right]\Delta X_J}{\Delta t} = \{\text{ufold}(2,k) - \text{uwgmz}\} + \{\text{vvfii} - \text{vvfjj}\} + \{\text{vwgm}(k)\} + \left(P_{jj}^n - P_{ii}^n\right)\bar{\alpha}_{v,k,J}^n\Delta X_J\Delta Z_k \\ - k_{w,x}^n\dot{m}_v^{n+1}\Delta X_J - \left(\frac{k_{vl,x}^n}{\overline{\alpha_v^n\rho_v^n}\Delta X_J L_k} + \frac{k_{ve,x}^n}{\overline{\alpha_v^n\rho_v^n}\Delta X_J L_k}\right)\dot{m}_v^{n+1}\Delta X_J \\ + \frac{k_{vl,x}^n}{\overline{\alpha_l^n\rho_l^n}\Delta X_J L_k}\dot{m}_l^{n+1}\Delta X_J + \frac{k_{ve,x}^n}{\overline{\alpha_e^n\rho_l^n}\Delta X_J L_k}\dot{m}_e^{n+1}\Delta X_J + \text{vgamv} \tag{109}$$

Note that the sign of the pressure term is reversed. Next, the formula is arranged so that only the new-time mass flow rate appears on the LHS.

$$\dot{m}_v^{n+1} = \dot{m}_v^n + \frac{\Delta t}{\Delta X_J}\left[\text{ufold}(2,k) - \text{uwgm} + \text{vvfii} - \text{vvfjj} + \text{vwgm}(k) + \text{vgamv }\right] \\ + \frac{\Delta t}{\Delta X_J}\left[\bar{\alpha}_{v,k,J}^n\Delta X_J\Delta Z_k\right]\Delta P + \frac{\Delta t}{\Delta X_J}\left[-k_{w,x}^n\Delta X_J - \frac{k_{vl,x}^n}{\overline{\alpha_v^n\rho_v^n}\Delta X_J L_k} - \frac{k_{ve,x}^n}{\overline{\alpha_v^n\rho_v^n}\Delta X_J L_k}\right]\dot{m}_v^{n+1} \\ + \frac{\Delta t}{\Delta X_J}\left[\frac{k_{vl,x}^n}{\overline{\alpha_l^n\rho_l^n}\Delta X_J L_k}\right]\dot{m}_l^{n+1} + \frac{\Delta t}{\Delta X_J}\left[\frac{k_{ve,x}^n}{\overline{\alpha_e^n\rho_l^n}\Delta X_J L_k}\right]\dot{m}_e^{n+1} \tag{110}$$

One further simplification can be made by substituting A for the explicit terms, B for the terms that multiply by pressure drop, C for terms that multiply by new-time liquid mass flow rate, D for terms that multiply by new-time vapor mass flow rate, and E for terms that multiply by new-time entrained mass flow rate. This yields

$$\dot{m}_v^{n+1} = A_2 + B_2\Delta P + C_2\dot{m}_l^{n+1} + D_2\dot{m}_v^{n+1} + E_2\dot{m}_e^{n+1}. \tag{111}$$

The subscript is used to identify the field, and "2" is used to maintain consistency with the CTF source code ("1" is for liquid, and "3" is for droplets). As in the transverse vapor momentum equation, reductions can be performed for the other fields in both directions. The forms of the axial and transverse momentum equations are the same. The reduced liquid and entrained momentum equations are shown below.

$$\dot{m}_l^{n+1} = A_1 + B_1\Delta P + C_1\dot{m}_l^{n+1} + D_1\dot{m}_v^{n+1} \tag{112}$$

$$\dot{m}_e^{n+1} = A_3 + B_3\Delta P + D_3\dot{m}_v^{n+1} + E_3\dot{m}_e^{n+1} \tag{113}$$

Once the A–E terms are defined in CTF, as well as the old-time pressure drop, Eqs. (111)–(113) can be rewritten in matrix form as follows:

$$\begin{bmatrix} C_1 - 1 & D_1 & 0 \\ C_2 & D_2 - 1 & E_2 \\ 0 & D_3 & E_3 - 1 \end{bmatrix} \begin{Bmatrix} \dot{m}_l^{n+1} \\ \dot{m}_v^{n+1} \\ \dot{m}_e^{n+1} \end{Bmatrix} = \begin{Bmatrix} -A_1 - B_1\Delta P \\ -A_2 - B_2\Delta P \\ -A_3 - B_3\Delta P \end{Bmatrix}. \tag{114}$$

It is then a simple matter to solve Eq. (114) by Gaussian elimination and obtain the tentative mass flow rates.

3.2 LINEARIZATION AND SOLUTION OF MASS AND ENERGY EQUATIONS

At this point, the initial pressure field was used to calculate a velocity field. However the pressure field, which was based on initial conditions or the previous timestep information, may be changing, and the calculated velocities may not satisfy the conservation equations of mass and energy. Therefore, in this step it is determined what adjustments, if any, must be made to the independent variables such that the mass and energy equations are satisfied. Then the newly calculated pressure field can be used to correct the initial velocity field calculation.

The continuity and energy equations now form a system of equations that must be solved simultaneously such that they all equal zero, and mass and energy is conserved, as shown in Eq. (115).

$$C_l(\alpha_v, \alpha_v h_v, (1-\alpha_v)h_l, \alpha_e, P_J, P_{i=1\ldots nconn}) = 0 \tag{115a}$$

$$E_v(\alpha_v, \alpha_v h_v, (1-\alpha_v)h_l, \alpha_e, P_J, P_{i=1\ldots nconn}) = 0 \tag{115b}$$

$$E_l(\alpha_v, \alpha_v h_v, (1-\alpha_v)h_l, \alpha_e, P_J, P_{i=1\ldots nconn}) = 0 \tag{115c}$$

$$C_e(\alpha_v, \alpha_v h_v, (1-\alpha_v)h_l, \alpha_e, P_J, P_{i=1\ldots nconn}) = 0 \tag{115d}$$

$$C_v(\alpha_v, \alpha_v h_v, (1-\alpha_v)h_l, \alpha_e, P_J, P_{i=1\ldots nconn}) = 0 \tag{115e}$$

Note that the equations are not only functions of the mesh cell pressure in which the equations are being solved (P_J), but they are also functions of the surrounding mesh cells that connect to the cell ($P_{i=1...nconn}$). This is why a simultaneous solution of the pressure across the entire mesh must be obtained, as discussed next in Section 3.3.

Eq. (115) can be written more conveniently in vector notation, as follows:

$$\vec{f}(\vec{x}) = \vec{0}. \tag{116}$$

In Eq. (116), $\vec{f}$ is the vector representing the mass and energy equations, which are functions of the independent variables represented by the $\vec{x}$ vector. Assuming that all conservation equations are satisfied, they will equal the zero vector. Equation (116) can be solved numerically using a Newton-Raphson iteration, as written in Eq. (117).

$$\vec{f}(\vec{x}) = \vec{f}(\vec{x_0}) + D\vec{f}(\vec{x_0})(\vec{x} - \vec{x_0}) \tag{117}$$

$D\vec{f}(\vec{x_0})$ is the rate of change in each of our functions with respect to the variables. This term is known as "the Jacobian." It is multiplied by the change in the variables from one iteration step to the next and is added to the functions of the previous iteration variables to obtain the next iteration step function values. If the Jacobian term is expanded out for this case, then it will be the partial derivative of each conservation equation with respect to each partial derivative.

$$D\vec{f} = \begin{bmatrix} \frac{\partial}{\partial \alpha_v} C_l & \frac{\partial}{\partial \alpha_v h_v} C_l & \frac{\partial}{\partial (1-\alpha_v) h_l} C_l & \frac{\partial}{\partial \alpha_e} C_l & \frac{\partial}{\partial P_J} C_l & \frac{\partial}{\partial P_{i=1}} C_l & \dots & \frac{\partial}{\partial P_{nconn}} C_l \\ \frac{\partial}{\partial \alpha_v} E_v & \frac{\partial}{\partial \alpha_v h_v} E_v & \frac{\partial}{\partial (1-\alpha_v) h_l} E_v & \frac{\partial}{\partial \alpha_e} E_v & \frac{\partial}{\partial P_J} E_v & \frac{\partial}{\partial P_{i=1}} E_v & \dots & \frac{\partial}{\partial P_{nconn}} E_v \\ \frac{\partial}{\partial \alpha_v} E_l & \frac{\partial}{\partial \alpha_v h_v} E_l & \frac{\partial}{\partial (1-\alpha_v) h_l} E_l & \frac{\partial}{\partial \alpha_e} E_l & \frac{\partial}{\partial P_J} E_l & \frac{\partial}{\partial P_{i=1}} E_l & \dots & \frac{\partial}{\partial P_{nconn}} E_l \\ \frac{\partial}{\partial \alpha_v} C_e & \frac{\partial}{\partial \alpha_v h_v} C_e & \frac{\partial}{\partial (1-\alpha_v) h_l} C_e & \frac{\partial}{\partial \alpha_e} C_e & \frac{\partial}{\partial P_J} C_e & \frac{\partial}{\partial P_{i=1}} C_e & \dots & \frac{\partial}{\partial P_{nconn}} C_e \\ \frac{\partial}{\partial \alpha_v} C_v & \frac{\partial}{\partial \alpha_v h_v} C_v & \frac{\partial}{\partial (1-\alpha_v) h_l} C_v & \frac{\partial}{\partial \alpha_e} C_v & \frac{\partial}{\partial P_J} C_v & \frac{\partial}{\partial P_{i=1}} C_v & \dots & \frac{\partial}{\partial P_{nconn}} C_v \end{bmatrix} \tag{118}$$

Returning to Eq. (117), it is desirable to satisfy the mass/energy conservation requirements for $\vec{f}(\vec{x})$ to equal zero. Thus, the unknown becomes the amount that each variable must be changed by to achieve simultaneous solution of the system of equations. The change in the variables is conveniently noted as $\vec{x} - \vec{x_0}$, by $\Delta\vec{x}$, and the terms of Eq. (117) are moved around to achieve the following.

$$\vec{f'}(\vec{x_0})\delta\vec{x} = -\vec{f}(\vec{x_0}). \tag{119}$$

The Jacobian is calculated by taking the partial derivative of each equation with respect to each variable and then substituting in the variables from the previous timestep (or the initial values if on the first timestep). The RHS of Eq. (119) contains the conservation equations with the previous timestep values (or the initial values) used for the variables. If the velocity profile that was previously calculated by the momentum equation solution was correct and in no need of further correction, then the RHS term would be zero. However, during a transient, it likely will not be zero, but instead, there will be some residual value.

The unknown correction term $\Delta\vec{x}$ can be solved using Gaussian elimination if there were an equal number of unknowns and equations. However, by revisiting Eq. (117), it can see that the matrix will not be a $n \times n$ matrix because of the effect of pressure in the connecting cells, and in turn, there will be a greater number of unknowns *for the current scalar cell*. Recall that Eq. (119) is set up for one scalar mesh cell. Every cell in the mesh will have its own Jacobian and its own set of residuals. This problem is remedied by forming and solving the pressure matrix for the mesh.

3.3 SOLUTION OF THE PRESSURE MATRIX

For each scalar cell in the mesh, the Jacobian matrix is reduced by Gaussian forward elimination after having been formed. The bottom of the reduced matrix will contain the pressure of the current cell, and all connection cells and will be of the following form:

$$\delta P_J = a_5 + \sum_{i=1}^{\text{nconn}} (g_{5,i}\delta P_i). \tag{120}$$

Differential terms are seen here (i.e., δP_J) because we are solving for the *change* in variables over the timestep. There will be a pressure equation for each scalar mesh cell, with the total number of unknown pressures equaling the total number of scalar mesh cells. This forms the pressure matrix, which may be solved by direct inversion for small computational meshes or by the Gauss-Siedel iterative technique for large meshes.

The Gauss-Siedel iterative technique involves performing direct inversion over groups of cells specified by the user. The solution starts in one group, performing a direct inversion over all the cells contained within that group, whereas the cells in other groups that are attached to the current solution group retain their last iterate pressure. When direct inversion is complete, the process starts again for the next group, but this time the updated, most recent iterate value for the previous group is used (if it is connected to the new solution group). This process continues over all the groups.

This essentially reduces large multidimensional problems down to one-dimensional problems having as many cells as there are solution groups. Furthermore, convergence issues typical of problems having cells with large aspect ratios (long narrow cells) are eliminated if cells with large aspect ratios between them are placed in the same solution group.

Whereas the direct inversion occurs for cells within the group, the pressure variations in the surrounding group mesh cells are assumed to maintain their last iterate value. The process moves through each group,

updating the bounding cell pressure variations with their last iterate value along the way. This has the effect of reducing large multidimensional problems down to simpler problems.

The convergence efficiency can also be greatly enhanced with the use of rebalancing. This is the process of reducing the mesh to a 1D mesh and only solving pressure changes in the axial direction. Direct inversion is used, but the number of mesh cells is greatly reduced because the only concern is the axial direction. The solution obtained from the rebalancing approach is then used as an initial guess for each respective axial level, which starts the numerical solution closer to its actual next timestep solution. The rebalancing method is optional and must be specified by the user. If the option is not used, then the initial guess for linear pressure variation at each level is assumed zero.

3.4 BACK-SUBSTITUTION AND VELOCITY CORRECTION

With the pressure corrections calculated for the mesh, Eq. (120) can be solved for each scalar mesh cell to determine its new timestep pressure. With the bottom of the reduced Jacobian matrix known in every scalar cell, back-substitution can be used to calculate the other new timestep–dependent variables. Their forms will be as follows:

$$\delta\alpha_e = a_4 + f_4\delta P_J + \sum_{i=1}^{\text{nconn}} (g_{4,i}\delta P_i) \tag{121a}$$

$$\delta[(1-\alpha_v)h_l] = a_3 + e_3\delta\alpha_e + f_3\delta P_J + \sum_{i=1}^{\text{nconn}} (g_{3,i}\delta P_i) \tag{121b}$$

$$\delta(\alpha_v h_v) = a_2 + d_2\delta[(1-\alpha_v)h_l] + e_2\delta\alpha_e + f_2\delta P_J + \sum_{i=1}^{\text{nconn}} (g_{2,i}\delta P_i) \tag{121c}$$

$$\delta\alpha_v = a_1 + c_1\delta(\alpha_v h_v) + d_1\delta[(1-\alpha_v)h_l] + e_1\delta\alpha_e + f_1\delta P_J + \sum_{i=1}^{\text{nconn}} (g_{1,i}\delta P_i) \tag{121d}$$

An outer iteration loop is used to ensure that the mass and energy equation solution is sufficiently converged before moving to the next timestep. It is possible for the user to adjust the maximum number of outer iterations that can be taken during a timestep via the input file. This outer iteration loop algorithm is discussed further in Section 3.5. The timestep size is constrained by the Courant Friedrichs Lewy (CFL) criteria, as well as the time rate of the change of the dependent variables to prevent the computation from going unstable, which is discussed further in Section 3.6.

The velocity field is corrected for the newly calculated pressure field using the derivative of velocity with respect to pressure. It is a linear relationship which can be obtained directly from the momentum equations.

3.5 OUTER ITERATION LOOP

As discussed in the section above, the objective of the outer iteration is to ensure that the solution of the linearized equations is sufficiently representative of the nonlinear equations. In other words, the outer iteration loop ensures that the velocity field is satisfying the mass equation before marching in time. It is possible to use only one iteration (one solution of mass and energy equations) per timestep (i.e., implicit continuous Euler (ICE) method). In this approach, the code examines the rate of the change ($x^{n+1} - x^n$) for the primary dependent variables from one timestep to another and adjusts the timestep accordingly to maximize the accuracy and minimize the computer time. The obtained updated velocity fields will satisfy the mass and energy equations if the timestep is kept sufficiently small. This method can be used by setting the maximum allowable outer iterations to one.

By using the outer iteration loop, the algorithm is modified to that shown in Figure 8. The red diamond block is the check of the outer iteration tolerances, which are described in detail in Section 3.7.1. The green diamond block is the check of the rate of change for the independent variables, which is described in detail in Section 3.7.2.

As shown in Figure 8, the code will step into the outer iteration loop with a guessed velocity field and then solve for the change in the pressure equations. Then it will back substitute to obtain the change in the other dependent variables and evaluate the dependent variable at each outer iteration step, m, to be used for the next iteration. Within each outer iteration, the code will check for convergence in accordance with criteria described in Section 3.7.1. If any criteria are not met, then the code will attempt another outer iteration, unless the outer iteration counter has exceeded the maximum allowed outer iterations as set by the user, in which case, it will retry the timestep with a smaller timestep size. If all outer iteration criteria are met, then the code will check the change in independent variables as described in Section 3.7.2. If those convergence criteria are met, then the code will continue to the next timestep and, if not, it will restart the timestep and try again with a smaller timestep size.

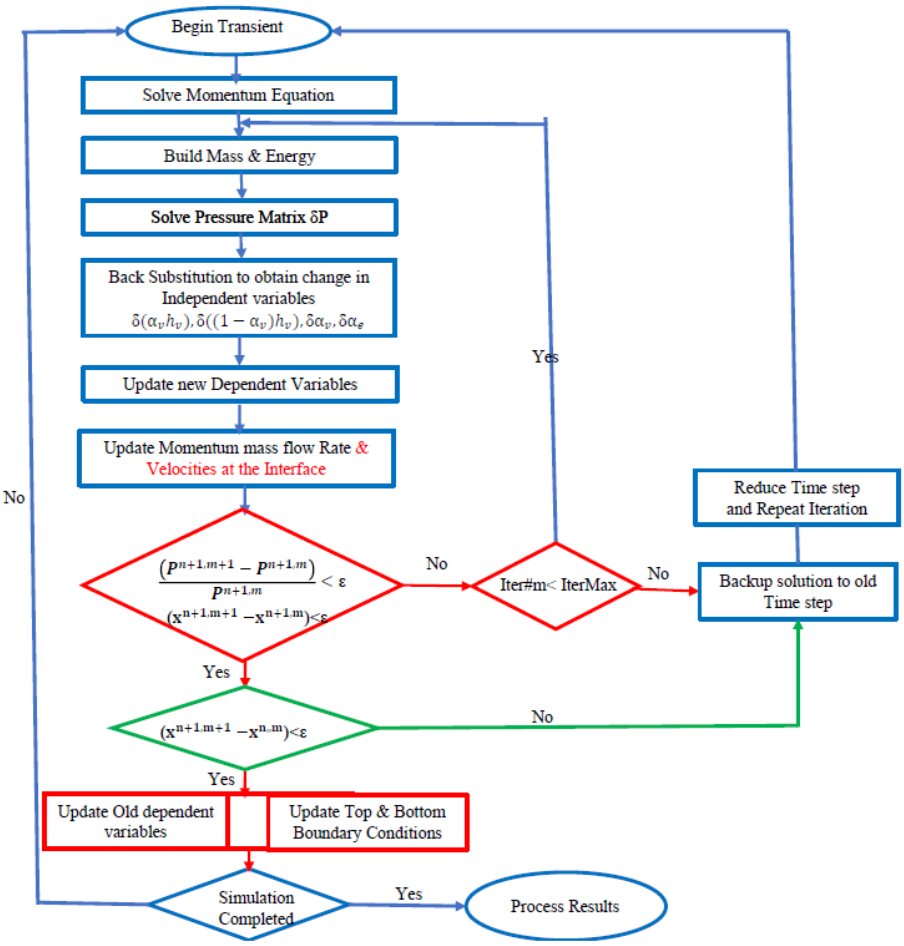

Figure 8. CTF outer iteration flowchart.

3.6 NUMERICAL CONTROLS

Several numerical controls are utilized for solving the linearized governing equations and ensuring that timestep size is set to values that balance a stable solution with a fast runtime. Figure 8 shows an overview of the steps taken during a timestep solution. The criteria used for controlling the steps in this flowchart are summarized in this section. Controls for the "Solve Pressure Matrix" step are shown in Section 3.6.1, controls for the "Update new Dependent Variables" step are shown in Section 3.7, stopping criteria for the outer iteration loop (red diamond in the figure) are shown in Section 3.5, and controls for the independent variable update (green diamond in the figure) are shown in Section 3.7.2. These aformentioned controls are used to determine when the outer iteration loop is converged or when the timestep is successful. In addition to this, CTF must also determine a suitable timestep size for the next timestep to be solved, as discussed in Section 3.7.3.

3.6.1 Pressure matrix solution

The pressure matrix is the combination of governing equation coefficients that link all cells together in the system, which means it is the largest matrix that must be solved for every outer iteration in the timestep. This matrix can be solved using a direct solver or an iterative solver. The solver itself is not a part of CTF, but rather is inherited from Futility or PETSc. PETSc is the preferred tool for performing the pressure matrix solution, and its documentation can be consulted for details on the inner workings of the solver. The CTF User Manual provides available solver options. The CTF user is able to set the relative solver tolerance and the maximum allowable number of iterations when using one of the iterative solvers in PETSc. The absolute solver tolerance is set to $1{\cdot}10^{-50}$.

3.7 BACK-SUBSTITUTION CONTROLS

After the pressure matrix solution is completed, the reduced Jacobian can be used with the new pressure corrections to determine the new values of the other independent variables. This is done for every cell in the model. During this process, several checks are made to ensure that the solution is not changing by an amount that would result in instability. In this section, a "failed timestep" means that the solution is reset to the solution at the completion of the last successful timestep, the timestep size is cut in half of its previous value, and the timestep is re-attempted by the code. The following criteria are enforced:

- Updated vapor void is forced to remain within a minimum bound of $1{\cdot}10^{-6}$ and a maximum bound of one minus $1{\cdot}10^{-6}$ (0.999999). If the solution drifts outside of this range, then the solution is forced to the minimum or maximum bound. This may result in a mass imbalance, but it is required to keep the void within reasonable bounds.
- Updated droplet void is forced to remain within the bounds of $5{\cdot}10^{-7}$ and $1-1\cdot10^{-6}-5\cdot10^{-7}$, similar to what was done for vapor void.
- Noncondensable gas pressure is forced to remain above 0.1 psia.
- If vapor void drops below 0.01, then the noncondensable gas pressure will be reset to the old iteration value.
- If the pressure goes outside the bounds of the fluid properties being used, then the timestep is failed.
- If the liquid enthalpy goes outside the bounds of the fluid properties being used, then the timestep is failed.
- If the vapor enthalpy goes above the maximum vapor enthalpy of the fluid properties being used or if it goes below the vapor saturation enthalpy minus 30 $\mathrm{BTU\,lbm^{-1}}$, then the timestep is failed.

- If the previous timestep vapor void was higher than 0.9998, then the liquid enthalpy is set to the liquid saturation enthalpy.
- If the vapor void is less than 0.01, then the vapor enthalpy is set to the vapor saturation enthalpy.
- If the liquid void is less than $1 \cdot 10^{-4}$, then the liquid enthalpy is set to the liquid saturation enthalpy.

3.7.1 Outer Iteration Controls

The acceptance criteria of the outer iteration that determine when the convergence is established are based on the ℓ_2 and ℓ_∞ norms. Either the ℓ_2 or the ℓ_∞ must be below the stopping criteria for the outer iteration to succeed and for the code to move on to the next timestep. If both the ℓ_2 and ℓ_∞ are not satisfied, then another outer iteration will be performed. The ℓ_2 norm is calculated as

$$\ell_2 = \sqrt{\Sigma_i = 1^N (M \Delta v_i^2)/N}, \tag{122}$$

where Δv is the change in the independent variable from the previous iteration to the current iteration (e.g., pressure, vapor void), and i is a counter over N cells in the model. M is a ramp used for certain independent variables to reduce the importance of a criterion in the case of phase depletion, which will be defined below. The ℓ_∞ is calculated as

$$\ell_\infty = \max(\Delta v_i), \tag{123}$$

which is simply the maximum change in independent variable over all cells in the model.

The ramp M that will be multiplied by the noncondensable gas pressure and $\alpha_v h_v$ variables is defined as

$$M = \max(0.0, \min(1.0, (\alpha_v - 0.001)/0.099)). \tag{124}$$

The ramp that will be multiplied by the $\alpha_e h_\ell$ term is defined as

$$M = \max(0.0, \min(1.0, (0.99999 - \alpha_\ell)/0.00009)). \tag{125}$$

Note that the M value will be 1.0 for all other terms (α_v, p, and α_e). Up to six independent variables will be checked, including α_v (vapor void), α_e (droplet void), $\alpha_v h_v$ (vapor enthalpy), $\alpha_e h_\ell$ (liquid enthalpy), p (pressure), and p_g (non-condensable gas pressure). If the noncondensable gas equation is not solved, then the last term is not considered. The variable change Δv is calculated as follows for each of these terms:

- $\Delta \alpha_v = \alpha_{v,m+1} - \alpha_{v,m}$
- $\Delta \alpha_e = \alpha_{e,m+1} - \alpha_{e,m}$
- $\Delta \alpha_v h_v = (\alpha_v h_v)_{m+1} - (\alpha_v h_v)_m$
- $\Delta \alpha_e h_\ell = (\alpha_e h_\ell)_{m+1} - (\alpha_e h_\ell)_m$
- $\Delta p = (p_{m+1} - p_m)/p_m$
- $\Delta p_g = (p_{g,m+1} - p_{g,m})/p_{g,m}$

Note that the two pressure terms are presented as relative changes, and the others are presented as absolute changes. This is important to consider for the definition of the stopping criteria. The ℓ_2 criteria are listed below:

- $\epsilon_{\alpha_v} = 1 \cdot 10^{-2}$
- $\epsilon_{\alpha_e} = 1 \cdot 10^{-2}$
- $\epsilon_{\alpha_v h_v} = 2.0$ BTU/lbm
- $\epsilon_{\alpha_e h_\ell} = 2.0$ BTU/lbm
- $\epsilon_p = 1 \cdot 10^{-3}$
- $\epsilon_p = 1 \cdot 10^{-3}$

The ℓ_∞ criteria are currently set to the same value as the ℓ_2 criteria. Note that the value of 2 BTU/lbm corresponds to an error of approximately 1 K in temperature. When the outer iteration loop is enabled, these tolerances are relaxed after each iteration by multiplying them by the number of outer iterations that have been taken. For example, on the second iteration, all tolerances are doubled, on the third, all tolerances are tripled, and so on.

3.7.2 Timestep Controls

With the back-substitution step successfully completed and the outer iteration loop stopping criteria satisfied, CTF checks the validity of the solution. The following checks are made, and if any fail, the timestep will be failed and tried again with a smaller timestep size:

- The maximum change in vapor void shall be less than or equal to 0.1 in one timestep.
- The maximum change in pressure shall be less than or equal to 10 psia.
- The timestep will fail if the change in vapor enthalpy is greater than 20 BTU lbm^{-1} when the vapor void is greater than 0.01 in the cell where the vapor change occurred.

These criteria were present in the original version of COBRA-TF when it was obtained by ORNL and seem to work well for all tests in the CTF assessment matrix.

3.7.3 Timestep Size Determination

The timestep size will be set prior to starting the solution of a timestep. Note that CTF has separate timestep sizes for the fluid and solid solutions. Although the solid and fluid timestep sizes can be different, they are scaled so that the completion of a fluid timestep will always result in the two time scales being in sync. For example, the fluid timestep size may be 0.01 s, and the solid timestep size may be 0.005 s, in which case two solid timesteps will be taken during the one fluid timestep so that the solution time is consistent for both sets of equations. The only reason for a solid timestep size to be less than the fluid timestep size is if the axial or azimuthal conduction terms are included in the solution, which are explicit terms that place additional stability constraints on the timestep size. These are discussed in Section 10.2.3. It is also possible for the timestep size to be larger than the fluid one by a multiplier set by the user. This feature can only be used for a steady-state solution to drive the conduction solution to its steady-state value more quickly. This feature is discussed in the CTF User Manual.

The size for the very first fluid timestep of the transient (not a restart case) will be set to the minimum allowable timestep size that was set by the user via the input deck. For every timestep after this, CTF will determine the size of the timestep using an algorithm that attempts to grow the timestep as large as possible, ranging up to the maximum allowable timestep size that was set by the user while still maintaining solution stability. When setting the next timestep size, CTF will try to grow the timestep as follows:

$$\Delta t_e = \Delta t^n (1.2 - (N_o - 1)/N_{\max}). \tag{126}$$

Here, the n superscript represents the previous timestep size. N_o is the number of outer iterations that were taken on the previous timestep calculation, and $N_{\max}$ is the maximum number of outer iterations allowed by the user. In this way, CTF will increase the timestep by a factor of 1.2 over the old timestep size at most, but if multiple outer iterations are required, it will reduce the growth to as much as zero, because a high number of outer iterations indicates trouble converging the timestep.

After this timestep is calculated, CTF will then consider the current solution and how it changed over the previous timestep to determine if the timestep size needs to be more limited. A summary of the timestep controls employed by CTF include the following:

- material CFL limit
- maximum void change in the model
- maximum pressure change in the model

Because CTF uses a semi-implicit solution approach, it is primarily controlled by a modified form of the material Courant limit. The traditional Courant limit is calculated as shown in Eq. (127), where Δt is the timestep size, ΔX represents the size of a mesh cell, and U is the velocity of the fluid.

$$\Delta t < \left| \frac{\Delta X}{U} \right| \tag{127}$$

The modification employed by CTF relates to the way in which the velocity U is calculated for the three fields. CTF calculates the net mass flow rate out of a given cell for each of the three fields (total flow out of the cell minus total flow into the cell). This net mass flow rate is then divided by the density of the phase in the cell to obtain an effective velocity for that cell. Because the flow is leaving and the density of the cell is used (calculated as $\alpha_k \rho_k$, where α_k is the void fraction of the field and ρ_k is the density of the phase), this is effectively the upwind scheme. This is done for each of the three fields, and then the maximum effective velocity is taken as the velocity to use in the CFL criteria. Note that the net flow coming into the cell will be considered as was done in the outlet flow of other cells so that the maximum velocity of the entire mesh is used.

There is currently a defect in the code in which the gas velocity and vapor velocity are erroneously added together rather than considering them separately in the determination of the max velocity. When the non-condensable gas model is enabled, this results in the velocity used in the CFL criteria being about twice as high as it should. This defect has not yet been removed because it has a stabilizing effect on some test cases, but it is possible for the user to work around the issue by changing the CFL number in the CTF input deck as defined in the CTF User Manual.

When calculating the CFL limited timestep size, CTF actually considers the maximum of three different velocities to calculate the Courant limit: new time velocity, old time velocity, and an extrapolated velocity, using Eq. (128).

$$U_{\text{extrap}} = 2 * U_{\text{new}} - U_{\text{old}} \tag{128}$$

Each of these velocities is the maximum velocity in the mesh. The maximum of the three velocities and a lower limit of 1×10^{-8} is used to calculate the Courant limit. Therefore, the maximum timestep size allowed by the CFL limit is

$$\Delta t_c = C / \max(1 \cdot 10^{-8}, U^n, U^{n-1}, U_{\text{extrap}}). \tag{129}$$

C is the CFL number which is set to 0.8 by default in CTF. The U term is the maximum system velocity as calculated above, and n denotes the timestep number.

The pressure controlled timestep is calculated as

$$\Delta t_p = \frac{\Delta t}{\max 1.0, \Delta p_{\max} / \Delta p_{\lim} /}, \tag{130}$$

where $\Delta p_{\lim}$ is the code-defined pressure limit, which is 5 psia, and $\Delta p_{\max}$ is the maximum pressure change in any given cell in the model. The Δt value on the right-hand side is the increased timestep size that was calculated by Eq. (126). If the maximum pressure change is less than or equal to the limiting pressure, then the pressure-limited timestep size will be the same as the base one, but if the maximum pressure is larger, it will begin to decrease the size of the timestep.

Finally, the timestep resulting from void change is calculated as shown in Eq. (131).

$$\Delta t_v = \frac{\Delta t}{\max 1.0, |\Delta \alpha_{v,\max}| / 0.1}, \tag{131}$$

where the absolute value of the maximum void change in the model is divided by the maximum allowable void change of 0.1. If the void changes by less than this amount, then the expanded timestep will be unaffected by the void control, but if the maximum void change is larger, then the timestep size will begin to be decreased. Finally, the new timestep size will be calculated as the most limiting of the expanded timestep and the three limited ones:

$$\Delta t^{n+1} = \min \Delta t_e, \Delta t_c, \Delta t_p, \Delta t_v. \tag{132}$$

3.7.4 Numerical Stability

Ramps are used throughout the code to ensure numerical stability. For example, closure terms like *interfacial shear* and *interfacial heat transfer* are dependent on flow regime, so they require the use of different models. Ramps are used to ensure that closure terms change gradually, even if a model changes from one timestep to the next.

All phasic constitutive variables such as shear and heat transfer coefficients are ramped to zero as a phase is depleted in a cell. These ramps are applied over a small range of void fractions, usually less than one percent.

Smoothing is also performed over time by using logarithmic interpolation between current and old timestep values, as shown in Eq. (133).

$$y(t + \Delta t) = y(t + \Delta t)^a y(t)^{1-a}. \tag{133}$$

Here, a is some parameter between 0 and 1.0 used to ramp the old timestep value of y to the new timestep calculated value in an exponential fashion. The value of a in CTF is typically 0.1.

3.8 NULL TRANSIENT CRITERIA

CTF includes an option to run a null transient, which means the solution is run until steady-state is reached. If this option is utilized, then the solution is not true steady-state because the time term still appears in all governing equations. The solution is still solved as a transient, but at every timestep, CTF will evaluate a set of simulation convergence criteria to determine if the solution has become steady. Convergence is judged by evaluating five terms:

1. the amount of energy stored in the fluid,
2. the amount of energy stored in the solids,
3. the amount of mass stored in the system,
4. the global energy balance, and
5. the global mass balance.

Each of these terms is discussed in further detail below.

3.8.1 Transient Storage of Energy

The stored energy criteria account for energy stored during the given timestep in the fluids and the solid conductors in the model. Energy storage is calculated as the change in energy in the system over the previous timestep. This is normalized by dividing through by the total power input delivered to the system from the rods. The equation for solid energy storage is as follows:

$$E_{\text{solid storage}} = \frac{E_{\text{rod}} + E_{\text{struc}}}{Q_{\text{rod}} + Q_{\text{fluid}}} \cdot 100. \tag{134}$$

Energy stored in the solids is the energy change in the rods and unheated conductors over the current timestep, normalized by the rod power, Q_{rod}, and the direct power to the coolant, Q_{fluid}. The energy changes in the solids are divided by the timestep size so that the units ($^{\text{BTU}}/_{\text{s}}$) match the units of the denominator. The resulting term is multiplied by 100 to convert the units to percent.

The fluid energy storage terms are similarly calculated as follows:

$$E_{\text{fluid storage}} = \frac{E_{\text{fluid}}}{Q_{\text{rod}} + Q_{\text{fluid}}} \cdot 100. \tag{135}$$

The numerator accounts for the energy change in the fluid over the previous timestep.

To expand on these terms, the energy stored in the fluid, E_{fluid}, is calculated as

$$\begin{aligned} E_{\text{fluid}} = \Big\{ \Sigma_{\text{cell}=1}^{\text{ncells}} \Big[\Big| (\alpha_l + \alpha_d)^{n+1} h_l^{n+1} \rho_l^{n+1} - \left(\alpha_l^n + \alpha_d^n\right) h_l^n \rho_l^n \Big|_{\text{cell}} + \\ \left| \alpha_v^{n+1} h_v^{n+1} \rho_v^{n+1} - \alpha_v^n h_v^n \rho_v^n \right|_{\text{cell}} \Big] \Big\} \frac{A_x \Delta X}{\Delta t}. \end{aligned} \tag{136}$$

In other words, it is the current iteration energy minus the previous iteration energy (recall that the n superscript denotes an old iteration value). This is done for both energy fields (recall that the droplets and liquid share an energy equation). This difference between iterations is calculated for each scalar cell, and all cell storage terms are summed together to obtain the total system energy storage. Note that the absolute value

of the liquid-energy storage is also taken for the vapor energy storage. It is possible that some cells may be losing energy during an iteration while others are gaining energy. Without the absolute value, it is possible for such terms to cancel each other out. It is also possible for energy to pass between phases, which is why individual absolute values are taken for the two individual fields. Using the absolute value terms prevents a judgement of convergence when energy is actually migrating through the system. The difference term is multiplied by the scalar cell volume and divided by the timestep size to convert the units to energy per time.

The storage terms for the solids conductors are calculated as follows:

$$E_{\text{solid}} = \Sigma_{\text{cell}=1}^{\text{ncells}} m_{\text{cell}} \text{Cp}_{\text{cell}} \left| T_{\text{cell}}^{n+1} - T_{\text{cell}}^{n} \right| \frac{1}{\Delta t}. \tag{137}$$

The transient storage of energy in a solid is the mass of the solid, m_{cell}, times its specific heat, Cp_{cell}, times the change in temperature over the timestep. Again, an absolute value is used to prevent opposite energy changes in different cells from canceling one another.

3.8.2 Global Balance of Energy

The global energy balance term accounts for all energy in and out of the system during the timestep. The equation is written as follows:

$$E_{\text{balance}} = \frac{Q_{\text{rod}} + Q_{\text{fluid}} + Q_{\text{inlet}} - Q_{\text{outlet}} - Q_{\text{amb}}}{Q_{\text{rod}} + Q_{\text{fluid}} + Q_{\text{inlet}}} \cdot 100. \tag{138}$$

The energy put into the system includes power deposited into the rods, Q_{rod}, power deposited into the coolant, Q_{fluid}, and energy coming in at the inlet of the model, Q_{inlet}. The energy leaving the system includes energy leaving the outlet, Q_{outlet}, and energy being lost to the environment, Q_{amb}. This term is normalized to the sum of the energy storage terms and the energy at the inlet. The units of the heat balance term are percentage.

3.8.3 Transient Storage of Mass

The mass storage accounts for mass stored in the system during the timestep. The calculation includes all fluid cells in the mesh. This is written as follows:

$$M_{\text{stor}} = \frac{M_{\text{fluid}}}{M_{\text{inlet}}} \cdot 100. \tag{139}$$

The stored mass is simply the amount of mass stored in all fluid cells normalized by the mass entering the system at the inlet. The units of this term are converted to percentage. The mass stored in the coolant is simply as follows:

$$M_{\text{fluid}} = \Sigma_{\text{cell}=1}^{\text{ncells}} \left[\frac{\Sigma_{k=1}^{3} \left| \alpha_k^{n+1} \rho_k^{n+1} - \alpha_k^{n} \rho_k^{n} \right|}{\Delta t} \right]. \tag{140}$$

It is the mass in a fluid cell at the current time (summed over all fields) minus the mass in the fluid cell at the previous iteration. An absolute value wraps each field to prevent a judgement of convergence when mass is migrating between fields or throughout the system.

3.8.4 Global Balance of Mass

As for the energy balance, the mass balance accounts for all the mass entering and leaving the system.

$$M_{\text{balance}} = \frac{M_{\text{inlet}} - M_{\text{outlet}}}{M_{\text{inlet}}} \cdot 100 \tag{141}$$

The term is normalized by the amount of mass entering the system, and units are again converted to percentage.

4. FLOW REGIME MAP

4.1 INTRODUCTION

The conservation equations described in Chapter 2 contain terms that must be solved to close the equations. These terms include the interfacial heat transfer, interfacial drag, and wall drag terms. However, these terms are dependent on the behavior of the two-phase flow, which is classified as one of several flow regimes using a flow regime map.

Flow regimes can generally be categorized into one of two categories: hot wall or normal wall. Hot wall flow regimes are unique because the wall cannot be wetted as a result of the Liedenfrost effect. This leads to liquid not touching the wall unless the surface is cool enough to quench. The normal wall flow regimes, on the other hand, involve the wall being wetted.

An example of hot wall flow regimes is shown in Figure 9. This figure denotes common behavior in a quench front scenario, where a subcooled liquid is rising in a hot channel. This is typical behavior in a large-break loss-of-coolant accident (LBLOCA) reflood transient. Below the quench front, the wall is wet, leading to normal wall flow regimes, and above it, the wall is vapor blanketed. Depending on the subcooling of the liquid and the quench front velocity, an inverted annular flow regime may be encountered. At higher voids, the flow regime will comprised dispersed droplets in mostly vapor. Another common scenario is for a top quench front to form, which leads to a falling film at high voids and a deluge at lower voids. CTF explicitly recognizes four hot wall flow regimes, which include: quench front, bottom reflood, falling film, and deluge. Bottom reflood covers both inverted annular and dispersed flow behavior as shown in the figure.

Normal flow regimes include those shown in Figure 10. CTF explicitly identifies four possible flow regimes: small bubble, large bubble (slug), churn/turbulent, and annular/mist flow. Note that single-phase liquid flow will be identified as small bubble, but the void will be insignificant so that two-phase closure terms will have virtually no impact on the solution.

Pertaining to the actual source code, the flow regime is defined for the momentum cells and not the scalar mesh cells. This is logical for the interfacial drag and wall drag calculations because those terms are utilized in the axial and transverse momentum equations only. However, the interfacial heat transfer term should be available in the scalar mesh cells—while it is calculated for the axial momentum cells, the interfacial heat transfer is calculated for the scalar mesh cells using linear averaging of values in adjacent axial momentum cells.

This chapter discusses the flow regime determination criteria and the approximations used for calculating the interfacial area for each recognized flow regime. The criteria used for determination of the flow regime are discussed in Section 4.2. Each section after that discusses how interfacial area is calculated for that regime, which includes the interfacial area for interfacial drag and the interfacial area for heat transfer. CTF includes an interfacial area transport equation, but this only captures the interfacial area of the droplets, so additional closures are still needed for flow regimes where the droplets are not the dominant cause of field interactions.

4.2 FLOW REGIME MAP CRITERIA

Figure 11 presents a flow chart of the algorithm for flow regime identification. If any surface T_w, facing a control volume is equal to or greater than the hot wall criteria T_{hot}, then the flow regime will be placed into one of the hot wall categories. If the hot wall criteria are not met but a the flow regime in the control volume at the previous time step was bottom reflood, then the hot wall logic will still be used to determine

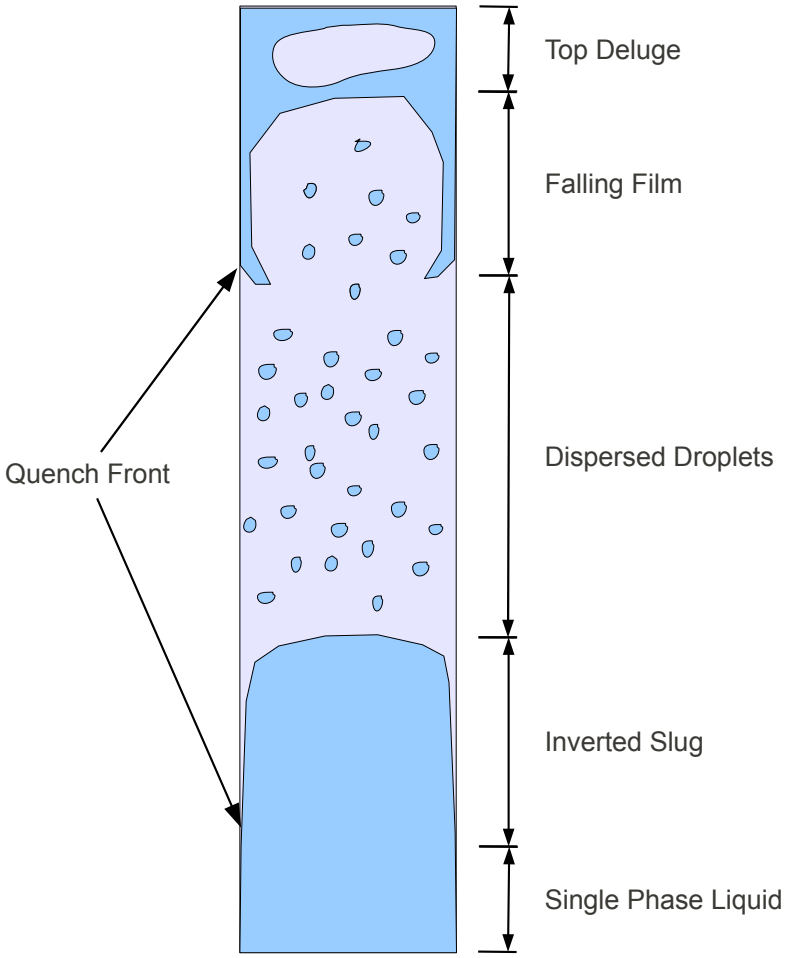

Figure 9. CTF hot wall flow regimes.

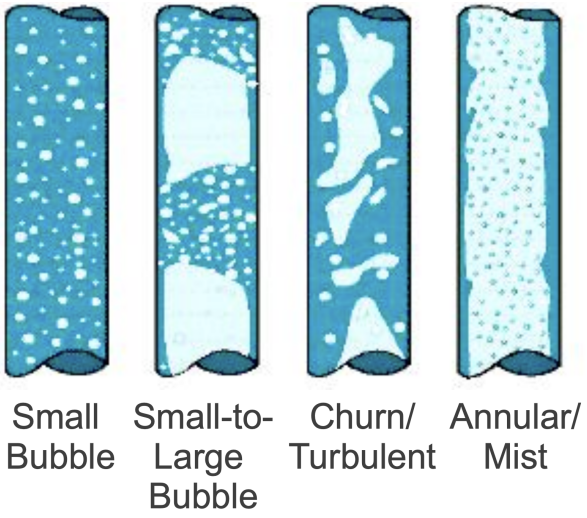

Figure 10. Normal wall flow regimes recognized by CTF.

the flow regime. This is done to ensure that the surface temperatures drop below the limit where they can be quenched and where a normal wall flow regime determination would be applicable. If the hot wall criteria are not exceeded and the previous flow regime was not bottom reflood, then the normal wall flow regime map will be used.

The hot wall temperature used in CTF is as follows:

$$T_{\text{hot}} = \min(T_{\text{crit}}, T_f + 75^{\circ}\text{F}). \tag{142}$$

In this equation, T_{crit} is the critical point temperature, which is obtained from the fluid properties being used, and T_f is the saturation temperature. If the hot wall logic is being used, then the ultimate flow regime classification depends on some specific factors:

- If all of the surface temperatures are below the quenching temperature T_{quench}, then the flow regime will be quench type.
- If any of the mesh cells above the current one contain a normal wall flow regime, then a top quench front exists, and the flow regime will be identified as falling film for high void or deluge for low void conditions.
- If all mesh cells above the current one contain hot wall flow regimes, then the flow regime of the current cell will be bottom reflood.

The T_{quench} value is calculated as $T_f + 10^{\circ}\text{F}$. Note that while this figure presents the flow regimes being identified using relatively simple criteria, there is overlap between the models used for different flow regimes. For example, the same interfacial heat transfer models are used for all of the hot wall flow regimes. These details are clarified in the sections and chapters that discuss calculation of closure models for each of the flow regimes.

The normal wall flow regime map criteria depend on which version of the flow regime map is being used: the legacy flow regime map or the drift-velocity–based map. The legacy map uses void-based flow regime transition criteria, which are summarized in Table 2.

Table 2. CTF legacy flow regime map

Small bubble regime	Large bubble regime	Churn/turbulent regime	Annular/mist regime
$0 < \alpha \leq 0.2$	$0.2 < \alpha \leq 0.5$	$0.5 < \alpha \leq \alpha_{crit}$	$\alpha_{crit} < \alpha \leq 1.0$

The transition to annular flow is defined by Eq. 143. Testing of the code indicated that this expression tends to push the transition to annular flow to unrealistically high values of 0.9 or larger for prototypical BWR conditions:

$$\alpha_{\text{trans}} = \max \begin{cases} 1 - \dfrac{2\sigma}{\rho_v |v_{v\ell}|^2 D_h} - \alpha_\ell \\ \\ 0.8 \end{cases} \tag{143}$$

To improve this, the drift-flux–based map was added as an option. This map, which is based on GE Hitachi's licensing topical report [20], generally leads to more physically correct predictions for annular transition.

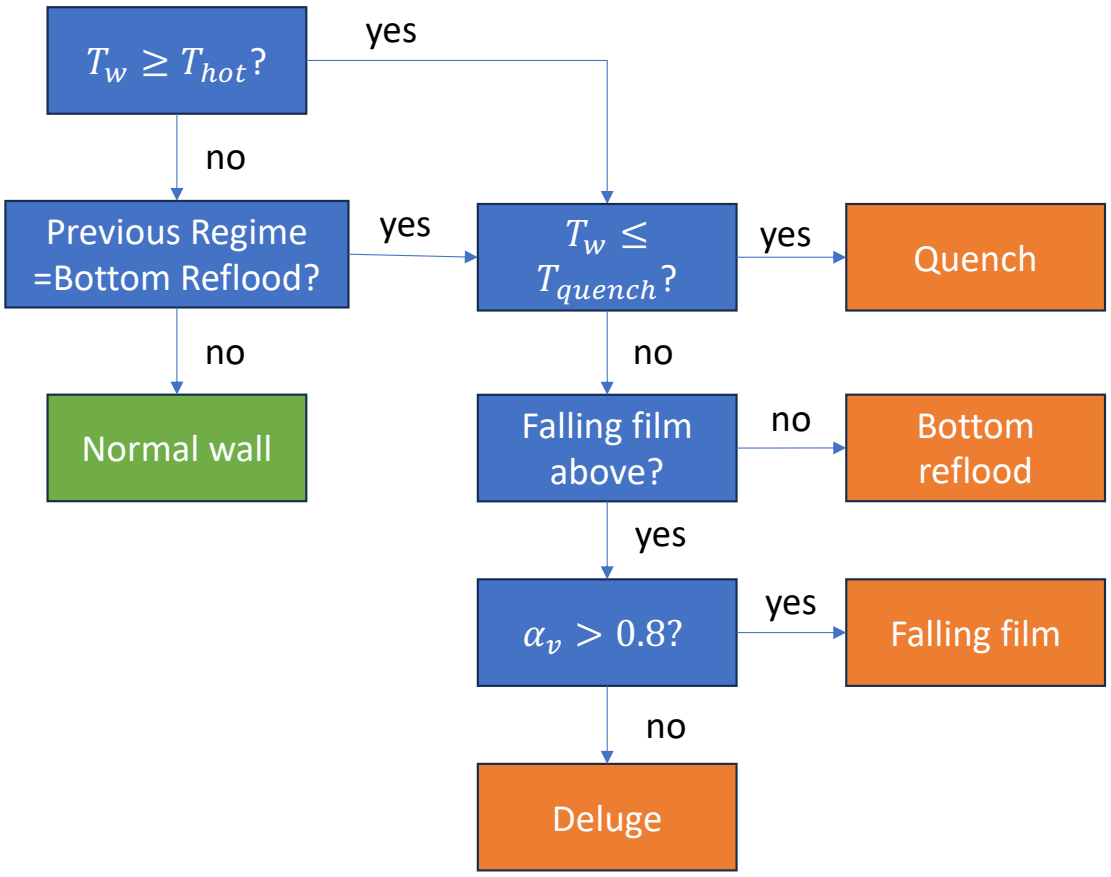

Figure 11. Flow regime selection logic used by CTF. If the flow regime is determined to be *normal wall,* then a specific set of criteria are used to determine which normal wall flow regime exists.

The criteria in this model are based on when the liquid in the film can be lifted by the vapor flow relative to the liquid in the churn flow regime. This criterion is satisfied at the void fraction where the same drift velocity is predicted for churn flow as for annular flow. This drift velocity–based correlation differs from the traditional two-phase flow-regime criteria based on the gas and liquid superficial velocities such as that from Steen Wallis [21], which may not be suitable for analyses of rapid transient or entrance flows by the two-fluid model. A comparison and discussion on the difference of this correlation to that of Steen Wallis can be found in Hizoum [22]. Table 3 summarizes the transition criteria used by this map.

Table 3. CTF improved flow regime map

Small bubble regime	Small to large bubble regime	Churn/turbulent regime	Annular/mist regime
$0 < \alpha \leq 0.2$	$0.2 < \alpha \leq \alpha_{trans} - 0.1$	$\alpha_{trans} - 0.1 < \alpha \leq \alpha_{trans}$	$\alpha_{trans} < \alpha \leq 1.0$

The criteria for annular transition are shown below:

$$\alpha_{trans} = \frac{j + 4\sqrt{\frac{\rho_g}{\rho_\ell}}\left((1 - C_0)\, j - 1.53\left(\frac{\sigma\Delta\rho g}{\rho_\ell^2}\right)^{\frac{1}{4}}\right) + 0.5\sqrt{\frac{\Delta\rho g D_H}{0.015\rho_\ell}}}{C_0 j + 1.53\left(\frac{\sigma\Delta\rho g}{\rho_\ell^2}\right)^{\frac{1}{4}} + 0.5\sqrt{\frac{\Delta\rho g D_H}{0.015\rho_\ell}}}, \tag{144}$$

where j is the total volumetric flux of the mixture, ρ_v and ρ_ℓ are vapor and liquid density, σ is surface tension, D_H is hydraulic diameter, $\Delta\rho$ is the density difference defined as $(\rho_\ell - \rho_v)$, g is the gravitational acceleration, and C_0 is the distribution parameter [23] given in the following form:

$$\begin{aligned} C_0 &= C_\infty - (C_\infty - 1)\sqrt{\frac{\rho_v}{\rho_\ell}}, \\ C_\infty &= 1.399 - 0.0155 ln(Re_\ell) \end{aligned} \tag{145}$$

where Re_ℓ is the liquid Reynolds number.

It is also worth noting that some numerical controls are used to adjust the void used for determination of the normal wall flow regime, which are described here. A void fraction check is made to ensure that the mesh cell flow regime is consistent with those around it. It is made between adjacent axial mesh cells, as shown below:

$$\Delta\alpha_v = \alpha_v(i, j+1) - \alpha_v(i, j), \tag{146}$$

where i is the channel index number and j is the axial node index. If the void fraction difference is large (i.e. $|\Delta\alpha_v| > 0.2$), then a ramp is defined as

$$F_{\Delta\alpha} = \min\left\{ \begin{array}{c} 1.0 \\ \frac{|\Delta\alpha_v| - 0.2}{0.2} \end{array} \right. \tag{147}$$

This ramp is then used to redefine mesh cell (i, j) void fraction, which is later used for calculation of interfacial quantities. The void fractions for each of the three fields become

$$\alpha_v = F_{\Delta\alpha}\alpha_v(i,j) + \frac{1}{2}(1 - F_{\Delta\alpha})[\alpha_v(i,j) + \alpha_v(i,j+1)], \tag{148a}$$

$$\alpha_l = F_{\Delta\alpha}\alpha_l(i,j) + \frac{1}{2}(1 - F_{\Delta\alpha})[\alpha_l(i,j) + \alpha_l(i,j+1)], \textit{and} \tag{148b}$$

$$\alpha_e = F_{\Delta\alpha}\alpha_e(i,j) + \frac{1}{2}(1 - F_{\Delta\alpha})[\alpha_e(i,j) + \alpha_e(i,j+1)]\,. \tag{148c}$$

If the mesh cell $(i, j-1)$ is in the annular/mist or a hot wall regime, then α_v and α_l are reset for subsequent calculations to the following:

$$\alpha_v = \max \begin{cases} \alpha_v(i,j-1) \\ \alpha_v, \quad \text{from Eq. (148)} \end{cases} \tag{149a}$$

$$\alpha_l = \min \begin{cases} \alpha_l(i,j-1) \\ \alpha_l, \quad \text{from Eq. (148)} \end{cases} \tag{149b}$$

If $|\Delta\alpha| > 0.2$ and $\Delta\alpha < 0$, then it is likely that an inverted pool exists, and the void fractions used to determine the flow regime and interfacial terms in cell (i, j) are as follows:

$$\alpha_v = F_{\Delta\alpha}\alpha_v(i,j+1) + \frac{1}{2}(1 - F_{\Delta\alpha})[\alpha_v(i,j) + \alpha_v(i,j+1)] \tag{150a}$$

$$\alpha_l = F_{\Delta\alpha}\alpha_l(i,j+1) + \frac{1}{2}(1 - F_{\Delta\alpha})[\alpha_l(i,j) + \alpha_l(i,j+1)] \tag{150b}$$

$$\alpha_e = F_{\Delta\alpha}\alpha_e(i,j+1) + \frac{1}{2}(1 - F_{\Delta\alpha})[\alpha_e(i,j) + \alpha_e(i,j+1)]\,. \tag{150c}$$

When a large void gradient between two cells is not present, the void fractions at the momentum cell center are assumed to be equal to the average void fractions in the accompanying continuity cells:

$$\alpha_v = \frac{1}{2}[\alpha_v(i,j) + \alpha_v(i,j+1)] \tag{151a}$$

$$\alpha_l = \frac{1}{2}[\alpha_l(i,j) + \alpha_l(i,j+1)] \tag{151b}$$

$$\alpha_e = \frac{1}{2}[\alpha_e(i,j) + \alpha_e(i,j+1)]\,. \tag{151c}$$

With the appropriate void fraction determined, CTF then selects the flow regime. The normal wall flow regimes are discussed in the following sub-sections.

4.3 SMALL BUBBLE REGIME

The small bubble flow regime consists of small bubbles dispersed in a continuous liquid. The regime exists for void fractions ranging from 0.0 to 0.2. The upper range of the flow regime is the point at which small bubbles begin to coalesce and form larger bubbles. The void fraction of 0.2 was selected based on the work of several authors.

First, Griffith and Wallis [24] conducted experiments with air-water mixture in tubes with diameter up to 1.0 inch and observed that below a void fraction of 0.18, there was no indication of slug formation. Additional experiments by Griffith and Snyder [25] indicated that the void fraction the bubbly-to-slug transition occurs in the range of 0.25 to 0.30. Mishima and Ishii [26] recommended a transition from small bubble to slug at a void fraction of 0.3. Similarly, Radovicich and Moissis [27] postulated that the maximum void fraction for bubbly flow is attained when the bubble collision frequency becomes very large, and they considered this to be a void fraction of 0.30.

The INTFR subroutine is used to determine the flow regime and flow regime–dependent closure terms. After selecting the flow regime to be small bubble, the interfacial area is calculated by assuming that the bubbles are spherical in geometry. The interfacial area is calculated in two ways: one that calculates interfacial drag, and one that calculates interfacial heat transfer.

4.3.1 Interfacial Area for Interfacial Drag

The radius is defined using a critical Weber number of 10.0. This calculation is performed as follows:

$$r_b^* = \frac{0.5 We_{\text{crit}} \sigma g_c}{\rho_l \vec{u}_{vl}^2} + 1 \cdot 10^{-5} \tag{152}$$

The $\vec{u}_{vl}$ is a vector, which includes both axial and transverse components of relative velocity between the liquid and vapor phases. The bubble radius is limited so that it cannot become larger than one-half the cell hydraulic diameter or 0.02 ft, whichever is smaller. This can be written as follows:

$$r_b = \begin{cases} r_b^* \\ \frac{D_h}{2} \\ 0.02 \text{ ft} \end{cases} \tag{153}$$

The interfacial area used in the interfacial drag coefficient calculations is then estimated as

$$A_{i,sb} = 3 \alpha_v A_x \frac{\Delta X}{r_b}, \tag{154}$$

where A_x is the momentum cell area.

4.3.2 Interfacial Area for Interfacial Heat Transfer

If the liquid is superheated, then the bubble diameter is calculated as follows:

$$D_b = \min\left(2 r_b, D_b^*\right), \quad \text{where} \tag{155a}$$

$$D_b^* = 2 \left[\frac{3}{4\pi} \frac{\max\left(\alpha_v, 0.001\right)}{N_b} \right]^{0.333}, \quad \text{or} \tag{155b}$$

$$D_b^* = 1.24 \left[\frac{\max\left(\alpha_v, 0.001\right)}{N_b} \right]^{0.333}. \tag{155c}$$

N_b is the minimum bubble number density and is defined as

$$N_b = \frac{2000}{\max(\alpha_v, 0.001)}. \tag{156}$$

N_b is in units of number of bubbles per cubic foot. It was formulated in this manner to capture the fact that coalescence of bubbles occurs as vapor increases in the flow. The model yields a bubble radius of 0.1 inches at a void fraction of 0.2. The purpose of this model is to provide an interfacial area for the initiation of flashing.

The interfacial area for interfacial heat transfer coefficient calculations is

$$A_{i,sb} = \frac{6\max(\alpha_v, 0.001)A_x\Delta X}{D_b}. \tag{157}$$

4.4 LARGE BUBBLE REGIME

The small-to-large bubble regime exists for void fractions ranging from 0.2–0.5. The upper limit corresponds to the work of Taitel, Bornea, and Dukler [28]. Their work found that, considering spherical bubbles packed into a cubic lattice, bubbles begin to touch at a void fraction of 0.52. This was assumed to represent the upper limit of bubbly flow.

This regime is considered to consist of a combination of small bubbles and large bubbles, as shown in Figure 10. Their distribution is determined by assuming that the void fraction of small bubbles stays constant at 0.2, the upper limit for the small bubble flow regime, with the remainder of vapor void existing in the form of large bubbles. The large bubble size increases with void fraction until its diameter equals the channel size or 3 inches, whichever is less. The large bubbles are also considered spherical in shape when calculating interfacial area.

The small bubble regime calculations, as described in Section 4.3, are performed assuming that all of the vapor is in the form of small bubbles, and the interfacial area is stored as a temporary variable. Calculations assuming that all of the vapor is in the form of large bubbles are performed next. The results for the two different bubble types are then interpolated.

The large bubble radius is first calculated as follows:

$$r^*_{lb} = \left[0.2387\left(\alpha_v - \frac{\alpha_{sb}\alpha_l}{1-\alpha_{sb}}\right)A_x\Delta X\right]^{0.3333}. \tag{158}$$

The large bubble radius is calculated by subtracting the small bubble volume from the total vapor volume to obtain the large bubble volume, and then assuming spherical geometry of the large bubbles to calculate the large bubble radius (see Box 1 for more details). The result is compared to the channel hydraulic diameter, the small bubble radius, and a limiting factor in the following axiom:

$$r_{lb} = \max\left\{\begin{array}{c}\min\left\{\begin{array}{c}0.25\,\text{ft}\\ 0.5D_h\\ r^*_{lb}\end{array}\right.\\ r_{sb}\end{array}\right. \tag{159}$$

For large bubbles, the interfacial area in a computational cell is equal to the surface area of a single bubble times the number of bubbles in the cell. The number of large bubbles in a mesh cell is equal to the total

large bubble volume divided by the single large bubble volume (the two values will clearly be equal if only one large bubble exists):

$$N_{lb} = \frac{V_{lb}}{\frac{4}{3}\pi r_{lb}^3} \tag{160}$$

Assuming that all vapor is in the form of large bubbles and multiplying this by the surface area of a single large bubble, the surface area of the large bubbles is as follows:

$$A_{i,lb} = \frac{\alpha_v A_x \Delta X}{\frac{4}{3}\pi r_{lb}^3} 4\pi r_{lb}^2. \tag{161}$$

Simplifying this leads to

$$A_{i,lb} = 3\alpha_v A_x \frac{\Delta X}{r_{lb}}. \tag{162}$$

This expression is used to calculate large bubble interfacial drag coefficient.

To prevent a dependence on the adjacent void fraction, α_v of cells (i, j) and $(i, j+1)$ are compared:

$$A_{i,lb}^* = \frac{\min\left(\alpha_v(i,j), \alpha_v(i,j+1)\right)}{\alpha_v} A_{i,lb}. \tag{163}$$

With the small bubble interfacial area calculated in Section 4.3, Eq. (157) and the large bubble interfacial area presented in Eq. (163), the interfacial area for the small-to-large bubble flow regime is calculated by interpolation.

$$A_{i,slb} = F_{sb} A_{i,sb} + (1 - F_{sb}) A_{i,lb}^*. \tag{164}$$

F_{sb} is the ratio of vapor volume in the form of small bubbles to the total volume of vapor in the cell:

$$F_{sb} = \frac{V_{sb}}{V_c}. \tag{165}$$

Using the definition of V_{sb}, which was calculated in Eq. (170) during the large bubble radius derivation in Box 1, we can expand this to:

$$F_{sb} = \frac{\alpha_{sb}\alpha_l}{(1 - \alpha_{sb})\alpha_v}. \tag{166}$$

Box 1: Calculation of Large Bubble Radius

The large bubble radius can be calculated from the large bubble volume if we assume spherical geometry:

$$V_{lb} = \frac{4}{3}\pi r_{lb}^{*\,3} \tag{167}$$

The total large bubble volume is simply equal to the total volume minus the small bubble volume:

$$V_{lb} = V_v - V_{sb} \tag{168}$$

V_{sb} is calculated by considering that the small bubble void, α_{sb}, is the small bubble volume divided by the sum the of liquid and small bubble volumes.

$$\alpha_{sb} = \frac{V_{sb}}{V_l + V_{sb}}. \tag{169}$$

Solving for V_{sb}, we get the following:

$$V_{sb} = \frac{\alpha_{sb} V_l}{1 - \alpha_{sb}}. \tag{170}$$

For a given momentum mesh cell with a cross-sectional area of A_x and a height of ΔX, the liquid volume is:

$$V_l = \alpha_l A_x \Delta X. \tag{171}$$

Substituting Eq. (171) into Eq. (170), we are left with the small bubble volume in terms of known variables (because it was assumed that small bubble void was at the upper limit for the small bubble flow regime, $\alpha_{sb} = 0.2$):

$$V_{sb} = \frac{\alpha_{sb}\alpha_l A_x \Delta X}{1 - \alpha_{sb}}. \tag{172}$$

Substituting this into Eq. (168), along with the definition of total vapor volume, the large bubble volume is

$$V_{lb} = \left(\alpha_v - \frac{\alpha_{sb}\alpha_l}{1 - \alpha_{sb}}.\right) A_x \Delta X \tag{173}$$

Assuming that the total large bubble volume is all in a single large bubble, the large bubble radius is calculated by equating this equation to Eq. (167) and solving for r_{lb}^*, with the result shown in Eq. (158). If the total large bubble volume is in fact spread amongst several large bubbles, then the limit presented in Eq. (159) will act to reduce the large bubble radius.

4.5 CHURN/TURBULENT REGIME

The churn/turbulent region exhibits large bubble flow behavior but is more chaotic in nature. In CTF, its behavior is captured by blending the small-to-large bubble regime and the annular/mist regime characteristics. The transition criteria will depend on the flow regime map option that is used as discussed in Section 4.2.

Because the churn/turbulent regime is a mixture of small-to-large bubble flow regime properties and annular/

mist properties, calculations are performed for both flow regimes if α is between the lower and upper bounds of the flow regime. Calculations for the interfacial area of the small-to-large bubble regime are presented in Section 4.4. Calculations for the interfacial area of the annular/mist regime are presented next in Section 4.6.

No interpolation is performed for the interfacial area term in the source code. Instead, the interfacial drag and heat transfer terms are calculated for the small-to-large bubble and annular/mist regimes, and those terms are then interpolated using the F_a interpolation factor as shown below:

$$F_a = \frac{\alpha_v - 0.5}{\alpha_{\text{crit}} - 0.5}. \tag{174}$$

The term is used for calculating churn/turbulent closure terms, as follows:

$$P_{\text{CT}} = F_a P_{\text{AM}} + (1 - F_a) P_{\text{SLB}}. \tag{175}$$

P denotes the term being calculated (i.e., either interfacial drag or interfacial heat transfer) and CT, AM, and SLB represent the corresponding closure term for the churn/turbulent, annular/mist, and small-to-large bubble regimes, respectively.

4.6 ANNULAR/MIST REGIME

The annular/mist flow regime is characterized by a continuous liquid film surrounding a vapor core that may or may not contain a droplet field. The droplet diameter is calculated using the droplet interfacial area, which is calculated using the interfacial area transport equation (discussed in Section 2.4). The droplet diameter is also limited, as shown below:

$$D_d = \max \begin{Bmatrix} \dfrac{6\alpha_e}{A'''_{i,d}} \\ 0.0005 \text{ ft.} \end{Bmatrix} \tag{176}$$

The droplet diameter is later used for calculation of the interfacial drag on the droplet field. It is necessary to calculate the interfacial area for both the continuous liquid and droplet fields separately and then add them together. The interfacial area of the droplet field is very simply:

$$A_{i,d} = A'''_{i,d} A_x \Delta X \tag{177}$$

The interfacial area of the film is calculated by assuming that the vapor core is cylindrical in shape and then calculating its surface area[29]. The result is:

$$A_{i,f} = \frac{4\sqrt{\alpha_v + \alpha_e} A_x \Delta X}{D_h}. \tag{178}$$

To keep the transition between adjacent mesh cells smooth, Eq. (178) is multiplied by a ramp, as follows:

$$A_{i,f} = \sqrt{\frac{\alpha^*}{\alpha_v + \alpha_e}} \left(\frac{4\sqrt{\alpha_v + \alpha_e} A_x \Delta X}{D_h} \right), \quad \text{where} \tag{179a}$$

$$\alpha^* = \min \begin{Bmatrix} 1 - \alpha_l \\ 1 - \alpha_l(i, j+1) \end{Bmatrix}. \tag{179b}$$

4.7 BOTTOM REFLOOD

This regime consists of an annular film of vapor surrounding a liquid core. The regime may also contain dispersed droplets depending on the droplet void. If the continuous liquid void is very small, then the regime will be purely dispersed droplet. The interfacial area of the liquid core is calculated assuming that it is cylindrical in shape:

$$A'''_{i,f} = \frac{P_w \sqrt{\alpha_l}}{A_x}. \tag{180}$$

This can be rewritten in terms of hydraulic diameter as

$$A'''_{i,f} = \frac{4 \sqrt{\alpha_l} A_x \Delta X}{D_h}. \tag{181}$$

The droplet's interfacial area is determined by the interfacial area transport equation, later presented in Section 2.4. The interfacial area for a mesh cell is as follows:

$$A_{i,d} = A'''_{i,d} A_x \Delta X. \tag{182}$$

4.8 FALLING FILM REGIME

A falling film exists if any cell above the current one is experiencing a normal wall flow regime. If the cell has a hot wall flow regime and it is in the top section of the model—meaning that there is no cell above—then there will be no falling film above. The regime consists of film flowing down and vapor flowing up. The interfacial area for the film is calculated in the same way as in the normal wall regime, annular/mist:

$$A'''_{i,f} = \frac{4 \sqrt{1 - \alpha_v}}{D_h}. \tag{183}$$

The droplet interfacial area is once again determined from the solution of the interfacial area transport equation:

$$A_{i,d} = A'''_{i,d} A_x \Delta X. \tag{184}$$

4.9 TOP DELUGE REGIME

The top deluge regime consists of large liquid slugs with a diameter equal to the channel hydraulic diameter. Like the falling film regime, the top deluge regime results from the existence of a top quench front (i.e., the mesh cell is in the hot wall regime with a normal wall regime in the mesh cell above). The regime occurs when void fraction is below 0.8.

The interfacial area of the slugs is calculated assuming that the slugs are spherical in geometry. The interfacial area will then be the number of slugs in the volume times the interfacial area of each sphere:

$$A'''_{i,s} = N'''_s \pi D_s^2. \tag{185}$$

D_s is the diameter of a slug; however, it is assumed that the slug diameter is equal to the hydraulic diameter. The number of slugs is calculated by dividing the total liquid volume by the volume of one slug:

$$N_s''' = \frac{\alpha_l}{\frac{\pi D_h^3}{6}}. \tag{186}$$

Substituting Eq. (186) into Eq. (185) yields:

$$A_{i,s} = \frac{6\alpha_l}{D_h} A_x \Delta X \tag{187}$$

The interfacial area of the droplet field is once again determined by the solution of the interfacial area transport equation:

$$A_{i,d} = A_{i,d} A_x \Delta X \tag{188}$$

4.10 QUENCH FRONT REGIME

The quench regime exists simply to indicate that the flow regime was identified as a hot wall regime in the previous time step but that the surface temperatures have dropped below the quenching criteria. The interfacial area will be addressed according to whatever flow regime was previously identified for the cell. For example, if the cell is found to be hot wall with a falling film above, then the interfacial area will be calculated as shown in Section 4.8, or if there is no top quench front, then it will be calculated as shown in Section 4.7.

5. WALL SHEAR AND FORM LOSS MODELS

The wall shear model is briefly introduced in Section 2.3.2.2 as part of the discussion of the finite-differenced form of the momentum conservation equations. The wall shear term is restated here as a coefficient times the field mass flow rate.

$$\tau_{w,x} = k_{w,x}\dot{m}\Delta X. \tag{43}$$

The wall shear in CTF is also visualized as a combination of frictional losses and flow form losses, as follows:

$$\tau_{w,x} = \left[\left(\frac{dP}{dX}\right)_{\text{fric}} + \left(\frac{dP}{dX}\right)_{\text{form}}\right]\Delta X. \tag{189}$$

Combining this equation with Eq. (43) allows for the definition of the wall drag coefficient $K_{w,x}$:

$$K_{w,x} = \left(\frac{dP}{dX}\right)_{\text{fric}}\frac{1}{\dot{m}} + \left(\frac{dP}{dX}\right)_{\text{form}}\frac{1}{\dot{m}}. \tag{190}$$

To further this derivation of the wall drag loss coefficient, the friction and form pressure loss components are defined in the following subsections.

5.1 FRICTION LOSS MODEL

CTF uses a two-phase pressure drop model based on the work of Wallis[30] as follows:

$$\left(\frac{dP}{dX}\right)_{\text{fric}} = \frac{f_w G_x^2}{2D_h\rho}\Phi_x^2 \tag{191}$$

It must be noted that this is a generalized definition of the frictional pressure gradient, and in the following section, the model-specific pressure gradient is discussed in detail. G_x is the mass flux of the field of interest, and Φ_x is a (phasic) two-phase multiplier defined according to two different classes of models: void-based models (function of the void fraction), and quality-based models (function of quality). Two-phase multiplier models which are a function of the gas/liquid void fraction are tightly coupled with the interfacial drag making an independent assessment/calibration of the wall shear and interfacial drag difficult. This is ameliorated with a quality-based model. Accordingly, two quality-based models are implemented in CTF, which are described in the following sections.

The friction factor f_w is defined using phase Reynolds number Re and surface roughness ϵ. The friction factor correlations are provided in Table 4. Note that all correlations except for the Churchill correlation return the Darcy friction factor. The Churchill correlation returns the Fanning friction factor, which is four times smaller than the Darcy friction factor. Because the CTF model uses the Darcy friction factor, the Fanning friction factor is multiplied by 4.

The phase Reynolds number is based on phasic properties:

$$\mathrm{Re} = \frac{D_h |G_k|}{\mu_k}. \tag{192}$$

The subscript k represents the phase and can be either liquid or vapor. Addition of surface roughness requires a special treatment of calculating the frictional pressure drop when there are different rod types in the same subchannel with different surface roughnesses. CTF determines a surface area's weighted average surface roughness for the channel.

$$\epsilon_{i,\mathrm{eff}} = \frac{\sum_r \epsilon_r P_{w,r}}{P_{w,i}}. \tag{193}$$

In the equation, the r subscript is a counter over the rod surfaces touching the channel i. The term $P_{w,r}$ is the wetted perimeter of the rod segment that touches the channel, and ϵ_r is the roughness of that rod segment. The denominator $P_{w,i}$ is the total wetted perimeter of Channel i.

It is important to note that the sum of $P_{w,r}$ over all rod surfaces touching the channel does not necessarily equal the total channel wetted perimeter, $P_{w,i}$. The user is free to set the channel wetted perimeter, $P_{w,i}$, as desired, independent of the actual dimensions of the rods touching the channel. This feature is most commonly used for specifying a wall around a rod bundle without explicitly modeling the solid objects that make up the wall. In this way, the wall shear effect can be captured without actually modeling the wall. *The surface roughness is only considered for rod and unheated conductor surfaces*. Therefore, in a boundary channel of a rod bundle with a fuel canister, for example, the wall will always be assumed smooth, regardless of the roughness of the attached rod.

Additionally, the effect of wall drag in the lateral momentum cell is also considered in gaps that touch a wall. However, walls that touch gaps are also considered smooth. The following sections review the two-phase multiplier models currently available in CTF.

5.1.1 Lockhart-Martinelli Model

The Lockhart-Martinelli model is a quality-based two-phase multiplier model and is formulated on two assumptions: single-phase pressure drop relations can be applied to each phase, and the pressure gradients of the two-phases are equal at any axial position [31]. The two-phase frictional pressure gradient is related to a single-phase pressure drop gradient assuming each phase flows alone at its actual flow rate. Following from 191, the two-phase pressure drop gradient is defined as follows:

$$\left.\frac{dP}{dX}\right)^{\mathrm{TP}}_{\mathrm{fric}} \equiv \left.\frac{dP}{dX}\right)^{\mathrm{l}}_{\mathrm{fric}} \Phi_l^2 \equiv \left.\frac{dP}{dX}\right)^{\mathrm{v}}_{\mathrm{fric}} \Phi_v^2, \tag{194}$$

where the single-phase liquid and vapor pressure gradients are defined as follows:

$$\left.\frac{dP}{dX}\right)^{\mathrm{l}}_{\mathrm{fric}} = \frac{f_l}{D_h} \frac{G_m^2 (1 - x_{\mathrm{flow}})^2}{2\rho_l}, \tag{195}$$

$$\left.\frac{dP}{dX}\right)^{\mathrm{v}}_{\mathrm{fric}} = \frac{f_v}{D_h} \frac{G_m^2 x_{\mathrm{flow}}^2}{2\rho_v}, \tag{196}$$

where D_{h} is the channel hydraulic diameter, x_{flow} is the flow quality, f_k is the friction factor of the k^{th} phase, and G_{m} is the mixture/total mass flux. From 194, 195, and 196, the liquid and vapor two-phase multipliers are obtained as follows:

$$\Phi_l^2 = \frac{f_{TP}}{f_l}\frac{\rho_l}{\rho_m}\frac{1}{(1-x_{\text{flow}})^2}, \tag{197}$$

$$\Phi_v^2 = \frac{f_{TP}}{f_v}\frac{\rho_v}{\rho_m}\frac{1}{x_{\text{flow}}^2},, \tag{198}$$

where f_{TP} is the two-phase friction factor. Lockhart and Martinelli [32] define the parameter X as the ratio of the liquid to vapor frictional pressure gradients as follows:

$$X^2 \equiv \frac{\left.\frac{dP}{dX}\right)_{\text{fric}}^{\text{l}}}{\left.\frac{dP}{dX}\right)_{\text{fric}}^{\text{v}}} = \frac{\Phi_v^2}{\Phi_l^2}. \tag{199}$$

Therefore, from its definition, X can be obtained as follows:

$$X = \left(\frac{\rho_v}{\rho_l}\right)^{0.5}\left(\frac{f_l}{f_v}\right)^{0.5}\frac{(1-x_{\text{flow}})}{x_{\text{flow}}}. \tag{200}$$

Lockhart and Martinelli [32] postulated that the liquid and vapor frictional multipliers can be correlated uniquely as a function of X. Using data from horizontal adiabatic two-phase flows, Lockhart and Martinelli [32] graphically represented 199 by the following curves:

$$\Phi_l^2 = 1 + \frac{C}{X} + \frac{C}{X^2}, \tag{201}$$

$$\Phi_v^2 = 1 + CX + X^2. \tag{202}$$

The constant C varies according to different combinations of the phasic flow type (laminar or turbulent), and the values of C are summarized in [31]. The C value (C=20) corresponding to turbulent liquid-turbulent vapor flow regime is typically used across all regimes [31]. Finally, using the liquid frictional multiplier defined in 201 and the liquid single-phase pressure gradient 195, the two-phase frictional pressure drop can be obtained from 194 or 191.

5.1.2 Chisholm Model

The Chisholm model is also a quality-based two-phase multiplier model and is derived for evaporating flow. In the Chisholm model, a simplified set of conservation equations is solved to obtain an analytical expression for the two-phase pressure drop gradient which was obtained graphically in the Lockhart and Martinelli model (201) [33]. The following parameters are required for the Chisholm model. The pressure gradient, as if the whole mixture flows as liquid or vapor, is defined for both phases, as follows:

$$\left.\frac{dP}{dX}\right)_{\text{fric}}^{\text{lo}} = \frac{f_{\text{lo}}}{2d_h}\frac{{G_m}^2}{\rho_l}, \tag{203}$$

$$\left.\frac{dP}{dX}\right)_{\text{fric}}^{\text{vo}} = \frac{f_{\text{vo}}}{2d_h}\frac{{G_m}^2}{\rho_v},, \tag{204}$$

where f_{lo} and f_{vo} are liquid only and vapor only friction factors and are functions of the mixture mass flux. Defining the physical property coefficient, Γ as

$$\Gamma^2 = \frac{\left.\frac{dP}{dX}\right)_{\text{fric}}^{\text{lo}}}{\left.\frac{dP}{dX}\right)_{\text{fric}}^{\text{vo}}}. \tag{205}$$

Substituting equations (204) and (203) into (205) leads to the following:

$$\Gamma = \left(\frac{\rho_l}{\rho_v}\right)^{0.5}\left(\frac{f_{\text{vo}}}{f_{\text{lo}}}\right)^{0.5}.. \tag{206}$$

Finally, the Chisholm two-phase flow multiplier expression is given as follows:

$$\Phi_{lo}^2 = 1 + \left(\Gamma^2 - 1\right)\left(Bx_{\text{flow}}\left(1 - x_{\text{flow}}\right) + x_{\text{flow}}^2\right), \tag{207}$$

where B is defined as

$$B = \frac{C\Gamma - 2}{\Gamma^2 - 1}, \tag{208}$$

and C is a constant given by

$$C = \left(\frac{U_l}{U_v}\right)\left(\frac{\rho_l}{\rho_v}\right)^{0.5} + \left(\frac{U_v}{U_l}\right)\left(\frac{\rho_v}{\rho_l}\right)^{0.5}, \tag{209}$$

where U_{l} and U_{v} are the total relative (local) liquid and vapor velocities. It must be noted that the Chisholm two-phase flow multiplier satisfies the boundary condition at the limits of single-phase liquid $x = 0$ and single-phase vapor $x = 1$. This can be easily verified by substituting the limiting values in the literature (207).

5.1.3 Wallis Model

The default two-phase multiplier model in CTF is a void-based model founded on annular flow theory [30]. It must be noted that the same expression can be obtained using 201 and a void fraction correlation from the Lockhart-Martinelli model [31]. The void-based model, henceforth known as the *Wallis' model*, is defined as follows:

$$\Phi_l = \begin{cases} 1/\alpha_l & \text{for normal wall conditions} \\ 1/\alpha_v & \text{for hot wall conditions} \end{cases} \tag{210}$$

Table 4. CTF friction factor correlations.

Original correlation: $f_w = \max \begin{cases} 64.0/Re & \text{, laminar} \\ \max(1.691Re^{-0.43}, 0.117Re^{-0.14}) & \text{, turbulent} \end{cases}$
McAdam's correlation:[34] $f_w = \max \begin{cases} 64.0/Re & \text{, laminar} \\ 0.204Re^{-0.2} & \text{, turbulent} \end{cases}$
Zigrang-Sylvester correlation:[35] $f_w = \max \begin{cases} 64.0/Re & \text{, laminar} \\ (-2.0log(\frac{\epsilon}{3.7D} + \frac{2.51}{Re}[1.14 - 2log(\frac{\epsilon}{D} + \frac{21.25}{Re^{0.9}})]))^{-2} & \text{, turbulent} \end{cases}$
Churchill correlation [a] *:[36]* $f_f = 2[(\frac{8}{Re})^{12} + \frac{1}{(a+b)^{3/2}}]^{1/12}$ where $a = (2.475ln[\frac{1}{(\frac{7}{Re})^{0.9}+0.27(\frac{\epsilon}{D})}])^{16}$ $b = (\frac{3.753x10^4}{Re})^{16}$
User-defined function [b] *:* $f_w = \max \begin{cases} 64.0/Re & \text{, laminar} \\ A + BRe^C & \text{, turbulent} \end{cases}$

[a] Applies to all three flow regimes; laminar, transition and turbulent.
[b] A, B and C are user-defined coefficients.

5.2 FORM LOSS MODEL

The form pressure drop is defined as follows:

$$\left.\frac{dP}{dX}\right)_{\text{form}} = \alpha_k \frac{K_x}{2\Delta X}\rho_k |U_k| U_k \tag{211}$$

Again, k represents the phase, but in this case, it can be liquid, vapor, or entrained droplets, and U is the field velocity. Note that whereas frictional loss is only calculated for liquid and vapor fields, the form loss is experienced and calculated for all three fields. K_x is the form loss coefficient which may be user-supplied, code-calculated, or a combination of both, depending on the modeling circumstances. In INTFR, K_x is either user-supplied or code-calculated.

The flow blockage coefficient, if chosen to be code-modeled, is calculated using the following equation:

$$K_{\text{grid}} = \min\left(20, 196\text{Re}_{\text{mix}}^{-0.333}\right) f_{\text{loss}} A_{\text{block}}^2. \tag{212}$$

f_{loss} is a user-defined pressure loss coefficient multiplier, then A_{block} is the user-defined ratio of blocked area to flow area, and Re_{mix} is the liquid/vapor mixture Reynolds number, defined by Eq. (213):

$$\text{Re}_{\text{mix}} = \frac{G_T D_h}{\mu_{\text{mix}}}, \quad \text{where} \tag{213a}$$

$$\mu_{\text{mix}} = \min(\mu_{\text{vapor}}, \mu_{\text{liquid}}), \quad \text{and} \tag{213b}$$

$$\mu_{\text{vapor}} = \mu_l (1 - \alpha_v)^a, \quad \text{where} \tag{213c}$$

$$a = \frac{-2.5(\mu_v + 0.4\mu_l)}{\mu_v + \mu_l}$$

$$\mu_{\text{liquid}} = \mu_v \alpha_v^b, \quad \text{where} \tag{213d}$$

$$b = \frac{-2.5(\mu_l + 0.4\mu_v)}{\mu_v + \mu_l}.$$

5.3 SIMPLIFICATION OF WALL/FORM LOSS MODEL

The friction pressure loss term of Eq. (190) is defined separately in the INTFR subroutine; however, the form loss term has simplifications made during its formulation. Therefore, Eq. (190) is reformulated using the substitution of Eq. (211):

$$K_{w,x} = \left.\frac{dP}{dX}\right)_{\text{fric}} \frac{1}{\dot{m}} + \frac{\alpha_k \rho_k U_k K_x |U_k|}{2\Delta X \dot{m}}. \tag{214}$$

It is evident that the mass flow rate term, $\dot{m}$, can be canceled with some of the numerator terms in the form loss term; however a simplification is made in the source code at this point, which can be a significant source of confusion when analyzing the source code. Recall that the wall drag loss coefficient, $K_{w,x}$, is multiplied by $\dot{m}\Delta X$ to represent the wall shear stress or units of force, as shown in Eq. (43). The momentum equations are solved to calculate the field mass flow rates, $\dot{m}$. Returning to Eq. (42), which is the discretized form of the Cartesian x-momentum equation, there are mass flow rate terms on both the LHS and RHS of the equation.

On the LHS, the mass flow term is multiplied by $(\Delta X A_x)/\Delta t$, which is carried over to the RHS during the solution process. As a result, the wall drag loss coefficient in the governing equation solution subroutine is multiplied by $\Delta t/\Delta X$. The cross-sectional area does not appear in the governing equation subroutine because it is eliminated with the cross-sectional area term that appears in the closure model subroutine. Therefore, when further simplifying Eq. (214), care is taken to move the cross-sectional area back to the LHS, as follows:

$$K_{w,x}A_x = \left.\frac{dP}{dX}\right)_{\text{fric}} \frac{A_x}{\dot{m}} + \frac{K_x|U_k|}{2\Delta X}. \tag{215}$$

Now, the A_x on the LHS of Eq. (215) will cancel with the A_x on the LHS of Eq. (42), which is why these A_x terms never appear in the INTFR or XSCHEM subroutines and why the wall drag loss coefficient takes the form of Eq. (215). To avoid any additional confusion, $K_{w,x}$ is multiplied by ΔX first in XSCHEM (upon being received from INTFR), and then it is later multiplied by $\Delta t/\Delta X$ (from the LHS of the discrete form of the momentum equation) during the momentum equation solution.

The equations shown above are presented with regard to flow in the axial direction, but a wall drag loss coefficient is also calculated for the transverse direction. In this case, mass flow rates, field velocities, and geometry parameters are related to the transverse direction. The phase Reynolds number, for example, is calculated as shown in Eq. (216):

$$\text{Re}_k = \frac{G_{z,k}\left(\frac{2L_g}{F_w}\right)}{\mu_k}. \tag{216}$$

The hydraulic diameter is represented in terms of the transverse distance between subchannels, L_g, and the wetted wall multiplier, F_w, which is a user-defined parameter that declares the number of wetted walls in a transverse momentum cell. The F_w term also appears in the frictional pressure drop term as shown in Eq. (217), which is used along with the L_g term to represent hydraulic diameter.

$$\left.\frac{dP}{dZ}\right)_{\text{fric},k} = \frac{F_w f_{wk} G_{z,k}^2}{4L_g \bar{\rho}_k}. \tag{217}$$

With F_w set to zero, no frictional pressure drop will be calculated in the transverse direction. With F_w set to 0.5, frictional pressure drop is calculated for an area equal to $\Delta X \Delta Z$, which is one side of a lateral momentum cell.

Pertaining to the form loss coefficient, there is no option to use a code calculated value—the form loss coefficient in the lateral direction must be user supplied. A value of 0.5 is recommended for flow across a single bank of tubes. For gaps defined to model more than one physical gap, the number of modeled physical gaps should be multiplied by 0.5. The transverse gap loss coefficients are defined on Card Group 3 of the input deck.

In CTF, the liquid phase is assumed to carry all of the wall drag in the normal flow regimes unless void fraction is very high. The reverse is true for hot wall flow regimes, with the vapor phase carrying all the wall drag. To accomplish this desired behavior in the code, the frictional pressure drop term of Eq. (215) is multiplied by multiplication factors F_l (for the liquid phase wall drag loss coefficient) and F_v (for the vapor phase wall drag loss coefficient). The equations for liquid and vapor phase wall drag loss coefficients are shown in Eq. (218).

$$K_{w,x,l} = \left.\frac{dP}{dX}\right)_{\text{fric},l} \frac{A_x}{\dot{m}_{lx}} F_l + \frac{K_x|U_l|}{2\Delta X} \tag{218a}$$

$$K_{w,x,v} = \left.\frac{dP}{dX}\right)_{\text{fric},v} \frac{A_x}{\dot{m}_{vx}} F_v + \frac{K_x|U_v|}{2\Delta X} \,. \tag{218b}$$

The terms F_l and F_v are defined as follows:

$$F_l = \begin{cases} (1 - F_{\text{spv}}) & \text{for normal wall regimes} \\ F_{\text{spl}} & \text{for hot wall regimes} \end{cases} \tag{219a}$$

$$F_v = \begin{cases} F_{\text{spv}} & \text{for normal wall regimes} \\ (1 - F_{\text{spl}}) & \text{for hot wall regimes} \end{cases} \tag{219b}$$

F_{spv} and F_{spl} are defined as follows:

$$F_{\text{spv}} = \max \left\{ \min \left\{ \begin{array}{c} 1.0 \\ \frac{\alpha_v - 0.9990}{0.9999 - 0.9990} \end{array} \right. \right. \\ \left. \left. 0.0 \right. \right. \tag{220a}$$

$$F_{\text{spl}} = \max \left\{ \min \left\{ \begin{array}{c} 1.0 \\ \frac{\alpha_v - 0.001}{0.0001 - 0.001} \end{array} \right. \right. \\ \left. \left. 0.0 \right. \right. \tag{220b}$$

Some analysis of Eq. (220) reveals that, except for very high void fractions over 0.999, F_{spv} will be zero. If the cell is in a normal wall flow regime, then F_l will be 1, and F_v will be 0, leading to all wall drag being carried by the liquid phase. Conversely, F_{spl} will be 1 for all instances except when void fraction is very low (less than 0.001). If the cell is in a hot wall regime, F_v will be 1, and F_l will be 0, leading to all wall drag being carried by the vapor phase.

The calculation of F_l and F_v differs slightly for the transverse momentum cell solution. Consideration is made for the fact that flow can go from a cell having a normal wall flow regime to a cell having a hot wall flow regime. If either of the continuity cells that the transverse momentum cell connects to a hot wall flow regime, then the F_{spl} ramping factor will be used over the F_{spv} ramping factor. This is demonstrated in Eq. (221):

$$F_l = \begin{cases} (1 - F_{\text{spv}}) & \text{both cells in normal wall flow regime} \\ F_{\text{spl}} & \text{at least one cell in hot wall flow regime} \end{cases} \tag{221a}$$

$$F_v = \begin{cases} F_{\text{spv}} & \text{both cells in normal wall flow regime} \\ (1 - F_{\text{spl}}) & \text{at least one cell in hot wall flow regime} \end{cases} \tag{221b}$$

6. INTERFACIAL DRAG MODELS

The shear force present between different fields (vapor/droplets or vapor/liquid) is needed during the momentum equation solution. The interfacial drag force is calculated using the drag force equation.

$$F_D = \frac{1}{2} C_D \rho |v| v A \tag{222}$$

In CTF, the interfacial drag force, τ_i, is defined as a coefficient times the relative velocity between the phases. For interfacial drag between liquid and vapor in the axial direction,

$$\tau_{i,vl} = k_{vl,x} U_{vl,x} \Delta X_j. \tag{223}$$

The momentum cell height, ΔX_j, is required for calculating total drag force because the CTF source code defines the interfacial drag coefficient on a per-unit-length basis. This differs in form from the drag force equation in that the squared velocity was split apart into an explicit velocity term times an implicit velocity term. The implicit relative axial velocity between phases, $U_{vl,x}$, is solved during the momentum equation solution. The explicit velocity term, which is available using old time step information, is absorbed into the interfacial drag force coefficient, $k_{vl,x}$, along with the old time step density, interfacial area, and drag coefficient, C_D.

Both the drag coefficient, C_D, and the interfacial area, A, of Eq. (222), will be highly dependent on the nature of the flow (i.e., flow regime); therefore, CTF includes different models for calculating these terms, depending on the determined flow regime. Section 4 presents the manner by which CTF determines the flow regime and also shows how the interfacial area for that flow regime is calculated.

The following sections present the flow regime–specific calculation of the drag coefficient term needed for calculation of the interfacial drag force. Interfacial drag calculations are performed in the INTFR subroutine. Calculations are performed for the axial momentum cells and then transverse momentum cells. Consideration is made for both flow directions in discussing the flow regime–specific interfacial drag models that follow.

6.1 SMALL BUBBLE REGIME

The small bubble regime is characterized by uniformly dispersed vapor bubbles in a continuous liquid media. Because the bubbles are small, their geometry can be assumed as spherical. The small bubble regime is entirely composed of a uniform distribution of small bubbles; however, small and large bubbles can be found in other flow regimes, such as large bubble and churn-turbulent flow. The following interfacial drag models may also be applicable for the aforementioned flow regimes. Note that CTF provides options for two different approaches to modeling interfacial drag in the small bubble regime. This section presents the legacy approach, which seeks to determine the drag coefficient of the bubbles and use it with the drag force equation to determine drag. Section 6.3 discusses the alternate approach, which uses the drift flux model to back-calculate the interfacial drag using the drift flux model.

The interfacial drag coefficient is defined for the axial momentum cell as follows:

$$k_{vl,x} = \frac{1}{2} \frac{C_D \rho_l \bar{U}_{vl} A_{p,sb}}{\Delta X_j}. \tag{224}$$

The projected area of the bubbles, $A_{p,sb}$, is used in determining the drag force—not the interfacial area. However, the interfacial area is related to the projected area for spherical geometry.

$$A_{p,sb} = \frac{A_{i,sb}}{4} \tag{225}$$

The interfacial drag coefficient calculation appears in the CTF code as

$$k_{vl,x} = \frac{1}{8}\frac{C_D \rho_l |U_v - U_l| A_{i,sb}}{\Delta X_j}. \tag{226}$$

It can be calculated for the lateral direction by using the lateral velocity instead of axial, along with the appropriate terms for the transverse momentum cell.

$$k_{vl,z} = \frac{1}{8}\frac{C_D \rho_l |W_v - W_l| A_{i,sb}}{\Delta Z_k} \tag{227}$$

The interfacial area is calculated for the transverse momentum cell in the same manner that was used for the axial momentum cells: the interfacial area is described by Eq. (154) and is repeated here:

$$A_{i,sb} = 3\alpha_v A_x \frac{\Delta X}{r_b}. \tag{154}$$

Substituting the gap cross-sectional area for the axial momentum cell cross-sectional area produces the transverse momentum cell small bubble interfacial area. Substituting this result into Eq. (227) leads to the form of the transverse drag force coefficient correlation used in CTF.

$$k_{vl,z} = \frac{3}{8}\frac{C_{Db} \rho_l |w_{vl}| (1 - \alpha_v) L_g \Delta Z_k}{r_b} \tag{228}$$

As discussed by Ishii [23] and Ishii and Chawla [37], the bubble drag coefficient is dependent on the bubble Reynolds number, as well as the regime (i.e., viscous regime, distorted particle regime, cap bubble regime, or Newton's regime). In the viscous region, bubbles behave like solid spheres. As the Reynolds number increases and the flow enters the distorted particle region, the bubbles become distorted and exhibit irregular motion. As the Reynolds number increases further, the bubbles become spherical-cap shaped, and the bubble drag coefficient becomes constant.

6.1.1 Viscous Region

For the viscous region, Ishii [23] assumed that a particle in a multiparticle system has the same functional form as that of a single particle in an infinite media. The bubble drag coefficient is defined as

$$C_{Db} = \frac{24}{\mathrm{Re}_b}\left(1.0 + 0.1\mathrm{Re}_b^{0.75}\right). \tag{229}$$

The bubble Reynolds number is defined as

$$\mathrm{Re}_b = \frac{2 r_b \rho_l |\bar{u}_{vl}|}{\mu_{mb}}. \tag{230}$$

Three terms are further defined. First, the velocity is the relative vector velocity between phases.

$$\bar{u}_{vl} = \sqrt{(w^*_{vl})^2 + u^2_{vl}} \tag{231}$$

Take note that u_{vl} is defined for the axial momentum cell, whereas w_{vl} is defined for the transverse momentum cell, which is staggered from the axial momentum cell location. Therefore, the transverse velocity at the axial location, j, must be calculated by averaging the transverse velocities above $(J + 1)$ and below (J).

$$w^*_{vl} = |0.5(w_{v,J} + w_{v,J+1}) - 0.5(w_{l,J} + w_{l,J+1})| \tag{232}$$

Secondly, the mixture viscosity must be appropriately calculated for the assumption that the particle in the multiparticle system behaves as a single particle in an infinite media. In a multiparticle system, a particle experiences greater resistance than in a single-particle system because the particle must deform not only the fluid, but also neighboring particles. Ishii [23] defined this as

$$\mu_{mb} = \mu_l(1 - \alpha_v)^{-2.5\frac{(\mu_v + 0.4\mu_l)}{(\mu_v + \mu_l)}} \tag{233}$$

Third, and finally, the bubble radius is required for calculation of the bubble Reynolds number. The bubble radius is defined in Section 4 by Eq. (152) and is assumed to depend on a Weber number criterion, with the Weber number, We, equal to 10. It is repeated here for convenience.

$$r_b = \frac{0.5\mathrm{We}_b \sigma g_c}{\rho_l \bar{u}^2_{vl}} \tag{152}$$

The bubble radius is limited in the code to a maximum size of one half of the hydraulic diameter, or 0.02 ft, whichever is smaller. When considering the transverse momentum cell, the bubble radius is calculated for the two channels to which the gap is connected, and the maximum bubble radius of the two channels, ii and jj, is chosen for the transverse momentum cell. The transverse momentum cell bubble radius is further limited to be the minimum of the aforementioned bubble radius, or half of the true gap width, which is the input gap width divided by the physical number of gaps, as follows

$$r_{b,t} = \min\left[r_{b,\max}, \frac{1}{2}\frac{L_g}{N_g}\right]. \tag{234}$$

The transverse momentum cell is prevented from being zero by being set to either half the true gap width or 0.02 ft, whichever is smaller, if it is found to be zero.

6.1.2 Distorted Particle Region

As for the viscous region, it is assumed that a single particle behaves as a particle in an infinite media. It is also assumed that churn-turbulent flow will exist when in the distorted particle region. The bubble drag coefficient is given as

$$C_{Db} = \frac{\sqrt{2}}{3} N_\mu \mathrm{Re}'_b (1 - \alpha_v)^2, \tag{235}$$

where

$$N_\mu = \frac{\mu_l}{\left[\rho_l \sigma \sqrt{\frac{\sigma}{(\rho_l - \rho_v)} g}\right]^{\frac{1}{2}}}. \tag{236}$$

In the churn-turbulent regime, a particle tends to move in the wake caused by other particles, so the drift velocity is used in the calculation of the bubble Reynolds number.

$$\mathrm{Re}'_b = \frac{2 r_b \rho_l |\bar{u}_{vj}|}{\mu_m} \tag{237}$$

The drift velocity, $\bar{u}_{vj}$, is defined as $(1 - \alpha_v)|\bar{u}_{vl}|$. Again, the vector velocity is used as was defined for the viscous region. The mixture velocity is defined as follows:

$$\mu_m = \frac{\mu_l}{(1 - \alpha_v)}. \tag{238}$$

6.1.3 Cap Bubble Region

The drag coefficient for the cap bubble region is simply

$$C_{Db} = \frac{8}{3}(1 - \alpha_v)^2. \tag{239}$$

The bubble drag coefficient is calculated by each of the aforementioned means. The viscous regime drag coefficient is used if it is larger than the distorted particle regime drag coefficient. If the distorted particle regime drag coefficient is larger than the viscous regime drag coefficient but smaller than the cap bubble regime drag coefficient, then the distorted particle regime drag coefficient is used. Otherwise, if the distorted particle regime drag coefficient is larger than the other two drag coefficients, then the cap bubble regime drag coefficient is used.

It should be noted that, in the source code, both the vector and the axial relative liquid-vapor velocities are limited to a maximum value of 1.4 ft/s. This is to prevent the interfacial drag forces from growing to exceedingly large values, which is possible because of the large interfacial area in the small bubble regime.

6.2 LARGE BUBBLE REGIME

The large bubble regime is characterized by a mixture of small and large bubbles. Note that CTF provides two options for modeling the interfacial drag in this regime. This section presents the legacy approach, which seeks to explicitly model the bubble drag coefficient based on bubble geometry. Section 6.3 presents the alternative drift-flux based approach.

The small bubble drag coefficient calculations presented in the previous section are also used for the large bubble regime. The small bubbles are primarily in the viscous regime, whereas large bubbles may be in Newton's regime. Bubbles in the slug regime move relative to the average volumetric flux. Therefore, the small bubble drag coefficient is modified by using the drift velocity instead of simply the relative phase velocity.

$$C_{Db} = C_{Db}(1 - \alpha_v)^2 \tag{240}$$

For spheres in the Newton regime, the drag coefficient becomes independent of the Reynolds number and instead becomes a constant of 0.45. The large bubbles also move relative to the average volumetric flux such that the large bubble drag coefficient is calculated as follows:

$$C_{Db} = 0.45(1 - \alpha_v)^2 \tag{241}$$

The maximum of the viscous regime and Newton regime drag coefficients is taken for calculating the drag force coefficient. The axial drag force coefficient is calculated using Eq. (224). The limits on relative velocity still apply for the large bubble regime. The drag for the large bubble regime is obtained by interpolating between the small and large bubble drag coefficients using the ratio of small bubble volume to total vapor volume, F_{sb}, as follows:

$$k_{vl,x} = k_{vl,x,sb}F_{sb} + k_{vl,x,lb}(1 - F_{sb}) \tag{242}$$

F_{sb} was defined in Section 4.4 but is repeated below.

$$F_{sb} = \frac{\alpha_{sb}\alpha_l}{(1 - \alpha_{sb})\alpha_v} \tag{166}$$

6.3 DRIFT FLUX APPROACH FOR SMALL AND LARGE BUBBLES

Work performed in CASL let do the establishment of an initial validation matrix, which includes several two-phase experiments, particularly for void fraction measurement. Testing of CTF against this data revealed that the code overpredicts void fraction [38] [39] [40] in the bubbly churn flow region. Additionally, a study by Porter [41] has shown a sensitivity of void prediction in the BWR Full-size Fine-mesh Bundle Tests (BFBT) to the interfacial drag closure models. As described above, drag was formulated explicitly with a correlation combined with the void weighted relative phasic velocity to give an interfacial drag force. This drag formulation led to overestimating the interfacial shear forces which caused a reduced slip between vapor and liquid and hence an overpredicted void fraction. To improve the code's predictive capability, an option was added that reformulates the interfacial drag based on the drift-flux approach. This approach has been used successfully in two-fluid computational thermal hydraulic codes such as Transient Reactor Analysis Code GE (TRACG) [42], TRAC/RELAP Advanced Computational Engine (TRACE) [43], and THERMIT-2 [44] to describe the interfacial drag in vertical dispersed upward flow, which in turn defines the relative phasic velocity and void fraction prediction. In CTF, the interfacial shear is described in the general form as follows:

$$\tau'''_{i,\ell v} = C_i \left|\overline{\overline{V}}_r\right| \overline{\overline{V}}_r, \tag{243}$$

where C_i is the drag coefficient and $\overline{\overline{V}}_r$ describes the relative velocity between phases defined as the difference in the void-fraction–weighted mean velocities $\overline{v}_k = \frac{\langle \alpha_k v_k \rangle}{\langle \alpha_k \rangle}$, which is given as

$$\overline{\overline{V}}_r = \overline{v}_v - \overline{v}_\ell \tag{244}$$

In the drift-velocity approach, the drag coefficient is formulated from a local steady-state force balance in the flow direction between buoyancy and interfacial drag forces for the gas and liquid phases. The liquid

and gas pressures are assumed to be equal. The interfacial drag per unit volume is therefore equal to the buoyancy force [23]. Thus,

$$\tau'''_{i,\ell v} = \langle \alpha_v \rangle (1 - \langle \alpha_v \rangle) g \Delta \rho. \tag{245}$$

In bubbly flow, the standard drag force per unit volume that acts on multiple particles under steady-state conditions can be given in terms of the drag coefficients C_d, the bubble diameter d_b, and relative velocity $\overline{\overline{V}}_r$ as

$$\tau'''_{i,\ell v} = \frac{3}{4} \frac{C_d}{d_b} < \alpha_v > \rho_\ell \left| \overline{\overline{V}}_r \right| \overline{\overline{V}}_r. \tag{246}$$

Therefore, substituting the expression in Eq. (245) into the interfacial drag from Eq. (246) and solving for the drag coefficient, the interfacial drag coefficient in the drift-velocity approach is given as

$$C_d = \frac{4}{3} \frac{(1 - < \alpha_v >) \Delta \rho g d_b}{\rho_\ell \overline{V}_r^2}. \tag{247}$$

Within the context of the drift flux model, the relative velocity between the phases is not the difference between the phasic velocities, but is instead a weighted difference between the phase velocities as given by

$$\overline{V}_r = \frac{1 - C_0 \langle \alpha_v \rangle}{(1 - \langle \alpha_v \rangle)} \overline{v}_v - c_0 \overline{v}_\ell, \tag{248}$$

where C_0 is the distribution parameter given by

$$\begin{aligned} C_0 &= C_\infty - (C_\infty - 1) \sqrt{\frac{\rho_v}{\rho_\ell}}. \\ C_\infty &= 1.399 - 0.0155 ln(Re_\ell) \end{aligned} \tag{249}$$

The average relative velocity is related to the weighted average drift flux velocity $\overline{v}_{gj}$ as follows:

$$\overline{\overline{V}}_r = \frac{\overline{v}_{gj}}{1 - \langle \alpha_v \rangle} \tag{250}$$

To convert the drift flux model into drag, specification of the drift flux velocity ($\overline{v}_{gj}$), bubble diameter (d_b), and distribution parameter C_0 is required. The dispersed gas phase in bubbly flow regime is characterized using a combination of small and large bubbles. The average diameter is calculated from a critical Weber number (We_{crit}) of 10 and is given by

$$d_b = \frac{\sigma We_{crit}}{\rho_l \overline{\overline{V}}_r^2}. \tag{251}$$

Many correlations can be found in literature for the drift velocity, and all are in the form given below:

$$\overline{v}_{gj} = k\left(\frac{\sigma\Delta\rho g}{\rho_\ell^2}\right)^{\frac{1}{4}}, \tag{252}$$

where k is a constant that is flow regime-dependent. Ishii [23] and Kataoka [45] recommended the following:

$$k = \begin{cases} \sqrt{(2)} & \text{if } \alpha_v \leq 0.2 \\ 0.0019\min\left(30, D_H^\star\right)^{0.809}\left(\frac{\rho_g}{\rho_\ell}\right)^{-0.157}\left(N_{\mu_l}\right)^{-0.562} & \text{if } 0.2 < \alpha_v \leq \alpha_{trans} - .1 \end{cases}, \tag{253}$$

with the nondimensional hydraulic diameter, $D_H^\star$, defined as

$$D_H^\star = \frac{D_H}{\sqrt{\sigma/g\Delta\rho}}, \tag{254}$$

and the liquid viscosity number, N_{μ_l}, given in the form of

$$N_{\mu_l} = \frac{\mu_l}{\left(\sigma\rho_l\sqrt{\sigma/g\Delta\rho}\right)^{1/2}}. \tag{255}$$

Substituting Eq. (252) and Eq. (251) into Eq. (243) allows the coefficient C_i to be determined:

$$C_i = \frac{1}{k^4}\frac{<\alpha_v>(1-<\alpha_v>)^5\rho_\ell^2}{\sigma}\frac{\overline{V}_r^4}{\overline{V}_r^2} \tag{256}$$

In the region where voids are still concentrated close at the wall—which is the case of subcooled boiling—the mean velocity of vapor can be less than the mean liquid velocity because the bulk liquid moves with the high-core velocity. Because of this, the distribution parameter in Eq. (248) shall be less than unity or near zero at the beginning of two-phase flow region. This allows for high relative velocity and hence high void fraction prediction. To account for this effect, Ishii [23] extended the expression of the distribution parameter given in Eq. (249) to this region, as shown below:

$$C_0 = \left(C_\infty - (C_\infty - 1)\sqrt{\frac{\rho_v}{\rho_\ell}}\right)(1 - e^{-18\alpha_v}). \tag{257}$$

6.4 CHURN/TURBULENT REGIME

The churn/turbulent regime is considered to be a transition region between large bubble and annular mist. The interfacial drag coefficient is interpolated between the interfacial drag coefficients calculated for the large bubble and annular mist flow regime values.

$$k_{vl,x} = F_{ct}k_{vl,am} + (1 - F_{ct})k_{vl,s} \tag{258}$$

The interpolation factor is defined as

$$F_{ct} = \frac{\alpha_v - \alpha_{lb}}{\alpha_{\text{crit}} - \alpha_{lb}}. \tag{259}$$

The large bubble-to-churn/turbulent transition void fraction α_{lb} and the churn/turbulent-to-annular/mist transition criteria α_{crit} depend on the choice of flow regime map.

The lateral direction interfacial drag for the churn/turbulent region is calculated in the same way as the axial direction.

6.5 ANNULAR/MIST REGIME

The annular mist regime consists of a continuous liquid film that is spread across the solid surfaces in the cell and a suspension of uniformly distributed droplets throughout the vapor core. The drag force coefficient is calculated for both the liquid and droplet fields separately.

6.5.1 Droplet drag

The droplet field is characterized by uniformly dispersed droplets in the continuous vapor core. The droplet drag is calculated considering that the droplet behaves like a single particle in an infinite media, much like has been done for the small bubble regime. The model is based on the work of Ishii [23]. The drag coefficient is calculated as

$$k_{ve,x} = \frac{1}{8} C_{Dd} \rho_v |u_{ve}| \frac{A_{i,d}}{\Delta X}. \tag{260}$$

u_{ve} is the relative velocity between the vapor and droplet fields. The projected area of the droplets, $A_{i,d}$, is given by

$$A_{i,d} = \frac{3\alpha_e A_x \Delta X}{r_d}. \tag{261}$$

The droplet can exist in either the viscous or Newton regime. For the viscous regime, the droplet drag coefficient is calculated using a process similar to that used for small bubbles using Eq. (229). The exception is that the Reynolds number of the droplet is used instead of bubble Reynolds number. Droplet Reynolds number is calculated as follows:

$$\text{Re}_d = \frac{D_d \rho_v \vec{u}_{ve}}{\mu_m} \tag{262}$$

The droplet diameter is calculated using the droplet field's interfacial area, as shown in Eq. (176). The mixture viscosity, μ_m, is calculated in a manner similar to used for mixture viscosity for small bubble flow.

$$\mu_m = \mu_v \alpha_v^{-2.5 \frac{\mu_l + 0.4\mu_v}{\mu_l + \mu_v}} \tag{263}$$

If the droplet is in the Newton regime, then the drag coefficient is held constant at 0.45. The maximum of the viscous regime and Newton regime drag coefficients is used for droplet drag.

6.5.2 Film drag

The form of the film drag force coefficient is as follows:

$$k_{vl,x} = \frac{1}{2} f_i \rho_v |u_v - u_l| \frac{A_{ix}}{\Delta X} \tag{264}$$

The drag on the film is calculated using the interfacial area instead of the projected area, as was done for bubble and droplet fields. Furthermore, the friction factor is used in place of the drag coefficient. The interfacial area of the film can be determined considering a cylindrical geometry.

$$\begin{aligned} A_{ix} &= P_w \sqrt{\alpha_v + \alpha_e} \Delta X \\ &= 4 \sqrt{\alpha_v + \alpha_e} A_x \frac{\Delta X}{D_h} \end{aligned} \tag{265}$$

For lateral flow, the physical number of gaps, N_g, is considered.

$$A_{iz} = N_g \sqrt{\alpha_v + \alpha_e} \Delta X \Delta Z \tag{266}$$

The interfacial friction factor is dependent on the nature of the film: stable or unstable. An unstable film will have large waves which increase pressure drop and cause a higher friction factor. The stable film friction factor correlation was obtained from Wallis [30]. The unstable film friction factor was obtained from the work of Henstock and Hanratty [46].

The Wallis annular flow interfacial friction correlation is

$$f_{iw} = 0.005(1 + 75(1 - \alpha_v)). \tag{267}$$

The Henstock and Hanratty correlation for unstable film is

$$f_{iu} = f_s \left(1 + 1400F \left[1 - \exp\left(\frac{-(1 + 1400F)^{1.5}}{G_a 13.2F} \right) \right] \right). \tag{268}$$

The single-phase friction factor, f_s, is calculated using one quarter of the CTF rod friction factor model result for the vapor Reynolds number.

$$f_s = \frac{1}{4} \left[0.204 \mathrm{Re}_v^{-0.2} \right] \tag{269}$$

The terms F and G_a are defined as follows:

$$F = \frac{\left[(0.707 \mathrm{Re}_l^{0.5})^{2.5} + (0.0379 \mathrm{Re}_l^{0.9})^{2.5} \right]^{0.4}}{\mathrm{Re}_v^{0.9}} \frac{\mu_l}{\mu_v} \sqrt{\frac{\rho_v}{\rho_l}} \tag{270}$$

$$G_a = \frac{\rho_l g D_h}{\rho_v u_v^2 f_s} \tag{271}$$

The friction factor of the film is selected as the maximum of the unstable film friction factor and five times the stable film friction factor. The factor of 5 was obtained from observed differences between stable and unstable film pressure drop characteristics [47].

$$f_{if} = \max\left[5f_{iw}, f_{iu}\right] \tag{272}$$

For the lateral direction, only stable film is considered, and the film friction factor is calculated as the number of physical gaps, N_g, times the Wallis correlation shown in Eq. (267).

6.6 BOTTOM REFLOOD REGIME

The bottom reflood may include a continuous liquid and dispersed droplets. If the liquid void is high enough to support a continuous liquid, then the liquid travels in the center of the subchannel without contacting the wall.

6.6.1 Droplet drag

The droplet drag is modeled in a manner similar to that done for the droplets in annular/mist flow as discussed in Section 6.5. However, the viscous regime droplet drag coefficient correlation takes on a slightly different form.

$$C_{Dd} = \frac{24}{\mathrm{Re}_d}\left(1 + 0.15\mathrm{Re}_d^{0.687}\right) \tag{273}$$

The droplet Reynolds number is also calculated differently using the vapor viscosity in place of the mixture viscosity.

$$\mathrm{Re}_d = \frac{D_d \rho_v \vec{u}_{ve}}{\mu_m} \tag{274}$$

The droplet diameter is still calculated from the interfacial area transport equation, but minimum and maximum bounds of 1×10^{-4} mm and 2 mm are set on possible droplet size. The droplet drag coefficient for hot wall conditions, as for normal wall conditions, is calculated as the maximum of the Newton regime value (0.45) and the viscous regime value. For the transverse momentum cells, the drag coefficient is assumed to be characterized by the Newton regime; therefore, the drag coefficient is 0.45. The lateral droplet drag force coefficient is as follows:

$$k_{ve,z} = \frac{3}{8} * 0.45\rho_v |w_v - w_e| \frac{\alpha_e L_g \Delta Z}{r_d} \tag{275}$$

6.6.2 Liquid core

The liquid core is treated differently, depending on whether a transverse or axial momentum cell is being solved. The transverse momentum cell considers the existence of bubbles inside the core, whereas the axial momentum cell considers the liquid slug to have no bubbles. Furthermore, the interfacial drag between the film and vapor is calculated differently. The droplet drag force coefficient is calculated as

6.6.3 Transverse momentum cells

The interfacial drag is comprised of two components: drag on the interface between the vapor film and liquid core, and drag on bubbles inside of the vapor core. The film drag is calculated in the same manner as for annular/mist flow film, except that only stable film is considered using the Wallis correlation [30]. The Wallis correlation was shown in Eq. (267). Note that the correlation is multiplied by a factor of 5, just as it was for the annular/mist flow regime. Furthermore, it is also multiplied by the physical number of gaps, N_g.

The bubble drag is calculated assuming that the bubbles are in the Newton regime, as was done for the slug regime. The drag correlation is repeated below:

$$C_{Db} = 0.45(1 - \alpha_v)^2 \tag{241}$$

6.6.4 Axial momentum cells

The drag coefficient is calculated as follows:

$$C_{Db} = 500 \min(1, 2.78\alpha_\ell^2) \tag{276}$$

The drag force coefficient is calculated as follows:

$$k_{vl,x} = 1.6\alpha_v C_{Db}\mu_v \frac{A_i}{d_r} \tag{277}$$

Here, A_i is an interfacial area that is calculated assuming a cylindrical geometry:

$$A_i = P_w \sqrt{\alpha_\ell}, \tag{278}$$

and d_r is set to a constant of 0.0312.

6.7 FALLING FILM REGIME

The falling film regime results from formation of a top quench front. Above the quench front, a stable film forms on the solid surfaces. The film behaves in a manner similar to that of the annular/mist flow regime except that the film is always assumed to be stable. Therefore, only the Wallis [30] friction factor correlation is used to determine the interfacial friction coefficient, as repeated here:

$$f_{iw} = 0.005(1 + 75(1 - \alpha_v)) \tag{267}$$

The friction coefficient is not multiplied by a factor of 5 as it was for the annular/mist flow regime because the film is assumed to be stable. The falling film flow regime is not considered for transverse momentum cells. The interfacial drag force coefficient is calculated as

$$k_{vl} = \frac{1}{2} f_{iw}\rho_v |u_v - u_l| \frac{A_i}{\Delta X}. \tag{279}$$

The interfacial area is used as was done for the annular/mist regime. In fact, the interfacial area calculation is the same and can be found in Section 4. To account for film dryout, a ramp is multiplied by the interfacial drag force coefficient.

$$R = \max\left[0.001, \min\left(1.0, \frac{\alpha_l}{0.005}\right)\right] \tag{280}$$

Dispersed droplets can also exist in the vapor core. The interfacial drag is calculated as discussed in Section 6.6.

6.8 TOP DELUGE REGIME

The deluge regime consists of large liquid chunks falling down through the channels. It can be a result of upper plenum injection during accident conditions. It exists for hot wall conditions and void fractions less than 0.8.

The interfacial drag is modeled considering droplets in the viscous or Newton regime. The viscous regime drag coefficient is calculated in a manner similar to that used for the small bubble regime in Eq. (229); however, the vapor phase Reynolds number is used instead of the bubble Reynolds number.

$$C_D = \frac{24}{\mathrm{Re}_v}\left[1.0 + 0.1\mathrm{Re}_v^{0.75}\right] \tag{281}$$

The Reynolds number for the vapor phase is calculated as

$$\mathrm{Re}_v = \frac{G_v D_h}{\mu_v}, \tag{282}$$

where

$$G_v = \frac{\dot{m}_v \alpha_v}{A_x}. \tag{283}$$

The Newton regime drag coefficient is a constant of 0.45. The maximum of the viscous regime and Newton regime drag coefficients is used in calculating the interfacial drag force coefficient for the top deluge regime. The interfacial drag force coefficient is calculated as

$$k_{vl} = \frac{1}{2} C_D \rho_v |u_v - u_l| \frac{A_i}{4\Delta X}. \tag{284}$$

The interfacial area is converted to the projected area in this case, and because the liquid void is high, the droplets are treated as continuous liquid, and the liquid velocity is used instead of the droplet velocity.

For vapor void below 0.6, the top deluge interfacial drag dominates; however, as vapor void increases above that, the falling film drag effects begin to have an effect. A linear ramp is used between 0.6 and 0.8 for the top deluge and falling film drag force coefficients.

6.9 QUENCH FRONT REGIME

The quench regime exists simply to indicate that the flow regime was identified as a hot wall regime in the previous time step but that the surface temperatures have dropped below the quenching criteria. The interfacial drag will be calculated according to whatever flow regime was identified for the cell prior to determining that the cell is quenching.

6.10 INTERCELL DRAG MODELS

The intercell drag model exists to account for interphase drag that may occur between mesh cells if there is a large void fraction gradient. Typical causes for the existence of intercell interfacial drag include areas where liquid can pool (e.g., upper core tie plate) and channels that contain a vapor jet. CTF will check for large void fraction gradient interfaces between axially connected mesh cells (horizontal interface) and between transversally connected mesh cells (vertical interface).

The mesh void fraction gradient is checked in the INTFR subroutine to detect interfaces. If one exists, then the intercell interfacial drag is also calculated in INTFR. To illustrate the model, consider two adjacent cells, a and b. CTF declares an interface to exist when $\alpha_i > 0.8$ and $\alpha_j < 0.6$—the cell void fractions could be opposite, with cell a having the higher void fraction, but it is assumed here that cell a is the vapor side, and cell b is the liquid side.

An interface can exit between cells that are laterally connected (vertical interface) or between cells that are vertically connected (horizontal interface). As an example, refer to Figure 12, where the blue cells represent continuity mesh cells, the red cells represent axial momentum cells, and the green cell represents a transverse momentum cell. A vertical interface could exist between continuity mesh cells (ii, J) and (jj, J) if α_v were less than 0.6 in one cell and greater than 0.8 in the other—the resulting intercell interfacial force would be applied to the adjacent axial momentum cells. A horizontal interface could exist between continuity mesh cells $(ii, J-1)$ and (ii, J) if the correct void fraction gradient existed: the resulting intercell interfacial force would be applied to the adjacent transverse momentum cells.

The important thing to note in this example is that the intercell interfaces are defined using the void fractions of the continuity mesh cells; however, the resulting intercell interfacial forces are applied in the momentum cells. Because the momentum and continuity mesh cells are staggered, the interface area must be chosen carefully (as discussed in the "Model as Coded" section).

The drag force equation is used, with the relative velocity between the vapor (a side) and liquid (b side) being used for the velocity. The interfacial drag coefficient, f_i, is set to 0.08, and the average density between adjacent cells is used. The drag force equation for intercell interfacial drag is depicted in Eq. (285) for vertical and lateral directions.

$$F_{I,x} = \frac{1}{2} f_i \bar{\rho}_v \left|(U_{v,a} - U_{l,b})\right| (U_{v,a} - U_{l,b}) A_{I,x} \tag{285a}$$

$$F_{I,z} = \frac{1}{2} f_i \bar{\rho}_v \left|(W_{v,a} - W_{l,b})\right| (W_{v,a} - W_{l,b}) A_{I,z} \tag{285b}$$

There was no explicit intercell interfacial drag term declared in the axial and transverse momentum equations in Section 2. In the source code, the intercell terms are summed up for each cell in the current axial level in INTFR. Consideration is made for which channel contains vapor and which contains liquid and, consequently, whether the intercell interfacial drag force should be added or subtracted from the total for a given cell. Note that when intercell interfacial drag force is added to cell a, the same force must be subtracted from the connected cell b. These values are then passed to XSCHEM, where they are added to the explicit portion of the momentum equation solutions. This is shown in see terms A_1, A_2, and A_3 in Eqs. (111)–(113).

Upon finding an intercell phase interface, CTF calculates the intercell interfacial drag. For a vertical interface, the interface area used in Eq. (285) is calculated as follows:

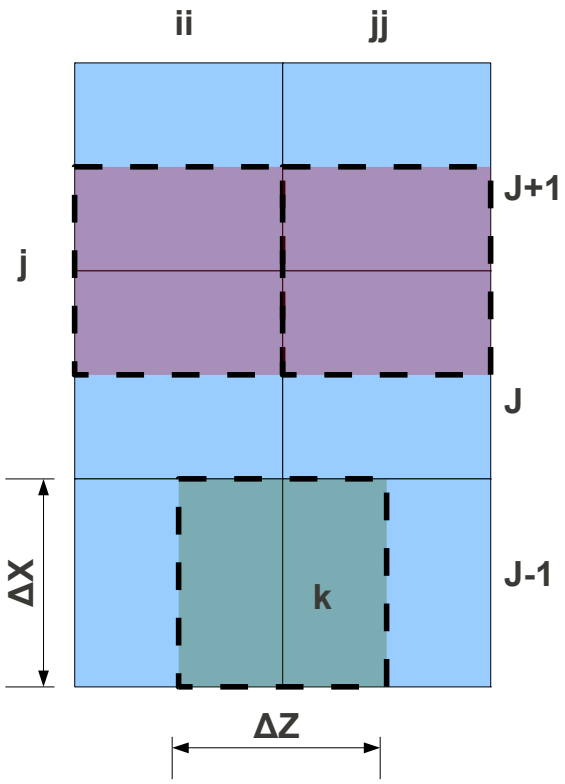

Figure 12. Example of meshing of two adjacent sub-channels, *ii* and *jj*.

$$A_{I,x} = \frac{1}{2} L_g \Delta X |\Delta \alpha_l| \tag{286}$$

See Figure 12 for discussion of this equation. L_g is the gap width (the dimension of the green transverse momentum cell going in and out of the page), and ΔX is the gap height. The reason for multiplying this by $1/2$ is because, as previously discussed, the gap interphase interface is defined between *continuity* mesh cells. However, the intercell interfacial drag force is added to the momentum equations, which are solved for the *momentum* mesh cells. For example, if an intercell interface exists between $(ii, J)/(jj, J)$, but not between $(ii, J+1)/(jj, J+1)$, then the axial momentum cells (ii, j) and (jj, j) should only experience intercell interfacial drag from continuity mesh cells $(ii, J)/(jj, J)$. Likewise, the intercell interfacial drag force between continuity mesh cells $(ii, J)/(jj, J)$ should be equally distributed between the axial momentum cells above and below.

The $\Delta\alpha_l$ term of Eq. (286) represents the difference in liquid void fraction between the adjacent continuity mesh cells. The practice is to multiply by this term because, for an interfacial drag force, the objective is to determine the contact area of vapor and liquid phases. Taking the difference in liquid void fractions estimates the contact area of the liquid and vapor phases in the adjacent cells.

For the case of a horizontal interface, the interface area is defined as

$$A_{I,z} = \frac{1}{2} L_g \Delta Z. \tag{287}$$

Note the absence of the liquid void fraction gradient term: liquid water is assumed to pool at the top or bottom of the adjacent cells, leading to total liquid/vapor contact across the entire interface.

7. INTERFACIAL HEAT TRANSFER MODELS

The interfacial heat transfer coefficients are used to determine the implicit vapor generation rate (or condensation rate) and, in turn, the transfer of energy from one phase to another. The interfacial heat transfer can be thought of as going from the phase to the interface or vice versa. Interfacial heat transfer coefficients are calculated for both field interfaces (i.e. droplet/vapor and liquid/vapor) and for four different possible scenarios:

1. Subcooled Liquid
2. Superheated Liquid
3. Subcooled Vapor
4. Superheated Vapor

For example, if a subcooled liquid is present, regardless of what the vapor temperature is, a subcooled liquid heat transfer coefficient will be calculated. Heat transfer is from the interface to the liquid, and condensation is the result. The magnitude of the condensation is dependent on the difference between interface and subcooled liquid temperature. All four interfacial heat transfer coefficients are calculated for both field interfaces. CTF then later checks whether the fluid is subcooled or superheated, and the appropriate terms are then zeroed.

The resulting interfacial heat transfer coefficients for both field interfaces are combined (subcooled liquid/vapor interfacial heat transfer is added to subcooled droplet/vapor interfacial heat transfer, superheated liquid/vapor interfacial heat transfer is added to superheated droplet/vapor interfacial heat transfer, etc.).

The interfacial heat transfer terms are used to calculate the rate of phase change in the continuity/energy conservation equation solution. The calculated mass transfer rate is then also used in the momentum equation solution to calculate momentum transfer by phase change in the next time step. Because the terms are defined for the momentum equation but are used in the continuity/energy equation solution, adjacent momentum cell values are averaged to find the continuity mesh cell value located between the two. The mass transfer rate Γ''' is calculated as shown in Eq. (288).

$$\begin{aligned}
\Gamma_{\text{evap,shl}} &= \frac{h_{\text{int,shl}}}{(h_g - h_f)C_{p,l}}|h_l - h_f| \\
\Gamma_{\text{evap,shv}} &= \frac{h_{\text{int,shv}}}{(h_g - h_f)C_{p,v}}|h_v - h_g| \\
\Gamma_{\text{cond,scl}} &= \frac{h_{\text{int,scl}}}{(h_g - h_f)C_{p,l}}|h_l - h_f| \\
\Gamma_{\text{cond,scv}} &= \frac{h_{\text{int,scv}}}{(h_g - h_f)C_{p,l}}|h_v - h_g|
\end{aligned} \tag{288}$$

Subcooled liquids and vapors lead to condensation, and superheated fluids lead to evaporation. The h_f and h_g terms are the saturation enthalpies of liquid and vapor, the h_l and h_v terms are the liquid and vapor enthalpies (which may be less than or greater than the saturation enthalpies depending on if the fluid is superheated or subcooled), and $C_{p,l}$ and $C_{p,v}$ are the specific heats of liquid and vapor.

Two of the four terms in Eq. (288) will be zero because a fluid cannot be both superheated *and* subcooled. The mass transfer rates are also multiplied by ramps for code stability. The total mass transfer is found by simply subtracting condensation terms from evaporation terms, as shown in Eq. (289).

$$\Gamma_{\text{net}} = \left[\Gamma_{\text{evap,shl}} + \Gamma_{\text{evap,shv}}\right] - \left[\Gamma_{\text{cond,scl}} + \Gamma_{\text{cond,scv}}\right] \tag{289}$$

The total phase change contributes to the continuity equation residuals. When mass changes phases, it also takes phase enthalpy along with it: evaporation cools a superheated liquid, whereas condensation warms a subcooled liquid. Energy exchange by phase mass transfer is calculated as shown in Eq. (290).

$$\Gamma_{\text{net}} h = \left[\Gamma_{\text{evap,shl}} - \Gamma_{\text{cond,scl}}\right] h_f + \left[\Gamma_{\text{evap,shv}} - \Gamma_{\text{cond,scv}}\right] h_g \tag{290}$$

The interfacial heat transfer coefficients—$h_{i,\text{shl}}$, $h_{i,\text{scl}}$, $h_{i,\text{shv}}$, and $h_{i,\text{scv}}$—will be dependent on the flow regime, as will be the interfacial area for heat transfer. Models for calculating the interfacial heat transfer coefficients are discussed in the following sections. The interfacial area for heat transfer is discussed in Section 4.

7.1 SMALL BUBBLE REGIME

7.1.1 Superheated Vapor

The interfacial heat transfer coefficient for a superheated vapor is assumed to be a constant in CTF.

$$h_{i,\text{shv}} = 2.78^{\text{BTU}/\text{ft}^2\cdot\text{sec}\cdot{}^\circ\text{F}} A_i \tag{291}$$

7.1.2 Superheated Liquid

The interfacial heat transfer coefficient for a superheated liquid is calculated considering two effects: conduction and convection. Convection is calculated using a correlation by Rowe [48].

$$h_{i,\text{shl,conv}} = \frac{k_f}{D_b}\left(2.0 + 0.74\text{Re}_b^{1/2}\text{Pr}_l^{1/3}\right) \tag{292}$$

The bubble Reynolds number is found as follows:

$$\text{Re}_b = \frac{\rho_l \|\vec{u}_r\| D_b}{\mu_l} \tag{293}$$

The velocity utilized is the vector sum of axial and transverse components of *relative* (i.e. relative between vapor and liquid) velocities.

The conduction component of interfacial heat transfer is defined using the Jakob number:

$$h_{i,\text{shl,cond}} = \frac{k_f}{D_b}\text{Ja}, \quad \text{where} \tag{294a}$$

$$\text{Ja} = \frac{\rho_l(h_l - h_f)}{\rho_v h_{\text{fg}}} \tag{294b}$$

The maximum of the convective and conduction heat transfer coefficients is used for the interfacial heat transfer of a superheated liquid. The effect of nucleation at heated surfaces is added to this term,

$$h_{i,\text{shl}} = h_{i,\text{shl}} A_i + h_{\text{nb}} A_{pw}, \tag{295}$$

where

$$h_{\text{nb}} = \frac{k_f}{D_b} \max\left(8.0, 0.023\left(\frac{\rho_l \|\vec{u}_l\| D_b}{\mu_m}\right)^{0.8} \text{Pr}_l^{0.4}\right). \tag{296}$$

The mixture viscosity is defined by Eq. (233). The heat transfer area for nucleate boiling is simply the heated perimeter times the cell height.

7.1.3 Subcooled Vapor

The subcooled vapor interfacial heat transfer coefficient is set to a constant value, as was done for the superheated vapor.

$$h_{i,\text{scv}} = 2.78 \, \text{BTU/ft}^2\text{·sec·°F} A_i \tag{297}$$

7.1.4 Subcooled Liquid

The subcooled liquid interfacial heat transfer coefficient is calculated as follows [49]:

$$h_{i,\text{scl}} = 1.1284 \sqrt{\frac{k_f}{D_b} \vec{u}_{vl} \rho_l C_{p,l} A_i} \tag{298}$$

7.2 LARGE BUBBLE REGIME

The large bubble regime is a combination of small and large bubbles. The small bubble interfacial heat transfer coefficient models are shown in the previous section. The following models are for large bubbles. The previously defined ramping factor F_{sb} (see Section 4.4) is used to perform a linear interpolation between interfacial heat transfer coefficients for each of superheated liquid, superheated vapor, subcooled liquid, and subcooled vapor. The calculation of F_{sb} is repeated:

$$F_{sb} = \frac{\alpha_{sb} \alpha_l}{(1 - \alpha_{sb}) \alpha_v} \tag{166}$$

The large bubble regime interfacial heat transfer coefficients are calculated as follows:

$$h_{i,\text{shl}} = F_{sb} h_{i,\text{shl},sb} + (1 - F_{sb}) h_{i,\text{shl},lb} \tag{299a}$$

$$h_{i,\text{shv}} = F_{sb} h_{i,\text{shv},sb} + (1 - F_{sb}) h_{i,\text{shv},lb} \tag{299b}$$

$$h_{i,\text{scl}} = F_{sb} h_{i,\text{scl},sb} + (1 - F_{sb}) h_{i,\text{scl},lb} \tag{299c}$$

$$h_{i,\text{scv}} = h_{i,\text{scv},lb} \tag{299d}$$

7.2.1 Superheated Liquid

A constant value is assumed for the superheated liquid interfacial heat transfer coefficient.

$$h_{i,\text{shl}} = 278.0\,^{\text{BTU}/\text{ft}^2\cdot\text{sec}\cdot^\circ\text{F}} \tag{300}$$

7.2.2 Superheated Vapor

The interfacial heat transfer coefficient for superheated vapor is calculated using the correlation of Lee and Ryley[50].

$$h_{i,\text{shv}} = \frac{k_v}{D_b}\left(2.0 + 0.74\text{Re}^{0.5}\text{Pr}^{0.33}\right)A_i \tag{301}$$

7.2.3 Subcooled Liquid

The same correlation that was used for the small bubble regime is used for the large bubble regime to calculate the subcooled liquid interfacial heat transfer coefficient.

$$h_{i,\text{scl}} = 1.1284\sqrt{\frac{k_f}{D_b}\vec{u}_{vl}\rho_l C_{p,l}A_i} \tag{298}$$

7.2.4 Subcooled Vapor

The interfacial heat transfer coefficient for subcooled vapor is calculated using the Lee and Ryley correlation—as in Eq. (301)—that was used for the superheated vapor interfacial heat transfer coefficient.

7.3 CHURN-TURBULENT REGIME

The churn-turbulent flow regime is a combination of the annular/mist and large bubble flow regimes. An interpolation factor is defined in Eq. (259) and is repeated below.

$$F_{ct} = \frac{\alpha_v - \alpha_{lb}}{\alpha_{\text{crit}} - \alpha_{lb}} \tag{259}$$

The interfacial heat transfer coefficients calculated for the large bubble and annular/mist flow regimes are used to calculate the churn-turbulent interfacial heat transfer coefficients.

$$h_{i,\text{shv}} = F_{ct}h_{i,\text{shv,AM}} + (1 - F_{ct})h_{i,\text{shv,S}} \tag{302a}$$

$$h_{i,\text{shl}} = F_{ct}h_{i,\text{shl,AM}} + (1 - F_{ct})h_{i,\text{shl,S}} \tag{302b}$$

$$h_{i,\text{scv}} = F_{ct}h_{i,\text{scv,AM}} + (1 - F_{ct})h_{i,\text{scv,S}} \tag{302c}$$

$$h_{i,\text{scl}} = F_{ct}h_{i,\text{scl,AM}} + (1 - F_{ct})h_{i,\text{scl,S}} \tag{302d}$$

7.4 ANNULAR/MIST REGIME

The annular/mist regime consists of a liquid film and a suspended droplet field. The first four following subsections describe the interfacial heat transfer coefficients for the film, and the remaining four subsections describe the interfacial heat transfer coefficients for the droplets. The droplet and film interfacial heat transfer coefficients are simply added together for each of the four cases (superheated liquid, superheated vapor, subcooled liquid, and subcooled vapor).

7.4.1 Film Superheated Liquid

There are three possible expressions for the superheated liquid. The first evaluation is between a constant value of 278 $^{\text{BTU}/\text{ft}^2\cdot\text{sec}\cdot^\circ\text{F}}$ or the conduction through the film. The minimum value of these two expressions is taken. The third is the Colburn analogy[51] for heat transfer from a film using the Hughmark[52, 53] correlation for the film friction factor. The maximum of the Colburn analogy and the result of the first evaluation is taken. This is denoted mathematically as follows:

$$h_{i,\text{shl}} = \max[h_{i,\text{shl,colburn}}, \min(278\ ^{\text{BTU}/\text{ft}^2\cdot\text{sec}\cdot^\circ\text{F}}, h_{i,\text{shl,cond}})] \tag{303}$$

The conduction heat transfer term is defined using the saturated liquid conductivity, k_f, and the film thickness, δ_l.

$$h_{i,\text{shl,cond}} = \frac{2k_f}{\delta_l} P_w \Delta X \tag{304}$$

The Colburn analogy[51] is as follows:

$$h_{i,\text{shl,colburn}} = f_{\text{HM}} \rho_l C_{p,l} |u_{vl}| \text{Pr}^{-2/3} A_{i,f} f_{ai} \tag{305}$$

The Hughmark[53] friction factor correlation is defined as follows:

$$f_{\text{HM}} = 3.850\text{Re}^{-2/3}, \quad \text{if Re}_l < 1000 \tag{306a}$$

$$f_{\text{HM}} = 0.5402\text{Re}^{-0.38}, \quad \text{if Re}_l >= 1000 \tag{306b}$$

In CTF, however, the leading coefficient for the case of $\text{Re}_l < 1000$ is cut in half.

$$f_{\text{HM}} = 1.925\text{Re}^{-2/3}, \quad \text{if Re}_l < 1000 \tag{307}$$

Returning to Eq. (305), the result is multiplied by the interfacial area of the film, $A_{i,f}$, as well as a multiplication factor, which is designed to ramp the interfacial heat transfer to zero as the liquid film dries out. The factor begins to decrease from 1.0 as the liquid void drops below 0.01.

$$f_{ai} = \max[0.0, \min(1.0, 111.1(\alpha_l - 0.001))] \tag{308}$$

7.4.2 Film Superheated Vapor

The Colburn analogy[51] is used for calculating the superheated vapor interfacial heat transfer coefficient. However, unlike the case of superheated liquid, the friction factor is determined using the method of Wallis[30] (stable film) or Hanratty[46] (unstable film). The vapor density is used, the vector relative velocity is used, the vapor-specific heat capacity at the film temperature is used, and no multiplication factor is necessary for the case of dryout.

$$h_{i,\text{shv}} = f_i \rho_v C_{p,\text{film}} \vec{u}_{vl} \text{Pr}^{-2/3} A_{i,\text{film}} \tag{309}$$

The Wallis and Hanratty correlations were are shown in Eqs. (267) and (268), respectively. The film temperature is defined as the average of the heated surface wall temperature and the bulk vapor temperature.

7.4.3 Film Subcooled Liquid

The subcooled liquid interfacial heat transfer coefficient is calculated using the same form of the Colburn analogy[51] that was used for superheated liquid (Section 7.4.1).

7.4.4 Film Subcooled Vapor

The subcooled vapor interfacial heat transfer coefficient is calculated using the form of the Colburn analogy[51] that was used for the case of superheated vapor (Section 7.4.1).

7.4.5 Droplet Superheated Liquid

The superheated liquid interfacial heat transfer coefficient is set equal to the value calculated for the subcooled liquid heat transfer coefficient, which is discussed in Section 7.4.7.

7.4.6 Droplet Superheated Vapor

The Lee-Ryley correlation shown in Eq. (301) is used to calculate the droplet interfacial heat transfer coefficient.

7.4.7 Droplet Subcooled Liquid

This correlation is derived by multiplying the Anderson correlation [54] by 2.7.

$$h_{i,\mathrm{scl}} = 8.88 \frac{k_\ell}{R_d} A_{i,d} \tag{310}$$

7.4.8 Droplet Subcooled Vapor

The subcooled vapor interfacial heat transfer coefficient takes on the value of the superheated vapor interfacial heat transfer coefficient, which is discussed in Section 7.4.6.

7.5 BOTTOM REFLOOD

The bottom reflood regime consists of a liquid core traveling in the center of the subchannel and dispersed droplets throughout the vapor phase. For low liquid void, there may be no liquid core. The first four subsections present the closures for the heat transfer between the liquid core and the vapor, and the following four subsections present the closures for the heat transfer between the droplets and the vapor. The droplet and liquid core interfacial heat transfer coefficients are simply added for each category (superheated liquid, superheated vapor, etc.) to obtain the total interfacial heat transfer.

7.5.1 Core Superheated Liquid

The interfacial heat transfer coefficient for superheated liquid is a constant value.

$$h_{i,\mathrm{shl}} = 278.0 \, \mathrm{BTU/ft^2 \cdot sec \cdot ^\circ F} \tag{311}$$

7.5.2 Core Superheated Vapor

A correlation in the same form as the Lee-Ryley correlation, shown in Eq. (301), is used to calculate the interfacial heat transfer coefficient. This correlation is modified by Frössling[55], which changes the leading coefficient. Furthermore, the correlation is divided by a modification factor defined by Yuen and Chen[56] which accounts for the evaporation of the droplet field.

$$h_{i,\text{shv}} = \frac{\frac{k_v}{D_h}\left(2.0 + 0.55\text{Re}^{0.5}\text{Pr}^{0.33}\right)A_i}{F_{yc}} \tag{312}$$

Note that the vapor conductivity is used, and it is evaluated at the film temperature, which is the average of the heated surface temperature and the bulk vapor temperature. The Yuen and Chen factor is defined below:

$$F_{yc} = 1.0 - 0.5\frac{h_v - h_f}{h_{fg}} \tag{313}$$

7.5.3 Core Subcooled Liquid

For subcooled liquid, the interfacial heat transfer is given by

$$h_{i,\text{scl}} = 17.77\frac{k_\ell}{D_h}A_i. \tag{314}$$

7.5.4 Core Subcooled Vapor

The subcooled vapor interfacial heat transfer coefficient is assumed to be a constant value.

$$h_{i,\text{scv}} = 2780\,\text{BTU/ft}^2\cdot\text{sec}\cdot^\circ\text{F} \tag{315}$$

7.5.5 Droplet Superheated Liquid

The interfacial heat transfer coefficient for droplets when the liquid is superheated is set to a constant value.

$$h_{i,\text{shl},hw} = 27.8\,\text{BTU/ft}^2\cdot\text{sec}\cdot^\circ\text{F}A_{i,d} \tag{316}$$

7.5.6 Droplet Superheated Vapor

The modified Lee-Ryley equation shown in Eq. (312) is also used for the droplets. The only difference is that the hydraulic diameter of the subchannel found in the denominator is replaced with the droplet diameter. The Yuen and Chen modification is also used for the droplets.

7.5.7 Droplet Subcooled Liquid

The subcooled liquid heat transfer coefficient (HTC) is calculated in the same way as for droplets in annular/mist flow, as discussed in Section 7.4.7.

7.5.8 Droplet Subcooled Vapor

A constant value is used for subcooled vapor.

$$h_{i,\text{scv},hw} = 2780\,\text{BTU/ft}^2\cdot\text{sec}\cdot^\circ\text{F} \tag{317}$$

7.6 FALLING FILM REGIME

The interfacial heat transfer coefficient closure models used for the falling film regime are identical to those used for bottom reflood, as discussed in Section 7.5.

7.7 TOP DELUGE REGIME

The interfacial heat transfer coefficient closure models used for the deluge regime are identical to those used for bottom reflood, as discussed in Section 7.5.

7.8 QUENCH FRONT REGIME

The quench regime exists simply to indicate that the flow regime was identified as a hot wall regime in the previous time step but that the surface temperatures have dropped below the quenching criteria. The interfacial heat transfer will be calculated according to whatever flow regime was identified for the cell prior to determining that the cell is quenching.

8. TURBULENT MIXING AND VOID DRIFT

This section defines the source terms in the CTF governing equations that act to capture turbulent mixing and void drift. The turbulent mixing terms are modeled by a simple diffusion approximation using mixing length theory. They act only in the lateral directions (i.e. in the gaps of the model) between adjacent subchannels. As stated in Todreas and Kazimi[31], the net two-phase turbulent mixing of mass between two subchannels can be captured using the following relationship:

$$W_{ij}^{D'} = \epsilon \frac{s_{ij}}{z_{ij}^T}(\rho_f - \rho_g)[\alpha_{v,j} - \alpha_{v,i} - (\alpha_{v,j} - \alpha_{v,i})_{\text{equil}}] \tag{318}$$

This is an equal-volume model, meaning that equal volumes of fluid are mixed between adjacent subchannels, as opposed to mixing equal masses of fluid. In this equation, ϵ and z_{ij}^T are the eddy diffusivity and the turbulent mixing length, respectively. These terms result from mixing length theory being used to characterize turbulent exchange. CTF has models for defining the eddy diffusivity term which are discussed near the end of this section. The s_{ij} term is simply the width of the gap between the adjacent subchannels. To simplify the notation going forward, the term $\epsilon \frac{s_{ij}}{z_{ij}^T}$ is condensed into the single variable V^T.

Two components are inside the square brackets of the previous equation. The first, $\alpha_{v,j} - \alpha_{v,i}$, represents the turbulent mixing driving force. By this model, the two-phase turbulent mixing will act to drive the liquid mass to the higher void channel and the vapor mass to the lower void channel. In reality, this is indeed the observed trend, but only to a point. A second phenomenon known as *void drift* acts to drive vapor to the larger area subchannels. This effect is captured with the second term in the brackets, $(\alpha_{v,j} - \alpha_{v,i})_{\text{equil}}$, which is known as the *equilibrium void distribution*. By subtracting this term from the first, the turbulence will mix the adjacent channel masses to a point of equilibrium, which is a balance of the two phenomena: turbulent mixing and void drift.

Because CTF uses a segregated flow solution (i.e., vapor and liquid governing equations are individually solved), it is necessary to separate Eq. (318) into two components: one for vapor and one for liquid.

$$W_{ij,v}^{D'} = -V^T \rho_g [\alpha_{v,j} - \alpha_{v,i} - (\alpha_{v,j} - \alpha_{v,i})_{\text{equil}}] \tag{319}$$

$$W_{ij,l}^{D'} = V^T \rho_f \left[\left(1 - \alpha_{v,j}\right) - (1 - \alpha_{v,i}) - \left(\left(1 - \alpha_{v,j}\right) - (1 - \alpha_{v,i})\right)_{\text{equil}}\right] \tag{320}$$

To simplify the derivation, the above equations are separated further into individual terms for turbulent mixing and void drift. The vapor turbulent mixing and void drift of mass are show in Eqs. (321) and (322), respectively.

$$W_{ij,v,TM}^{D'} = -V^T \rho_g [\alpha_{v,j} - \alpha_{v,i}] \tag{321}$$

$$W_{ij,v,VD}^{D'} = V^T \rho_g [(\alpha_{v,j} - \alpha_{v,i})_{\text{equil}}] \tag{322}$$

The equations for the liquid are as follows:

$$W^{D'}_{ij,l,TM} = V^T \rho_f [\left(1 - \alpha_{v,j}\right) - (1 - \alpha_{v,i})], \tag{323}$$

and

$$W^{D'}_{ij,l,VD} = -V^T \rho_f [(\left(1 - \alpha_{v,j}\right) - (1 - \alpha_{v,i}))_{\text{equil}}]. \tag{324}$$

At this point, the focus is on turbulent mixing and void drift, which are addressed separately in the following two subsections, to complete the derivation.

8.1 TURBULENT MIXING

Equations (321) and (323) have presented models for capturing turbulent mixing of vapor and liquid mass between subchannels, respectively. However, the turbulent mixing will also affect the other two fields in CTF: noncondensable gas and droplets. To obtain the droplet mass turbulent mixing equation, some algebraic manipulation is performed on the liquid mass turbulent mixing equation.

$$W^{D'}_{ij,l} = -V^T \rho_f [(1 - \alpha_{v,j}) - (1 - \alpha_{v,i})] \tag{325}$$

This is equivalent to the following:

$$W^{D'}_{ij,l} = -V^T \rho_f [(\alpha_{l,j} + \alpha_{e,j}) - (\alpha_{l,i} + \alpha_{e,i})] \tag{326}$$

This can now be separated into individual equations for the liquid and droplet fields, which are now in terms of the liquid and droplet void fractions.

$$W^{D'}_{ij,l} = -V^T \rho_f [\alpha_{l,j} - \alpha_{l,i}] \tag{327}$$

$$W^{D'}_{ij,e} = -V^T \rho_f [\alpha_{e,j} - \alpha_{e,i}] \tag{328}$$

Next, the noncondensable gas is considered. Because the noncondensable gas occupies the same volume as the vapor, it is derived from the vapor equation in a manner similar to how the droplet equation was taken from the liquid equation. The details of the derivation are omitted, and the equation is presented below. One notable point of departure from the vapor equation is that the vapor density must be substituted by the noncondensable gas density, which is tracked separately in CTF.

$$W^{D'}_{ij,\text{gas}} = -V^T [\rho_{\text{gas},j} \alpha_{v,j} - \rho_{\text{gas,i}} \alpha_{v,i}] \tag{329}$$

Note that the model has now been reduced so that field mass—whether it is vapor, liquid, or droplet mass—will always travel down the field gradient. For example, vapor mass will move from the high to low vapor void channel, liquid mass will move from the high to low liquid void channel, and droplet mass will move from the high to low droplet void channel.

Up to this point, the phase densities have been assumed to be equal to the saturation densities, which are also constant through space. This assumption is not made in CTF; phase density is not necessarily equal to saturation density, and it is also allowed to vary from cell to cell. Therefore, the saturation densities are

replaced with the true space-dependant liquid and vapor densities in the vapor, liquid, and droplet turbulent mixing equation.

$$W_{ij,v}^{D'} = -V^T[\rho_{v,j}\alpha_{v,j} - \rho_{v,i}\alpha_{v,i}] \tag{330}$$

$$W_{ij,l}^{D'} = -V^T[\rho_{l,j}\alpha_{l,j} - \rho_{l,i}\alpha_{l,i}] \tag{331}$$

$$W_{ij,e}^{D'} = -V^T[\rho_{l,j}\alpha_{e,j} - \rho_{l,i}\alpha_{e,i}] \tag{332}$$

This completes the derivation of the four field turbulent mixing equations for mass; however, energy and momentum can also be mixed. Rather than repeating the previous lengthy derivation, the transported quantities for turbulent mixing of energy and momentum are noted, and the final forms of the energy and momentum turbulent mixing equations, which conveniently have the same form as the mass equations, are then presented. The transported quantity for the energy equation is ρh, and the transported quantity for the momentum equation is ρV. Note that there is no turbulent mixing of noncondensable energy or momentum, so no equation is provided for the field. The energy turbulent mixing source terms are as follows:

$$W_{ij,v}^{H'} = -V^T[\rho_{v,j}\alpha_{v,j}h_{v,j} - \rho_{v,i}\alpha_{v,i}h_{v,i}] \tag{333}$$

$$W_{ij,l}^{H'} = -V^T[\rho_{l,j}\alpha_{l,j}h_{l,j} - \rho_{l,i}\alpha_{l,i}h_{l,i}] \tag{334}$$

$$W_{ij,e}^{H'} = -V^T[\rho_{l,j}\alpha_{e,j}h_{l,j} - \rho_{l,i}\alpha_{e,i}h_{l,i}] \tag{335}$$

The momentum mixing equations are derived using the mass flowrate term in CTF. Dividing this by the cell cross-flow area results in $\alpha_k\rho_k V_k$, which is the momentum of Phase k.

$$W_{ij,v}^{M'} = -V^T[\frac{\dot{m}_{v,j}}{A_j} - \frac{\dot{m}_{v,i}}{A_i}] \tag{336}$$

$$W_{ij,l}^{M'} = -V^T[\frac{\dot{m}_{l,j}}{A_j} - \frac{\dot{m}_{l,i}}{A_i}] \tag{337}$$

$$W_{ij,e}^{M'} = -V^T[\frac{\dot{m}_{e,j}}{A_j} - \frac{\dot{m}_{e,i}}{A_i}] \tag{338}$$

The previous derivation of the source terms was performed for the sake of completeness. In reality, CTF makes certain simplifying assumptions and does not include all source terms in all cases. There are two possible scenarios in a simulation: (1) the flow regime is single-phase, small bubble, slug flow, or churn-turbulent, or (2) the flow regime is annular-mist or mist. In Case 1, there is no turbulent mixing in the droplet field because there will not be a significant amount of droplets in such flow regimes. In Case 2, there is no turbulent mixing in the liquid field because it will only exist as a thin film or not at all.

8.2 VOID DRIFT

This process begins with the void drift equations for vapor and liquid mass, which were presented as Eqs. (322) and (324). Note that there is no void drift impact on the droplets; however, there will be an impact on the noncondensable gas, which exists in the vapor space. For all void drift equations, it is necessary to define the equilibrium void distribution term, $(\alpha_{v,j} - \alpha_{v,i})_{\text{equil}}$. To obtain a definition of this term, we begin with Lahey's derivation of the equilibrium density distribution[57]:

$$(\langle\overline{\rho_i}\rangle - \langle\overline{\rho_j}\rangle)_{\text{equil}} = -(\rho_f - \rho_g)\frac{\langle\alpha_{v,ave}\rangle}{G_{ave}}(G_i - G_j)_{\text{equil}} \tag{339}$$

In this equation, the equilibrium density distribution is posed as a function of the equilibrium mass flux distribution. It is a suitable approximation to use the actual mass flux distribution, $(G_i - G_j)$, in place of the equilibrium mass flux distribution, $(G_i - G_j)_{\text{equil}}$. The angle bracket operators in this equation represent an area-weighted average of the term in the brackets; these brackets can be omitted because the control volume discretization approach of CTF will lead to an averaged uniform value for each term in each mesh cell. The "ave" subscripts indicate that the term (G and α) is the area-weighted average between the adjacent subchannels under consideration.

It is important to note that both the density and mass fluxes given here are that of the two-phase mixture. The first step to obtain Lahey's equation in terms of the equilibrium void distribution, is to place the two-phase mixture density in void and saturation density terms and also to expand the average void and mass flux terms.

$$\begin{aligned}(\rho_f(1-\alpha_{v,i}) + \rho_g\alpha_{v,i} - \rho_f(1-\alpha_{v,j}) - \rho_g\alpha_{v,j})_{\text{equil}} = \\ -(\rho_f - \rho_g)\frac{\alpha_{v,i}A_i + \alpha_{v,j}A_j}{(A_i + A_j)(G_iA_i + G_jA_j)/(A_i + A_j)}(G_i - G_j)\end{aligned} \tag{340}$$

At this point, a simplifying assumption is made that the adjacent subchannel areas, A_i and A_j, are equal, thus eliminating them from the equation. Furthermore, it can be shown that the left-hand side expression can be reduced as follows:

$$-(\rho_f - \rho_g)(\alpha_{v,i} - \alpha_{v,j})_{\text{equil}} = -(\rho_f - \rho_g)\frac{\alpha_{v,i} + \alpha_{v,j}}{G_i + G_j}(G_i - G_j) \tag{341}$$

This can be further reduced to eliminate the difference between saturation densities. Additionally, a scaling factor, K_a, is added to account for geometry differences of different models.

$$(\alpha_{v,i} - \alpha_{v,j})_{\text{equil}} = K_a(\alpha_{v,i} + \alpha_{v,j})\frac{G_i - G_j}{G_i + G_j} \tag{342}$$

The scaling factor is typically taken to be 1.4 [31], but it is made accessible via the CTF input deck, so the user may adjust the value. This derivation is then substituted back into the void drift mass equations. In the process, the saturation densities for actual space-dependent liquid and vapor density are also substituted.

$$W^{D'}_{ij,v,VD} = V^T\left[K_a(\rho_{v,i}\alpha_{v,i} + \rho_{v,j}\alpha_{v,j})\frac{G_i - G_j}{G_i + G_j}\right] \tag{343}$$

$$W^{D'}_{ij,l,VD} = -V^T \left[K_a (\rho_{l,i}\alpha_{v,i} + \rho_{l,j}\alpha_{v,j}) \frac{G_i - G_j}{G_i + G_j} \right] \tag{344}$$

Note that the direction of the void drift term is opposite for vapor and liquid. The noncondensable gas mass void drift is formed by replacing vapor density with noncondensable gas density.

$$W^{D'}_{ij,\text{gas},VD} = V^T \left[K_a (\rho_{\text{gas},i}\alpha_{v,i} + \rho_{\text{gas},j}\alpha_j) \frac{G_i - G_j}{G_i + G_j} \right] \tag{345}$$

This completes the derivation of the CTF void drift mass source terms. The void drift energy and momentum terms are derived in a manner similar to that used for the turbulent-mixing terms. Equations (346) and (347) show the vapor and liquid energy mixing by void drift, respectively. No energy mixing takes place in the noncondensable gas or droplet fields by void drift.

$$W^{H'}_{ij,v,VD} = V^T \left[K_a (\rho_{v,i}\alpha_{v,i}h_{v,i} + \rho_{v,j}\alpha_{v,j}h_{v,j}) \frac{G_i - G_j}{G_i + G_j} \right] \tag{346}$$

$$W^{H'}_{ij,l,VD} = -V^T \left[K_a (\rho_{l,i}\alpha_{v,i}h_{l,i} + \rho_{l,j}\alpha_{v,j}h_{l,j}) \frac{G_i - G_j}{G_i + G_j} \right] \tag{347}$$

Finally, Eqs. (348) and (349) show the vapor and liquid momentum mixing by void drift.

$$W^{M'}_{ij,v,VD} = V^T \left[K_a (\rho_{v,i}\alpha_{v,i}v_{v,i} + \rho_{v,j}\alpha_{v,j}v_{v,j}) \frac{G_i - G_j}{G_i + G_j} \right] \tag{348}$$

$$W^{M'}_{ij,l,VD} = -V^T \left[K_a (\rho_{l,i}\alpha_{v,i}v_{l,i} + \rho_{l,j}\alpha_{v,j}v_{l,j}) \frac{G_i - G_j}{G_i + G_j} \right] \tag{349}$$

In CTF, mass flow rate is the solved term, so these equations are modified into the following forms:

$$W^{M'}_{ij,v,VD} = V^T \left[K_a \left(\frac{\dot{m}_{v,i}}{A_{v,i}}\alpha_{v,i} + \frac{\dot{m}_{v,j}}{A_{v,j}}\alpha_{v,j} \right) \frac{G_i - G_j}{G_i + G_j} \right] \tag{350}$$

$$W^{M'}_{ij,l,VD} = -V^T \left[K_a \left(\frac{\dot{m}_{l,i}}{A_{l,i}}\alpha_{v,i} + \frac{\dot{m}_{l,j}}{A_{l,j}}\alpha_{v,j} \right) \frac{G_i - G_j}{G_i + G_j} \right] \tag{351}$$

As in the turbulent-mixing terms, the void drift source terms are not applied in all cases. If the flow regime is annular mist or post-critical heat flux (CHF), then all void drift terms are omitted from the CTF governing equations.

8.3 MIXING COEFFICIENT

The process now returns to the definition of the mixing term, which was previously condensed into the term V^T.

$$V^T = \epsilon \frac{s_{ij}}{z_{ij}^T} \tag{352}$$

As previously noted, s_{ij} is the gap width, which will be available in CTF from user input. The remainder of the term, ϵ/z_{ij}^T must be defined. To do this, the choice is made to start from the mixing parameter β, which is defined as follows:

$$\beta = \frac{\text{Transverse Mass Flux}}{\text{Axial Mass Flux}} \tag{353}$$

Symbolically, this becomes

$$\beta = \frac{W_{ij}^{H'}/s_{ij}}{\overline{G}}, \tag{354}$$

where $W_{ij}^{H'}$ is the turbulent transverse mixing rate from Channel i to j. It is divided by the gap width to convert it to mass flux. The $\overline{G}$ term is the area-weighted axial mass flux between the adjacent subchannels. The area-averaged axial mass flux is used because this is the definition of the mixing parameter; if the Channel i axial mass flux were used instead, the mixing Stanton number would be formed. The transverse mixing rate will have both molecular and turbulent components, defined as shown below:

$$W_{ij}^{H'} = \mu s_{ij} \left[\frac{1}{z_{ij}^L} + \frac{\epsilon}{z_{ij}^T \nu} \right] \tag{355}$$

This mixing term is actually defined for mixing of energy, but it is assumed that energy, mass, and momentum are mixed at equal rates, which is a valid assumption for LWR conditions in which the turbulent Prandtl number will be close to unity. The first term in the brackets represents the molecular component of mixing. This term is neglected in CTF because the turbulent effects will dominate the mixing as a result of the relatively high mass flow rates found in LWRs. Making this simplification allows this equation to be reduced to the following:

$$W_{ij}^{H'} = \frac{\epsilon \rho s_{ij}}{z_{ij}^T} \tag{356}$$

Substituting the definition of the lateral mixing mass flux back into Eq. (354),

$$\beta = \frac{(\epsilon/z_{ij}^T)\rho s_{ij}/s_{ij}}{\overline{G}} \tag{357}$$

.

This can now be reformulated to solve for ϵ/z_{ij}^T.

$$\frac{\epsilon}{z_{ij}^T} = \frac{\beta \overline{G}}{\overline{\rho}} \tag{358}$$

At this point, it is also assumed that the density, ρ, that was used to define the kinematic viscosity, should be the area average of the two adjacent subchannels under consideration. Now the mixing velocity, ϵ/z_{ij}^T, can be fully defined if a value for β is provided. This can either be provided by user input or calculated via the internal Rogers & Rosehart correlation[58]. This is discussed below; however, in CTF, the mixing term for two-phase flow must also be known. This term will be higher than the single-phase value. This is obtained by introducing a multiplier term, Θ, which is defined as follows:

$$\Theta = \frac{(\epsilon/z_{ij}^T)_{\text{TP}}}{(\epsilon/z_{ij}^T)_{\text{SP}}} \left(1 - \frac{\rho_g}{\rho_l}\right) \tag{359}$$

This term can be multiplied by the single-phase term to obtain the two-phase value.

$$\left(\frac{\epsilon}{z_{ij}^T}\right)_{\text{SP}} \Theta = \Theta \frac{\beta \overline{G}}{\rho_i} \tag{360}$$

$$\left(\frac{\epsilon}{z_{ij}^T}\right)_{\text{TP}} = \Theta \frac{\beta \overline{G}}{\rho_i} \tag{361}$$

It is noted that both $\overline{G}$ and ρ should be calculated with consideration that the fluid is actually a two-phase mixture. Definitions for Θ and β are now provided; this will fully close the turbulent mixing and void drift source terms.

The Beus correlation[59] provides definition for Θ. The author demonstrates that the behavior of this multiplier is highly dependent on the flow regime. The multiplier was found to increase linearly with respect to flow quality up until the flow regime changed from slug to annular. As the flow quality continued to increase, the multiplier decreased in a hyperbolic fashion after that point. This behavior is shown graphically in Figure 13. Equations representing this behavior are shown below.

$$\Theta = 1 + (\Theta_M - 1)\left(\frac{x}{x_M}\right), \quad \text{if } x < x_M \tag{362a}$$

$$\Theta = 1 + (\Theta_M - 1)\left(\frac{x_M - x_0}{x - x_0}\right), \quad \text{if } x > x_M \tag{362b}$$

Note that in Figure 13, the value of Θ for zero flow quality is 1.0. This will reduce the ϵ/z_{ij}^T term to its single-phase quantity. Therefore, it is suitable to always apply the Θ multiplier to the calculated single-phase mixing parameter, β.

The quality is denoted by x, the quality at the slug-annular transition point is denoted by x_M, and the value of the two-phase mixing coefficient at the transition point is denoted by Θ_M. The equation capturing the hyperbolic nature of the two-phase mixing coefficient contains another term, x_0, which is simply the asymptote to which the hyperbola converges. The flow quality is defined as follows in CTF:

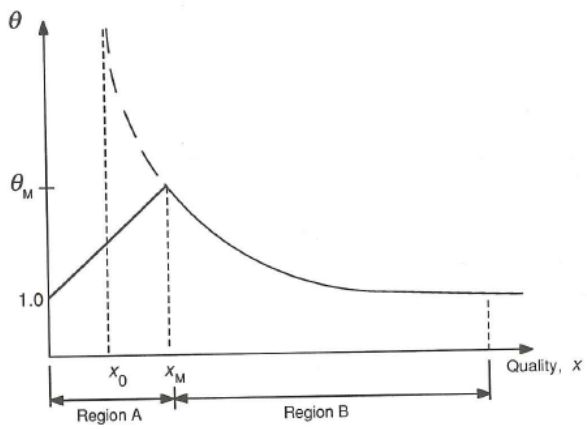

Figure 13. Behavior of the Beus two-phase mixing parameter.

$$x = \frac{\dot{m}_v}{\dot{m}_l + \dot{m}_e + \dot{m}_v} \tag{363}$$

The flow quality is calculated for the two adjacent subchannels and then averaged to one value using area weighting. The quality at the slug-annular transition point is determined using Wallis's model [30].

$$x_M = \frac{\frac{0.4[\rho_f(\rho_f - \rho_g)gD_h]^{1/2}}{G} + 0.6}{\left(\frac{\rho_f}{\rho_g}\right)^{1/2} + 0.6} \tag{364}$$

The value of Θ_M was determined to be 5 by Faya [60]; however, CTF allows for the user to input their own value for Θ_M. The value for the vertical asymptote, x_0, is given as a function of Reynolds number.

$$x_0 = x_M \mathrm{Re}^{0.0417} \tag{365}$$

One modification was made to the Beus correlation: the calculation of the asymptote value was modified to decrease the steep slope of the resulting hyperbola and improve numerical stability. The calculation of the asymptote instead becomes

$$x_0 = 0.75 x_M \mathrm{Re}^{0.0417}. \tag{366}$$

The mixing parameter, β, can be specified using a flow-dependent correlation developed by Rogers & Rosehart[58]. The correlation produces a single-phase mixing coefficient, as follows:

$$\beta_{sp} = 0.5\lambda \mathrm{Re}^{-0.1}\left[1 + \left(\frac{D_{h,j}}{D_{h,i}}\right)^{1.5}\right]\frac{D_{h,i}}{D_{\mathrm{rod}}}, \quad \text{if } D_{h,i} < D_{h,j} \tag{367a}$$

$$\beta_{sp} = 0.5\lambda \mathrm{Re}^{-0.1}\left[1 + \left(\frac{D_{h,i}}{D_{h,j}}\right)^{1.5}\right]\frac{D_{h,j}}{D_{\mathrm{rod}}}, \quad \text{if } D_{h,j} < D_{h,i} \tag{367b}$$

The mixing coefficient is calculated for adjacent subchannels i and j. The Reynolds number is calculated using the subchannel with the smaller hydraulic diameter, D_h. If Re is zero, then the single-phase mixing coefficient β_{sp} is set to zero. The coefficient λ is calculated as follows:

$$\lambda = 0.0058\left(\frac{s_{ij}}{D_{\text{rod}}}\right)^{-1.46} \tag{368}$$

9. ENTRAINMENT MODELS

9.1 INTRODUCTION

The physical processes of entrainment and de-entrainment must be modeled to account for interaction between the continuous liquid and droplet fields. Four scenarios are considered in CTF when modeling droplet sources:

1. Entrainment from liquid film
2. Entrainment during bottom reflood
3. Entrainment during top-down reflood
4. Spacer grid droplet breakup

The first three cases involve mass leaving the liquid field and entering the droplet field, but this occurs through different processes. The fourth case does not add droplets by entrainment from the liquid field; instead, it accounts for the increase in droplets and droplet surface area caused by droplets breaking up on spacer grids—an effect that is important to core cooling during an accident in which core dryout occurs.

Mass can also move from the droplet field to the liquid field by the process of de-entrainment. Four scenarios are considered when modeling de-entrainment:

1. De-entrainment in film flow
2. De-entrainment in crossflow
3. De-entrainment due to area changes
4. De-entrainment at solid surfaces and liquid pools

9.2 LIQUID FILM ENTRAINMENT/DE-ENTRAINMENT

9.2.1 Entrainment

Two cases are considered when calculating the entrainment rate in the annular/mist flow regime: entrainment in co-current flow, and entrainment in counter-current flow. The phenomenon responsible for entrainment from film is the same for the two cases. Waves on the film surface will grow as a result of hydrodynamic and surface tension forces. When the pressure differential over the wave exceeds the surface tension caused by the amplitude of the wave growing large, the wave will break, and liquid will be entrained. The wave behavior and entrainment rate will differ, however, depending on whether the flow is co-current, with low amplitude roll waves with droplets being sheared off of the wave crest [52], or counter-current with abrupt, large-amplitude waves.

CTF will check whether the flow is counter-current by checking for negative liquid mass flow rate and positive vapor mass flow rate in the momentum cell below the current one. If in counter-current flow, then the maximum of the co-current and counter-current entrainment rates is taken. For either case, the entrainment rate is limited to the smaller of two values: the calculated entrainment rate or a function of the maximum flow in the cell:

$$S_E = \min[S_E, (F_{se} + 0.05\alpha_l\rho_l A_x)] \tag{369}$$

The maximum flow is calculated by considering the total liquid lateral flow—which includes all gap liquid flow into the cell plus any boundary condition injection flows—and the axial liquid flow rate.

9.2.1.1 Counter-Current Flow

For counter-current flow, it is assumed that anything in excess of the critical liquid flow rate is sheared off into the droplet field.

$$S_{E,\text{counter}} = \dot{m}_l - \dot{m}_{l,\text{crit}} \tag{370}$$

Expanding,

$$S_{E,\text{coutner}} = (\alpha_l - \alpha_{l,\text{crit}})\rho_l |U_l| A_x \tag{371}$$

The critical liquid void fraction is calculated from the critical vapor void fraction:

$$\alpha_{l,\text{crit}} = 1 - \alpha_{\text{crit}} \tag{372}$$

The critical vapor void fraction is determined from a force balance between opposing forces acting on the wave—the pressure gradient over the wave crest and the surface tension.

$$\alpha_{\text{crit}} = 1 - 2\frac{\sigma}{\rho_v \vec{U}_{vl}^2 D_h} \tag{373}$$

A modified relative velocity is used to calculate the critical void. The maximum of the relative vapor-liquid vector velocity and a modified axial relative velocity is used.

$$\vec{U}_{vl} = \max\left[\vec{U}_{vl}, (u_{v,j-1} - u_{l,j-1})\frac{1-\alpha_l}{1-2.5\alpha_l}\right] \tag{374}$$

9.2.1.2 Co-Current Flow

Whalley, Hewitt, and Hutchinson[61] correlated entrainment data for air-water mixtures as a function of interfacial shear stress, τ_i, surface tension, σ, and a roughness factor acting as the length scale, k_s, using the dimensionless group

$$S_k = k_s \frac{\tau_i}{\sigma}. \tag{375}$$

This was modified by Wurtz[62] by multiplying by the dimensionless velocity to correlate data for both air-water and steam-water mixtures, according to

$$S_w = \frac{k_s \tau_i \vec{U}_v \mu_l}{\sigma^2}. \tag{376}$$

This form was later used by Paleev and Filippovich[63] to correlate air-water data. Wurtz used this dimensionless group to obtain the following relationship which is used in CTF for co-current entrainment rate:

$$S_E = \left[0.41 \text{ lbm ft}^{-2} \text{ s}\right]\left[\frac{k_s \tau_i \vec{U}_v \mu_l}{\sigma^2}\right] P_w \Delta X \tag{377}$$

The roughness parameter is given by

$$k_s = 0.57\delta + 6623\,\text{ft}^{-1}\delta^2 - 3.56 \times 10^6\,\text{ft}^{-2}\delta^3 + 1.5767 \times 10^9\,\text{ft}^{-3}\delta^4. \tag{378}$$

The interfacial shear is calculated using the interfacial friction factor for the film, f_i, which is discussed in Section 6.5:

$$\tau_i = f_i \rho_v \vec{U}_{vl}^2 \tag{379}$$

9.2.2 De-Entrainment

De-entrainment in film flow is the result of the random turbulent motions of the droplets that cause some of them to impact the film and be absorbed. The de-entrainment rate is calculated using the correlation of Cousins[64], which uses a droplet concentration gradient diffusion model. The form of the correlation is

$$S_{DE} = k_0 C P_w \Delta X. \tag{380}$$

The droplet concentration, C [lbm ft^{-3}], is a function of the droplet mass and the vapor/droplet volume:

$$C = \frac{\alpha_e \rho_l}{\alpha_e + \alpha_v}. \tag{381}$$

The mass transfer coefficient k_0 was correlated by Whalley[65] as a function of surface tension given by

$$k_0 = \max \begin{Bmatrix} 3.0492 \times 10^{12} \sigma^{5.3054} \\ 12.491 \sigma^{0.8968} \end{Bmatrix} \tag{382}$$

with k_0 in ft s^{-1} and σ in lbf ft^{-2}.

Other terms in the correlation include wetted perimeter, P_w, and cell height, ΔX.

9.3 BOTTOM REFLOOD ENTRAINMENT

9.3.1 Entrainment

The bottom reflood process involves the quenching of fuel rods that existed in a hot wall flow regime. Film boiling occurs, and as the rods cool, transition boiling occurs, and finally, nucleate boiling takes place. These processes cause a large vapor generation rate and a corresponding high vapor velocity which causes a large amount of droplet entrainment. The actual entrainment mechanisms can be a result of liquid core breakup caused by surface instabilities in the case of subcooled liquid or bubbles breaking through the liquid core surface in the case of saturated liquid. The model used in CTF is based on the work of Kataoka, Ishii, and Mishima[66], which considers droplet entrainment caused by vapor bubbling through liquid pools.

$$S_E = \left(\alpha_v \frac{U_v}{U_{\text{crit}}} \right)^2 \dot{m}_v \tag{383}$$

The actual form used in CTF is

$$S_E = \min\left[2.5\,\text{lbm}, \left(\frac{U_v}{U_{\text{crit}}}\right)^2\right]\dot{m}_v. \tag{384}$$

The critical velocity, U_{crit}, is the vapor velocity required to lift a droplet with radius defined by the critical Weber criterion against the pull of gravity. It is defined as follows:

$$U_{\text{crit}} = \left(\frac{4\text{We}_d}{3C_{D,d}}\right)^{1/4}\left(\frac{\sigma g^2 \Delta\rho}{\rho_v^2}\right)^{1/4} \tag{385}$$

The Weber number, We_d, is taken to be 2.0 as a result of reflood experiments in the FLECHT tests. The droplet drag is taken to be 0.45. The density difference, $\Delta\rho$, is the difference between the liquid and vapor density. The droplet flow rate entering the cell is subtracted from the entrainment rate. It is further multiplied by a factor to account for low liquid void fractions.

$$S_E = \max[0, S_E - \dot{m}_e]\min[1, 5\alpha_l]. \tag{386}$$

9.3.2 De-Entrainment

De-entrainment is not considered for the case of bottom reflood.

9.4 TOP-DOWN REFLOOD ENTRAINMENT/DE-ENTRAINMENT

9.4.1 Entrainment

Top-down reflood occurs as a result of upper plenum injection during accident conditions. After the core has dried out and hot wall conditions exist, the core may be quenched from coolant injection that falls from above the core. Two mechanisms for entrainment are compared for this case. The first mechanism involves film falling faster than the downward moving quench front. If liquid moves lower than the quench front into hot wall regions, then the liquid will quickly sputter, breaking up into droplets. The second mechanism of entrainment is caused by entrainment off of the film surface caused by upward flowing vapor. The counter-current flow entrainment model that was used for the annular/mist regime (Section 9.2) is used for the second mechanism.

For the first mechanism, it can be assumed that all film that falls to the quench front and is not vaporized is entrained. This can be written as follows:

$$S_E = -\dot{m}_l - \Gamma_q \tag{387}$$

The mass flow rate of the liquid film that reaches the quench front is $\dot{m}_l$, and the vapor generation rate at the quench front is Γ_q. The vapor generation rate is simply the old time step vapor generation rate for the cell in which the quench front resides. The mass flow rate is the old time step liquid mass flow rate into the cell in which the quench front resides. The liquid mass flow rate will be negative in CTF because the film is falling: hence, the preceding negative in the above equation.

The second mechanism uses Eq. (371) from Section 9.2, repeated below:

$$S_{E,\text{coutner}} = (\alpha_l - \alpha_{l,\text{crit}})\rho_l |U_l| A_x \tag{371}$$

Substituting the definition of the critical void fraction leads to the following equation:

$$S_E = \left(\alpha_l - \frac{2\sigma}{D_h \rho_v \vec{U}_{vl}^2} \right) |\dot{m}_l| \tag{388}$$

The maximum of the two entrainment model results is taken as the entrainment rate for the falling film. Some additional considerations are then made. If the void fraction is less than 0.8, then the deluge flow regime is considered. If the void fraction is less than 0.6, then the entrainment rate is zeroed. If the void fraction is between 0.6 and 0.8, then a ramp is used to alter the falling film entrainment rate: the rate is ramped between 0 % for void fractions of 0.6 and 100 % for void fractions of 0.8. The ramp function is

$$S_{\text{ramp}} = \max[0.0, \min(5(\alpha_v - 0.6), 1.0)]. \tag{389}$$

For void fractions greater than 0.8, an additional consideration is made in which the maximum of the falling film entrainment rate and the liquid mass flow rate is taken for the entrainment rate:

$$S_E = \max[0.0, S_E, -\dot{m}_l] \tag{390}$$

9.4.2 De-Entrainment

The de-entrainment in the top-down reflood region is assumed to be caused by random turbulent motions of the drops, which causes drops to impact the film and be absorbed. The same model that was used for the annular/film region is used here. The model of Cousins[64] is repeated:

$$S_{DE} = k_0 \Delta C P_w \Delta X. \tag{380}$$

Definition of the equation terms can be found in Section 9.2. One modification is made to Eq. (380) to account for the quench front. Only droplets impacting the film are de-entrained, so it is necessary to know the fraction of the cell which is quenched to determine the de-entrainment rate. This fraction is multiplied by the Cousins model:

$$S_{DE} = k_0 \Delta C P_w \Delta X F_q \tag{391}$$

The fraction of the cell that is quenched, F_q, is calculated:

$$F_q = \frac{X_b - X_{qf}}{\Delta X}. \tag{392}$$

The top of the momentum cell, which is the global location of the boundary between adjacent continuity mesh cells, is X_b, and the code-calculated quench front global location is X_{qf}. The difference of these values is the length of the quenched portion, which is divided by the momentum cell height to get the quenched fraction of the heater rods.

9.5 CROSSFLOW DE-ENTRAINMENT

The crossflow de-entrainment is modeled by considering flow across tube banks. De-entrainment is calculated for each gap connecting to a channel using a rod-bundle de-entrainment efficiency term, η_{DE}.

$$S_{DE} = \frac{1}{2}\eta_{DE}|\dot{m}_{e,Z}|. \tag{393}$$

The rod bundle de-entrainment efficiency term is input by the user. The lateral droplet mass flow rate through the gap, $\dot{m}_{e,Z}$, is used. The de-entrainment rate is calculated for each gap connecting to a channel, and total de-entrainment rate is calculated by summing the individual gap contributions together.

9.6 DE-ENTRAINMENT IN AREA CHANGES

Droplets will de-entrain if they move through a change in flow area, thus forming a film on the surface. This effect is most prominent during accident conditions when entrained droplets flow through the upper core tie plate. Droplets will de-entrain when moving through the plate and form a film which will provide the initial liquid for the top quench front. De-entrainment is captured by simply using the ratio of the areas.

$$S_{DE} = \max[0.0, \dot{m}_{e,j-1}]\left(1 - \frac{A_j}{A_J}\right) + \max[0.0, -\dot{m}_{e,j}]\left(1 - \frac{A_{j-1}}{A_J}\right) \tag{394}$$

The equation has two components to account for the possibility that entrained flow is moving in the top-down direction; one of the components will be zero. The ratio between momentum cell and continuity mesh cell area is taken. Because of the staggered mesh approach, the momentum cell will lie on the top boundary of the continuity mesh cell with the same level index.

9.7 DE-ENTRAINMENT AT SOLID SURFACES

It is assumed that droplets that move normal to a solid surface are de-entrained on the surface. Furthermore, droplets that flow into a bubbly flow regime are also assumed to be de-entrained. This is handled in CTF by checking whether a mass flow boundary condition was chosen for the momentum cell above or below the continuity mesh cell. A mass flow boundary condition would imply that there is a solid surface from which the injection is occurring. If a mass flow boundary condition is in the momentum cell above, then the entrainment rate is

$$S_{DE} = \max[0.0, S_{DE,\text{cousins}}, \dot{m}_{e,j-1}]. \tag{395}$$

The Cousins[64] model is used for comparison against the entrained droplet flow rate. The model is in the same form as that used for the top-down reflood de-entrainment rate calculation. For a mass flow rate boundary condition below the continuity mesh cell, the negative of the droplet mass flow rate in the momentum cell above is used.

$$S_{DE} = \max[0.0, S_{DE,\text{cousins}}, -\dot{m}_{e,j}] \tag{396}$$

Consideration is made for de-entrainment in the wet film on quenched unheated conductors, if they exist. One-third of the droplets is de-entrained on a quenched housing, as follows:

$$S_{DE,h} = \frac{1}{3}X_q P_{w,c}\Delta X\frac{\alpha_e\rho_l}{\alpha_e + \alpha_l}. \tag{397}$$

The fraction of the conductor which is quenched is X_q, and the wetted perimeter of the housing is $P_{w,c}$. The quenched housing de-entrainment rate is added to the solid surface de-entrainment rate.

$$S_{DE} = S_{DE} + S_{DE,h} \tag{398}$$

9.8 SPACER GRID DROPLET BREAKUP MODEL

Dispersed droplets in the flow field can be shattered as they impact spacer grids. Experiments performed by the Central Electricity Generating Board of the United Kingdom[67], the University of New York at Stony Brook[68], and Westinghouse/Carnegie-Mellon University[69] show that this breakup phenomenon can be significant. It is important to capture this phenomenon because the resulting field of smaller droplets evaporates more easily than larger droplets, which reduces vapor superheat and improves rod heat transfer during accident conditions. To capture this phenomenon, droplet breakup caused by the spacer grid is determined, and the increase in small droplet interfacial area is calculated, which is added to the interfacial area source term in the interfacial area transport equation (see Section 2.4).

The spacer grid droplet breakup model can be found in the GRID subroutine. Calculations are only performed if less than 99 % of the grid height is quenched. The goal of the grid droplet breakup model is to provide the interfacial area transport equation with information on the rate of small droplet creation and the small droplet diameter so that the effect on droplet interfacial area can be determined. CTF actually considers two stages of breakup: the breakup of large droplets into small droplets, and the breakup of small droplets into micro-droplets. In the end, however, the small droplet and micro-droplet number fluxes (breakup rate), and diameters are merged into one set of information for a single small droplet field.

The large droplet field breakup is considered first. The number of droplets in the flow field that break on the grid strap are calculated as a function of the grid blockage ratio and the droplet flow rate.

$$\dot{m}_{db} = \eta \left(\frac{A_{x,g}}{A_x} + \frac{1}{2} \frac{A_{x,s}}{A_x} \right) \dot{m}_e \tag{399}$$

The leading factor, η, is a breakup efficiency factor estimated at 0.6. The area blockage ratio is the sum of the grid strap blockage ratio and half of the grid spring flow blockage ratio. With the droplet breakup rate, it is necessary to then calculate the new droplet diameter so that the interfacial area source may be calculated. Droplet breakup data taken from Wachters ([70] and [71]) and Takeuchi[72] was used to characterize the Sauter mean diameter of shattered droplets as a function of initial droplet diameter and original droplet Weber number. The correlation of the data can be seen in Figure 14.

The correlation for the diameter of the shattered droplets is as follows:

$$\frac{D_{sd}}{D_i} = 6.167 \mathrm{We}_d^{0.53} \tag{400}$$

At low droplet Weber numbers, Eq. (400) will return shattered droplet diameters close to the incident droplet diameter. Such droplets have large diameters and should not be considered in the small droplet field. Therefore, for We_d < 30.9 , the calculated large droplet breakup, is not considered to enter the small droplet field. Instead, the code checks for small droplets breaking up into micro-droplets. For We_d > 250, all large droplets that shatter, as calculated by Eq. (399), are considered to enter the small droplet field, and the small droplet field number flux is calculated accordingly. For 30.9 < We_d < 250, a linear interpolation is performed between zero, large droplets breaking up into small droplets, and the full value calculated by Eq. (399). The ramping factor multiplied by the droplet breakup rate is

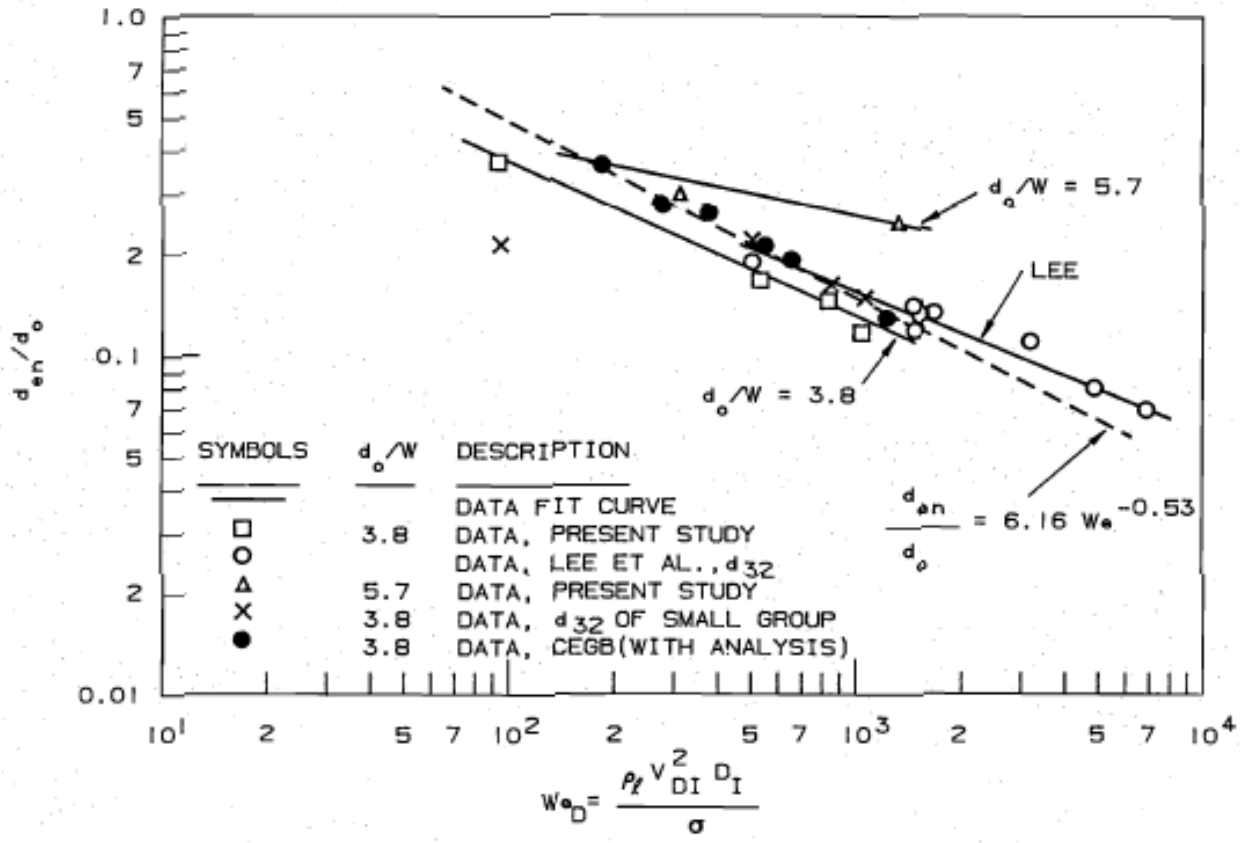

Figure 14. Ratio of shattered droplet diameter to incident droplet diameter dependence on droplet Weber number.

$$R = \frac{\mathrm{We}_d - 30.9}{250 - 30.9}. \tag{401}$$

A similar check is performed for the small droplet field breakup. If the small droplet Weber number is less than 30.9, then no small droplets are considered to break up into micro-droplets. If, however, $\mathrm{We}_d > 30.9$, then the small droplets break on the spacer at the full droplet breakup rate. The logic for this approach is best summarized in the flowchart shown in Figure 15.

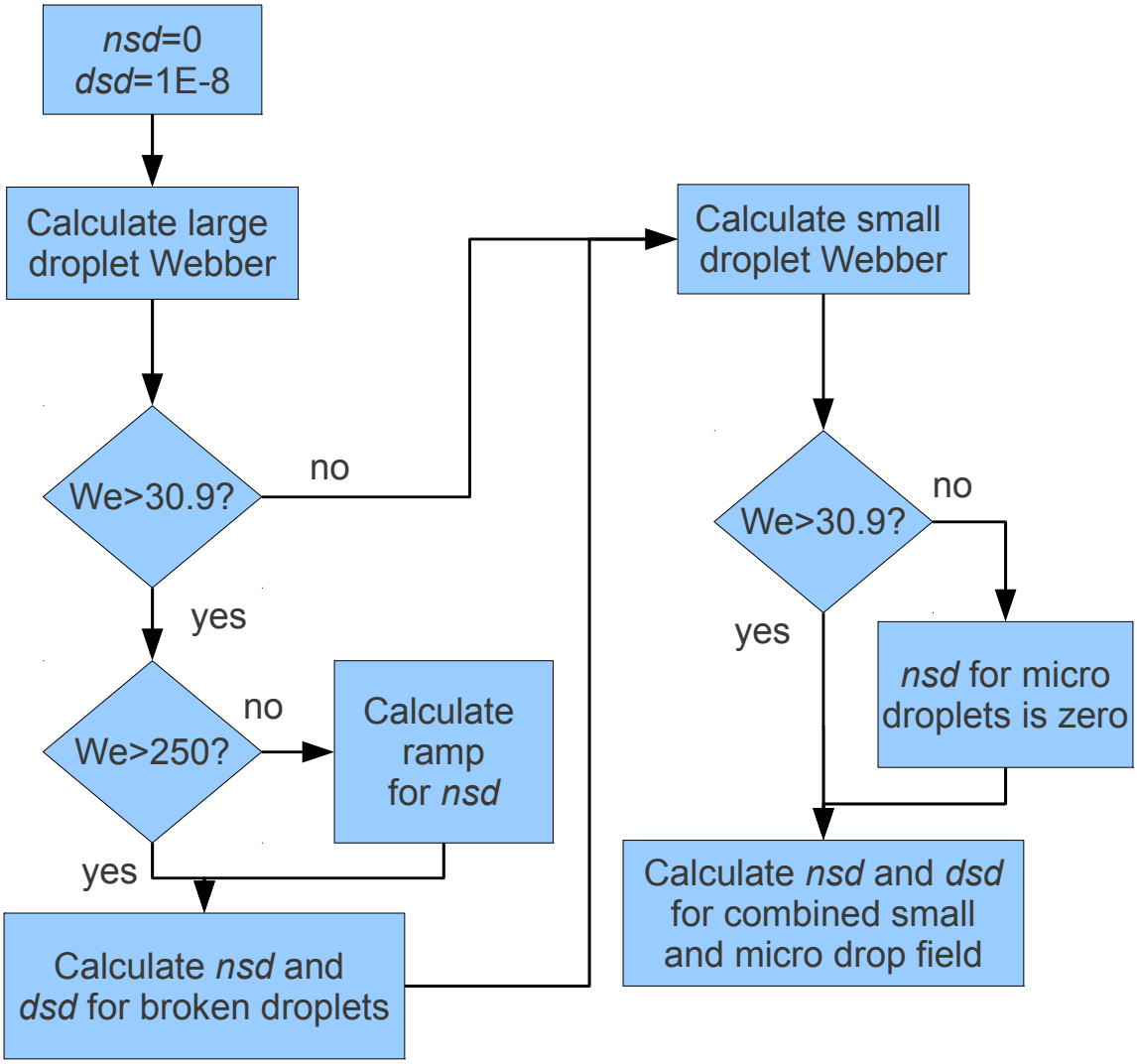

Figure 15. Flowchart for the spacer grid droplet breakup model found in the GRID subroutine.

In Figure 15, nsd is the droplet number flux—it is the number of droplets entering a droplet field per unit time caused by shattering from larger droplets. The shattered droplet diameter is represented with the dsd term. The droplet number flux and shattered droplet diameter are initialized to 0 and $1 \cdot 10^{-8}$, respectively.

The large incident droplet Weber number is calculated first. If it is smaller than 30.9, then the small droplet number flux stays at zero because any large droplets that do shatter are shattered into large droplets which remain in the large droplet field. Otherwise, the small droplet mass flow rate is calculated by Eq. (399). The

droplet number flux is then calculated using the mass flow rate from the large-to-small droplet field and the mass of a single small droplet.

$$\text{nsd} = \frac{\dot{m}_d}{m_{d,\text{single}}}. \tag{402}$$

The single drop mass is calculated from the shattered droplet Sauter mean diameter of a droplet obtained from Eq. (400), which is used to calculate the droplet volume. The droplet volume is multiplied by the liquid density to obtain the droplet mass.

$$\text{nsd} = \frac{\dot{m}_d}{1/6\pi d_{sd}^3 \rho_l} \tag{403}$$

For $\text{We}_d < 250$, a ramping factor is calculated by Eq. (401) and multiplied by the small droplet number flux to reduce the number of shattered droplets that enter the small droplet field.

This process is repeated for the small droplet field. It is important to note here that the shattered droplet number flux is defined on a per channel basis. Therefore, the shattered droplet number flux includes droplets that were shattered not only by the current grid being analyzed, but also by the upstream grid (if one exists) that caused droplet shattering. Even if the large droplet Weber number were smaller than 30.9 and if no large droplets shattered on the current grid entered the small droplet field, then there could still be small droplets that shatter into micro- droplets caused by shattering from upstream grids.

After the small-to-micro droplet shattering rate is determined, the small and micro-droplet number flux and diameters are combined into a single set of values. This is done for the shattered droplet number flux by first adding the small and micro-droplet field mass flow rates. Second, Eq. (403) is used to calculate the number flux for the combined small and micro-droplet field, but using the Sauter mean diameter of the combined fields.

The Sauter mean diameter of the combined fields is calculated by a mass flow rate averaging process. The small droplet mass flow rate is divided by the small droplet diameter, and likewise, the micro-droplet mass flow rate is divided by the micro-droplet diameter. These terms are added and divided into the total small droplet and micro- droplet mass flow rate to obtain the Sauter mean diameter of the combined fields, as shown below:

$$d_{sd,\text{combined}} = \frac{\dot{m}_{\text{small}} + \dot{m}_{\text{micro}}}{\frac{\dot{m}_{\text{small}}}{d_{\text{small}}} + \frac{\dot{m}_{\text{micro}}}{d_{\text{micro}}}}. \tag{404}$$

10. HEATED AND UNHEATED CONDUCTOR MODELS

10.1 INTRODUCTION

Thus far, emphasis has been placed on modeling of the flow field using conservation equations and associated models for conservation equation closure terms. CTF also contains a capability for modeling solid components such as fuel rods, electric heaters, and unheated conductors. This chapter discusses these models.

A flowchart for the general solution of conductor temperature profiles is shown in Figure 16—the flow of source code subroutines is presented. The conduction solution is performed after setting model boundary conditions, but prior to solving the fluid solution. If the fine-mesh renoding capability is enabled, the quench front will be located (if one exists) and the mesh will be refined in the quench front vicinity. Heat transfer coefficients are then calculated for each surface depending on the heat transfer regime prior to performing the conduction solve. This includes calculation of radiative heat transfer if the user enabled this option.

The models used for tracking the quench front are discussed in Section 12.14.3, but the remeshing of conductors is discussed in this section. The location of the CHF point and the calculation of the CHF temperature are discussed in Section 12.9 and, specifically, Sub-section 12.9. Wall convective heat transfer models are discussed in Section 12. Radiative heat transfer models are discussed in Section 12.13. This leaves determination of the heat transfer through the conductor and the resulting temperature profile (subroutine TEMP), which is discussed further in this chapter.

Two general types of conductor models are included in CTF: one for rods, and one for generic conductors. The rod models can be used for modeling solid or hollow heater rods, as well as nuclear fuel rods. Models are included for gap conductance, fuel rod deformation, and heat generation accounting for nuclear reactions, as well as metal-water reaction in cladding. Rods can be active or passive (i.e., heated or unheated), and they may exceed the CHF temperature and thus require the CHF models. Generic conductors, however, are always considered passive and have no internal heat sources. Furthermore, they need not be of cylindrical geometry, and it is assumed that they always remain below the CHF temperature and therefore never require the use of the CHF models.

The common feature of the different conductor type models is the conduction equation—it is discussed first in the following section. After this, the conductor remeshing package is discussed, which is used to refine or collapse the mesh used for the conductors depending on the location of the quench front. These are the only models used for modeling generic conductors or solid or hollow heater rods. Nuclear fuel rods, however, require special considerations which are discussed in the final section, Section 11.

10.2 CONDUCTION EQUATION

10.2.1 Formulation of the General Conduction Equation

CTF includes capabilities for modeling fuel rods, electric heater tubes, and walls using a finite-difference form of the heat conduction equation which is formulated using the heat balance approach[73]. This approach divides the conductor into control volumes, with nodes being located at the control volume centers or surfaces.

An example of this meshing approach is shown for a cylindrical geometry in Figures 17 and 18. Figure 17 shows side and top views of a meshed nuclear fuel rod. The rod is divided into four axial levels, with j being the index for axial level. Each axial level of the rod will be meshed into both radial and azimuthal segments. Figure 18 provides a closer look at the internal meshing of the fuel rod for a single axial level.

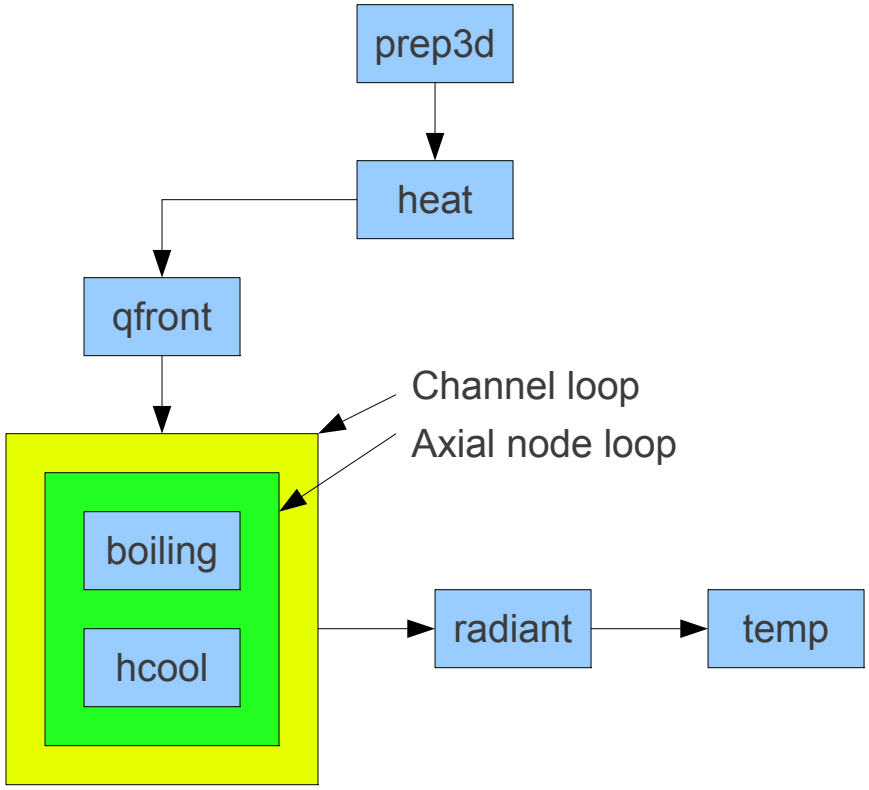

Figure 16. Flowchart for heated and unheated conductor temperature solution.

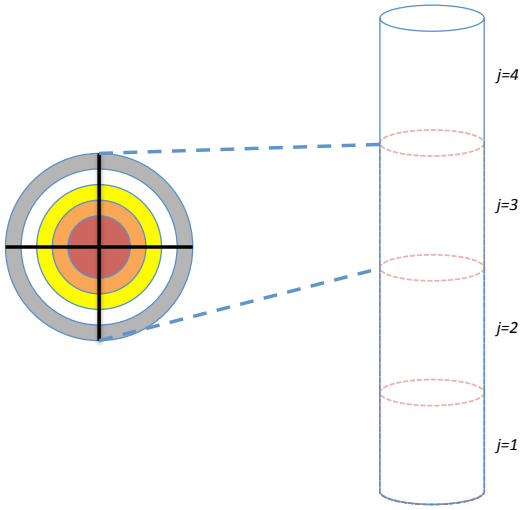

Figure 17. General CTF meshing approach for nuclear fuel rod.

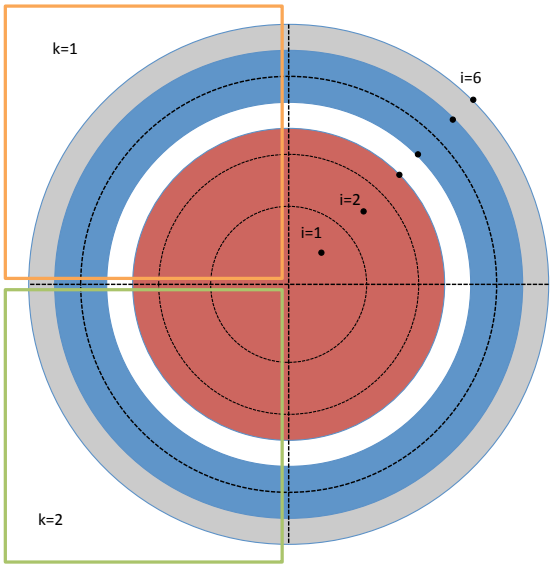

Figure 18. A closer look at CTF internal meshing of nuclear fuel rod.

The rod is divided into four azimuthal segments labeled using k. The orange and green boxes highlight two of the azimuthal segments, $k = 1$ and $k = 2$. Note that an azimuthal segment will be created for each rod/channel connection. If a pin-centered subchannel approach is employed for cases in which each rod connects to only one channel, then there will only be one azimuthal segment in the rod. Also note that azimuthal segments will be indexed in CTF according to the indexing of channels and rods, so the labeling presented in Figure 18 is an example for illustration purposes only.

Figure 18 also illustrates an example of the radial meshing of the fuel rod. The fuel pellet is represented in red, the gap is white, the clad is blue, and the optional Crud layer is gray. The fuel pellet is divided into three mesh cells. The clad is divided into two regions, and the Crud layer is represented using only one region. For a nuclear fuel rod, the radial meshing (number of mesh cells) of the fuel pellet can be controlled by the user via input; however, the number of regions for other areas (gap, clad, and Crud) are controlled by CTF.

Attention is now given to the node locations. Nodes inside the fuel pellet will always be in the center of the mesh cell volume for internal mesh cells. However, the fuel pellet surface mesh cell will have its node on the surface of the fuel pellet. The two clad mesh cells will have their nodes on the opposite surfaces of the clad. Likewise, the crud layer will have its node on the fuel rod surface. Shifting the node locations from mesh-cell center to surface allows for CTF to define a temperature at needed locations (i.e., fuel pellet surface, clad inside and outside surfaces, and fuel rod surface).

A non-nuclear cylindrical geometry will be discretized similarly. The primary differences will be that (1) the user may divide the rod into any number of regions, and (2) each region may have any number of nodes. Unheated conductors, or "slabs," have a plate-like geometry. The i index counts nodes across the wall thickness, j in the axial direction, and k indices count along the wall width in the lateral direction. Meshing the geometry using this control volume heat balance approach allows for the following:

- unequal mesh spacing
- temperature dependent material properties
- space dependent material properties

- changes in internal resistance to heat transfer (e.g. gaps)
- changes in internal heat generation.

The general conduction equation for a solid mesh cell is shown in Eq. (405).

$$\frac{d}{dt}\int_V \rho C_p V T = \oint_A \boldsymbol{n}_k Q_k dA + \int_V Q''' dV - \oint_A Q_s dA \tag{405}$$

The LHS term is the transient term, with ρ being material density, C_p being material specific heat, T being the material temperature, and t being the timestep size of the solid conduction equation solution. On the RHS, the first term is a surface integral over the solid mesh cell that accounts for energy conduction in axial, azimuthal, and radial directions. The $\boldsymbol{n}$ is the unit vector orthogonal to the surface, k is the current surface, and A is the surface area of the solid mesh cell. The second term represents volumetric generation of energy caused by fission or electrical heating, with Q''' being the volumetric energy generation rate, and V being the cell volume.

The third and final term of the equation is the convective heat transfer at the cell surface which transports energy from the solid to surrounding fluid or vice versa. Note that only mesh cells exposed to the coolant will have this final term. Furthermore, only mesh cells having some heating source will have the volumetric energy generation term. For a nuclear fuel rod, energy generation can include the heat generation from fission in the pellet, as well as heat generation in the clad from zirconium-water reaction. Energy generation in solid and hollow electric heater rods comes from electrical heating. Rod heat rates may be dependent on radial and axial location in the rods and are input by the user. For unheated conductors, the energy generation term remains absent.

Note that the mass of the control volume (i.e. ρV) is always evaluated at the cold-state properties. This is because the nodal locations are fixed once they are defined in CTF, but in reality, they may move as a result of thermal expansion. If ρV were allowed to change with temperature without allowing the control volume dimensions to also change, then a mass imbalance would occur.

The CTF rod solution algorithm works by looping over each rod, then each axial level of the rod, then each azimuthal segment at that level. For a single segment, CTF then loops over each radial node and sets up the terms that will form the equation for that node. At the end of each radial node loop, the system of equations will be solved by Gaussian elimination. Therefore, the rod conduction solution is implicit in only the radial direction; azimuthal and axial conduction terms are added to the conduction equations explicitly.

In the CTF solution, the thermal conduction term Q_k will be expanded for each surface of the current cell being set up. Each conduction term will take on the form shown in Eq. (406), where a represents the mesh cell being solved, and b represents a connected mesh cell.

$$Q_{a\to b} = k_{ab}\left(T_b - T_a\right) \tag{406}$$

Both T_a and T_b will be unknown if Cells a and b are connected in the radial direction. If either cell is connected in the axial or azimuthal direction, then the temperature of that cell will be explicitly given from a previous time step. The average thermal conductivity between Cell a and b will be some combination of the individual thermal conductivities of the two cells, k_a and k_b. This averaged thermal conductivity is defined using the concept of thermal resistances shown in Eq. (407), where $R_{a\to\text{boundary}}$ is the thermal resistance from the node of Cell a to the boundary between Cells a and b, and $R_{\text{boundary}\to b}$ is the thermal resistance from the boundary to the node of Cell b.

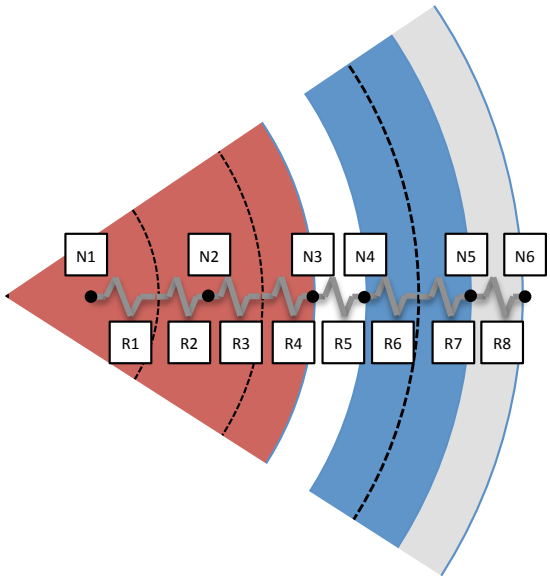

Figure 19. CTF model for fuel rods as a thermal resistance network.

$$k_{ab} = \frac{1}{R_{a\rightarrow\text{boundary}} + R_{\text{boundary}\rightarrow b}} \tag{407}$$

The thermal resistances can be defined for cells connected by a varying surface area (e.g., cylindrical mesh cells connected in the radial direction) or a constant surface area (e.g., rectangular mesh cells or cylindrical mesh cells connected in the axial or azimuthal directions). An example of a system of thermal resistances for a cylindrical geometry is shown in Figure 19.

In this example, the fuel rod is divided into six mesh cell volumes, each having a node labeled as N1–N6 that is either at the mesh cell center or surface. As a result, there are eight thermal resistances, labeled as R1–R8. Note that cells having nodes at their centers will have two thermal resistances—one to communicate with each cell boundary. Because the crud layer has only one node at its outside surface, it requires only one thermal resistance.

The formulation for the thermal resistances given above (radial direction) will be that of a cylindrical geometry, as shown in Eq. (408).

$$R = \frac{\ln\left(\frac{r_o}{r_i}\right)}{2\pi k L} \tag{408}$$

Here, r_o and r_i are the outside and inside radii of the cylindrical mesh cell, k is the thermal conductivity, and L is the axial height of the cell. Figure 20 shows an example of the resistance in the axial direction for a nuclear fuel rod. Because heat transfer in the axial and azimuthal directions is through a constant area, A, the resistance is linear and is defined as shown in Eq. (409).

$$R = \frac{L}{kA} \tag{409}$$

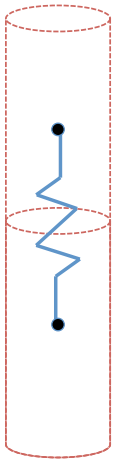

Figure 20. Example of resistance in the axial direction for nuclear fuel rod.

The fact that azimuthal and axial conduction and the convective boundary term are all explicit in the solid governing equation means that some controls are needed to keep the solution stable. Additionally, the CTF solid modeling capabilities include some features for capturing behavior of nuclear fuel rods, such as changes in gap conductance from rod geometry changes, and changes in fuel pellet conductivity from cracking and sintering. These matters are discussed in the following sections, along with the concept of thermal resistances.

10.2.2 Conductor and Flow Field Boundary

The conductors modeled by CTF must contact the fluid field at some, if not all, of their surfaces. Any conductor surface that does not join a fluid mesh cell either contacts another conductor, transfers heat to some outside environment, or is assigned an adiabatic boundary condition and transfers no heat. The conductors are coupled to the flow field solution by three possible conditions in CTF: convective heat transfer to the fluid, heat transfer from droplet impingement and vaporization, and radiative heat transfer to the fluid and other bodies around the conductor. A heat flux is calculated for each of these effects and is added to the conduction equation for surface cells that contact the fluid. If the conductor surface does not exchange heat with the fluid field, then CTF has an option for the user to prescribe a heat transfer coefficient and sink temperature for modeling heat loss to some external environment.

The calculation of heat transfer coefficients based on heat transfer regime is discussed in Section 12. Radiative heat transfer modeling is discussed in Section 12.13. It is important here to also discuss the general approach for applying these terms in calculating heat flux and the special consideration that must be made for the nucleate boiling regime. This is discussed in Section 10.2.2.1. The third vector for heat transfer between rod and fluid, droplet impingement heat transfer at flow blockages, is discussed in Section 10.2.2.2.

10.2.2.1 Convective Heat Transfer

Because the fluid may be two-phase, the heat flux is a sum of heat transfer to liquid and vapor phases.

$$q'' = H_l \left(T_s - T_l^n \right) + H_v \left(T_s - T_v^n \right) \tag{410}$$

Heat transfer coefficients for the liquid and vapor phases are represented by H_l and H_v. The conduction equation solution is performed prior to the flow-field solution for any given timestep. Therefore, the conductor cell temperature, T_s, is the current time-step surface temperature of the conductor, and the liquid and vapor fluid temperatures are obtained from the old timestep (hence the n superscript). Section 12 discusses the wall heat transfer models and calculation of the H_l and H_v heat transfer coefficients for all heat transfer regimes modeled by CTF.

Before Eq. (410) can be added to the conduction equation, special consideration must be made for the heat flux to the liquid phase. For the case of nucleate boiling, there is a strong dependency between wall surface temperature and heat flux. Therefore, the wall heat transfer and surface temperature are coupled implicitly in a noniterative manner by considering the linearized derivative of the heat transfer coefficient with respect to wall temperature when calculating the heat flux to be used as the wall boundary condition. The liquid heat flux becomes

$$q_l'' = H_l\left(T_s - T_l^n\right) + \left(\frac{\partial H_l}{\partial T_s}\right)\left(T_s - T_s^n\right)\left(T_s^n - T_l^n\right). \tag{411}$$

In this manner, the change in the heat transfer coefficient from the previous timestep is considered in calculating the new surface temperature. This modified heat flux is added to the conduction equation.

10.2.2.2 Droplet Impingement Heat Transfer

The droplet impingement heat transfer model is for a special scenario in which accident conditions cause the localized swelling of fuel cladding. As cladding swells into the flow channel, the cladding of different rods can meet and cause a blockage of the flow. Droplets entrained in the vapor flow can impact the swollen cladding. When the droplets impact and then vaporize, the heat transfer between the rods and the coolant is improved. A model was developed by Kendell and Rohsenow[74] to capture this effect, and it has been implemented into CTF. This heat transfer effect is only applied for flow blockages caused by rod swelling in the local vicinity of the blockage; outside of this region, no droplet impingement heat transfer is imposed on the rods.

Photographs taken of droplets impinging on an unquenched flat plate heated above the Leidenfrost point undergo a process of deformation, flattening, and reformulation[70][71]. The Kendell/Rohsenow model predicts this type of droplet behavior and the resulting evaporation efficiency. The droplets are viewed as cylindrical in shape, and as they impact, the radius grows such that the droplet morphs into a large-radius thin sheet of liquid. The predicted heat transfer efficiency from droplet evaporation is then used in CTF to calculate the heat transfer between the rod and fluid. The heat transfer from droplet evaporation is as follows:

$$Q = G_e h_{fg} \epsilon A_z, \tag{412}$$

where G_e is the mass flux of droplets in the blocked flow channel ($\mathrm{kg/m^2 s}$), h_{fg} is the latent heat of vaporization, ϵ is the droplet evaporation efficiency (provided by the Kendell/Rohsenow model), and A_z is the projected area normal to the flow. The user supplies the surface area of the rod portions that constitute the blockage, along with the angle of the blockage with respect to the flow direction. This angle is used by CTF to determine the droplet velocity perpendicular to the rod surface. The Kendell/Rohsenow model for droplet heat transfer efficiency is given as follows:

$$\epsilon = 2.6\left(\frac{\rho_v}{\rho_l}\right)^{1/2}\left(\frac{\bar{R}}{D}\right)\mathrm{We}_p^{1/8}\left[\frac{\beta_2 k_v(T_w - T_s)}{h_{fg}\,(\rho_v \sigma g_c D)}\right]^{1/2} \left[0.225\frac{\mu_v h_{fg}}{\beta_2 k_v\,(T_w - T_s)} + 1.5\right]^{-1/4} \tag{413}$$

The droplet Weber number, We_p, is defined using the initial inertia of a spherical drop perpendicular to the wall.

$$\mathrm{We}_p = \frac{\rho_l V_p^2 D}{\sigma g_c} \tag{414}$$

The velocity of the droplet, V_p, is the perpendicular velocity of the droplet with respect to the rod surface. The Weber number in CTF is set to a minimum of 30. The $\bar{R}$ term of Eq. (413) is the average drop extension radius over the impact period, and it is calculated as follows:

$$\bar{R} = \frac{R_{\max} + 0.43D}{2}, \tag{415}$$

where $R_{\max}$ is the maximum extension radius. This term is derived by equating the initial kinetic energy of the drop to the surface tension energy in the drop when it has come to complete rest in its new flat-sheet form. This leads to the following equality:

$$\frac{R_{\max}^2}{D^2} = \frac{2}{3}\left(1 + \frac{\mathrm{We}_p}{12}\right)\cos^2\left[\frac{1}{3}\left\{\arccos\left(\frac{-1.225}{\left(1 + \frac{\mathrm{We}_p}{12}\right)^{3/2}}\right)\right\}\right] \tag{416}$$

A special consideration is required here owing to the fact that the droplets are assumed to be a cylindrical geometry in the Kendell/Rohsenow model, whereas the droplet Weber number is for a spherical droplet. Before deformation, the surface tension energies of a drop and cylinder are not equal if the volumes are equal, and an initial amount of kinetic energy is required to account for this difference. Therefore, Eq. (416) is only applicable for droplet Weber numbers greater than 1.74. For values less than this, it is assumed that $R_{\max} = 0.43D$, which is then consistent with Eqs. (415) and (413).

Finally, the β_2 term in Eq. (413) is used to account for the nonlinear temperature profile in the vapor film between the droplet and the wall.

$$\beta_2 = \frac{1}{1 + 0.3\frac{C_p(T_w - T_s)}{h_{fg}}} \tag{417}$$

10.2.3 Explicit Term Stability Criterion

Because there are explicit terms in the heat conduction equation (if azimuthal or axial conduction are considered), there is also a stability criterion used in CTF. At the beginning of the conduction equation solution, the time step for the conduction equation is either set to be equal to or less than the flow solution time step. The user is responsible for providing CTF with a ratio that will be used to calculate the conduction equation time step with respect to the flow solution time step.

If axial or azimuthal conduction are modeled, then CTF will calculate a maximum allowable timestep size for the heat conduction equation for each cell. The smallest of all the allowable timestep sizes for a single conductor (rod or wall) will be the limiting timestep size for the conduction equation for *that particular conductor*. For example, the limiting timestep, dtexp, is set equal to the initial heat conduction timestep when analysis starts on a conductor. It is re-initialized every time analysis moves to a new conductor. Then, if axial and azimuthal conduction are modeled, dtexp will be calculated for each cell after the explicit terms (axial and azimuthal conduction into or out of the current cell) are calculated. The stability criterion is basically a reformulation of the conduction equation written only for the axial and azimuthal conduction terms. The axial and azimuthal heat conduction from all adjacent cells is limited to the energy change in the current cell by solving for the time step. Specifically, the criterion is written as

$$\Delta t = \frac{(MC_p)_{(i,j,k)}}{K_{(i,j-1,k)} + K_{(i,j+1,k)} + K_{(i,j,k-1)} + K_{(i,j,k+1)}}. \tag{418}$$

This is the maximum allowable time step size for the given cell based on heat conduction from or to the adjacent cells. The limiting timestep for the entire conductor is found by taking the minimum of the Δt for all the cells in the conductor. Prior to the implicit solution, the initial heat conduction timestep is compared to the minimum of the maximum allowable timesteps for all the cells. If the heat conduction timestep is greater than the smallest maximum allowable timestep, then the heat conduction timestep is reduced by half or more. The reduction in the timestep size is dependent on the degree by which the conduction timestep exceeds the smallest maximum allowable timestep. This is done numerically in CTF by dividing the heat conduction timestep, dht, by the smallest maximum allowable timestep, dtexp. The conduction heat transfer timestep is then divided by one plus the integer portion of this result. Numerically, this is written as follows:

$$\text{dht} = \frac{\text{dht}}{1 + \text{INT}\left(\frac{\text{dht}}{\text{dtexp}}\right)} \tag{419}$$

Here, the *INT* function returns the integer portion of the division. Therefore, if *dht* is at all greater than *dtexp*, then it will at least be reduced by half. If *dht* is twice as large than *dtexp*, then it will be reduced by a third, and so on. Clearly, it is necessary to use integer division so that the resulting number of conduction equation timesteps will fit into a single flow-field time step. That is, at the end of conduction equation and flow-field equation solutions, the conductor and flow-field will be at the same time in the transient.

10.3 CONDUCTOR REMESHING

In a reactor core, during accident conditions, the special case of core re-wetting may occur. In this case, the liquid coolant that is introduced by safety injection systems refills the core and causes a quench front to form. At this quench front, where liquid coolant recovers the once vapor-blanketed fuel rods and conductors, there are steep gradients in conductor/fluid heat flux and conductor temperatures. The behavior of the entire boiling curve—nucleate boiling, critical heat flux, transition boiling, and film boiling—may be experienced by the conductor/fluid interface in a relatively small locality. If this behavior is all captured by one large

conductor mesh cell as a single averaged heat flux, then the temperature through the conductor will not be correctly resolved. This is not only nonphysical, but it will also result in stepwise cell-by-cell quenching and will produce flow oscillations that will prevent the correct hydrodynamic solution from being obtained.

To remedy this problem, the capability to remesh the conductor in this vicinity has been implemented into CTF. Superimposing a finer mesh into the once coarse mesh of the quench front region allows the conductor temperature profile to be correctly resolved. The heat flux is solved for each refined conductor cell. The heat flux is then integrated over the refined cells to obtain the correct cell-averaged value to be applied to the adjacent fluid continuity mesh cell.

The initial meshing procedure in CTF for conductors is to create an axial conductor mesh cell for each adjacent axial fluid continuity mesh cell. An example is shown in Figure 21.

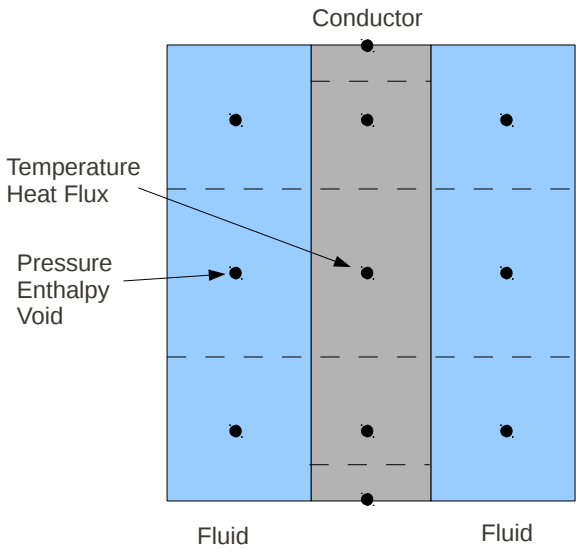

Figure 21. Example of how a conductor is meshed based on adjoining fluid mesh.

The conductor temperature and heat flux are calculated at the mesh cell center, indicated in Figure 21 by black dots, just as the fluid pressure, enthalpy, and void fraction are solved at the cell centers. The axial lengths of the conductor and fluid cells are the same, and the axial nodal locations of the conductor and fluid cells match up after the initial meshing. The exception is for the top and bottom of the conductor, where an extra conductor node is inserted. For the bottom conductor mesh cells, the cell height is 25% of the adjacent fluid cell height—the cell height of the conductor mesh cell directly above the bottom cell is 75%. In this manner, the top boundary of the second conductor mesh cell still meets with the boundary of the adjacent fluid mesh cell. Also, the second node is still at the same axial location as the adjacent fluid node. The meshing is performed in the same manner for the top conductor mesh cell.

When it is determined that remeshing is necessary because of the criteria discussed below, a node is simply inserted halfway between pre-existing axial conductor nodes. This is shown in Figure 22 for the case of the first and second axial conductor cells, which are 25% and 75% the height of the adjacent fluid cell, respectively.

When a cell is inserted, it is necessary to assign a temperature to that node. This must be done using an energy balance to ensure that energy is conserved in the conductor. This is shown as follows:

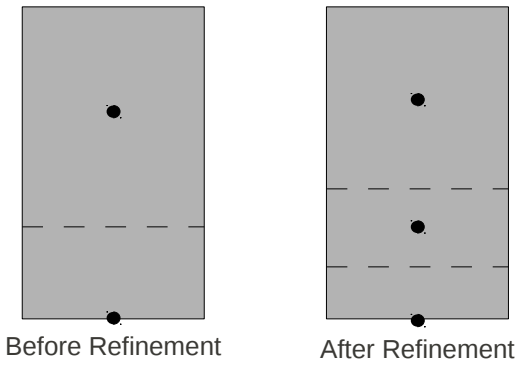

Figure 22. Example of conductor mesh cell refinement for the first and second cells of a conductor.

$$\mathrm{Cp}_1 \left(T_1 - T_I\right) \frac{\Delta X}{2} + \mathrm{Cp}_2 \left(T_2 - T_I\right) \frac{\Delta X}{2} = 0 \tag{420}$$

$$T_I = \frac{(\mathrm{Cp}T)_1 + (\mathrm{Cp}T)_2}{(\mathrm{Cp}_1 + \mathrm{Cp}_2)}$$

The subscripts 1 and 2 represent the original first and second cell values, and the subscript I represents the new inserted cell value. The benefit of the remeshing procedure in CTF is that, not only does the code watch for zones that must be refined because heat flux and temperature excursions, but it also watches for zones that can be coarsened when the quench front passes to other regions. If the mesh in a region has been refined, then merging criteria will also be evaluated for that region to determine when it is acceptable to coalesce the mesh cells back to form a coarser mesh. If the quench front no longer exists in a region that was refined, then the mesh will eventually return to the original mesh that existed prior to refinement. This provides a benefit in computational resources.

The QFRONT subroutine is responsible for determining if a conductor cell should be split or if an already-split cell should be coalesced. The QFRONT subroutine is called at the beginning of the HEAT subroutine prior to the determination of the heat transfer regime and associated heat transfer coefficients. QFRONT is called if there are any conductors being modeled by CTF. The QFRONT routine loops over all the rods in the model. For each rod, it then loops over each axial level of fluid cells adjacent the rod. For each axial fluid cell level, the routine loops over each conductor cell that is located within the bounds of the bottom and top of the adjacent fluid cell axial level (recall from Figures 21 and 22 that the boundaries of fluid cells always meet with conductor cell boundaries and that multiple conductor cells may exist for a single adjacent fluid cell). Finally, for each axial level of conductor cells in the rod, the routine loops over each surface of the rod.

It is within this loop that the routine checks criteria to determine whether to remesh or not. In this way, every surface cell of the rod is checked, and axial remeshing is performed when needed. QFRONT will then call the MOVE subroutine to perform the actual remeshing process if it is deemed necessary for any surface in a given axial level of conductor cells. The criteria used to determine whether to split or merge refined cells are discussed in the following section.

10.3.1 Remeshing Criteria

The decision on whether a conductor cell should be split, coalesced with its neighbor cells, or left alone is a rather complicated one in CTF. Put most basically, the decision whether to remesh or not will be based on the following:

- Axial temperature gradient
- Local behavior of the heat transfer regimes
- Pre-quench heat transfer differences in the axial direction

To best describe this procedure in as much detail as possible, initially, a flowchart of the decision process is presented in all of its complexity. Next, each step of the procedure is described, discussing the meaning of the terms and the condition being evaluated. The procedure is roughly divided into two sections: assessing whether to coalesce the mesh, and assessing whether to split (refine) the mesh. The flowchart blocks have been given unique identification numbers to make referencing easier. Figure 23 presents the CTF procedure for deciding what to do with a conductor cell.

Before discussing the criteria, it is first important to note that for the case of mesh refinement, the key interest is on two conductor nodes. If certain criteria are not met (e.g., temperature and heat flux differences between those two conductor nodes are too high), then the two cells will be split into three by inserting a node between them. When considering whether to coalesce a cell (i.e., eliminate it), the focus is on three conductor nodes. If certain criteria are met (e.g., temperature differences between the first and third cells are not too high), then the second conductor mesh cell may be eliminated and absorbed back into mesh cells 1 and 3.

10.3.1.1 Coalescence Criteria

Starting with Block 100, the first step is to check whether ΔX, the conductor mesh cell axial height, is less than the user-specified minimum allowable conductor node size, ΔX_{min}. The mesh cell will not be split any further if this is the case. Likewise, if the total number of axial heat conductor nodes in a rod exceeds the limit of 72 (Block 101), the conductor node will not be further split. Furthermore, the mesh cell will not be further split if the heat transfer regime (*imode*) is either single-phase vapor or single-phase liquid (Block 103). If any of these three blocks evaluate to true, then CTF will check whether the mesh cell should be coalesced or left alone.

Block 500 asks the question, is the conductor mesh cell (*jr1*) communicating with the same fluid cell that it was before remeshing was performed (*jf* or jf_{+1})? If it is, then that means that the conductor mesh cell is the same as the original configuration and that no coalescence is needed, so the mesh cell is left alone. If not, Block 501 checks to determine if the last axial conductor node in the rod, *nhtn*, has been reached. If so, the analysis moves on to the next conductor, the current conductor is completed, and no further checks are made on whether any conductor mesh cell in the current conductor should be split, merged, or left alone.

Following from this point (Block 502), a mesh cell will be coalesced into the conductor cells above and below if (1) the heat transfer regime is either subcooled boiling or nucleate boiling and (2) if the resulting temperature difference between axial cells after merging takes place is small enough. For the first point, it is important to note that the *imode* definition of Block 502 differs from that of Blocks 102, 103, and 300. In Block 502, *imode* is the minimum of the heat transfer regime indices of conductor mesh cells 1 and 3 as opposed to mesh cells 1 and 2.

As for Block 600, the meaning of the terms present are defined. During this remeshing process, three conductor are being analyzed nodes: mesh cell 2 would be the inserted node (if remeshing previously took

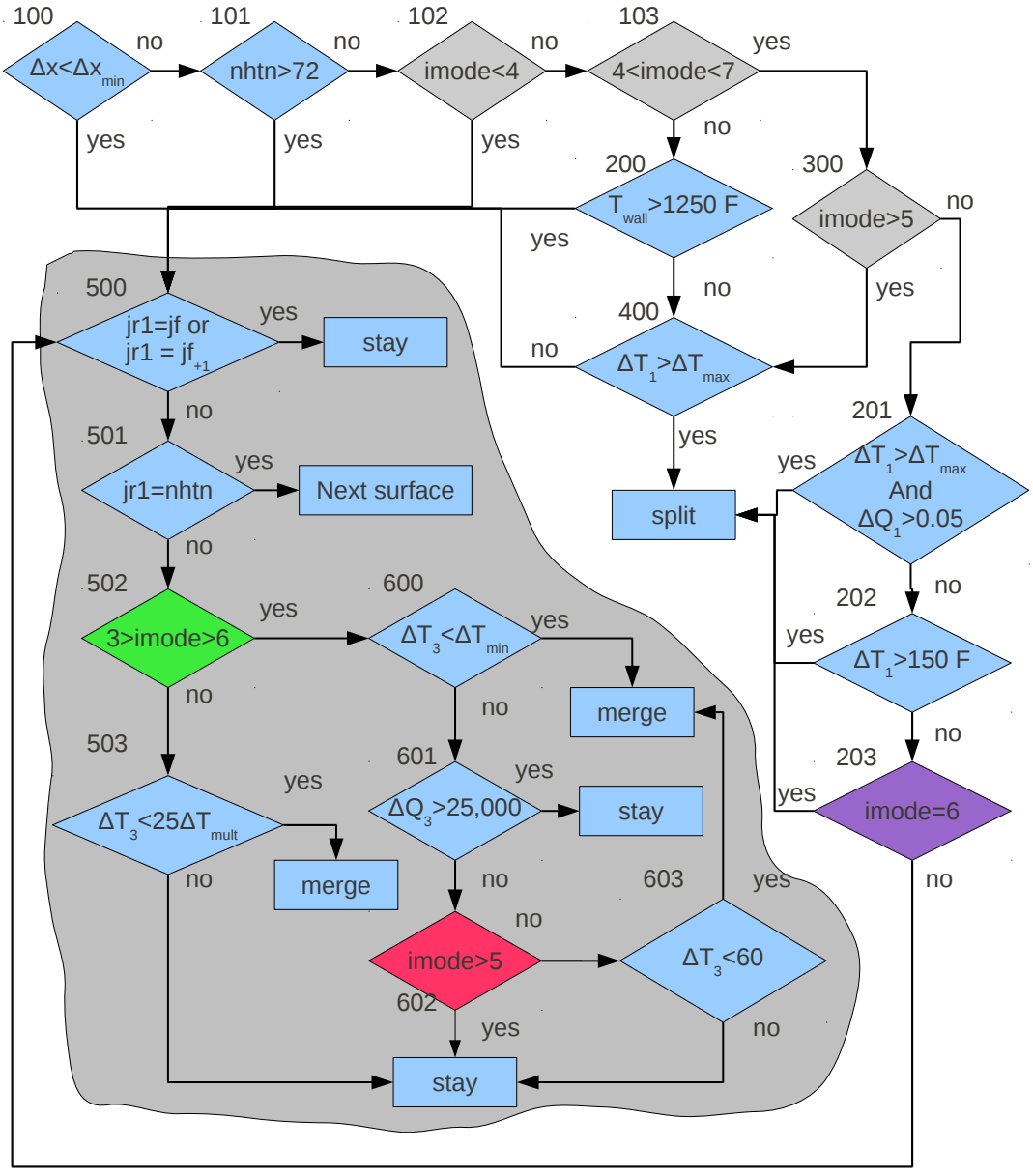

Figure 23. CTF procedure for determining whether conductor cells should be split, merged, or left alone.

place), mesh cell 1 would be the cell below the inserted node, and mesh cell 3 would be the cell above the inserted node. If the inserted node is coalesced, then mesh cells 1 and 3 grow and take its place. Therefore, ΔT_3 is defined in such a way that it captures the amount of temperature change over these three conductor cells. In equation form:

$$\Delta T_3 = |T_2 - T_1| + |T_2 - T_3| \,. \tag{421}$$

$\Delta T_{\min}$ is the minimum temperature difference between conductor cells which will allow for their merging. This value is defined as a function of the rod surface temperature factor, $T_{w,\text{chf}}$.

$$\Delta T_{\min} = \text{dtmult}\left[2 + \frac{1}{2} T_{w,\text{chf}}^2 * 15\right] \tag{422}$$

dtmult is a multiplication factor that is set to 1 unless dealing with the top-most conductor cell that connects to the current fluid cell under analysis. In that case, the multiplier is set to 0.5 to cut the minimum temperature difference for coalescence in half. The criterion becomes more stringent because the conductor cells communicate with more than one fluid mesh cell in this case. $T_{w,\text{chf}}$ is a factor between 0 and 1 that captures how close to CHF the surface temperature is. The surface temperatures close to the CHF temperature will produce a value near or equal to zero, and surface temperatures far from the CHF temperature will produce values near or equal to 1. The factor is calculated by choosing the highest surface temperature, T_w, of the three conductor cells under analysis. Then the following calculation is performed:

$$T_{w,\text{chf}} = \max\left(0, \min\left[1, \frac{T_{\text{chf}} - T_w}{\max\left(T_{\text{chf}} - T_f, 5\right)}\right]\right) \tag{423}$$

If the surface temperature is close to CHF, then the allowable axial temperature difference will correspondingly also need to be small. However, for surface temperatures much smaller than CHF temperature, larger axial temperature differences are allowable. Barring a failure of Block 600 to be satisfied, there are still other means by which the inserted cell could be coalesced.

As shown in Block 601, having too large of a difference in heat flux requires the inserted cell to be left alone. If the difference in heat flux, ΔQ_3, in the region of the three conductor cells being analyzed is greater than $25,000\ \text{BTU/ft}^2\text{·hr}$, then the conductor is not coalesced but is left alone. ΔQ_3 is defined as ΔT_3 was defined in Eq. (421) to capture the changes in heat flux over all three conductor cells.

If the heat flux change in the three cells is small enough, Block 602 will be evaluated. If the heat transfer regime is either film boiling or dispersed flow boiling, it is necessary to keep the inserted node. Note again that the definition of *imode* in Block 602 differs from all the other *imode* definitions in that it is the maximum of the indices of all three conductor nodes. Therefore, any of three conductor nodes may be in the transition or film boiling regime for the inserted cell to be left alone. Otherwise, there is one last criterion to check in Block 603. If the temperature change across the three conductor cells is less than 60 °F, then the inserted cell can be coalesced, but if not, it must be left alone.

One remaining section of this portion of the flowchart that was neglected: Block 502 evaluated the heat transfer regime. If the heat transfer regime were either nucleate boiling or saturated boiling, then evaluation of Block 600 commenced. However, if the regime were not nucleate boiling or saturated boiling, then CTF would check whether the temperature difference in the three conductor cells is less than 25 °F (Block 503). If this is true, then the inserted cell can be coalesced, and if not, it must be left alone. This criterion is tightened to 12.4 °F if the conductor cells communicate with more than one fluid mesh cell.

This portion of the flowchart discussed to this point covers all the criteria evaluated to determine if it is possible to coalesce the inserted cell. This is outlined in the gray section of Figure 23.

10.3.1.2 Splitting Criteria

To cover the remainder of the flowchart, attention is now directed to Block 103, having just established that the heat transfer regime is not single-phase vapor or liquid. At this point, *imode* was defined as the minimum of the heat transfer regime numbers for conductor mesh cells 1 and 2. Therefore, if Block 103 evaluates to false, then both conductor cells are experiencing some sort of film boiling. CTF checks whether the surface temperature of both mesh cells 1 and 2 exceed 1250 °F. If they do, then the inserted cell should be considered for coalescence. If one of these wall temperatures is less than this limit, then the temperature difference between Cells 1 and 2 are compared to the maximum allowable temperature difference. If this value is exceeded, then another cell must be inserted between the two to further refine the mesh. Otherwise, the inserted cell may be considered for coalescence. The maximum allowable temperature difference between cells is calculated as follows:

$$\Delta T_{\max} = 25\,^{\circ}\mathrm{F} + \mathrm{dtwall} * 150\,^{\circ}\mathrm{F}, \quad \text{where} \tag{424a}$$

$$\mathrm{dtwall} = \frac{1}{2}\left(1 + \min\left[1, \max\left(0, \frac{T_w - T_{\min}}{1250\,^{\circ}\mathrm{F} - T_{\min}}\right)\right]\right) \tag{424b}$$

This indicates that the higher the surface temperature in the film boiling regime, the larger the maximum allowable temperature difference will be.

Returning to Block 103, if the heat transfer regime is nucleate boiling or transition boiling, Block 300 is evaluated. If the heat transfer regime is transition boiling in one of the conductor cells, then the conductor cell temperature difference will be compared to the maximum allowable temperature difference (previously defined). Otherwise, the conductor cell temperature difference will still be compared to the maximum allowable temperature difference, but the heat flux difference between the two cells will also be limited. If the heat flux difference is greater than $50,000\,\mathrm{BTU/ft^2 \cdot hr}$, then the mesh will be further refined.

Otherwise, Block 202 is evaluated where the mesh cell 1 and 2 temperature difference is compared to an upper limit of 150 °F. If that evaluation does not result in a mesh cell refinement, then a final criterion is checked. Block 203 redefines the *imode* term to represent the heat transfer regime of the *other* conductor mesh cell. In other words, Block 203 asks if *both* conductor mesh cells are experiencing transition boiling. If they are, then the mesh is refined, and if not, then the mesh can be considered for coalescence.

11. NUCLEAR FUEL ROD MODELS

CTF includes a package of special models for simulating the heat transfer behavior in nuclear fuel rods. Whereas Chapter 10 discusses the general governing equations solved for the supported solid geometries, this chapter focuses on the closure models specific to nuclear fuel rod geometry and behavior needed to define source terms in those equations (e.g., gap heat transfer behavior). The nuclear fuel rod model is suited specifically for UO_2/MOX fuel and Zircaloy cladding. Fill gases composed of helium, xenon, argon, krypton, hydrogen, and nitrogen are accommodated. Material properties such as the conductivity and specific heat of the aforementioned metals and gases were taken from the MATPRO-11 handbook[75].

For a nuclear fuel rod with ceramic fuel pellets encased in a Zircaloy cladding, three regions are considered to be modeled:

1. The metal cladding with the Zircaloy cladding properties (Section 10.2)
2. The gap between the cladding and the fuel pellet. Thin gap approximation is such that convection heat transfer can be neglected, so conduction through the fill gas and radiative heat transfer between the pellet and cladding are modeled (Sections 11.2.1 and 11.2.3).
3. The fuel pellet. Under thermal treatments, the fuel pellets can expand/contract and may lead to possible contact between the pellet and cladding (Section 11.2.2). The change in fuel pellet dimensions has an effect on the gap size and gap heat transfer (Section 11.1).

The following sections discuss this modeling process in detail. Determination of the gap thickness accounting for thermal expansion and pellet cracking is achieved with the fuel deformation model (Section 11.1). After this, the dynamic gap conductance model is discussed. There are three components of gap conductance: conduction through the gas (Section 11.2.1), radiative heat transfer (Section 11.2.3), and conduction through the pellet/clad interface (if contact exists) (Section 11.2.2). Finally, it has been mentioned that CTF also models heat generation in the cladding from possible zirconium-water reaction (Section 11.3).

11.1 FUEL DEFORMATION MODEL

The fuel deformation model is encountered after the conductivity and specific heat material properties are defined for the pellet and cladding. Temperature-driven expansion/contraction drives fuel rod deformation. Thermal expansion can directly cause fuel pellet and cladding geometry changes. Thermal expansion of the fuel pellet could also indirectly cause cladding deformation through mechanical stresses if the pellet and cladding come in contact (i.e., the expanding pellet could push on the cladding). The fuel pellet may also crack from thermal expansion, which will cause relocation of the fuel inside the rod. This will in turn cause a change in fuel pellet conductivity, as well as fuel pellet geometry. This can impact the thermal conductivity of the material (now partially a gas), as well as the pellet size. This section describes all models that capture physical effects that result in a change in the pellet/clad/gap dimensions.

For an open gap (i.e., no pellet/clad contact), mechanical stress may be imposed on the cladding because of an imbalance between rod fill gas pressure and system operating pressure. For a closed gap in which the pellet and clad are in contact, expansion of the fuel pellet may impose a mechanical stress on the cladding. Other stresses and strains due to bending forces and creep deformation are ignored. The phenomena affecting the gap thickness include: pellet thermal expansion $(\Delta r_{th})_{fuel}$, fuel relocation due to cracking $(\Delta r_{rel})_{fuel}$, fuel burnup-induced swelling $(\Delta r_{sw}))_{fuel}$, clad thermal expansion $(\Delta r_{th})_{clad}$, clad burnup-induced creep $(\Delta r_{cr})_{clad}$, and clad elastic expansion $(\Delta r_{el})_{clad}$. Models for calculation of each of these individual components are further described in the following sections. The components of the dynamic gap thickness,

δ, can be summarized into a single equation as follows. Note that all terms are denoted as being added to the initial gap thickness, but naturally, several of these terms will act to reduce the gap thickness and therefore will have a negative sign when calculated in CTF.

$$\delta = \delta_0 + (\Delta r_{\text{th}})_{\text{fuel}} + (\Delta r_{\text{sw}})_{\text{fuel}} + (\Delta r_{\text{rel}})_{\text{fuel}} + (\Delta r_{\text{th}})_{\text{clad}} + (\Delta r_{\text{el}})_{\text{clad}} + (\Delta r_{\text{cr}})_{\text{clad}} + \tag{425}$$

11.1.1 Fuel and Clad Thermal Expansion

The fuel pellet radial and axial thermal expansion are calculated using a thermal expansion coefficient (α) and the temperature gradient that drives the expansion (ΔT), as shown in the following equation.

$$\epsilon = \alpha \Delta T \tag{426}$$

A constant value of 1×10^{-5} m m^{-1} K^{-1} is used for α. The temperature gradient ΔT is the difference between the current and previous timestep temperatures. For the fuel pellet, the temperature used is the average of the centerline and surface temperature.

The cladding expansion is similarly calculated using the average clad temperature (average of inner and outer surface temperatures). However, separate strain correlations exist for the axial and radial directions for Zircaloy (Section 15.2).

11.1.2 Fuel Pellet Relocation

The fuel pellet may also crack, causing it to creep further into the pellet/clad gap and to even contact the clad. The relocation model to account for this cracking-induced movement of the fuel pellet is the FRACAS-I mechanics model[76]. The amount of pellet relocation in an open gap is expressed as a function of cold-state rod geometry by Coleman[77].

$$(\Delta r_{\text{rel}})_{\text{fuel}} = \delta_0 - 0.005 r_f, \tag{427}$$

where dimensions are in feet, δ_0 is the as-fabricated fuel/clad gap size, and r_f is the cold-state radius of the fuel pellet. Δr is the amount by which the fuel pellet radius changes, which will remain constant as long as the gap remains open (i.e., no pellet/clad contact). The gap is considered to be closed when the gap thickness decreases to less than 1.8 (or user-provided value for factor_gapcriterion) times the sum of the clad and pellet surface roughness. If the gap is closed, then fuel relocation is modified to be large enough to keep the gap closed: fuel relocation will not cause mechanical expansion of the cladding. This is written in CTF as follows:

$$(\Delta r_{\text{rel}})_{\text{fuel}} = \max\left[0, \delta - 1.8(\epsilon_{\text{fuel}} + \epsilon_{\text{clad}}) + (\Delta r_{\text{rel}})_{\text{fuel}}\right], \tag{428}$$

where ϵ_{fuel} and ϵ_{clad} represent the pellet and clad surface roughnesses in feet, respectively. The expression ensures that the amount of pellet relocation caused by cracking is no bigger than the gap thickness.

11.1.3 Cladding Elastic Deformation

The cause of cladding elastic deformation depends on the state of the gap. If the gap is open, then cladding stresses will be caused by a differential in fill gas pressure and reactor system pressure. If the gap is closed, then cladding stresses will be caused by fuel pellet thermal expansion. For both cases, the cladding is assumed to be sufficiently thin so that stress, strain, and temperature can be considered uniform throughout the cladding thickness.

The concept for either an open or closed gap is to calculate the clad stress and to use Hook's Law to obtain the radial displacement of the cladding. The hoop stress σ_θ and axial stress σ_Z that exist in the cladding—both of which are functions of the cladding inside and outside pressure—are defined as follows:

$$\sigma_\theta = \frac{r_i P_i - r_o P_o}{t_c}, \tag{429}$$

and

$$\sigma_Z = \frac{\pi r_i^2 P_i - \pi r_o^2 P_o}{\pi \left(r_o^2 - r_i^2\right)}. \tag{430}$$

The i and o subscripts represent the inner and outer faces of the cladding, and the cladding thickness, t_c, accounts for changes in cladding dimensions caused by expansion. With the hoop and axial stresses calculated, it is possible to use Hook's law to convert these values to cladding displacement using Young's modulus and the shear modulus (see Section 15.2).

$$\epsilon_\theta = \frac{\Delta r}{\bar{r}} = \frac{1}{E}\left(\sigma_\theta - \nu\sigma_Z\right) \tag{431}$$

$$\epsilon_Z = \frac{\Delta l}{l} = \frac{1}{E}\left(\sigma_Z - \nu\sigma_\theta\right) \tag{432}$$

The radial deformation of the cladding can simply be calculated by multiplying the mean cladding radius, $\bar{r}$, by hoop strain.

$$\left(\Delta r_{\text{el}}\right)_{\text{clad}} = \epsilon_\theta \bar{r} \tag{433}$$

The axial deformation is calculated by summing the axial expansion of each control volume in the axial direction.

$$\left(\Delta l_{\text{el}}\right)_{\text{clad}} = \Sigma_{j=1}^{\text{NDX}} \epsilon_Z \Delta X_j \tag{434}$$

The distinction between cladding deformation caused by an open gap and a closed gap lies in the cladding interior pressure used to calculate the cladding stresses in Eqs. (429) and (430). For an open gap, the fill gas pressure, P_g, is substituted for P_i. The fill gas pressure is from the previous time step, because fill gas pressure is calculated at the end of the deformation model. It is calculated using a static lumped pressure model similar to those in FRAP and GAPCON. The pressure is assumed to be uniform throughout the fuel pin with constant fission gas inventory.

$$P_g = \frac{MR}{\frac{V_p}{T_p} + \Sigma_{j=1}^{NDX} \pi \Delta X_j \left[\frac{\left(r_{ci}^2 - r_{fo}^2\right)}{T_g} + \frac{r_v^2}{T_v} + \frac{\left(r_{fo}^2 - r_f^2\right)}{T_F} \right]_j} \tag{435}$$

Terms are defined as follows:

M = gram-moles of gas in the fuel rod
R = universal gas constant (6.1313 $^{\text{ft·lbf}}/_{\text{g·mole·K}}$)
V_p = gas plenum volume (ft^3) with expansion effects included
T_p = gas plenum temperature (°K) (defined as the outlet fluid temperature plus 10 °K)
ΔX_j = computational cell height at axial level j (ft)
r_{ci} = cladding inside radius (ft) including expansion effects
r_{fo} = fuel outside radius (ft) including thermal expansion and relocation effects
r_f = fuel outside radius (ft) considering thermal expansion only
r_v = radius of the central void in the fuel (ft) (given by user input)
T_g = gas gap temperature (°K)
T_v = temperature of the fuel central void (°K)
T_f = average fuel pellet temperature (°K)

For the closed gap scenario, the interface pressure P_{int} is used as the inner clad surface pressure in Eqs. (429) and (430). The interface pressure is caused by radial displacement of the fuel from thermal expansion, which in turn causes radial displacement of the cladding. The cladding radial displacement is a combination of fuel rod thermal expansion, relocation, and cladding thermal expansion. Cladding radial displacement is defined as

$$\Delta r_{\text{clad}} = 1.8\left(\epsilon_{\text{fuel}} + \epsilon_{\text{clad}}\right) - \delta_0 + (\Delta r_{\text{th}})_{\text{fuel}} - (\Delta r_{\text{th}})_{\text{clad}} + (\Delta r_{\text{rel}})_{\text{fuel}}. \tag{436}$$

The first term on the RHS defines the closed gap width accounting for the surface roughness of the cladding and fuel. Followed by this term are the cold-state gap width, fuel thermal expansion, cladding thermal expansion, and fuel relocation caused by cracking. This amount of cladding displacement can be substituted into the hoop strain equation—Eq. (431)—which is the function of the hoop stress σ_θ and axial stress σ_Z. The stress terms are functions of the interior pressure, P_i which is actually the interface pressure, P_{int}. Consequently, a single equation can be formed for interface pressure as

$$P_{\text{int}} = \frac{\Delta r_{\text{clad}} E t_c \left(r_o^2 - r_i^2\right)}{\bar{r}\left[r_i\left(r_o^2 - r_i^2\right) - r_i^2 t_c \nu\right]} + P_o \frac{r_o\left(r_o^2 - r_i^2\right) - r_o^2 t_c \nu}{r_i\left(r_o^2 - r_i^2\right) - r_i^2 t_c \nu}. \tag{437}$$

Note that cladding dimensions do not account for any previously calculated elastic and thermal expansion.

Table 5. Constants for the ESCORE creep model.

A	Value	B	Value
1	$1.388{\cdot}10^{8}$	1	$2.35{\cdot}10^{-21}$
2	$3.29{\cdot}10^{-5}$	2	0.811
3	2.28	3	0.595
4	0.997	4	1.352
5	0.770	5	22.91
6	0.956	6	1.58
7	$23{\cdot}10^{3}$	7	2.228

11.1.4 Clad Creep

The cladding is known to "creep down" (diameter reduced) because of the thermal and irradiation exposure in a reactor environment. For Zircaloy cladding, the Hoppe model can be used to calculate the irradiation-induced creep strain rate, and the Hays model can be used to calculate the thermal creep rate. The details of these two models can be found in Hales [78]. Both models are adopted in CTF. The ESCORE creep model [79] is also adopted as an option, as shown in Eqs. 438 and 439, for thermal and irradiation-driven creep, respectively.

$$\epsilon^{c}_{\text{th}} = A_1\left[\sinh\left(A_2\sigma_\theta^{A_3}\right)\right]^{A_4} t^{A_5}\sigma^{A_6}_{\text{yield}}\exp\left(\frac{-A_7}{T}\right) \tag{438}$$

$$\epsilon^{c}_{\text{ir}} = B_1 t^{B_2}\Phi^{B_3}\sigma_\theta^{B_4}\left[\exp\left(\frac{-B_5}{T}\right)\right]\sigma^{B_6}_{\text{yield}}\left[\cos\left(\theta_{\text{max}}\right)\right]B_7 \tag{439}$$

In these equations, ϵ is the diametral strain in m/m, t is the time of exposure in hr, Φ is the fast neutron flux (energy greater than 1 MeV) in n/cm^2-s, σ_θ is the midwall hoop stress in MPa, T is the cladding temperature in K, σ_{yield} is the cladding yield strength at room temperature in MPa, and $cos(\theta_{\text{max}})$ is the Cosine of the angle of maximum intensity of basal pole or radial direction normal to the axial direction. Cladding yield strength is set to 370 MPa and θ_{max} to 30° according to Franklin [80]. The A and B values are constants, the values of which are summarized in Table 5.

As shown, both thermal creep and irradiation creep are nonlinear functions of hoop stress, irradiation time, and temperature. Irradiation creep is also a function of fast neutron flux. Given that all these four variables usually change at each time step because of the changes in operation conditions of the clad, when using the integral forms directly, one has to assume these variables to be constant, which can cause large discrepancies in the calculated creep strains. These models have been implemented to consider accumulation of creep strain in each time step. Time derivatives were taken of both equations, and the incremental creep strains of each time step are calculated in CTF using the time derivatives.

11.1.5 Fuel swelling

Fuel is known to swell under irradiation as a result of accumulations of both solid and gaseous fission products. For the solid fission product swelling, the MATPRO correlation [81], a linear function of burnup, is implemented in CTF. The FRAPCON swelling model [82] was adopted in CTF with modifications for gaseous fission product swelling. It was found that close agreements in temperature results were observed when the FRAPCON model used in CTF was compared to the physics-based Simple Integrated Fission Gas Release and Swelling (SIFGRS) model [83]. For the modified FRAPCON model in CTF, the multiplier

to the swelling strain was changed from a step function to a linear function of burnup until it reached 40 GWd/MTU.

Before the modification, the multiplier was set to zero when burnup is less than 40 GWd/MTU and to a linear function of burnup for burnup between 40 and 50 GWd/MTU and then 1.0 for burnups greater than 50 GWd/MTU. After the modification, the multiplier was set to a linear function of burnup for burnups less than 40 GWd/MTU and then 1.0 for burnups greater than 40 GWd/MTU. This modification helps CTF avoid an abrupt change in temperature results when burnup approaches 40 GWd/MTU and produces close temperature results to BISON, as is shown in Hu [83].

The MATPRO gaseous fission product swelling model is shown in Eq. (440), and this formula calculates the incremental swelling strain at a given burnup step. Given that current infrastructure in CTF does not allow accumulation of the swelling strains, this formula was integrated over burnup before being used in CTF. When using the integrated formula, one has to assume a constant temperature, which introduces an error in the calculation. Thus an empirical multiplier was introduced to adjust the swelling strain in CTF for this MATPRO model. This multiplier was adjusted to a value of 0.45, which was found to produce close agreement with BISON [83]. Such adjustment can be eliminated when infrastructure in CTF is put in place in the future to allow for accumulation of gaseous fission product swelling over burnup steps.

$$\Delta\epsilon_{\mathrm{sw-g}} = 1.96e-31\rho\Delta\mathrm{Bu}\,(2800-T)^{1}\,1.73\exp\left(-0.0162(2800-T)\right)\exp\left(-0.0178\rho\mathrm{Bu}\right) \tag{440}$$

11.1.6 Fuel Pellet Cracking and Sintering Effect on Conductivity

When the fuel pellet expands and cracks, the conductivity is reduced as a result of the lower conductivity rod fill gas replacing the fuel pellet material in the cracks. An example of a cracked fuel pellet is shown in Figure 24.

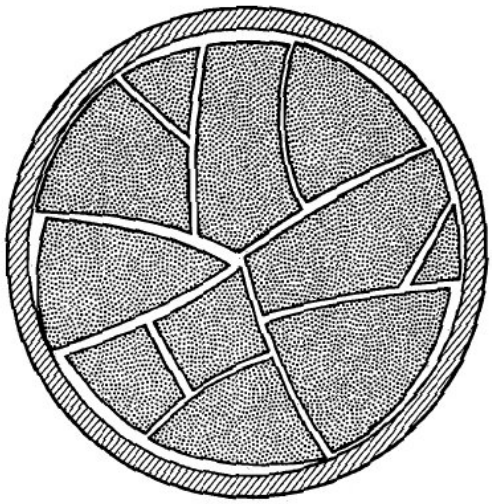

Figure 24. Illustration of fuel pellet cracking.

The method for accounting for fuel thermal conductivity degradation was taken from the FRACAS-I mechanics model[76]. The conductivity is changed by multiplication by a conductivity factor, R.

$$K_{\mathrm{eff}} = RK_{\mathrm{lab}} \tag{441}$$

The new cracked fuel thermal conductivity, K_{eff}, is obtained by multiplying the conductivity factor by the uncracked fuel thermal conductivity, K_{lab}. The conductivity factor is a function of the gas conductivity and the volume available for cracking, which is given by

$$R = 1 - 0.3\,\text{m}^{-1} C_{\text{rel}} \left[1 - \frac{k_g}{k_{\text{lab}}} \right]. \tag{442}$$

The term C_{rel} represents the volume available for cracking. It is the initial gap thickness, δ_0, divided by $0.8{\cdot}10^{-4}$. Because cracked fuel will never fully solidify when compressed, C_{rel} will never be less than 0.25. The gas mixture conductivity, k_{g}, is determined as discussed in Section 11.2.1. The uncracked fuel pellet conductivity, k_{lab}, is obtained from the UO_2/MOX thermal conductivity correlation (see Section 15.1).

Crack healing is assumed to occur as the fuel temperature approaches the sintering temperature for UO_2. The conductivity factor R is set to 1 when the fuel temperature exceeds 4,304 °F, which is nine-tenths of the UO_2 sintering temperature.

11.2 DYNAMIC GAP CONDUCTANCE MODEL

The gap conductance (or total conductance across the gap) is defined in the dynamic gap conductance model as

$$H_{gap} = H_{gas} + H_{contact} + H_{rad}, \tag{443}$$

in which the conduction in the gap is composed of three components: conduction through the fill gas H_{gas}, solid-solid contact conductance H_{solid}, and radiative heat transfer in the gap H_{rad}. It is assumed that the gap between the fuel rod and the cladding is thin enough so that there is no convection heat transfer caused by the gas; therefore, conduction heat transfer will be dominant heat transfer.

11.2.1 Conduction Through the Fill Gas in the Gap

Conduction heat transfer through the fill gas will exist whether the gap is open or closed as a result of fuel expansion, but the calculation of heat conduction in the fill gas in a closed gap is slightly different than for that of an open gap. The model used for calculating gap fill gas heat conduction was taken from GAPCON-2, which was based on a linear regression analysis of Ross-Stoude data by Lanning and Hann[84]. For either case, the heat conduction is defined as the gas mixture conductivity divided by the gap thickness.

$$H_{\text{gas}} = \frac{k_{\text{gas}}}{\delta_{\text{gas}}} \tag{444}$$

However, the gap thickness accounts for the fact that the temperature gradient in the fill gas is not linear. Instead, there is a jump in temperature near the pellet and clad surface as a result of incomplete thermal mixing of the gas molecules in that localized region. This concept is illustrated in Figure 25. To account for this discontinuity, a temperature jump distance is added to the physical gap thickness. Accounting for the temperature jump distances, g_1 and g_2, the heat conduction is defined as

$$H_{\text{gas}} = \frac{k_{\text{gas}}}{t_g + 1.845\,(g_1 + g_2)}, \tag{445}$$

where the gas conductivity is given in units of $^{\text{BTU}}/_{\text{hr·ft·F}}$, and the physical gap thickness, t_g, and jump distance units are in feet.

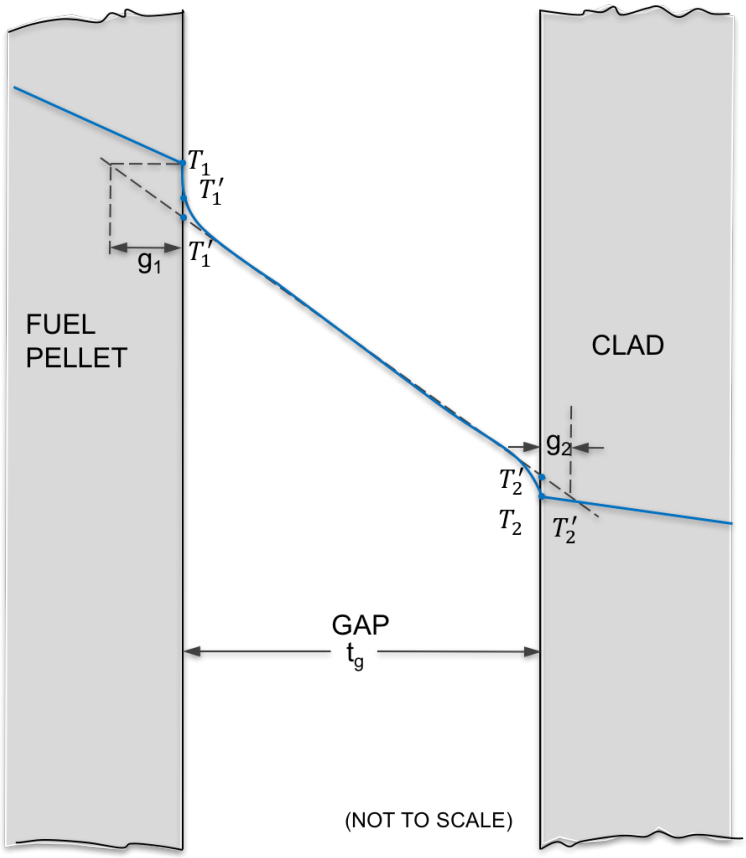

Figure 25. Illustration of the temperature jump near fuel pellet and clad surfaces in a fuel rod gap.

For a closed gap, there are still regions of fill gas where conduction occurs because of the surface roughness of the pellet and clad. A gap is considered closed when the gap thickness is less than 1.8 times the sum of the surface roughnesses. The gap thickness for a closed gap is taken as half of this value times a modification factor that accounts for the contact pressure between cladding and gap, which was previously defined in Section 11.1. The jump distances in the gap are still considered. Equation (444), for a closed gap, is written as follows:

$$H_{\text{gas}} = \frac{k_{\text{gas}}}{1.8\left(C\left(R_1 + R_2\right) + \left(g_1 + g_2\right)\right) - 4.2 \cdot 10^{-7}}. \tag{446}$$

The surface roughness of fuel and clad are given by R_1 and R_2 in feet. For numerical stability, a lower limit of $1{\cdot}10^{-6}$ is imposed for the denominator. The dimensionless modification factor that accounts for interface pressure, P_{int}, is given as C in the above equation. It is defined as

$$C = 1.98 \exp -8.8 \cdot 10^{-5} P_{\text{int}}. \tag{447}$$

For the open and closed gap models, it is necessary to define the gap gas conductivity and the surface temperature jump distances, which appear in the above heat conduction equations.

11.2.1.1 Fill Gas Thermal Conductivity

The thermal conductivity for a mixture of gases is calculated considering the individual gas conductivities (see Section 15.3), as well as their molecular weights and mole fractions. The gas mixture thermal conductivity (BTU/hr-ft-F) is

$$\begin{aligned}
k_{\text{gas}} &= \Sigma_{i=1}^{N} \frac{k_i}{1 + \sum\limits_{\substack{j=1 \\ i \neq j}}^{N} \Psi_{ij} \frac{X_j}{X_i}} \\
\Psi_{ij} &= \phi_{ij} \left(1 + 2.41 \frac{\left(M_i - M_j\right)\left(M_i - 0.142 M_j\right)}{\left(M_i + M_j\right)^2} \right), \\
\phi_{ij} &= \frac{\left[1 + \left(\frac{k_i}{k_j} \right)^{1/2} \left(\frac{M_i}{M_j} \right)^{1/4} \right]^2}{2^{3/2} \left(1 + \frac{M_i}{M_j} \right)^{1/2}},
\end{aligned} \tag{448}$$

where the summations are performed over all gases in the mixture, where N is the total number of gases (maximum of 6). X and M are the mole fraction and molecular weights of gases, respectively.

11.2.1.2 Temperature Jump Distance

The temperature jump distance is calculated from the GAPCON-2 modification of the Lloyd model[85] and is used in CTF as

$$(g_1 + g_2) = 2.0358 \cdot 10^{-5} \frac{k_{\text{gas}} \sqrt{\bar{T}_{\text{gas}}}}{P_{\text{gas}} \Sigma_{j=1}^{N} \frac{a_j f_f}{\sqrt{M_j}}}, \tag{449}$$

where k_{gas} is fill gas thermal conductivity ($^{\text{BTU}}/_{\text{hr - ft - F}}$), $\bar{T}_{gas}$ is mean gas gap temperature (°K), and P_{gas} is the fill gas pressure (psia); f_j, a_j, and M_j are the mole fraction, the accommodation coefficient, and the molecular weight of gas j, respectively.

The summation in the denominator is performed over all individual fill gases in the rod (total of 6). There is a temperature-dependent accommodation factor for each gas. Ullman[86] made measurements for helium and xenon on UO_2, and curve fits were made to these data for use in GAPCON-2. These curve fits were implemented into CTF and are given below:

$$\begin{aligned} a_{\text{He}} &= 0.425 - 2.3 \cdot 10^{-4} T_{\circ K} \\ a_{\text{Xe}} &= 0.749 - 2.5 \cdot 10^{-4} T_{\circ K}, \end{aligned} \tag{450}$$

and the linear interpolation is simply applied for the other gases that have molecular weights between those of helium and xenon, as:

$$a_j = \frac{a_{\text{Xe}} - a_{\text{He}}}{128} M_j + \left(a_{\text{He}} - 4 \frac{a_{\text{Xe}} - a_{\text{He}}}{128} \right). \tag{451}$$

Results were found to correlate with the data of Thomas[87] with reasonable accuracy.

11.2.2 Conduction in the Gap from Pellet/Clad Contact

The solid contact conduction term will only be nonzero if the clad and pellet are found to be in contact. When contact exists, the Mikic/Todreas model[88][89] is used to predict associated heat transfer.

$$H_{\text{solid}} = \frac{5 k_m}{\sqrt{R_f^2 + R_c^2}} \left(\frac{P_{\text{int}}}{H_Z} \right)^n \left(\frac{R_f}{\lambda_f} \right) \tag{452}$$

The interface pressure, P_{int}, is discussed as part of the fuel deformation model (Section 11.1). The Meyer hardness of Zircaloy, H_Z, is defined as a temperature-dependent correlation in Section 15.2. The roughness parameters, R_f and R_c, should be entered in units of inches. The conductivity at the interface is a function of fuel and cladding conductivities, defined as

$$k_m = \frac{2 k_f k_c}{k_f + k_c}. \tag{453}$$

The nondimensionalized interface pressure, P_{int}/H_Z, has an associated exponent, n, which is selected based on the value of the nondimensionalized interface pressure as

$$n = \begin{cases} 0.5 & \text{for} \quad P_{\text{int}}/H_Z < 0.0001 \\ 1.0 & \text{for} \quad P_{\text{int}}/H_Z > 0.01 \end{cases}, \tag{454}$$

and for values of $0.001 < P_{\text{int}}/H_Z < 0.01$, the entire expression, $(P_{\text{int}}/H_Z)^n$, is held to a constant of 0.01.

The final expression of Eq. (452) is the dimensionless ratio of mean fuel surface roughness to fuel wave length, R_f/λ_f. This expression is estimated in GAPCON-2 by the following equation:

$$\frac{R_f}{\lambda_f} = \exp[0.5285 \ln(R_f - 5.738)]. \tag{455}$$

It is important to note here that the fuel surface roughness in the expression must be entered in microinches.

11.2.3 Radiative Heat Transfer in the Gap

The radiation heat transfer in the gap is defined as the radiation heat flux divided by the gap temperature gradient.

$$H_{\text{rad}} = \frac{q_r''}{T_f - T_c} \tag{456}$$

Subscripts f and c stand for "fuel" and "cladding." The radiant heat flux is determined from the Stefan-Boltzmann equation.

$$q_r'' = \sigma_{SB} \frac{T_f^4 - T_c^4}{\frac{1}{\epsilon_f} + \frac{A_f}{A_c}\left(\frac{1}{\epsilon_c - 1}\right)} \tag{457}$$

Temperature is provided in units of Rankine. The Stefan-Boltzmann constant, σ_{SB}, is $1.714 \cdot 10^{-9}$ BTU/hr·ft^2·R^4. Uranium dioxide and Zircaloy emissivities are given in Sections 15.1 and 15.2.

11.3 METAL/WATER REACTION

For nuclear fuel rods with a zirconium-based cladding, there can be an exothermic reaction between the zirconium and water or steam at high temperatures.

$$2H_2O + \text{Zr} \rightarrow 2H_2 + \text{Zr}O_2 + 140500 \text{ cal/mole Zr} \tag{458}$$

According to the work of Cathcart and Pawel[90], the oxidation rate of zirconium at temperatures above 1000 °C follows a parabolic rate law.

$$W\frac{dW}{dt} = A \exp\left(\frac{-B}{RT}\right) \tag{459}$$

The terms are defined as follows:

W = total oxygen consumed (kg/m^2)
A = 16.8 kg^2/m^{4}s
B = activation energy, 39940 cal/gm·mole
R = gas constant, 1.987 cal/gm·mole·°K
T = temperature (°K)

In CTF, the focus is on two things: the thickness of the oxide layer, and the heat generation in the cladding from oxidation. Equation (459) indicates the amount of oxygen consumed by the cladding in units of mass per time. By dividing this equation by the density of zirconium, the change in the oxide layer thickness over time can be obtained.

$$\tau \frac{d\tau}{dt} = \frac{A}{\rho^2} \exp\left(\frac{-B}{RT}\right) \tag{460}$$

The oxide layer thickness is expressed here as τ. To determine the change in oxide layer thickness over a single time step, this equation is integrated over the time step size and from the old time step oxide layer thickness to the new time oxide layer thickness.

$$\int_{\tau_0}^{\tau} \tau d\tau = \frac{A}{\rho^2} \exp\left(\frac{-B}{RT}\right) \int_0^{\Delta t} dt \tag{461}$$

This leads to

$$\begin{aligned} \frac{1}{2}\left(\tau^2 - \tau_0^2\right) &= \frac{A}{\rho^2} \exp\left(\frac{-B}{RT}\right) \Delta t \\ \tau^2 &= \frac{2A}{\rho^2} \exp\left(\frac{-B}{RT}\right) \Delta t + \tau_0^2. \end{aligned} \tag{462}$$

The oxide layer radius is defined as the distance from the fuel centerline to the inner surface of the oxide layer in CTF, so this thickness is subtracted from the outer radius of the fuel rod to obtain the new oxide layer radius. In CTF, R is absorbed into B in the exp function, leading to a coefficient of 20070 °K. Using a zirconium density of 691.8 $\mathrm{kg/m^3}$ for the operating temperature and pressure leads to a leading coefficient of $7.02 \cdot 10^{-5}$ $\mathrm{m^2/s}$. The energy generated in the cladding is the second item of interest. This is calculated by multiplying the energy caused by oxidation by the amount of zirconium oxidized in a timestep.

$$q_o = Q_c \frac{V}{\Delta t} \tag{463}$$

The energy generation, q_o, is a rate term in units of $\mathrm{J/s}$. The energy released by oxidation, Q_c, is $4.044 \cdot 10^9$ $\mathrm{J/m^3}$. Expanding out the volume term V leads to

$$q_o = Q_c \frac{\pi\left(r^2_{\text{oxide,old}} - r^2_{\text{oxide,new}}\right)\Delta X}{\Delta t}. \tag{464}$$

The ΔX term is the axial height of the conductor mesh cell.

12. HEAT TRANSFER MODELS

12.1 INTRODUCTION

In addition to wall drag and form losses, the presence of solid components in the flow field may also lead to heat exchange with the fluid. Because CTF is using a two-fluid approach, the heat transfer is divided between the two phases, with the liquid phase being further divided into convective heat transfer and boiling heat transfer. Convective heat transfer results in explicit energy exchange with the liquid phase and the boiling heat transfer term results in implicit heat transfer as a result of vapor generation at the surface. Both liquid convective and boiling heat transfer lead to energy being deposited into the liquid phase, and the vapor convective heat transfer leads to energy being deposited into the vapor phase. In addition to these heat transfer mechanisms, CTF also considers radiative heat transfer from solid to fluid, but these heat transfer effects are grouped into one of the three primary HTCs. The heat flux at the solid surface is described in Eq. 465:

$$q'' = h_\ell(T_w - T_\ell) + h_v(T_w - T_v) + h_b(T_w - T_f) \tag{465}$$

The solid surface temperature, T_w, will be available from the conduction equation solution. The fluid temperatures (T_ℓ for liquid and T_v for vapor), will be available from the conservation equation solution discussed in Section 2, and the saturation temperature (T_f) will be available from the fluid properties. The calculation of the heat transfer coefficients (h_ℓ, h_v, and h_b for liquid, vapor, and boiling) are discussed in this section. Sections 12.4 through 12.10 discuss the modeling of convective heat transfer for all heat transfer regimes modeled by CTF. Section 12.13 covers radiative heat transfer, and Section 12.14 covers spacer grid heat transfer and the spacer grid re-wet model.

The heat transfer coefficient is highly dependent on the behavior of the flow and is calculated from either empirical or mechanistic models. Different models are used for each heat transfer "region." Heat transfer regions are depicted in Figure 30, which presents the boiling curve. Moving from left to right in the figure, heat flux begins to increase dramatically when a certain temperature difference between the heated surface and adjacent fluid is reached. This corresponds to the beginning of boiling and the increased heat removal that accompanies the phenomenon. Heat removal continues to rise with increased wall temperature until the vapor phase begins to blanket the heated surface and prevent further increase in heat removal—an occurrence known as departure from nucleate boiling (DNB) or CHF.

The region of decreasing heat flux with respect to increasing wall superheat is known as the *transition boiling region*, where the surface becomes increasingly blanketed by vapor, as indicated moving left to right in the plot. Once the minimum film boiling (MFB) temperature is reached, stable film boiling begins, and further increases in superheat lead to increasing heat transfer.

CTF recognizes the following heat transfer regimes:

1. Single-phase liquid convection (SPL)
2. Subcooled nucleate boiling (SCB)
3. Saturated nucleate boiling (NB)
4. Transition boiling (TRAN)
5. Inverted annular film boiling (IAFB)

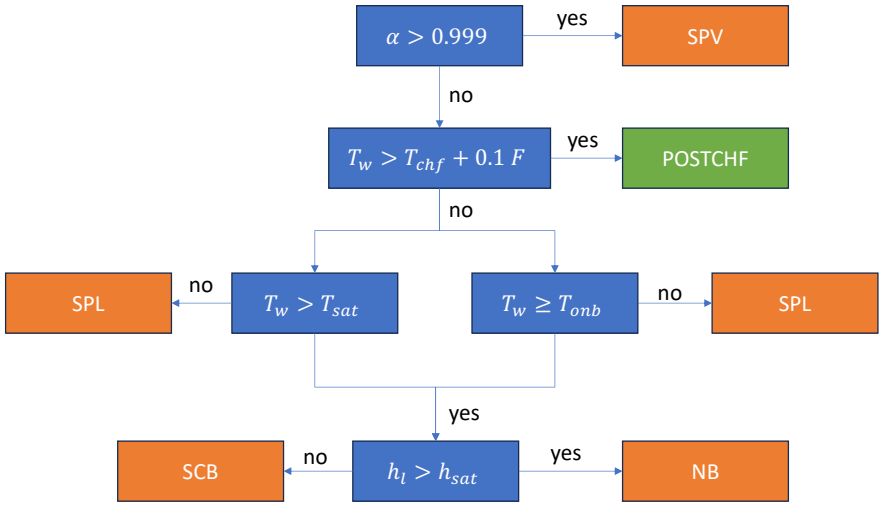

Figure 26. CTF selection algorithm for the heat transfer regime.

6. Inverted annular film boiling/dispersed flow film boiling transition
7. Dispersed flow film boiling (DFFB)
8. Single-phase vapor convection (SPV)

The first three heat transfer regimes are strictly pre-CHF regimes, and items 4–7 are strictly post-CHF regimes. The SPV regime may exist either as pre- or post-CHF and only depends on the void fraction. CTF selects the appropriate heat transfer regime after evaluating several criteria. If the heated surface temperature is less than T_{CHF} plus 0.1 °F, then a pre-CHF heat transfer regime will be selected. Two different approaches are available in CTF to determine when subcooled nucleate boiling begins. In the first approach, if the heated surface temperature is greater than or equal to either 0.1 °F above the local saturation temperature and the bulk liquid enthalpy is less than bulk liquid saturation enthalpy, then subcooled boiling will exist. This is referred to as the *non-onset of nucleate boiling (ONB)* approach. In the second approach, an ONB temperature is calculated, and if the local surface temperature is above this value and bulk liquid enthalpy is below bulk liquid saturation enthalpy, then subcooled boiling commences. This second approach is referred to as the *ONB* approach. When the bulk liquid enthalpy temperature is above bulk liquid saturation enthalpy, nucleate boiling exists. Note that the SPV convection regime will be selected if the void fraction is above 0.999, regardless of the heated surface temperature (see Section 12.4). However, if the heated surface temperature is greater than or equal to 0.1 °F above the critical heat flux temperature, then one of the post-CHF heat transfer regimes will be selected. An overview of the heat transfer region selection algorithm in CTF is depicted in Figure 26.

The block that contains "POSTCHF" is further expanded in Figure 27, which provides the logic for determining which post-CHF regime exists. Note that the predominant heat transfer mechanisms in post-CHF heat transfer are the effects found in dispersed flow film boiling (DFFB) (radiative heat transfer to the droplets and vapor, vapor convective heat transfer, etc.), so the HTCs for this regime will be calculated first.

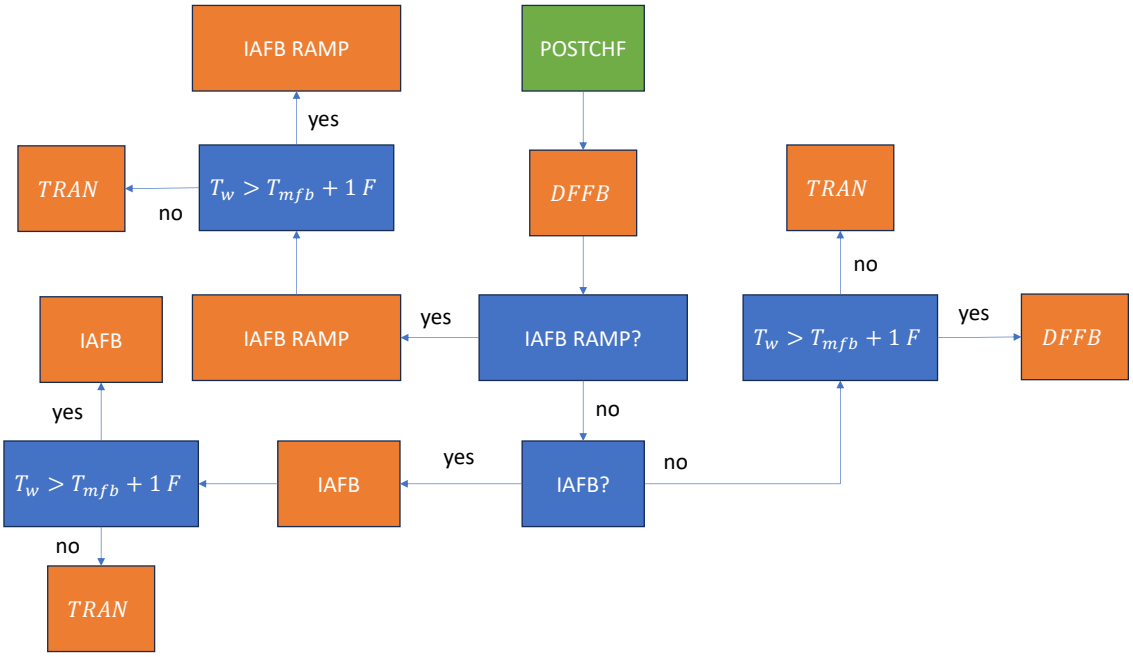

Figure 27. CTF selection algorithm for the heat transfer regime when heat transfer is considered post-CHF.

After this, some considerations must be made for the flow regime. If the void fraction is low enough, then the flow regime will either be inverted annular film boiling (IAFB) or will be transitioning between IAFB and DFFB. Encountering either of these conditions will modify the DFFB HTCs. One final check is then needed to determine if the surface temperature is above or below the MFB temperature. If the temperature is above the MFB temperature, then the heat regime will be its initial determination, which will be either DFFB, IAFB, or the transition between IAFB and DFFB. However, if the temperature is below the MFB temperature, then the heat transfer regime will be transition boiling, which is a combination of the previously determined heat transfer effects (i.e., DFFB and/or IAFB) and the CHF. The specific criteria that are used to determine if the flow regime is IAFB or if it is transitioning between IAFB and DFFB is given in Section 12.11.

12.1.1 Minimum Film Boiling Temperature

The minimum film boiling temperature is the temperature at which a stable film forms on the heated surface. It separates the transition boiling region—in which liquid intermittently contacts the heated surface— from the film boiling region—in which the surface is too hot to ever allow liquid to contact. For unheated conductors, this temperature is set to a constant value of 900 °F. For heated structures, the minimum film boiling temperature is set to a minimum value of 900 °F for void fractions less than 0.8 and to a minimum value of 700 °F for void fractions equal to or greater than 0.8. However, the minimum film boiling temperature may be much higher and is evaluated using two different methods.

First, T_{min} is calculated assuming it equals the wall temperature that results in an instantaneous contact temperature equal to the homogeneous nucleation temperature. The homogeneous nucleation temperature for water is a function of pressure.

$$T_{\text{hn}} = 705.44 - 4.722 \times 10^{-2}(P_{\text{crit}} - P) + 2.3907 \times 10^{-5}(P_{\text{crit}} - P)^2 - 5.8193 \times 10^{-9}(P_{\text{crit}} - P)^3 \quad (466)$$

The critical pressure of water is 3203.6 psi. The homogeneous nucleation temperature is given in units of °Fahrenheit. The effect of wall surface thermal properties is included by using a contact temperature correction.

$$T_{\text{min,hn}} = T_{\text{hn}} + (T_{\text{hn}} - T_l)\left[\frac{(k_p C_p)_l}{(k_p C_p)_w}\right]^{1/2} \tag{467}$$

The second method is by using Henry's modification of the Berenson correlation [91].

$$T_{\text{min,henry}} = T_B + 0.42(T_B - T_l)\left\{\left[\frac{(k_p C_p)_l}{(k_p C_p)_w}\right]^{1/2}\left[\frac{H_{\text{fg}}}{C_{\text{pw}}(T_B - T_{\text{sat}})}\right]\right\}^{0.6}, \tag{468}$$

where

$$T_B = T_{\text{sat}} + 0.127\frac{\rho_v H_{\text{fg}}}{k_v}\left[\frac{g(\rho_f - \rho_g)}{(\rho_f + \rho_g)}\right]^{2/3}\left[\frac{g_c\sigma}{g(\rho_f - \rho_g)}\right]^{1/2}\left[\frac{\mu_v}{g(\rho_f - \rho_g)}\right]^{1/3}. \tag{469}$$

To summarize, the minimum film boiling temperature for heated surfaces is selected using the following criteria:

$$T_{\text{min}} = \max\begin{cases} \min\begin{cases} 1158 \\ \max\begin{cases} T_{\text{min,hn}} \\ T_{\text{min,henry}} \end{cases} \end{cases} \\ 900 \text{ if } \alpha_v < 0.8 \\ 700 \text{ if } \alpha_v >= 0.8 \end{cases} \tag{470}$$

12.1.2 Calculation of T_{chf}

The CHF temperature is calculated iteratively as the intersection of the nucleate boiling heat flux and CHF using the user-selected models. The algorithm is summarized visually in the flowchart in Figure 28. The first step is setting minimum and maximum boundaries for T_{chf}. These minimum and maximum boundaries are 0.01 °F over the liquid saturation temperature for the minimum boundary and the maximum of 75 °F over the saturation temperature or the critical temperature of water (705.3 °F) for the maximum boundary.

The code then checks to see if the calculated CHF exceeds either of the boundaries. If it exceeds either boundary, then the CHF and T_{chf} values are set to the boundary that is exceeded. If it does not exceed either boundary, then the iterative process to find the actual T_{chf} begins. The process is to take the midpoint between T_{min} and T_{max}, use that to calculate heat flux at that temperature using the nucleate boiling correlation (i.e., Chen[92] or Thom[93]), and then compare that heat flux to the critical heat flux that was previously calculated. If q''_{chf} is less than q''_{nb} (the nucleate boiling heat flux), then the new minimum temperature becomes the current T_{chf} temperature. If q''_{chf} is larger than q''_{nb}, then the new maximum temperature becomes T_{chf}.

This effectively cuts the range of temperatures in half, and the next iteration commences using the new midpoint temperature. This process continues until q''_{nb} matches q''_{chf} to within a relative error of 0.01. The temperature that leads to the correct q''_{nb} value is returned as the temperature at CHF.

An example of this process is shown in Figure 29.

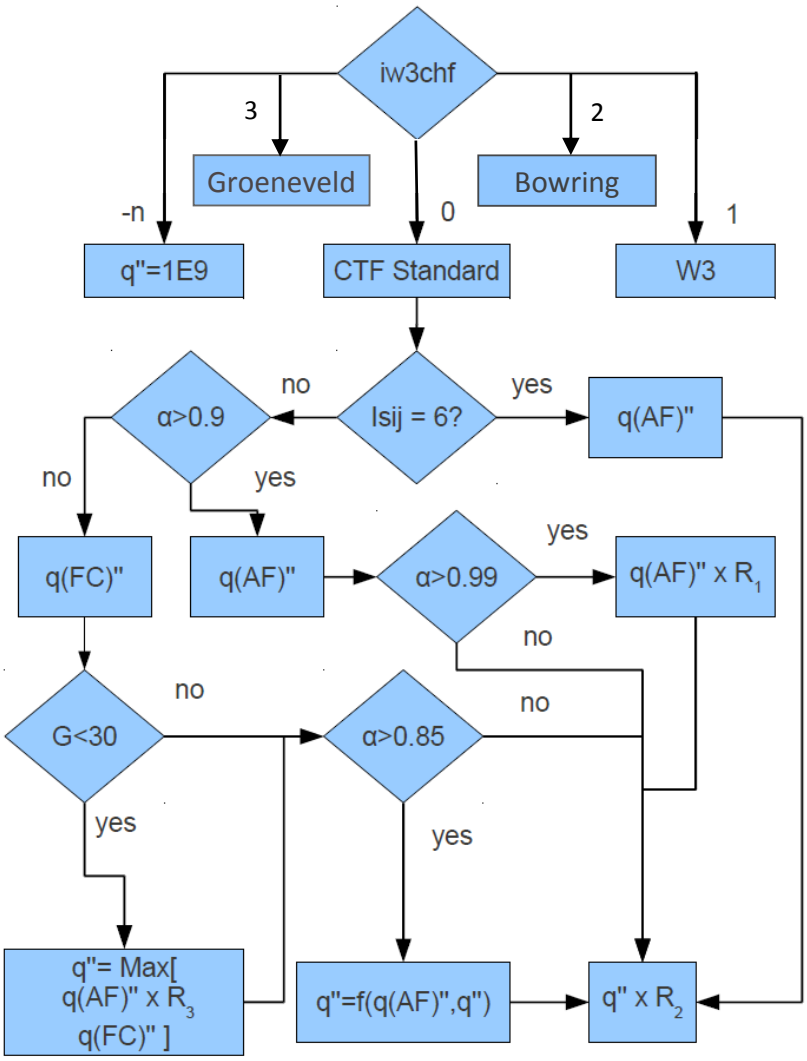

Figure 28. CTF algorithm for determining the temperature at CHF.

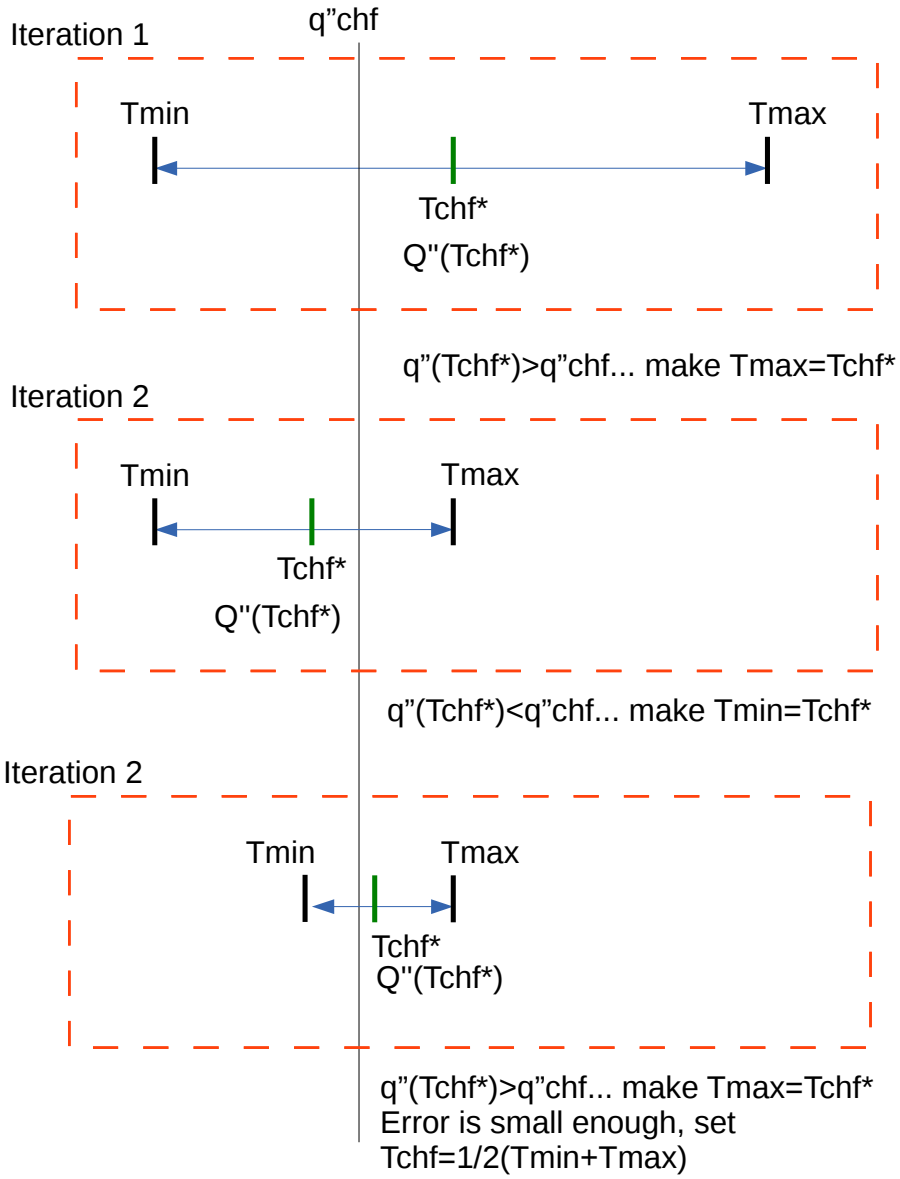

Figure 29. A simple example of how T_{CHF} is iteratively calculated.

12.2 HEAT TRANSFER TO FLUID

This section discusses how the heat transfer model is used to couple the solid and fluid energy equations and how it leads to mass transfer in the fluid mass equations. The liquid energy equation includes a source term for the surface heat transfer, which includes the liquid convective and boiling heat transfer components.

$$Q_{wl} = (h_\ell(T_w - T_\ell) + h_b(T_w - T_f))A_w \tag{471}$$

The surface area of the solid in contact with the fluid is denoted with A_w. The vapor energy equation source term will be as follows:

$$Q_{wv} = (h_v(T_w - T_v))A_w \tag{472}$$

The vapor generation at the surface can be calculated from the boiling heat transfer term as

$$m_b = h_b(T_w - T_f)A_w/h_{fg}, \tag{473}$$

where h_{fg} is the latent heat of vaporization. This term will be added to the vapor mass equation and subtracted from the liquid and droplet mass equations.

12.3 HEAT TRANSFER STABILITY

To improve numerical stability, the heat transfer coefficients are under-relaxed in time. First, the h_v term is calculated from the vapor heat transfer coefficient h_{wv}, as follows:

$$h_v = [F_v h_{wv}]^{0.2} \left[\max \left\{ \begin{array}{c} h_v^n \\ 1.0 \end{array} \right\}^{0.8} \right]. \tag{474}$$

h_v^n is the old time-step vapor heat transfer coefficient. The new time vapor heat transfer coefficient is weighted to the old time value to ensure slower transition and numerical stability. h_{wv} is the wall-to-vapor heat transfer coefficient, which is the boiling regime–dependent heat transfer coefficient (the calculation of which is further discussed later in this section). F_v is a damping factor which diminishes the vapor heat transfer coefficient if the vapor phase is depleted. It is calculated as follows:

$$F_v = \left\{ \begin{array}{ll} 1.0 & \text{if } \alpha_v >= 0.05 \\ \max \left\{ \begin{array}{c} \frac{\alpha_v - 0.01}{0.04} \\ 0.0 \end{array} \right. & \text{if } \alpha_v < 0.05 \end{array} \right. \tag{475}$$

Second, the liquid heat transfer coefficient also multiplies by a damping factor and is weighted to the old time value.

$$h_l = [F_l h_{wl}]^{0.2} \left[\max \left\{ \begin{array}{c} h_l^n \\ 0.1 \end{array} \right\} \right]^{0.8} \tag{476}$$

The damping factor, F_l, is defined as follows:

$$F_l = \left\{ \begin{array}{lll} 1.0 & , & \text{if } \alpha_v < 0.999 \\ \max \left\{ \begin{array}{c} \frac{0.9999 - \alpha_v}{0.0009} \\ 0.0 \end{array} \right. & , & \text{if } \alpha_v > 0.999 \end{array} \right. \tag{477}$$

The boiling heat transfer coefficient is calculated in the same manner as the liquid heat transfer coefficient using the same time-damping and damping factor.

12.4 SINGLE-PHASE VAPOR CONVECTION

The flow is assumed to be in the single-phase vapor regime when the void fraction is greater than 0.999. In that case, three correlations are used to determine the heat transfer coefficient. These are the Dittus-Boelter correlation [94], the Wong and Hochreiter correlation for turbulent forced convection [95], and a constant Nusselt number value for laminar forced convection. To ensure a seamless transition between the heat transfer coefficients predicted by different models, the maximum of the three correlations is selected if CTF determines that the boiling regime is single-phase vapor.

$$h_{wv} = \max \begin{cases} h_{wv,\mathrm{DB}} \\ h_{wv,\mathrm{WH}} \\ h_{wv,\mathrm{lam}} \end{cases} \tag{478}$$

First, the simplest model of the three is discussed. The heat transfer coefficient is determined assuming a constant Nusselt number of 10.

$$h_{wv,\mathrm{lam}} = 10 \frac{k_v}{D_h} \tag{479}$$

k_v is the conductivity of vapor, and D_h is the hydraulic diameter of the channel.

The Dittus-Boelter correlation was originally developed for turbulent flow in smooth tubes inside of automobile radiators, but it has found use for many turbulent flow modeling scenarios. The heat transfer coefficient is calculated as follows:

$$h_{wv,\mathrm{DB}} = 0.023 \frac{k_v}{D_h} \mathrm{Re}^{0.8} \mathrm{Pr}^n. \tag{480}$$

For heating, $n = 0.4$, and for cooling, $n = 0.3$. The fluid properties are evaluated at the mean film temperature.

The Wong and Hochreiter correlation was developed by applying a linear regression fit to experimental data obtained from rod bundle heat transfer tests performed on a 17×17 array of rods. The correlation is as follows:

$$h_{wv,\mathrm{WH}} = 0.07907 \frac{k_v}{D_h} \mathrm{Re}^{0.6774} \mathrm{Pr}_v^{0.333} \tag{481}$$

If grids are present in the flow field and this model is enabled by the user, then grid impact on heat transfer is modeled by multiplying the heat transfer coefficient by a grid effect factor, as follows:

$$h_{wv} = F_{\mathrm{grid}} h_{wv} \tag{482}$$

The grid heat transfer enhancement multiplier, F_{grid}, is calculated as discussed in Section 13.1. The liquid and boiling HTCs are set to zero if the heat transfer regime is single-phase vapor.

12.5 DROPLET-INDUCED TURBULENCE ENHANCEMENT

The presence of droplets in a dispersed flow can lead to turbulence enhancement in the droplet/vapor core, which leads to enhanced heat transfer between the fluid and solid. A model is implemented in CTF based on the momentum/heat transfer analogy, which relates wall shear and HTC as

$$h = \sqrt{\tau}. \tag{483}$$

A multiplication factor can be formulated that is defined as the ratio between the droplet/vapor HTC and the pure-vapor HTC. The idea is that this ratio can be multiplied by the single-phase vapor HTC that is calculated as discussed in Section 12.4 to obtain an enhanced HTC. The multiplier is calculated as follows:

$$F = \frac{h_{\text{enh}}}{h_{\text{spv}}} = \sqrt{\frac{\tau_{\text{mix}}}{\tau_{\text{spv}}}} \tag{484}$$

In this equation, "enh" represents the enhanced quantity, "mix" represents the droplet/vapor mixture, and "spv" represents the base heat transfer quantity. The base shear is calculated using the single-phase pressure drop model:

$$\tau_{\text{spv}} = \frac{1}{2}\rho_v f_w \frac{u_v^2}{D}, \tag{485}$$

where f_w is the friction factor that is based on the user-selected friction factor model, u_v is the vapor velocity, and D is the channel hydraulic diameter. The mixture shear is calculated as the sum of the wall shear and the droplet/vapor interfacial shear. The interfacial shear is calculated as

$$\tau_{\text{mix}} = \frac{3}{4}\alpha_e \rho_v C_d \frac{(U_v - U_e)^2}{D_d}. \tag{486}$$

The droplet drag coefficient is calculated using Eq. (273), but the droplet Reynolds number used in the C_d calculation is different from that in Eq. (274) because it uses vapor viscosity instead of mixture viscosity, as shown below.

$$\text{Re}_d = \frac{D_d \rho_v \vec{u}_{ve}}{\mu_v} \tag{487}$$

Furthermore, a lower limit of 2.0 is placed on the droplet Reynolds number. The droplet diameter D_d, is calculated using the interfacial area from the interfacial area transport equation and the local droplet void. A limiter is placed on the interfacial area:

$$D_d = \frac{6\alpha_e}{\max(0.01\ \text{ft}^{-1}, A_i''')} \tag{488}$$

Lower and upper bounds are also placed on the droplet diameter so that it is larger than 0.0001 ft and smaller than the channel equivalent diameter. Finally, an upper limit of 2.0 is placed on the droplet enhancement multiplier F calculated in Eq. (484).

12.6 SINGLE-PHASE LIQUID HEAT TRANSFER

The flow is in the single-phase liquid heat transfer regime if the liquid void fraction, α_l, is greater than 0.001. Single-phase liquid heat transfer coefficients are calculated for the case of laminar flow using a model recommended by Sparrow et al. [96], as shown in Eq. (489), and for the case of turbulent flow using Dittus-Boelter [94], as shown in Eq. (480), with liquid properties used instead of vapor properties. The maximum of these two calculations is taken as the liquid single-phase heat transfer coefficient.

$$h_{wl,\text{lam}} = 7.86 \frac{k_l}{D_h}. \tag{489}$$

The grid heat transfer enhancement will be made to the liquid heat transfer coefficient if that model is enabled by the user. The modification is similar to that implemented for vapor, as discussed in Section 13.1. Note that the single-phase heat transfer effects may exist alongside other heat transfer regimes such as subcooled or nucleate boiling, leading to a cumulative heat transfer effect.

12.7 SUBCOOLED NUCLEATE BOILING

The subcooled nucleate boiling regime is encountered when small bubbles begin to form on the heated surface. Liquid near the heated wall must achieve a certain amount of superheat for vapor to form; however, in subcooled nucleate boiling, the bulk fluid temperature will be lower than the saturation temperature. Because the bulk fluid temperature is not high enough to support the existence of void, bubbles that form at the wall will generally condense soon after they form, resulting in the existence of a very small void fraction. In the later stages of subcooled nucleate boiling, as the bulk temperature increases, bubbles may grow and detach from the wall, where they then later condense in the liquid. The bulk fluid temperature is still too low to support the bubbles' existence; however, this later region of subcooled nucleate boiling can have significant amounts of void in the flow. There are two approaches used in CTF to trigger the wall boiling model. In the first approach, bubbles are assumed to nucleate on the heated surface as soon as the heated surface temperature exceeds the local fluid saturation temperature, and a near-wall condensation model is used to limit the amount of vapor generated. In the second approach, a model is used to determine the temperature at which the boiling begins. The nucleate boiling heat transfer correlations and the vapor generation fraction for the first approach is discussed. This is followed by the second approach, in which the onset of nucleate boiling (ONB) model is described, along with the associated heat transfer correlations, followed by the calculation of the vapor generation fraction.

12.7.1 Approach 1: Non-ONB Model

In this approach, three processes in the two-phase regime under consideration affect heat transfer from the wall to the liquid:

1. Forced convection to the liquid
2. Vapor generation at the wall
3. Condensation of bubbles at the wall

CTF calculates the heat transfer coefficient in the subcooled nucleate boiling region using one of three correlations: the Chen correlation[92] (Section 12.7.3), the Thom correlation[93] (Section 12.7.4), or the Gorenflo model (Section 12.7.5). The user is responsible for choosing the correlation to use (see the User's Manual[6]). The convective and pool boiling heat transfer components are both considered in the original Chen and Thom publications. The condensation heat transfer effect was not considered in the references, but instead, it is added in after the fact in the code.

12.7.1.1 Near-Wall Condensation Heat Transfer

The near-wall condensation heat transfer is the last important term in the subcooled nucleate boiling regime. One of the subcooled nucleate boiling correlations will provide the overall heat transfer from the wall to the fluid, but in the subcooled boiling region, not all generated vapor will stay as vapor—much will inevitably condense back into liquid because the temperature of the bulk fluid is not high enough to support the existence of vapor. In reality, this is returning energy to the liquid phase through latent heat transfer. The condensation heat flux is needed to determine the ratio of latent heat to sensible heat transfer from the wall to the fluid.

The correlation of Hancox-Nicoll[97] is used to calculate the condensation heat flux, which gives the heat flux at the point where bubbles generated in the near-wall region collapse and recondense back to liquid.

The condensation heat flux, q''_{cond}, is thus equal to the heat flux into the liquid considering the condensation of all near-wall bubbles, q''_{hn}, by using the Hancox-Nicoll correlation as follows:

$$q''_{\text{cond}} = q''_{\text{hn}} = 0.4\left(\frac{Cp_f\mu_f}{D_h}\right)\left(\frac{G_l D_h}{\mu_f}\right)^{0.662}(T_{\text{sat}} - T_l) \tag{490}$$

12.7.1.2 Vapor generation fraction

For the latent and sensible heat transfer coefficients to the liquid, the fraction of heat that results in net vapor generation must be calculated. The heat flux predicted by Hancox-Nicoll is the total heat dissipation ability in the subcooled boiling region, which may be in excess of the actual wall heat flux. The single-phase heat flux (calculated from Dittus-Boelter) is subtracted from this term to get the excess heat removal ability in the subcooled boiling region. This term is then subtracted from the nucleate boiling heat flux predicted by the subcooled boiling model. This represents the heat flux that results in vapor generation in the subcooled boiling region. This is divided by the total heat flux to determine the vapor generation fraction.

$$F^*_{\text{gam}} = \frac{h_{\text{nb}}(T_w - T_{\text{sat}}) - q''_{\text{cond}}}{h_{\text{nb}}(T_w - T_{\text{sat}})} \tag{491}$$

The vapor that does escape the vapor layer near the wall will be replaced with subcooled liquid from the bulk. The wall layer will heat up this subcooled liquid before it can be boiled, so this will further reduce the ability of vapor generation. A model was proposed by Rouhani to capture this effect.

$$\epsilon_\Gamma = \frac{h_{\text{fg}}}{h_{\text{fg}} + (h_f - h_l)\frac{\rho_f}{\rho_g}} \tag{492}$$

This term is multiplied by Eq. (491) if the heat transfer regime is subcooled boiling. In bulk boiling, the heat flux to vapor is left unperturbed because the bulk coolant is now saturated.

12.7.2 Approach 2: Using an ONB Model

In the heat transfer in this two-phase regime, three processes will affect heat transfer from the wall to the liquid:

1. Forced convection to the liquid
2. Vapor generation at the wall
3. Bubble detachment enthalpy

CTF can use the same three boiling heat transfer models available in the first approach. In this approach, it is recommended that the user selects the Gorenflo correlation. Instead of a near-wall condensation model, a bubble detachment enthalpy is calculated. All the sub models are discussed in the following paragraphs.

12.7.2.1 Onset of Nucleate Boiling Model

The ONB model implemented in CTF is the model by Basu et al. [98] in which the available cavity diameter, D_c, is proportional to a cavity diameter, D_c^o, corresponding to the tangency condition and a wettability parameter, $F(\phi)$. The available cavity size is given as follows:

$$D_c = D_c^o F(\phi) \tag{493}$$

D_c^o, is obtained from a minimum superheat condition and is given as follows:

$$D_c^o = \sqrt{\frac{8\sigma T_{sat} k_f}{\rho_g h_{fg} q_w}}, \tag{494}$$

where q_w is the wall heat flux. Assuming that the nucleating cavity size is smaller than the thermal boundary layer thickness, the wall superheat at ONB is obtained from the Clausius-Clapeyron equation, with the excess pressure calculated from the Young-Laplace equation for a spherical bubble. The wall superheat at ONB is given as follows:

$$\Delta T_{onb} = \frac{4\sigma T_{sat}}{D_c \rho_g h_{fg}} \tag{495}$$

The empirically obtained wettability parameter is a function of the fluid-surface contact angle ϕ and is given as follows:

$$F(\phi) = 1 - exp\left[-\left(\frac{\pi\phi}{180}\right)^3 - 0.5\left(\frac{\pi\phi}{180}\right)\right], \tag{496}$$

where the contact angle ϕ for the combination of water and stainless steel is 38 degrees [99]. This value is currently hard-coded in CTF. Combining the four Eqs. (493), (494), (495), and (496), the wall superheat at ONB can be expressed as follows:

$$\Delta T_{onb} = \frac{\sqrt{2}}{F(\phi)} \sqrt{\frac{\sigma T_{sat} q_w''}{\rho_g h_{fg} k_f}} \tag{497}$$

Equation (497) is an implicit equation because the wall superheat is related to the wall heat flux. An explicit relationship can be obtained by first defining the wall heat flux as follows:

$$q_w'' = h_{fc} \left(T_{onb} - T_l\right) \tag{498}$$

Substituting Eq. (498) into Eq. (497) results in a quadratic equation. Solving the quadratic equation and ignoring the negative root, the minimum wall temperature for boiling incipience can be obtained as follows:

$$T_{onb} = T_{sat} + 0.5\left[\Delta T_{sat,onb} + \sqrt{\Delta T_{sat,onb}{}^2 + 4\Delta T_{sat,onb}\Delta T_{sub}}\right], \tag{499}$$

where ΔT_{sub} is the local liquid subcooling. Finally, ΔT_{sat}, is defined as follows:

$$\Delta T_{sat,onb} = \frac{2 h_{fc} \sigma T_{sat}}{F_{(\phi)}{}^2 \rho_g h_{fg} k_f}. \tag{500}$$

12.7.2.2 Bubble detachment enthalpy

The bubble detachment enthalpy is calculated based on the model of Saha-Zuber [100]. In this model, the balance between evaporation at the wall and near-wall condensation is estimated using a similarity parameter which is a function of the mass flux. At low mass fluxes, the near-wall condensation will be governed by thermal diffusion. Therefore, a constant Nusselt number of 455.0 is used as the similarity parameter. At high mass fluxes in which fluid advection is dominant, a constant Stanton number is the similarity parameter. The boundary between the regions is determined using the local Peclet number (product of Reynolds and Prandtl number). Both of these regions can be combined into a single equation to calculate the enthalpy of detachment of the vapor bubble, h_{cr}, as follows:

$$h_{\mathrm{cr}} = h_{\mathrm{f}} - \frac{\left(q_{\mathrm{nb}} D_h C p_f\right)}{(k_l.pe.st)}, \tag{501}$$

where "pe" is the Peclet number and "st" is the Stanton number with a fixed value of 0.0065. The Peclet number is determined as follows:

$$pe = max\left(7\mathrm{e}4, \frac{G_l D_h}{\mu_f} \frac{C p_f \mu_f}{k_l}\right) \tag{502}$$

Finally, the fraction of vapor generation is determined based on the mechanistic model of Lahey [101]. The vapor generation fraction is calculated by estimating the excess liquid enthalpy over the critical liquid enthalpy as a proportion of excess saturated liquid enthalpy to the critical enthalpy, given as follows:

$$F^*_{\mathrm{gam}} = \frac{(h_{\mathrm{l}} - h_{\mathrm{cr}})}{(h_{\mathrm{f}} - h_{\mathrm{cr}})} \tag{503}$$

Similar to the first approach, the pumping factor proposed by Rouhani is taken into account. Therefore, the effective vapor generation fraction is obtained by multiplying F^*_{gam} with 492 in the subcooled boiling region.

12.7.3 Chen Correlation

The Chen correlation separately calculates the heat transfer coefficients because of forced convection and vapor generation and adds them together. This may be summarized in equation form as

$$h_{\mathrm{chen}} = h_{\mathrm{fc}} + h_{\mathrm{nb}}, \tag{504}$$

where the subscripts "fc" and "nb" stand for "forced convection" and "nucleate boiling", respectively. The nucleate boiling term is calculated using a Forster-Zuber type of pool boiling equation [102].

The forced convection heat transfer coefficient is calculated by means of a modified Dittus-Boelter type correlation, presented by Chen as follows:

$$h_{\mathrm{fc}} = 0.023 F_{\mathrm{chen}} \left(\frac{k_l}{D_h}\right) \mathrm{Re}_l^{0.8} \mathrm{Pr}^{0.4} \tag{505}$$

The F_{chen} factor is used to account for the difference between a two-phase and a single-phase Reynolds number. Therefore, it will be equal to 1 in the subcooled boiling heat transfer regime, and the Dittus-Boelter equation will remain unmodified. The F_{chen} factor is discussed in the section on saturated boiling heat

transfer (Section 12.8), where it varies from 1. Additionally, the subcooled liquid properties will be used to determine the Reynolds number, the Prandtl number, and liquid conductivity in the Dittus-Boelter equation.

The second component to the Chen model (Eq. (504)) is the nucleate boiling heat transfer coefficient. This is modeled by a Forster-Zuber [102] type of pool boiling equation. However, modification is made to account for the fact that the correlation is modeling forced convection boiling instead of pool boiling. The difference stems from the difference in boundary layer size between pool boiling and convective boiling. It can be shown that the product of growth rate and bubble radius is constant for a given superheat. The fluid temperature varies across the boundary layer, but because the pool boiling boundary layer is large compared to the bubble diameter, the superheat around the bubble can be assumed to be uniform. This is not true of the temperature around bubbles in forced convective boiling, where the boundary layer is small and temperature gradients are steep. Therefore, Chen presented a suppression factor, S_{chen}, to account for this effect in the nucleate boiling heat transfer coefficient term. The nucleate boiling heat transfer correlation is as follows:

$$h_{\text{nb}} = 0.00122 S_{\text{chen}} \left(\frac{k_f^{0.79} C p_f^{0.45} \rho_f^{0.49} g_c^{0.25}}{\sigma^{0.5} \mu_f^{0.29} H_{\text{fg}}^{0.24} \rho_g^{0.24}} \right) (T_w - T_f)^{0.24} (P(T_w) - P(T_{\text{sat}}))^{0.75} \tag{506}$$

The boiling suppression factor, S_{chen}, is a function of the two-phase Reynolds number.

$$S_{\text{chen}} = \begin{cases} \left[1 + 0.12 \text{Re}_{2\Phi}^{1.14}\right]^{-1} & \text{if } \text{Re}_{2\Phi} < 32.5 \\ \left[1 + 0.42 \text{Re}_{2\Phi}^{0.78}\right]^{-1} & \text{if } 32.5 < \text{Re}_{2\Phi} < 50.9 \\ 0.1 & \text{Re}_{2\Phi} > 50.9 \end{cases} \tag{507}$$

The two-phase Reynolds number is calculated using the Chen Reynolds number factor; however, recall that F_{chen} will be 1 for the subcooled nucleate boiling region.

$$\text{Re}_{2\Phi} = (10^{-4}) \text{Re}_l F_{\text{chen}}^{1.25} \tag{508}$$

Returning to the calculation of the nucleate boiling heat transfer coefficient in Eq. (506), the terms $P(T_w)$ and $P(T_{\text{sat}})$ represent the pressure at the wall temperature and the pressure at the saturation temperature. The difference between these pressures is approximated as follows:

$$(P(T_w) - P(T_{\text{sat}})) = \left[\frac{5.4042 H_{\text{fg}}}{\nu_{\text{fg}} (T_{\text{sat}} + 460)} \right] (T_w - T_{\text{sat}})^A, \text{ where} \tag{509}$$

$$A = \frac{1.0306}{(\log_{10} P)^{0.017}} + \frac{0.0020632}{(\log_{10} P)^{1.087}} \max\{0.0, (T_w - T_{\text{sat}}) - 5.0\}$$

Before completing the calculation of the necessary heat transfer coefficients, recall that during the overall discussion of the wall heat transfer closure term in Section 12.2, it was noted that for the nucleate boiling regions, the heated surface temperature, T_w, and the wall heat transfer term were implicitly coupled by using the linearized derivative of heat transfer coefficient with respect to surface temperature. The derivative of heat transfer coefficient with respect to T_w is calculated from the nucleate boiling heat transfer coefficient presented in Eq. (506).

$$\frac{dh_{\text{chen}}}{dT_w} = [0.24 + 0.75\{\text{chen1} + \text{chen2}\}] \frac{h_{\text{nb}}}{T_w - T_{\text{sat}}} + \begin{cases} \frac{0.001547}{(\log_{10} P)^{1.087}} h_{\text{chen}} \ln(T_w - T_{\text{sat}}) & \text{if } (T_w - T_{\text{sat}}) > 5 \\ 0.0 & \text{if } (T_w - T_{\text{sat}}) < 5 \end{cases}, \text{ where} \tag{510}$$

$$\text{chen1} = \frac{1.0306}{(\log_{10} P)^{0.017}} \text{ and}$$

$$\text{chen2} = \frac{0.0020632}{(\log_{10} P)^{1.087}} \max\{0.0, (T_w - T_{\text{sat}}) - 5.0\}$$

12.7.4 Thom Correlation

Unlike Chen's work, the Thom correlation assumes that forced convection is negligible compared to nucleate boiling in this heat transfer regime. The boiling heat transfer coefficient was calculated using experimental data leading to forced convection and subcooled nucleate boiling in the test facility. With measured rod-surface temperatures, rod heat fluxes, and fluid temperatures, it was possible to develop a relationship between heat flux and rod surface temperature superheat ($\Delta T_{\text{sat}} = T_{\text{wall}} - T_{\text{sat}}$). By considering the noted dependence of ΔT_{sat} on pressure, pressure was also included in the correlation. The Thom correlation for heat flux caused by to subcooled boiling was derived as follows:

$$q''_{\text{nb}} = \frac{\exp\left(\frac{2P}{1260}\right)}{72^2} \Delta T^2_{\text{sat}} \tag{511}$$

The derivative of the heat transfer coefficient with respect to rod surface temperature must also be determined for Thom, as it is for Chen, to perform the implicit coupling between the rod heat flux to the fluid and rod temperature. This was calculated using a numerical approximation with a step size of 1 F, as follows:

$$\frac{d\text{HTC}}{dT_{\text{s}}} = \frac{q''_{\text{nb}}(\Delta T_{\text{sat}} + 1)}{\max(1 \cdot 10^{-6}, \Delta T) + 1} - \frac{q''_{\text{nb}}(\Delta T_{\text{sat}})}{\max(1 \cdot 10^{-6}, \Delta T)} \tag{512}$$

The temperature difference in the denominators will be $T_{\text{wall}} - T_{\text{liq}}$ for subcooled nucleated boiling.

12.7.5 Gorenflo Correlation

In CTF, the Gorenflo model employs the pool boiling correlation of Gorenflo and Kenning [103]. The Gorenflo model is based on a reduced heat transfer coefficient proportional to a reference state heat transfer coefficient, as well as factors representing the influence of the wall heat flux, reduced pressure (ratio of system pressure to critical pressure), and wall properties. The effects of fluid properties are represented in the correlation by the reduced pressure factor and the reference heat transfer coefficient. The heat transfer coefficient is given as follows:

$$h = h_o F(p^*) F_w \left(\frac{q''}{q''_o}\right)^n, \tag{513}$$

where h_{o} is the reference heat transfer coefficient, $F(\text{p}^*)$ is the influence of the reduced pressure where p^* is the reduced pressure, F_{w} is the influence of wall properties, and the wall heat flux factor is defined in terms of the reference heat flux, q''_{o}, where n is a function of the reduced pressure. The reference state is chosen

for fully developed nucleate boiling in industrial applications as follows: $q_o = 20\ kW/m^2$ and the reduced reference pressure, p_o* = 0.1. The reference state for the heater is defined as a copper cylinder with a mean surface roughness height of $R_o = 0.4\ \mu m$. The surface roughness factor, F_w, is set to unity in the code. The reference heat transfer coefficient for water, obtained experimentally at the reduced reference pressure, is 5,600 W/m^2K. The expressions for n and $F(p^*)$, obtained through fitting experimental data for water, are given as follows:

$$n\left(p^*\right) = 0.9 - 0.3p^{*0.15} \tag{514}$$

$$F\left(p^*\right) = 1.73p^{*0.27} + 6.1p^{*2} + \frac{0.68p^{*2}}{\left(1 - p^{*2}\right)} \tag{515}$$

An explicit expression for the pool boiling boiling heat flux can be obtained as follows:

$$q''_{pb} = \left(\frac{h_o F(p^*)\left(T_w - T_{sat}\right)}{q''^n_o}\right)^{1/(1-n)} \tag{516}$$

The superposition of the forced convective component and the pool boiling heat flux to obtain the flow boiling heat flux is calculated based on the power-law or flow additive approach. A detailed review of the approach is addressed in Steiner and Taborek [104]. In CTF, an exponent of 3 is used as proposed by Steiner and Taborek [104] in which the flow boiling heat flux is the cubic root of the superposition of the single-phase forced convective heat flux (cubed) and the pool boiling heat flux (cubed). This approach is as follows:

$$h_{nb} = \left(h^3_{fc} + h^3_{pb}\right)^{(1/3)} \tag{517}$$

This approach is modified to superposition heat fluxes, as it is applied for both subcooled and saturated boiling heat transfer regimes. Additionally, there is a sharp rise in the nucleate boiling heat flux when it is suddenly triggered at the onset of nucleate boiling. To smooth the transition, the approach of [105] is used. Based on this approach, the pool boiling heat flux using T_{ONB} is subtracted from the pool boiling heat flux using the current surface temperature. This results in the boiling heat flux addition being zero at T_{ONB} and growing as T_w becomes superheated. Therefore, the total nucleate boiling heat flux is given as follows:

$$q''_{nb,t} = \left(q''^3_{fc} + \left(q''_{pb} - q''_{bi}\right)^3\right)^{(1/3)}, \tag{518}$$

where q_{bi} is the pool boiling heat flux at the point of boiling initiation. q_{bi} is calculated by using the wall temperature at the onset of nucleate boiling in Eq. (516). To calculate the net heat flux available for vapor generation, the contribution of the forced convective heat transfer would have to be subtracted. Becasue it is difficult to isolate the contribution of the forced convective heat flux from 518, a simple approximation is used as follows:

$$q''_{nb} \simeq q''_{nb,t} - q''_{fc} \tag{519}$$

Finally, the heat transfer coefficient can be obtained by dividing 519 by $T_{wall} - T_{liq}$. The derivative of the heat transfer coefficient with respect to rod surface temperature is similar to the approach used in Thom because an analytical derivative of Eq. (519) is messy. Therefore, a numerical approximation of the derivative with a step size of 1 F is used, similar to that used in Eq. (512). The temperature difference in the denominators will be $T_{wall} - T_{liq}$ for subcooled nucleated boiling.

12.7.6 Calculation of Heat Transfer Coefficient Terms

With the main heat transfer phenomenon discussed and defined, it is now possible to calculate the three heat transfer coefficients—h_{wl}, h_{wb}, and h_{wv}—that will be needed in the CTF coupling between rods and coolant.

First, the wall heat transfer to vapor will be set to zero. The vapor generation fraction calculated for both of the approaches can lead to the calculation of the latent heat transfer to the liquid. The total boiling heat transfer term is multiplied by the fraction of heat transfer that results in stable vapor production. It must be noted that if the Thom correlation is used with the second approach, then the forced convective heat flux is subtracted from the nucleate boiling heat flux predicted by Eq. (511) to obtain the effective boiling heat transfer heat flux.

$$q''_{wb,\mathrm{scb}} = F_{\mathrm{gam}} q''_{\mathrm{nb}} \tag{520}$$

Because the concern here is with the heat transfer coefficient, the approach is to divide through by $(T_w - T_{\mathrm{sat}})$.

$$h_{wb,\mathrm{scb}} = F_{\mathrm{gam}} h_{\mathrm{nb}} \tag{521}$$

The energy that condenses out of the vapor phase is added to the sensible heat transfer term alongside the single-phase heat transfer term.

$$q''_{wl,\mathrm{scb}} = q''_{\mathrm{fc}} + (1 - F_{\mathrm{gam}}) q''_{\mathrm{nb}} \tag{522}$$

Once again, this is divided through by the temperature difference to obtain the heat transfer coefficient—this time the temperature difference is $T_w - T_l$.

$$h_{wl,\mathrm{scb}} = h_{\mathrm{fc}} + (1 - F_{\mathrm{gam}}) h_{\mathrm{nb}} \frac{T_w - T_{\mathrm{sat}}}{T_w - T_l} \tag{523}$$

12.8 SATURATED NUCLEATE BOILING

In the saturated nucleate boiling regime, the bulk fluid has reached the saturation temperature. The heat transfer mechanisms still include forced convection and nucleate boiling, but the near-wall condensation term is no longer of issue as it was in the subcooled nucleate boiling region.

The correlations from the subcooled boiling regime are also extended and used in the saturated boiling regime. The Chen correlation was actually derived from saturated boiling data, whereas the Thom correlation was developed for subcooled nucleate boiling data, although it is common to extend the Thom correlation to saturated boiling [106]. Because Chen was developed from low-pressure data (i.e., 1,000 psi compared to the pressure of 750–2,000 psi for Thom), it has been observed to underperform the Thom correlation for test conditions that reflect those of prototypical PWRs[106].

12.8.1 Chen Correlation

The forced convection component is revisited. The Dittus-Boelter type of equation is still used and is restated here for convenience.

$$h_{\mathrm{fc}} = 0.023 F_{\mathrm{chen}} \left(\frac{k_f}{D_h} \right) \mathrm{Re}_l^{0.8} \mathrm{Pr}^{0.4}$$

However, the conductivity, Reynolds number, and Prandtl number are calculated with consideration that a two-phase fluid exists instead of a single-phase fluid. Additionally, the forced convection term, F_{chen}, is no longer restricted to a value of 1.0 as in the case of subcooled nucleate boiling.

Note that the conductivity is that of a saturated liquid. Accounting for the fact that the fluid is two-phase, Re_l is calculated as

$$\text{Re}_l = \frac{G_l D_h}{\mu_f}. \tag{524}$$

The F_{chen} factor is a function of the Martinelli factor, χ_{TT}.

$$F_{\text{chen}} = \begin{cases} 1.0 & \text{if } \chi_{TT}^{-1} < 0.1 \\ 2.34(\chi_{TT}^{-1} + 0.213)^{0.736} & \text{if } \chi_{TT}^{-1} > 0.1 \end{cases} \tag{525}$$

The Martinelli parameter is the square root of the ratio of liquid friction pressure drop to vapor friction pressure drop.

$$\chi^2 = \frac{\left(\frac{dP}{dZ}\right)_{\text{fric}}^{l}}{\left(\frac{dP}{dZ}\right)_{\text{fric}}^{v}} \tag{526}$$

Equation (526) can be rewritten in terms of the phase viscosities and densities and quality. The inverse of the Martinelli parameter becomes

$$\chi_{TT}^{-1} = \left(\frac{x}{1-x}\right)^{0.9} \left(\frac{\rho_f}{\rho_g}\right)^{0.5} \left(\frac{\mu_g}{\mu_f}\right)^{0.1}. \tag{527}$$

In the code, this value is limited to a maximum value of 100.

$$\chi_{TT}^{-1} = \min[\chi_{TT}^{-1}, 100] \tag{528}$$

The quality x is calculated as

$$x = \max \begin{Bmatrix} \min \begin{Bmatrix} \frac{G_v}{G} \\ \frac{\bar{h} - h_f}{h_{\text{fg}}} \end{Bmatrix} \\ 0.0 \end{Bmatrix}. \tag{529}$$

The mixture enthalpy, $\bar{h}$, is a density-weighted enthalpy. It is calculated as follows:

$$\bar{h} = \frac{\alpha_v \rho_v h_v + (\alpha_l + \alpha_e)\rho_l h_l}{\alpha_v \rho_v + (\alpha_l + \alpha_e)\rho_l} \tag{530}$$

The boiling heat transfer coefficient is still calculated using the modified Foster-Zuber model that was shown in Eq. (506). However, the two-phase Reynolds number is calculated differently—it is multiplied by the F_{chen} factor to account for the increase caused by boiling.

$$\mathrm{Re}_{2\Phi} = 10^{-4}\mathrm{Re}_l F_{\mathrm{chen}}^{1.25} \tag{531}$$

This is used in the calculation of the boiling suppression factor, S_{chen}, in Eq. (507).

Finally, the derivative of the heat transfer coefficient with respect to temperature is calculated as it was for the subcooled nucleate boiling regime.

12.8.2 Thom Correlation

The Thom correlation is completely unmodified from its form in the subcooled nucleate boiling regime with Eq. (511).

As in the subcooled boiling region, $d\mathrm{HTC}/dT$ is calculated; however, the denominator of the numerical approximation, ΔT, will be defined as $T_{\mathrm{wall}} - T_{\mathrm{f}}$ (the wall temperature minus the liquid saturation temperature).

12.8.3 Gorenflo Correlation

The Gorenflo correlation, which is similar to the Thom correlation, is completely unmodified from its form in the subcooled nucleate boiling regime with Eq. (519).

As in the subcooled boiling region, $d\mathrm{HTC}/dT$ is calculated with the denominator of the numerical approximation, ΔT, defined as $T_{\mathrm{wall}} - T_{\mathrm{f}}$.

12.8.4 Calculation of Heat Transfer Coefficient Terms

Calculation of the heat transfer coefficient terms is simplified without the need for consideration of the near-wall condensation term when the first approach is used, or when bubble detachment enthalpy is used for the second approach. Additionally, the pumping factor is unity, so the effective vapor generation multiplier (fraction of boiling heat transfer that results in vapor production) calculated by both of the approaches is unity for saturated boiling. The latent heat transfer coefficient sums the forced convection and nucleate boiling terms.

$$h_{wb} = h_{\mathrm{fc}} + h_{\mathrm{nb}} F_B \tag{532}$$

Note that a ramp, F_B, is added in the code to ensure a smooth decrease in the boiling term as dryout occurs.

$$F_B = \min \begin{cases} 416.7(\alpha_l - 0.0001) \\ 1.0 \end{cases} \tag{533}$$

The sensible heat transfer coefficient, h_{wb}, is calculated as it would be for single-phase liquid—by choosing the maximum of the heat transfer coefficients predicted by the laminar flow model given in Eq. (489) or by the turbulent, Dittus-Boelter model given in Eq. (480).

The heat transfer coefficient to vapor, h_{wv}, is calculated as it was for the subcooled nucleate boiling region. It is zero unless void is above 0.999, in which case it is calculated as it was for single-phase vapor in Section 12.4

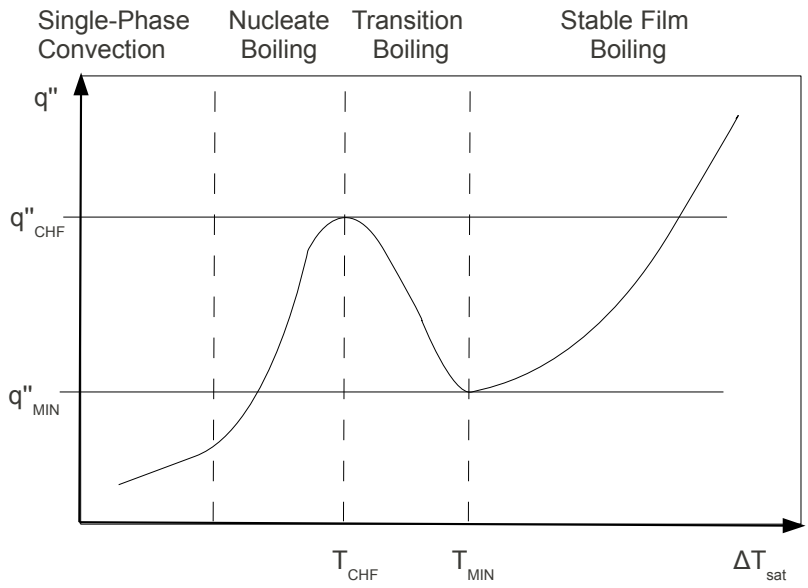

Figure 30. Boiling curve.

12.9 DEPARTURE FROM NUCLEATE BOILING (DNB)

DNB is the point at the top of the boiling curve shown in Figure 30. It is the point where vapor blanketing of the heated surface begins to decrease heat transfer from the surface to fluid with increasing temperature. Operating the rod in post-CHF heat transfer regimes can lead to high temperatures and subsequent rod failure.

The calculation of DNB is required to properly assign the heat transfer regime in CTF. The determination of the heat transfer regime is made by comparing the local heat flux to the CHF. CHF is the heat flux at which DNB occurs. In practice, CTF actually determines a temperature at which CHF occurs (T_{chf}) and then compares the local rod surface temperature to that value; if the local temperature is above T_{chf}, then the heat transfer regime changes to a post-CHF heat transfer regime. Otherwise, the heat transfer regime will be pre-CHF.

Calculating the CHF is the first step in this process. The local value of CHF is calculated using one of many available models in CTF. After CHF is calculated, T_{chf} is determined using an iterative process that is described in Section 12.1.2.

12.9.1 No Model

It is possible to use no model. In this case, the code will skip the CHF calculation and assume that the heat transfer regime is always pre-CHF. This feature should only be used when the user is certain that CHF will not be encountered. If the user is sure of this, some savings can be made in computational time.

12.9.2 Biasi Model

An overview of the CHF calculation algorithm for the Biasi model is shown in Figure 31. The standard model consists of considering three possible CHF scenarios:

1. Pool boiling
2. Forced convective boiling

3. Annular film dryout

If the mesh cell was labeled as having a hot wall in the INTFR subroutine, then CHF is calculated for the annular film dryout region. If the mesh cell does not contain a hot wall, then the void fraction is checked because the boiling regime could still be in annular film dryout. If $\alpha_v > 0.9$, the annular film dryout CHF is calculated and if $\alpha_v > 0.99$, then the annular film dryout CHF is multiplied by a ramping factor to reduce CHF down to 20 % of its calculated value as α_l approaches 0.005.

If α_v was less than 0.9, then CHF is calculated for the forced-convection boiling regime. If the mass flux is less than 30 $g/cm^2 \cdot s$, then the CHF is ramped to CHF for the pool boiling scenario—the maximum of either the forced-convection CHF or the annular film dryout CHF multiplied by a ramping factor to account for low liquid void is chosen.

Whether forced-convection or pool boiling is selected, a check is made for void over 0.85, and if so, then the CHF is ramped towards annular film dryout CHF as shown in Eq. (534). The heat flux, q'' in Eq. (534), could be either pool boiling CHF or forced-convection CHF, depending on the flow conditions.

$$f(q''_{\mathrm{AF}}, q'') = 20[q''(\alpha_l - 0.1) + q''_{\mathrm{AF}}(0.15 - \alpha_l)] \tag{534}$$

For any of the three scenarios, the CHF is ramped towards the single phase vapor heat transfer coefficient times a ΔT of 50 °F if α_v is greater than 0.99. The ramp is as follows:

$$R_2 = \min[1.0, 100(1 - \alpha_v)] \tag{535}$$

With the overview of the CHF selection algorithm complete, the reader's attention is now turned to defining the actual CHF model's employed.

12.9.2.1 Pool Boiling

The pool boiling critical heat flux is given by modification of the equation from Zumber et al. [107] as recommended by Bjornard and Griffith [108]. The Zuber equation is shown in Eq. (536).

$$q''_{\mathrm{chf}} = 0.9(1 - \alpha_v)\frac{\pi}{24} H_{\mathrm{fg}} \rho_g^{0.5} \left[g_c g \sigma (\rho_f - \rho_g) \right]^{0.25} \tag{536}$$

The constant recommended by Zuber, $0.9\pi/24$, is not used in CTF. The data presented by Zuber shows a range in the value of the leading constant going from 0.10 to 0.24 (compared to the recommended value of 0.1178). For CTF, the average of this range was taken (0.17) and was multiplied by 0.9, which is a multiplication factor for vertical rod geometry recommended by Lienhard and Dhir [109]. This results in a leading coefficient of 0.15.

$$q''_{\mathrm{chf}} = 0.15(1 - \alpha_v) H_{\mathrm{fg}} \rho_g^{0.5} \left[g_c g \sigma (\rho_f - \rho_g) \right]^{0.25} R_3 \tag{537}$$

The ramping factor, R_3, ranges between 0.2 and 1.0, with the magnitude increasing as liquid void decreases. It is defined as

$$R_3 = \max\left[0.2, (1 - \alpha_v)\right]. \tag{538}$$

Equation (537) is compared against the critical heat flux calculated with the forced convective boiling model, which is discussed in the following section. The maximum of Eqs. (537) and (541) is used for the pool boiling critical heat flux.

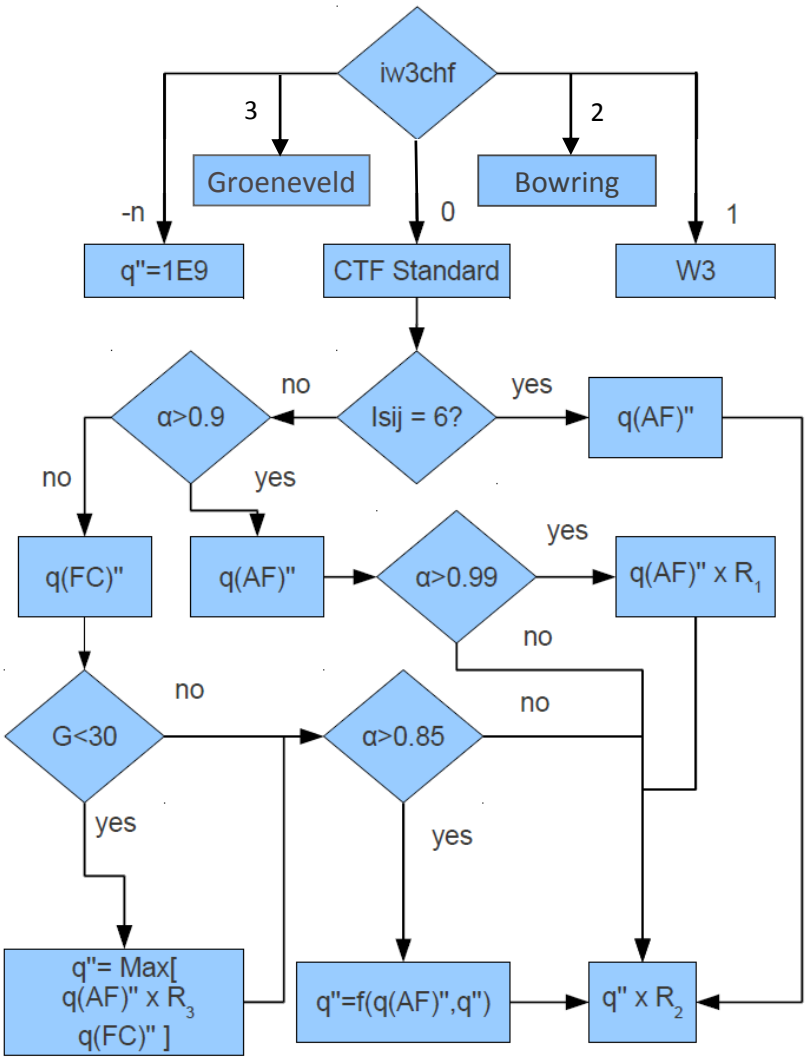

Figure 31. Flow chart for the CHF selection algorithm.

12.9.2.2 Forced Convection Boiling

The forced convection critical heat flux is given by the Biasi correlation. CTF uses the modified form of the Biasi correlation given by Sardh and Becker [110], which differs slightly from the original formulation given by Biasi [111]. The correlation consists of equations for low-quality and high-quality flow.

$$q''_{b1} = 8{,}761{,}800 \cdot G^{-1/6}\left[1.468F(P)G^{-1/6} - x\right]D_h^{-n} \tag{539a}$$

$$q''_{b2} = 47{,}701{,}900 \cdot H(P)(1-x)D_h^{-n}G^{-0.6}\,, \tag{539b}$$

here

$q'' =$ critical heat flux ($^{\mathrm{BTU}}/_{\mathrm{hr\cdot ft^2}}$)

$G =$ mass flux ($^{\mathrm{g}}/_{\mathrm{cm^2\cdot sec}}$)

$$n = \begin{cases} 0.6 & \text{if } D_h < 1.0\,\mathrm{cm} \\ 0.4 & \text{if } D_h > 1.0\,\mathrm{cm} \end{cases}$$

The functions $F(P)$ and $H(P)$ are functions of pressure in bars and are calculated as follows:

$$F(P) = 0.7249 + 0.099P\exp\left(-0.032P\right) \tag{540a}$$

$$H(P) = -1.159 + 0.149P\exp\left(-0.019P\right) + 8.99P\left(10 + P^2\right)^{-1} \tag{540b}$$

The critical heat flux is then calculated as the maximum of q''_{b1}, q''_{b2}, or a fixed value of $90,000\,^{\mathrm{BTU}}/_{\mathrm{hr\cdot ft^2}}$.

$$q''_{\mathrm{chf,fc}} = \max\begin{cases} q''_{b1} \\ q''_{b2} \\ 90,000\,^{\mathrm{BTU}}/_{\mathrm{hr\cdot ft^2}} \end{cases} \tag{541}$$

12.9.2.3 Annular Film Dryout

In this region, DNB occurs as a result of the film drying out, which is a complex function of several variables. Although CHF in the annular film dryout region is not limited by correlation, the critical heat flux is calculated using the Zuber equation, which was also used for pool boiling. The form used for the annular film dryout region is shown in Eq. (542).

$$q''_{\mathrm{chf}} = 0.15(1-\alpha_v)H_{\mathrm{fg}}\rho_g^{0.5}\left[g_c g\sigma(\rho_f - \rho_g)\right]^{0.25} \tag{542}$$

If the mesh cell is not in a hot wall flow regime and the void fraction is greater than 0.99, then Eq. (542) will be multiplied by a ramping factor to reduce CHF as liquid disappears.

$$R_1 = \max[0.2, 200(\alpha_l - 0.005)] \tag{543}$$

12.9.3 W-3 Correlation

The W-3 correlation developed by Tong ([112][113]) is the most widely used correlation for evaluating DNB in PWRs [114]. The critical heat flux is determined using the following equation:

$$\begin{aligned}\frac{q''_{\mathrm{w3,D_{heated},}u}}{10^6} =& \{(2.022 - 0.0004302p) + (0.1722 - 0.0000984p) \\ & \exp[(18.177 - 0.004129p)x_e]\}[(0.1484 - 1.596x_e + 0.1729x_e|x_e|)\frac{G}{10^6} + \\ & 1.037](1.157 - 0.869x_e)[0.2664 + 0.8357\exp(-3.151D_{heated})] \\ & [0.8258 + 0.000794(h_f - h_{\mathrm{in}})],\end{aligned} \tag{544}$$

where

$$\begin{aligned} q''_{\mathrm{w3,D_{heated},}u} &= \text{critical heat flux based on heated diameter } [\mathrm{BTU/hr{\cdot}ft^2}] \\ p &= \text{pressure [psia]} \\ x_e &= \text{local steam thermodynamic quality} \\ D_{heated} &= \text{heated hydraulic diameter [in]} = \\ h_{\mathrm{in}} &= \text{inlet enthalpy } [\mathrm{BTU/lbm}] \\ G &= \text{mass flux } [\mathrm{lbm/hr{\cdot}ft^2}] \end{aligned}$$

The W-3 correlation is applicable to the following range of operating conditions:

$$\begin{aligned} p &= 800 \text{ to } 2300 \text{ psia} \\ \frac{G}{10^6} &= 1.0 \text{ to } 5.0 \ \mathrm{lbm/hr{\cdot}ft^2} \\ D_{heated} &= 0.2 \text{ to } 0.7 \text{ in} \\ x_e &= -0.15 \text{ to } 0.15 \\ L &= 10 \text{ to } 144 \text{ in} \end{aligned}$$

Note that the original form of the W-3 correlation developed by Tong used the hydraulic diameter in place of the heated hydraulic diameter given in Eq. (544). However, Tong developed a cold wall factor to account for the effect of unheated surfaces. Consider two separate heated channels with the same hydraulic conditions (including the same wetted perimeter) and the same total heat added per unit length; if one of these channels is connected only to heated surfaces whereas the other channel is connected to a combination of heated and unheated surfaces, then the latter channel is expected to have a lower CHF value because there is less total liquid flow adjacent to the heated surfaces and therefore less ability to remove heat from the wall.

The cold wall factor provided by Tong is given by

$$\begin{aligned}\frac{q''_{\mathrm{w3,cold\ wall,u}}}{q''_{\mathrm{w3,D_{heated},u}}} =& 1.0 - \mathrm{Ru}[13.76 - 1.372e^{1.78x_e} \\ & - 4.732(\frac{G}{10^6})^{-0.0535} - 0.0619(\frac{p}{10^3})^{0.14} \\ & - 8.509(D_{heated})^{0.107}],\end{aligned} \tag{545}$$

where

$$Ru = 1 - \frac{D_h}{D_{heated}}$$

In CTF, the cold wall factor calculation is always enabled when using the W-3 correlation, and this factor is used in conjunction with the form of Eq. (544) using the heated hydraulic diameter, as prescribed by Tong.

Equation (545) gives the CHF for uniform axial heat flux profiles; however, the W-3 model also includes a factor for handling nonuniform axial heat flux profiles, known as the *Tong F-factor*. The factor is applied as shown below to provide a CHF for nonuniformly heated rods.

$$q''_{\text{chf,cold wall,nu}} = \frac{q''_{\text{w3,cold wall,u}}}{F} \tag{546}$$

The uniform CHF, calculated by Eq. (544), is represented by $q''_{\text{w3,u}}$, and the CHF for nonuniformly heated rods is represented by $q''_{\text{w3,nu}}$. The Tong F-factor is intended to capture the memory effect of the flow in CHF conditions. The boundary layer energy and bubble content affect the occurrence of CHF in both PWRs and BWRs. In the PWR, the boundary layer carries bubbles that result in a local peak of void near the wall, with a thin liquid film coating the wall. As energy and heat flux increases, the film may evaporate, which triggers CHF. In the BWR, the flow regime is typically annular, with a vapor core in the channel center and a liquid film coating the wall. Again, the film may dry out as heat flux increases and liquid subcooling decreases, resulting in CHF that depends on the local quality, mass flux, and pressure. In addition to the local effect, for BWRs, the power shape and heated length also affect CHF incipience because of the hydrodynamic interaction between the vapor core, liquid film, and wall boiling along the length of the channel. The CHF occurrence, therefore, is dependent on the upstream conditions that dictate local energy and void content of the flow, as well as phase interactions at high quality.

Tong used a theoretical basis to develop the F-Factor by analyzing a control volume over the boundary layer. His assessment takes upstream heating into account, resulting in an integration from the axial location where boiling starts to the current location being analyzed. This relationship is shown in Eq. (547).

$$F = \frac{C \int_0^l q''(z') \exp([-C * (l - z')]\, dz'}{q'' * l\,[1 - \exp(-C * l)]} \tag{547}$$

Note that the lower bound of the definite integration, 0, is referring to the ONB location. The l refers to the current axial location where CHF is being calculated. The Tong factor calculation has been implemented into CTF using a *semi*-analytical approach. This is done by solving the integral analytically for each rod level, assuming the heat flux is constant over that axial level. This is consistent with the control volume approach of CTF; all rod properties are constant for a discrete axial level. The analytical solutions are summed for each level from 0 to l to form an approximation of the total integral. In equation form, this appears as follows:

$$\frac{\Sigma_{j=J_{\text{ONB}}}^{J_l} q''(j)\,[\exp(-C(z(J_l) - z(j + 1/2))) - \exp(-C(z(J_l) - z(j - 1/2)))]}{q''(J_l)(1 - \exp(-Cz(J_l)))} \tag{548}$$

The j term is a counter over the discrete axial levels in the integration. J_{ONB} is the axial level where ONB has occurred, and J_l is the current axial level being analyzed in the code. The heat flux, $q''(j)$, is constant

for each axial level, j. The term in square brackets is the analytical solution of the definite integral for the given level, j. The axial location is substituted at the top, $z(j + 1/2)$, and bottom, $z(j - 1/2)$, of the axial level, j. Other terms include the axial location at the center of the current cell, $z(J_l)$, and the heat flux at the current axial level, $q''(J_l)$.

The C term is a factor that accounts for flow quality and mass flux as defined in Eq. (549).

$$C = 0.15\frac{(1.0 - x_{\text{DNB}})^4.31}{(G/10^6)^{0.478}} \tag{549}$$

G is the local mass flux near the rod surface, which is in units of lbm/hr-ft^2, and x is the equilibrium quality adjacent the surface. The C factor has units of in^{-1} and is converted to ft^{-1} before being used in Eq. (547). Note that in a subcooled flow, C will be large, and in turn, F will be close to 1.0, which means the local CHF will be determined by the local CHF predicted by the W-3 correlation. In flows with high quality content, C will be small, F will be large, and local CHF will be determined largely by upstream flow effects.

Note that the Tong F factor is calculated for each rod surface and level. This is different from the W-3 calculated CHF value given by Eq. (544), which is calculated for each fluid cell in the mesh. The Tong F factor is then applied to the adjacent fluid-cell CHF so that a CHF value is obtained for each rod surface and level. Also note that the Tong F-factor is not calculated for surfaces where boiling is not occurring; the F-factor is simply assigned a value of 1.0 in this case. Therefore, rods with no boiling along the axial length will be assigned an F-factor of 1.0 everywhere and will simply retain the uniform CHF value obtained from Eq. (544). The Tong F-factor is calculated automatically when the W-3 CHF correlation is selected; it is skipped when the W-3 correlation is not selected.

12.9.4 Bowring Correlation

As developed by R.W. Bowring [115], the Bowring CHF correlation was created for circular ducts under a wide range of pressures and mass fluxes. Bowring's correlation is based on experimental data from uniformly heated tubes. With known subcooling, pressure, mass flux, and tube length, Bowring would increase the heating rate to each tube until DNB was achieved at the exit. The Bowring correlation is therefore applicable to the following range of operating conditions:

$$\begin{aligned} p &= 34 \text{ to } 2,750 \text{ psi} \\ G &= 0.1 \text{ to } 13.7 \ ^{\text{Mlb}}/_{\text{hr·ft}^2} \\ D_h &= 0.08 \text{ to } 1.76 \text{ in} \\ L &= 6.0 \text{ to } 144.0 \text{ in} \end{aligned}$$

In the original paper, R.W. Bowring presents the equation for the CHF in the form

$$q''_{\text{chf}} = \frac{A - B\Delta h_{sub,in}}{C + L}, \tag{550}$$

where $\Delta h_{sub,in}$ is the subcooling at the inlet, and L is the length at which CHF occurs. The remaining portions of the correlation can be described as follows using traditional British units:

$$A = \frac{2.317\left(h_{fg}B\right)F_1}{1 + 3.092F_2D_h^{1/2}G} \tag{551}$$

$$B = \frac{DG}{4} \tag{552}$$

$$C = \frac{104.4 F_3 DG}{1 + 0.347 F_4 G^n} \tag{553}$$

$$n = 2.0 - 0.5 p_R \tag{554}$$

$$p_R = 0.001 p \tag{555}$$

The pressure dependent constants are as follows:

For $p_R < 1$ psi,

$$F_1 = \frac{p_R^{18.942} \exp\left[20.89\left(1 - p_R\right)\right] + 0.917}{1.917} \tag{556a}$$

$$F_2 = \frac{1.309 F_1}{p_R^{1.316} \exp\left[2.444\left(1 - p_R\right)\right] + 0.309} \tag{556b}$$

$$F_3 = \frac{p_R^{17.023} \exp\left[16.658\left(1 - p_R\right)\right] + 0.667}{1.667} \tag{556c}$$

$$F_4 = F_3 p_R^{1.649} \tag{556d}$$

For $p_R > 1$ psi,

$$F_1 = p_R^{-0.368} \exp\left[0.648\left(1 - p_R\right)\right] \tag{557a}$$

$$F_2 = \frac{F_1}{p_R^{-0.448} \exp\left[0.245\left(1 - p_R\right)\right]} \tag{557b}$$

$$F_3 = p_R^{0.219} \tag{557c}$$

$$F_4 = F_3 p_R^{1.649} \tag{557d}$$

The form given in Eq. (550) is restrictive because it requires knowledge of where the CHF occurs. A modified form can be obtained by algebraically manipulating Eq. (550):

$$q''_{\text{chf}} = \frac{A - B\left(q''_{\text{chf}} \frac{L}{B} - \Delta h_{sub,in}\right)}{C}. \tag{558}$$

Because Bowring's experiment was performed for uniformly heated tubes, an expression for the equilibrium quality can be developed from an energy balance:

$$x_e(z) = q''_o \frac{z}{B h_{fg}} - \frac{\Delta h_{sub,in}}{h_{fg}}, \tag{559}$$

where q''_o is the local heat flux at the axial location z. The critical equilibrium quality corresponding to the CHF can then be developed as follows:

$$x_{e,crit} h_{fg} = q''_{\text{chf}} \frac{L}{B} - \Delta h_{sub,in} \tag{560}$$

Substituting Eq. (560) into Eq. (558) and treating the critical equilibrium quality as the local equilibrium quality yields the final result for the modified Bowring CHF:

$$q''_{\text{chf}} = \frac{A - B h_{fg} x_e}{C} \tag{561}$$

The above expression is independent of the CHF location and yields the critical heat flux corresponding to any local equilibrium quality. This form is encoded into CTF for the Bowring correlation.

12.9.5 Groeneveld Look-up Tables

Developed by D. C. Groeneveld et al [116] from available experimental data in 8 mm tubes, the Groeneveld CHF look-up tables are simply a collection of tabulated values for the CHF as a function of equilibrium quality, pressure, and mass flux. The resulting Groeneveld CHF can be expressed as follows:

$$q''_{\text{chf}} = q''_{\text{LUT}} \prod_{i=1}^{8} K_i, \tag{562}$$

where q''_{LUT} is the interpolated CHF from the look-up tables. The Groeneveld look-up tables are applicable in the following range of operating conditions:

$$\begin{aligned} p &= 0.1 \text{ to } 21 \text{ MPa} \\ G &= 0.0 \text{ to } 8,000 \text{ kg/s·m}^2 \\ x_e &= -0.5 \text{ to } 0.9 \\ D_h &= 0.003 \text{ to } 0.025 \text{ m} \end{aligned}$$

The look-up tables are stored in CTF as a $15 \times 21 \times 23$ array in pressure, mass-flux, and equilibrium quality. The interpolation scheme begins by reducing the large array to a $2 \times 2 \times 2$ array that bounds the current state point. This resulting $2 \times 2 \times 2$ array is then linearly interpolated in pressure, then in mass-flux, and finally in equilibrium quality, resulting in a final interpolated value for q''_{LUT}. This can be seen in detail in the CTF Validation and Verification Manual [117].

If CTF calculates a parameter that is out of bounds in the Groeneveld look-up tables, then the value will be reset to the boundary. For instance, if the value $x_e = -0.7$ was passed to the Groeneveld function in CTF, then it would be reset to $x_e = -0.5$ (the lowest boundary), and the calculation would proceed. This makes the encoded Groeneveld function in CTF particularly difficult to break.

The Groeneveld look-up table values are accompanied by eight available forms or "K" factors [118] [119] which adjust the interpolated CHF value for various bundle or subchannel effects. The first available K-factor scales the look-up table CHF as determined from 8 mm tubes to a generic tube or hydraulic diameter:

$$K_1 = \begin{cases} \left(\frac{0.008}{D_h}\right)^{1/2} & \text{for} \quad 0.003 < D_h < 0.025\,\text{m} \\ 0.57 & \text{for} \quad D_h \geq 0.025\,\text{m} \end{cases} \tag{563}$$

The second K-factor scales bundle effects for subchannel considerations. This K-factor would be applied to a bundle-averaged solution to reconstruct subchannel effects:

$$K_2 = \min\left[1, \left(\frac{1}{2} + \frac{2\delta}{D_{rod}}\right)\exp\left(-\frac{x_e^{1/3}}{2}\right)\right] \tag{564a}$$

$$\delta = \text{Pitch} - D_{rod} \tag{564b}$$

The next applied K-factor describes the perturbation in the CHF from enhanced mixing due to spacer grids:

$$K_3 = 1 + A\exp -\frac{0.1L_{sp}}{D_h} \tag{565a}$$

$$A = 1.5\,(k_{loss})^{0.5}\left(\frac{G}{1000}\right)^{0.2}, \tag{565b}$$

where L_{sp} is the distance upstream from the spacer grid, and k_{loss} is the spacer grid loss coefficient. The so-called "heated length" K-factor is described as follows for $L/D_h > 5$:

$$K_4 = \exp\left[\left(\frac{D_h}{L}\right)\exp\left(2\alpha_{HEM}\right)\right] \tag{566a}$$

$$\alpha_{HEM} = \frac{x_e\rho_f}{x_e\rho_f + (1 - x_e)\rho_g}, \tag{566b}$$

where α_{HEM} is the void fraction as defined in the homogeneous equilibrium model. The value is initialized as zero in CTF and is only calculated for non-negative x_e. Finally, the axial heat flux distribution K-factor scales the CHF for nonuniform heating:

$$K_5 = \begin{cases} 1.0 & \text{for} \quad x_e \leq 0 \\ q''(z)/q''_{BLA} & \text{for} \quad x_e > 0 \end{cases}, \tag{567}$$

where q''_{BLA} is the boiling length averaged heat flux. This final K-factor has a similar purpose to the W-3 correlation's Tong factor. Unlike factors K_1 through K_4, which are fluid cell properties, the K_5 factor is a rod-surface–dependent property.

The next K-factor accompanying the Groeneveld look-up table scales the effect of the local radial power for radially nonuniform bundle power:

$$K_6 = \begin{cases} 1.0 & \text{for} \quad x_e \leq 0 \\ q''(z)_{avg}/q''(z)_{max} & \text{for} \quad x_e > 0 \end{cases} \tag{568}$$

Similar to K_2, this K-factor would be used to reconstruct local pin power effects from a bundle averaged calculation. The seventh K-factor shows the effect on CHF from varying flow orientation specifically from cross-flow:

$$K_7 = 1 - \exp\left[-\left(\frac{T_1}{3}\right)^{0.5}\right] \tag{569a}$$

$$T_1 = \left(\frac{1 - x_e}{1 - \alpha}\right)^2 \frac{f_L G^2}{g D_h \rho_f \left(\rho_f - \rho_g\right) \alpha^{0.5}}, \tag{569b}$$

where f_L is the friction factor of the channel and α is the void fraction. The final K-factor determines the effect of low vertical flow or reflood on the CHF:

$$\begin{cases} K_8 = 1.0 & \text{for} \quad G < -400\,\text{kg/s·m}^2 \\ \text{Linear interpolation between } q''_{LUT} & \\ \text{from } \mid G \mid \text{ and value predicted from} & \\ q''_{LUT} = q''_{LUT,G=0,x_e=0}\,(1 - \alpha_{HEM})\,C_1 & \text{for} \quad -400 \le G < 0\,\text{kg/s·m}^2 \end{cases} \tag{570a}$$

$$C_1 = \begin{cases} 1.0 & \text{for} \quad \alpha_{HEM} < 0.8 \\ \dfrac{0.8 + 0.2\rho_f/\rho_g}{\alpha_{HEM} + (1 - \alpha_{HEM})\rho_f/\rho_g} & \text{for} \quad \alpha_{HEM} > 0.8 \end{cases}, \tag{570b}$$

where $G = 0, x_e = 0$ refers to a pool boiling situation.

Currently, only K_1, K_4, and K_5 are encoded into CTF. K_2 is not currently considered as individual subchannel geometry and is already taken into account [119]. Likewise, K_6 and K_7 are not considered because cross-flow and nonuniform radial heating are already taken into account. The spacer grid k-factor, K_3, is not being used because the Yao, Hochreiter, and Leech correlation [120] is already accounting for enhanced mixing and heat transfer upstream of spacer grids. The K_8 factor is also not considered at this time.

12.10 DISPERSED FLOW FILM BOILING

The DFFB heat transfer regime is the base heat regime when post-CHF heat transfer is determined to exist. This means that the DFFB models will always be calculated first before checking if the other post-CHF regimes are encountered. The heat transfer effects may impact the occurrence of other heat transfer regimes or the magnitude of the heat transfer calculated for those other regimes. The DFFB regime is encountered whenever the surface exceeds the CHF temperature plus 0.1 °F. If the flow regime is not determined to be IAFB (see Section for information on the IAFB criteria) and the surface temperature is also above the MFB temperature, then the heat transfer regime will be pure DFFB.

The DFFB heat transfer is a combination of convective heat transfer to vapor, radiative heat transfer to vapor, radiative heat transfer to liquid (droplets), and boiling heat transfer occurring from the collision of droplets with the heated rods. The vapor convective heat transfer term was calculated in Section 12.4, and the radiative heat transfer terms are calculated in Section 12.13. Both of these terms are summed together to obtain the total vapor HTC. The liquid HTC is calculated using the radiative heat transfer to the droplets, which is also discussed in Section 12.13.

The droplet impingement is used to calculate the boiling HTC, which is discussed here. It is limited to the q''_{chf} value.

$$q''_b = \max[q''_{\text{chf}}, q''_{de}] \tag{571}$$

The de-entrainment boiling heat flux is calculated using a de-entrainment coefficient which is multiplied by total droplet mass flux and the latent heat of vaporization.

$$q''_{de} = h_{\text{fg}} C_{\text{de}} G_e \tag{572}$$

The de-entrainment coefficient C_{de} is calculated as follows:

$$C_{\text{de}} = 0.00172 \mu_f \sqrt{\frac{f}{D_e \sigma \rho_f}}, \tag{573}$$

where μ_f is the saturated liquid viscosity, f is the surface friction factor, D_e is the equivalent diameter of the channel, σ is the surface tension of the liquid, and ρ_f is the liquid saturation density.

Both axial and transverse components of velocity are included in the droplet mass flux term, G_e, which has units of $^{\text{lbm}}/_{\text{hr}\cdot\text{ft}^2}$. The boiling HTC is calculated considering that only a fraction of droplets contact the heated surface because of the high wall superheat. A wall-wetting fraction, ϵ_{wet}, is used to reduce the amount of heat transfer as follows:

$$h_{wb} = \frac{q''_{de} \epsilon_{\text{wet}}}{T_w - T_f} \tag{574}$$

This wall-wetting fraction was developed by Ganic [121] and is calculated as follows:

$$\epsilon_{\text{wet}} = \exp\left[1 - \left(\frac{T_w}{T_f}\right)^2\right] \tag{575}$$

12.11 INVERTED ANNULAR FILM BOILING

The inverted annular film boiling heat transfer coefficients are calculated if void is between 0.4 and 0.95 and if the inverted annular film boiling heat flux is greater than the DFFB heat flux. Therefore, the DFFB heat transfer is calculated first for comparison to the IAFB heat flux.

The IAFB heat flux is calculated with use of the modified Bromley correlation [122].

$$h_{\text{brom}} = 0.62 \left(\frac{D_h}{\lambda}\right)^{0.172} \left[\frac{k_v^3 \rho_v (\rho_f - \rho_g) h_{\text{fg}} g}{D_h \mu_v (T_w - T_f)}\right]^{1/4} \tag{576}$$

The critical wavelength, λ, is given as

$$\lambda = 2\pi \sqrt{\frac{g_c \sigma}{g(\rho_f - \rho_g)}} \tag{577}$$

The heat flux can then be obtained by multiplying the heat transfer coefficient by the wall superheat.

$$q''_{\text{brom}} = h_{\text{brom}}(T_w - T_f) \tag{578}$$

For the heat regime to be IAFB, the following inequality must be true:

$$q''_{\text{brom}} + q''_{\text{tb}} > q''_{\text{dffb}} \tag{579}$$

q''_{tb} is the modified annular film boiling heat flux. It is obtained by multiplying the Zuber equation for CHF—Eq. (542)—by the liquid void fraction and the liquid contact effectiveness previously given in Eq. (575). The expression is shown as follows:

$$q''_{\text{tb}} = q''_{\text{chf}} \alpha_l \epsilon_{\text{wet}}. \tag{580}$$

If the inequality of Eq. (579) is false, then the regime is not IAFB. In that case, the regime will be DFFB if the surface temperature is above the MFB temperature or transition boiling if it is below. However, if the inequality is true, then the regime will be pure IAFB if the void fraction is less than 0.4 or transition between IAFB and DFFB if the void fraction is between 0.4 and 0.95. In either case, there will be heat transfer contributions to the liquid and the vapor phases. The liquid HTC (h_ℓ) will be a result of the radiative heat transfer between the wall and the droplets, which was already discussed in Section 12.10. The boiling and vapor HTCs (h_b and h_v) will be calculated from the IAFB models. The determination of how much of the heat flux goes into one phase vs. the other is made using a linear ramp based on the wall temperature in comparison to the vapor temperature. This ramp is presented below:

$$F_q = 1.11 \alpha_v \sqrt{\frac{T_w - T_v}{T_w - T_f}} \tag{581}$$

If the wall temperature is less than the vapor temperature, then this factor is set to zero, which effectively means that all of the heat flux goes towards boiling heat transfer, and none of it goes to the vapor phase. For pure IAFB heat transfer, the boiling heat transfer and vapor heat transfer are calculated as follows.

$$h''_b = \frac{(1 - F_q) \max(q''_{\text{brom}} - q''_{v,\text{dffb}}, 0.0) + q''_{\text{tb}}}{T_w - T_f} \tag{582}$$

$$h''_v = h_{v,\text{dffb}} + \frac{F_q \max(q''_{\text{brom}} - q''_{v,\text{dffb}}, 0.0)}{T_w - T_v} \tag{583}$$

The boiling term is a combination of the Bromley heat flux and the CHF. Note that the DFFB heat flux to the vapor phase is subtracted from the Bromley heat flux with a limiter applied to ensure that the value remains greater than or equal to zero. This is done because the Bromley model was developed from experimental data that includes heat transfer to both vapor and liquid. The vapor heat transfer, which includes radiative heat transfer to vapor and convective heat transfer to vapor, is removed so that only the liquid heat transfer remains. This liquid heat transfer is then split using the F_q factor to increase its input to the vapor phase when the vapor becomes hotter than the wall surface. Note that in the case of the vapor HTC, the vapor heat transfer effects due to DFFB are added back to h_v. In the case of the boiling HTC, the full CHF is added.

When the void is greater than or equal to 0.4, the heat transfer effects are interpolated between DFFB and IAFB using the following factor:

$$F_r = \frac{0.95 - \alpha}{0.5} \tag{584}$$

The boiling and vapor HTCs are calculated as follows:

$$h_b'' = \max(h_{b,\text{dffb}}, \frac{F_r q_{\text{tb}}''}{T_w - T_f}) + \frac{F_r(1 - F_q)\max(q_{\text{brom}}'' - q_{v,\text{dffb}}'', 0.0)}{T_w - Tf} \tag{585}$$

$$h_v'' = h_{v,\text{dffb}} + \frac{F_r F_q \max(q_{\text{brom}}'' - q_{v,\text{dffb}}'', 0.0)}{T_w - T_v} \tag{586}$$

In this case, the ramped values of boiling and vapor IAFB heat fluxes are used. The CHF contribution to boiling is also ramped, but the maximum of this or the heat transfer caused by droplet impingement in DFFB is taken.

12.12 TRANSITION BOILING

Transition boiling will be a combination of heat transfer effects that occur in DFFB and/or IAFB and CHF. This is only encountered if the temperature is between CHF and MFB temperatures. The heat transfer effects of the combined regimes are determined using a linear interpolation between the CHF and the heat flux at the MFB point in the boiling curve. The total heat flux to the liquid is determined as follows:

$$q_{\text{trans}}'' = F_w R_d q_{\text{chf}}'' + (1 - F_w) q_{\text{min}}'' \tag{587}$$

The interpolation factor F_w, is determined using the model of Bjornard and Griffith [108]. This is calculated as a function of the surface temperature and MFB and CHF temperatures.

$$F_w = \left(\frac{T_w - T_{\text{min}}}{T_{\text{chf}} - T_{\text{min}}} \right)^2 \tag{588}$$

The other ramp, R_d, was added to diminish the heat flux as the liquid phase is depleted. It is defined as follows:

$$R_d = \min \left\{ \begin{array}{c} 1.0 \\ \max \left\{ \begin{array}{c} 0.0 \\ 400(\alpha_l - 0.0025) \end{array} \right. \end{array} \right. \tag{589}$$

The CHF heat flux of Eq. (587) q_{chf}'', is calculated based on whatever CHF model was selected for the simulation. The MFB heat flux q_{mfb}'', is calculated using the current hot-wall HTCs as follows:

$$q_{\text{mfb}}'' = h_\ell(T_{\text{mfb}} - T_\ell) + h_b(T_{\text{mfb}} - T_f) + h_v(T_{\text{mfb}} - T_v), \tag{590}$$

where the surface temperature is set to the MFB temperature. The HTCs depend on what heat regime has been determined. The heat regime may be DFFB, in which case the models of Section 12.10 apply, or it may be IAFB or transitioning between IAFB and DFFB, in which case the models of Section 12.11 apply. Once the total transition boiling heat flux is known, it must be split into the boiling and liquid heat transfer mechanisms. None of the transition boiling heat flux deposits into the vapor, but there still may be heat

flux to the vapor resulting from DFFB or IAFB heat transfer mechanisms. Whatever was calculated for vapor HTC from those heat regimes will be fully applied to the vapor phase in transition boiling. When determining the split between liquid and boiling, the subcooled boiling modification factor is used, which is determined from the Rouhani model presented in Eq. (492). The HTCs are calculated as follows:

$$h_b = \epsilon_\Gamma \frac{q''_{\text{trans}}}{T_w - T_f} \tag{591}$$

$$h_\ell = h_{\ell,\text{dffb}} + (1 - \epsilon_\Gamma) \frac{q''_{\text{trans}}}{T_w - \max(T_\ell, 1°\text{F})}, \tag{592}$$

where the ϵ_Γ term is the subcooled boiling modification factor, and the liquid HTC includes radiative heat transfer between the surface and droplets that was calculated for the DFFB regime, if any.

12.13 RADIATIVE HEAT TRANSFER

The radiative heat transfer models used in CTF were developed by Sun, Gonzalez, and Tien [123]. The basis is that the wall, liquid, vapor, and droplets can all be treated as single nodes between which radiative heat transfer occurs as long as the flow is assumed to be optically thin. The heat transfer between bodies can be modeled using a gray body factor, F, in conjunction with the temperature gradient between bodies (T_w is the wall temperature and T_b is the temperature of the body to which radiative heat transfer flows).

$$q''_r = F(T_w^4 - T_b^4) \tag{593}$$

The heat transfer coefficients for the radiative heat transfer can then be defined. Because the temperature, emissivity, and surface area differ for different bodies (i.e., drops, liquid core, vapor), the different fields will have different gray body factors and temperatures.

$$h_{rwv} = F_{wv} \frac{T_w^4 - T_v^4}{T_w - T_v} \tag{594a}$$

$$h_{rwe} = F_{we} \frac{T_w^4 - T_{\text{sat}}^4}{T_w - T_l} \tag{594b}$$

$$h_{rwl} = F_{wl} \frac{T_w^4 - T_{\text{sat}}^4}{T_w - T_l} \tag{594c}$$

The gray body factors are defined as a function of the Stefan-Boltzman constant, σ_{sb}, the emissivity of the surfaces of interest, and the surface areas of the bodies of interest. Variables R_1, R_2, and R_3 are introduced to simplify the upcoming presentation of the gray body factors. The variables are later defined. The gray body factors are calculated as follows:

$$F_{wv} = \frac{\sigma_{sb}}{R_1 \left(1 + \frac{R_3}{R_1} + \frac{R_3}{R_2}\right)} \tag{595a}$$

$$F_{we} = \min \left\{ \begin{array}{c} \frac{\sigma_{sb}}{R_2 \left(1 + \frac{R_3}{R_1} + \frac{R_3}{R_2}\right)} \\ F_{wl} \end{array} \right. \tag{595b}$$

$$F_{wl} = \frac{\sigma_{sb}}{\frac{1}{\epsilon_l} + \frac{A_w}{A_l}\left(\frac{1}{\epsilon_w} - 1\right)} \tag{595c}$$

The Stefan-Boltzman constant is 1.713×10^{-9} BTU/hr·ft^2·°R^4. A simplification is made for the liquid gray body factor. The only instance of radiation from the wall to the liquid is when inverted annular film flow exists—in this case, radiative heat transfer occurs between the wall and the column of water in the subchannel center. For this case, the liquid emissivity, ϵ_l, is assumed to be 1.0, the wall emissivity, ϵ_w, is assumed to be 0.7, and the vapor void is assumed to be 0.65. The ratio of the wall-to-liquid surface area can be reduced to a function of liquid void fraction if concentric cylinder geometry is considered:

$$\frac{A_w}{A_l} = \frac{D_h}{D_l} = \frac{1}{\sqrt{\alpha_l}} \tag{596}$$

Making these substitutions, the liquid gray body factor becomes a constant of 7.71×10^{-10}. To define the vapor and droplet gray body factors, the R variables are defined:

$$R_1 = \frac{1 - \epsilon_v}{\epsilon_v(1 - \epsilon_v\epsilon_e)} \tag{597a}$$

$$R_2 = \frac{1 - \epsilon_e}{\epsilon_e(1 - \epsilon_v\epsilon_e)} \tag{597b}$$

$$R_3 = \frac{1}{1 - \epsilon_v\epsilon_e} + \frac{1 - \epsilon_w}{\epsilon_w} \tag{597c}$$

The droplet and vapor emissivities are a function of the beam length and droplet and vapor absorption coefficients.

$$\epsilon_e = 1 - \exp(-0.85\alpha_{ea}L_b) \tag{598a}$$

$$\epsilon_v = 1 - \exp(-0.85\alpha_{va}L_b) \tag{598b}$$

The beam length is assumed to be equal to the hydraulic diameter, D_h. The droplet absorption coefficient is a function of droplet surface area and absorption efficiency, Ψ.

$$\alpha_{ea} = \Psi N_d \frac{\pi D_d^2}{4} \tag{599}$$

The droplet diameter is D_d, and the number of droplets is N_d. The absorption efficiency, Ψ_d, has a value of 0.74 for drops having diameters between 0.004 and 0.08 in. The number of droplets can be expressed as a function of void fraction.

$$N_d = \frac{6(1 - \alpha_v)}{\pi D_d^3} \tag{600}$$

The droplet absorption coefficient can then be reduced:

$$\alpha_{ea} = 1.11\frac{(1 - \alpha_v)}{D_d} \tag{601}$$

A modification is then made to lump the continuous liquid phase into the droplet phase absorption coefficient by considering the droplet and liquid void separately and using the equivalent diameter as the beam length for liquid.

$$\alpha_{ea} = 1.11\left(\frac{\alpha_e}{D_d} + \frac{\alpha_\ell}{D_e}\right) \tag{602}$$

The vapor absorption coefficient is a function of absolute fluid pressure, P, and vapor temperature.

$$\alpha_{va} = \frac{P}{14.7}\left[5.6\left(\frac{1000}{T_v + 460}\right)^2 - 0.3\left(\frac{1000}{T_v + 460}\right)^4\right] \tag{603}$$

The droplet and vapor emissivities are constrained to values between 0.001 and 0.75.

$$\epsilon_e = \max\left\{\begin{array}{c}\min\left\{\begin{array}{c}0.75\\ 1 - \exp(-0.85\alpha_e D_h)\end{array}\right.\\ 0.001\end{array}\right. \tag{604a}$$

$$\epsilon_v = \max\left\{\begin{array}{c}\min\left\{\begin{array}{c}0.75\\ 1 - \exp(-0.85\alpha_v D_h)\end{array}\right.\\ 0.001\end{array}\right. \tag{604b}$$

The liquid gray body factor for liquid is assumed to be zero because the effect is lumped into the droplet view factor, and the view factor will be calculated as

$$F^*_{we} = \min(7.71 \cdot 10^{-10}, F_{we}), \tag{605}$$

where F_{we} was calculated in Eq. (595b), and the starred value is used for calculation of surface-to-droplet radiative heat transfer. Because the liquid term is lumped into the droplet term, there is no explicit surface-to-liquid radiative heat transfer.

12.14 GRID RE-WET MODEL

During accident conditions where there is high vapor content in the flow and rod cooling is poor, the presence of spacer grids can lead to improved fuel rod cooling. The reason is that because grids have no internal heat source, they will be the first to quench, and impinging droplets will likely form a film. The presence of a film on the grids will lead to grid cooling and de-superheating of the vapor that flows past the grids. The de-superheated vapor will improve fuel rod cooling downstream. Furthermore, radiative heat transfer from the rods to the grids and radiative heat transfer from the vapor to the grids will be increased.

When grids are quenched, there will be a dry region and a wet region. The heat transfer to the grid will depend on whether the region is wet or dry. Heat balances are performed for each region of the grid as described in the following sections. The grid quench front model is also described, which will depend on the evaporation rate of the grid film, as well as the availability of water from impinging droplets. The grid quench front calculations are performed after the heat balances. The initial grid quench front location is supplied by user input.

12.14.1 Dry Region Heat Balance

The heat balance in the dry region includes the radiative heat transfer to the grid from the fuel rods and vapor, the convective heat flux from the grid to the vapor, and the heat flux from the grid caused by droplets impinging on its surface. This is summarized in equation form:

$$\rho_g C_{p,g} \frac{\partial T}{\partial t} = \frac{P_g}{A_c} \left(q''_{\text{rad}} - q''_{\text{conv}} - q''_{\text{dcht}} \right) \tag{606}$$

This equation is solved for the change in grid temperature from the previous time step. The specific heat, $C_{p,g}$, and the density, ρ_g, are the material properties of the grid. The wetted perimeter and cross-sectional area of the grid strap are characterized by P_g and A_c, respectively. The cross-sectional area of the grid strap is defined in terms of the grid strap thickness, t_g using the following expression:

$$A_c = \frac{1}{2} t_g P_g \tag{607}$$

Equation (606) can be reduced as follows:

$$\Delta T_g = \Delta t \frac{q''_{\text{rad}} - q''_{\text{conv}} - q''_{\text{dcht}}}{\frac{1}{2} t_g \rho_{\text{grid}} C_{p,\text{grid}}}. \tag{608}$$

This leaves the three heat flux terms to be calculated.

12.14.1.1 Radiative heat flux

For simplicity, it is assumed that the rod is completely enclosed by the grid as shown in Figure 32. The rod diameter is given by D_1, and the grid diameter (physically, the grid pitch) is given by D_2.

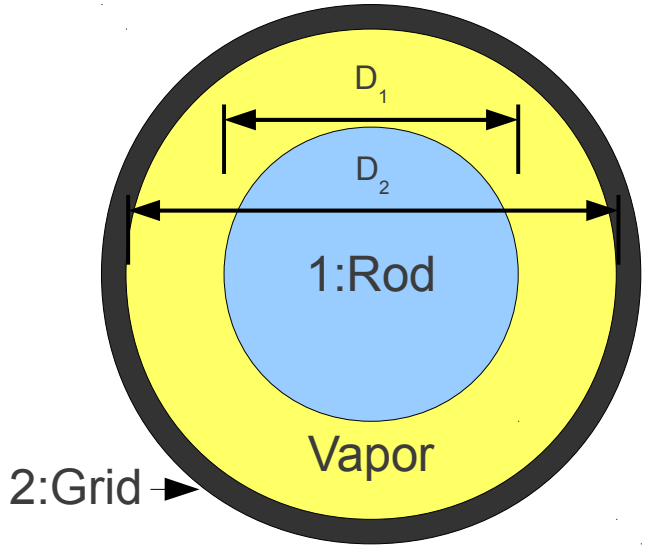

Figure 32. Model of rod and grid for calculating radiative heat transfer to grid.

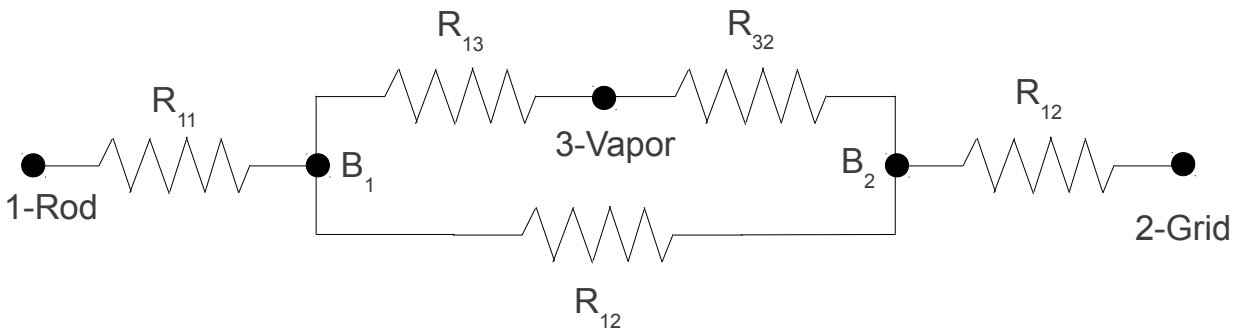

Figure 33. Grid-to-rod radiative heat transfer resistance network.

To determine the radiant heat flux to the grid, the model of Figure 32 is divided into a representative heat transfer resistance network which includes heat transfer from rod to vapor, rod to grid, and vapor to grid. It is shown in Figure 33.

The resistance network includes terms B_1 and B_2 that represent the black body radiosity of the rod and grid, respectively. The heat flux to the rod can be expressed as

$$q_1'' = \frac{B_1 - \sigma T_1^4}{A_1 R_{11}} \tag{609}$$

The Stefan-Boltzmann constant—σ—is $0.1714 \cdot 10^{-8}$ BTU/hr–ft^2·R^4. The surface area of the rod is given by A_1. The radiative heat transfer to the rod is also expressed in terms of the radiative heat transfer contributions from the grid and vapor.

$$q_1'' = \frac{B_1 - B_2}{A_2 R_{21}} + \frac{\sigma T_3^4 - B_2}{A_2 R_{23}} \tag{610}$$

The radiative heat transfer to the grid can also be defined as

$$q_2'' = \frac{B_2 - \sigma T_2^4}{A_2 R_{22}} = \frac{B_1 - B_2}{A_2 R_{21}} + \frac{\sigma T_3^4 - B_2}{A_2 R_{23}} \tag{611}$$

To solve for the radiative heat transfer to the rod and the grid, it is necessary to use Eqs. (609) and (610) to solve for the black body radiosity of the grid in terms of the black body radiosity of the rod. This expression can then be substituted into Eq. (611) to solve for the rod black body radiosity. The grid spacer black body radiosity is first obtained by manipulating Eqs. (609) and (610).

$$B_2 = \left[\frac{B_1 - \sigma T_1^4}{A_1 R_{11}} - \frac{\sigma T_3^4 - B_1}{A_1 R_{13}} \right] A_1 R_{12} + B_1 \tag{612}$$

This expression is substituted into Eq. (611), which is solved for B_1. This leads to a sizeable expression that is reduced using four coefficients.

$$B_1 = \frac{C_1 \sigma T_1^4 + C_2 \sigma T_2^4 + C_3 \sigma T_3^4}{C_4} \tag{613}$$

The coefficients are as follows:

$$C_1 = D(A_1R_{12})(A_1R_{13}) \tag{614a}$$

$$C_2 = (A_1R_{11})(A_1R_{13})(A_2R_{21})(A_2R_{23}) \tag{614b}$$

$$C_3 = (A_1R_{11})[(A_1R_{13})(A_2R_{21})(A_2R_{22}) + (A_1R_{12})D] \tag{614c}$$

$$C_4 = (A_1R_{11})(A_1R_{13})(A_2R_{21})[(A_2R_{23} + A_2R_{22})] + (A_1R_{12})[(A_1R_{13})D + (A_1R_{11})D] \tag{614d}$$

$$D = (A_2R_{21})(A_2R_{23}) + (A_2R_{22})(A_2R_{23} + A_2R_{21}) \tag{614e}$$

The rod's black body radiosity is a function of grid, rod, and vapor temperature; surface area; and radiative heat transfer resistance, and it can be solved. This expression can be substituted into Eq. (612) to define the grid black body radiosity, as well. The black body radiosities can then be substituted back into Eqs. (609) and (611) to obtain the rod and grid radiative heat fluxes, respectively. However, it is first necessary to define the radiative heat transfer resistances, which are functions of surface emissivity and surface area.

$$R_{11} = \frac{1 - \epsilon_1}{A_1\epsilon_1} \tag{615a}$$

$$R_{12} = \frac{1}{A_1F_{12}(1 - \epsilon_3)} \tag{615b}$$

$$R_{22} = \frac{1 - \epsilon_2}{A_2\epsilon_2} \tag{615c}$$

$$R_{21} = R_{12} \tag{615d}$$

$$R_{13} = \frac{1}{A_1\epsilon_3} \tag{615e}$$

$$R_{23} = \frac{1}{A_2\epsilon_3} \tag{615f}$$

The resistances are in units of ft^{-2}. The emissivity of the rod and grid—ϵ_1 and ϵ_2—are both assumed to be 0.9. The emissivity of the vapor is calculated using the Plank mean absorption coefficient as reported by Sparrow[124].

$$\epsilon_3 = 1.0 - \exp[-A_vPL_m] \tag{616}$$

The pressure is represented by P and the mean beam length by L_m. The mean beam length is a constant value of $6.9083{\cdot}10^{-3}$ ft. The vapor absorption coefficient (units of $(psi - ft)^{-1}$) is defined using the Plank mean absorption coefficient:

$$A_v = 2.146 \exp\left[-0.344523221 - \left(2.96092004 \cdot 10^{-3} - 0.444073925 \cdot 10^{-6}T_v\right)T_v\right] \tag{617}$$

The rod-to-grid view factor—F_{12}—which is the fraction of the radiation leaving the rod that is intercepted by the grid, is also necessary for the calculation of heat transfer resistance. Due to the modeling of the grid shown in Figure 32, the rod-to-grid view factor will be 1. Other view factors are provided below:

$$F_{11} = 0 \tag{618a}$$

$$F_{12} = 1 \tag{618b}$$

$$F_{21} = \frac{D_1}{D_2} \tag{618c}$$

$$F_{22} = 1 - \frac{D_1}{D_2} \tag{618d}$$

Equation (611) is solved to determine radiative heat transfer to the grid, which is later substituted into Eq. (608) as the first heat transfer term.

12.14.1.2 Grid convective heat transfer

The heat transfer from the grid is defined as follows:

$$q''_{\text{conv}} = h_{\text{rod}}(\tilde{T}_g - T_v) \tag{619}$$

The heat transfer coefficient used is the same heat transfer coefficient that was calculated for the rod-to-vapor in the HEAT subroutine. The grid temperature in the dry region, T_g, and the vapor temperature, T_v, are used. The grid is located at the top of the continuity mesh cell, so the upper-most fine-mesh node heat transfer coefficient is used. The old time step grid temperature is used explicitly.

12.14.1.3 Droplet impingement heat transfer

There is a final heat transfer term which results from droplets impacting the dry portion of the grid. As the droplets vaporize, they remove heat from the grid. The heat transfer caused by de-entrainment is assumed to be equal to the de-entrainment rate times the latent heat of vaporization and an efficiency factor that defines the number of droplets that evaporate.

$$q''_{\text{dcht}} = S_{de} h_{\text{fg}} \eta \tag{620}$$

Droplets are thought to impact the grid becasue of turbulent interchange causing lateral migration of grids. Therefore, a lateral deposition rate must be calculated using a coefficient times the droplet axial mass flux.

$$S_{de} = C_{de} G_e \tag{621}$$

The deposition coefficient is defined by Paik[125].

$$C_{de} = 0.102 \sqrt{\frac{\mu_v f}{D_h \sigma \rho_l}} \tag{622}$$

The droplet evaporation factor, η, is defined using the old time grid temperature and liquid saturation temperature (absolute values in units of Rankine).

$$\eta = \exp\left[1 - \left(\frac{T_g}{T_f}\right)^2\right] \tag{623}$$

This final heat flux calculated by Eq. (620) is substituted into the dry region heat balance—Eq. (608)—and the dry region grid temperature is calculated.

12.14.2 Wet Region Heat Balance

The wet region heat fluxes are calculated in a manner similar to that used for the dry region, but for a different purpose than determining the grid temperature. The grid temperature is assumed to be equal to the saturation temperature in the wet region because the grid is quenched. The purpose of the heat flux calculations is to determine the evaporation rate of the film that quenches the grid. This information is compared to the droplet deposition rate to determine whether the quench front will advance or recede. Droplet impingement in the wet region does not cause heat transfer from the grid; instead, it causes the quenching film to grow.

The heat balance is calculated using the radiative and convective components:

$$q = (q''_{\text{conv,w}} + q''_{\text{radw}})P_w L_{\text{qf}} \tag{624}$$

The product of the wetted perimeter, P_w, and the length of the quenched portion of the grid, L_{qf}, gives the surface area of the wetted region of the grid.

12.14.2.1 Radiative heat transfer

The calculation for the wet region radiative heat transfer from the fuel rods is similar to the radiative heat transfer calculation performed in the dry region. The black body radiosity of the rod is first repeated:

$$B_1 = \frac{C_1\sigma T_1^4 + C_2\sigma T_2^4 + C_3\sigma T_3^4}{C_4} \tag{613}$$

Because the grid temperature is equal to the saturation temperature, the black body radiosity is modified as follows:

$$B_{1,w} = \frac{C_1\sigma T_1^4 + C_2\sigma T_f^4 + C_3\sigma T_3^4}{C_4} \tag{625}$$

The emissivity of the liquid film is assumed to be equal to the grid emissivity calculated for the dry region. The radiative heat transfer is calculated as follows:

$$q''_{\text{radw}} = \frac{B_2 - \sigma T_f^4}{A_2 R_{22}} \tag{626}$$

12.14.2.2 Convective heat transfer

The convective heat flux is defined as

$$q''_{\text{conv,w}} = h_w(T_v - T_f). \tag{627}$$

The convective heat transfer coefficient is calculated in INTFR. The Nusselt number is calculated as follows:

$$\text{Nu} = \max\left[10, 0.0797\text{Re}_v^{0.6774}\text{Pr}_v^{0.333}\right], \quad \text{if } \text{Re}_v <= 25{,}200 \tag{628a}$$

$$\text{Nu} = 0.023\text{Re}_v^{0.8}\text{Pr}_v^{0.4}, \quad \text{if } \text{Re}_v > 25{,}200 \tag{628b}$$

The convective heat transfer coefficient is calculated using the film conductivity, the wetted grid surface area, and a two-phase enhancement factor.

$$h_w = T\frac{k_l}{D_h}\mathrm{Nu}A \tag{629}$$

The two phase enhancement factor is calculated as follows:

$$T = \min\left[10,\ \sqrt{1 + \frac{0.75\alpha_e D_h C_d}{D_d f}\min(1, \frac{(u_v - u_e)}{u_v^2}}\right], \tag{630}$$

where C_d is the droplet drag coefficient, and D_d is the droplet diameter. The friction coefficient is calculated as follows:

$$f = \frac{0.158}{\max[100, \mathrm{Re}_v]^{.25}} \tag{631}$$

12.14.3 Grid Quench Front Model

The grid quench front model tracks the fraction of the grid that is wetted. The wet region heat balance from the previous section is used to determine whether the quench front grows or recedes. This is done by comparing the evaporation rate (resulting from radiative and convective heat transfer into the grid film) with the droplet deposition heat transfer rate. The droplet deposition rate is the droplet flow rate times the blockage area times a de-entrainment efficiency factor.

$$\dot{m}_{de} = G_e\left(A_g + A_s\right)\eta \tag{632}$$

The droplet mass flux is given by G_e, and the grid and spring cross sectional areas—A_g and A_s—are summed to obtain the total grid blockage area. The final term, η, is used to account for the fact that all of the droplets deposited on the grid will not be available for film advancement. This is because some of the film will be blown off of the grid as a result of sputtering at the quench front. This factor is similar to the de-entrainment factor used in the dry grid region for droplet impingement heat transfer.

$$\eta = \max\left[0.025, \exp\left(1 - \left(\frac{T_g}{T_f}\right)^2\right)\right] \tag{633}$$

The heat transfer due to droplet deposition is as follows:

$$q_{\mathrm{dcht}} = \dot{m}_{de} h_{\mathrm{fg}} \tag{634}$$

This value is compared to the evaporation heat transfer value calculated for the wet region in the previous section. If the difference between the de-entrainment heat transfer and the evaporation heat transfer is positive, then there is more droplet deposition than what is evaporating away. Conversely, a negative value will lead to more evaporation than deposition, and the quench front will recede. The quench front velocity is calculated to determine how the quench front progresses on the grid. To determine a net deposition of droplets in the film (advancement of the quench front), the quench front velocity is calculated using the

two-region analytical conduction solution of Yamanouchi[126]. The quench front velocity is limited by conduction from the dry-to-wet regions of the grid.

$$V_q = \left[\frac{\rho_g C_{p,g}}{2} \left(\frac{\delta}{h_w k_g} \right)^{1/2} \left\{ \left(1 + 2 \frac{T_g - T_w}{T_w - T_f} \right)^2 - 1 \right\}^{1/2} \right]^{-1} \tag{635}$$

The terms are as follows:

ρ_g	Grid density
$C_{p,g}$	Grid specific heat
k_g	Grid conductivity
δ	Grid strap half thickness
h_w	Heat transfer coefficient of the wet region
T_w	Minimum film boiling temperature (T_f + 234 °F)

This velocity is limited using the wet region heat transfer. The heat transfer at the quench front should be at its maximum. The heat transfer coefficient is limited using the critical heat flux defined by Zuber [107], given by Eq. 536.

$$h_w = \frac{q''_{\text{chf}}}{T_w - T_f} \tag{636}$$

A second limit is placed on the quench front velocity to account for the fact that a limited amount of water is available for advancing the quench front. The net de-entrainment rate is as follows:

$$\dot{m}_{\text{QF,net}} = \dot{m}_{de} - \frac{(q''_{\text{radw}} + q''_{\text{conv}}) P_g L_g}{h_{\text{fg}}}. \tag{637}$$

The energy removed at the quench front cannot exceed the liquid availability times the latent heat of vaporization. The energy removed by quenching is a function of the velocity of the quench front. The limit can be imposed as follows:

$$\dot{m}_{\text{QF,net}} h_{\text{fg}} >= (\rho C_p A_x)_g V_{qf} (T_g - T_f) \tag{638}$$

This limits the quench front velocity to

$$V_{qf} <= \frac{\dot{m}_{\text{QF,net}} h_{\text{fg}}}{(\rho C_p A_x)_g (T_g - T_f)}. \tag{639}$$

If this limit is substituted into Eq. 635, then the Yamanouchi quench front velocity equation, the maximum value of the wet region heat transfer coefficient, can be determined.

$$h_w <= \left(\frac{\delta}{4 k_g} \right) \left(\frac{\dot{m}_{\text{QF,net}} h_{\text{fg}}}{P_g \delta (T_g - T_f)} \right)^2 \left[\left(\frac{2(T_g - T_w)}{T_w - T_f} + 1 \right)^2 - 1 \right] \tag{640}$$

The wet region heat transfer is limited to the values calculated by Eqs. 636 and 640. The wet region heat transfer is further limited to a maximum value of $1 \cdot 10^{-6}$ BTU/hr·ft²F.

If the net deposition rate is a negative value, and the quench front is receding, so the quench front velocity is calculated in a more straightforward manner.

$$V_{qf} = \frac{\dot{m}_{\text{QF,net}} h_{\text{fg}}}{(\rho C_p A_x)_g (T_g - T_f)} \tag{641}$$

The quench front location is calculated at each time step using the time-step size and velocity of the quench front.

$$L_{\text{qf}} = \tilde{L}_{\text{qf}} + V_{qf} \Delta t \tag{642}$$

13. SPACER GRID MODELS

13.1 GRID HEAT TRANSFER ENHANCEMENT

Spacer grids are used in nuclear reactors to maintain the rod-bundle geometry throughout the normal operation of the reactor. The presence of these grids is known to impact the flow because of their non-negligible thickness that causes acceleration/deceleration of the flow, creation of secondary flows, and disruption of the boundary layer. One of the most important effects of the grid spacers to be able to model is the effect that these flow redistributions have on rod-to-fluid heat transfer.

Yao, Hochreiter, and Leech [120] studied this effect for egg-crate and honeycomb-style spacer grids and proposed correlations for the effect of the grids on the Nusselt number. Their work focused on heat transfer effects both upstream and downstream of the spacer for both mixing and nonmixing vane grid styles. Noting the analogy between pressure-drop effects and heat-transfer effects, and using experimental heat-transfer enhancement data from a collection of grid styles and different flow conditions, they proposed the following exponentially decaying correlation for determining heat-transfer enhancement effects experienced downstream of the grid:

$$\frac{\mathrm{Nu}}{\mathrm{Nu}_0} = 1 + 5.55\epsilon^2 \exp\left[-0.13\frac{x}{D}\right]. \tag{643}$$

The heat transfer enhancement is a function of ϵ, which is the blockage ratio of the grid ($A_{\mathrm{blocked}}/A_{\mathrm{bare}}$), as well as the downstream nondimensional distance from the end of the spacer grid (x/D). The nondimensional distance from the end of the spacer grid is calculated by dividing the absolute distance from the end of the grid by the hydraulic diameter of the test section (bare region). This correlation applies to single-phase flow (liquid or vapor) for nonmixing vane grid designs.

Yao, Hochreiter, and Leech also suggest a means for capturing the swirling effect of vanes on the flow when mixing-vane grid styles are to be modeled. The presence of mixing vanes has been observed to cause the fluid to swirl, leading to increased local velocities and fluid mixing, which in turn lead to increased heat transfer. They propose a simple model that accounts for the fraction of the projected area of the vanes as seen by the flow, A, the angle of the vanes, Φ, and again, the downstream distance from the end of the grid, x/D.

$$\frac{\mathrm{Nu}}{\mathrm{Nu}_0} = \left[1 + A^2 \tan^2(\Phi) \exp\left[-0.034x/D\right]\right]^{0.4} \tag{644}$$

Because data from real mixing vane grids were not available, the Yao, Hochreiter, and Leech used in-tube gas-flow experimental data to develop the correlation. Because of this, the mixing-vane component of the correlation is not typically utilized.

Regardless, for maximum user flexibility, the model has been implemented into PSU RDFMG version of COBRA-TF (CTF) in its full form, except the coefficients have been replaced with user input variables a, b, c, and d, as shown in Eq. (645).

$$\frac{\mathrm{Nu}}{\mathrm{Nu}_0} = \left[1 + a\epsilon^2 \exp\left[b\frac{x}{D}\right]\right]\left[1 + A^2 \tan^2(\Phi) \exp\left[c\frac{x}{D}\right]\right]^d \tag{645}$$

In this way, the user is free to set d to 0.0, thus disabling the mixing-vane component of the correlation.

Yao, Hochreiter, and Leech also determined the upstream heat transfer effects of the grid to be linearly dependent on distance from the grid; however, that contribution of the grid to heat transfer has not been included in CTF. In activating the model, the user has the option to turn the model on for only single-phase vapor, or both single-phase liquid and single phase-vapor. If used for both phases and if two-phase conditions persist, then an equal heat transfer enhancement factor will be multiplied by the rod heat transfer coefficient of each of the phases.

14. FLUID PROPERTIES

CTF is capable of calculating thermal conductivity, specific heat, viscosity, surface tension, and enthalpy for water. Three conditions of water may exist that require separate attention: subcooled liquid, superheated vapor, and saturated mixtures of both phases. These cases are separately addressed in the following three sections.

14.1 ORIGINAL WATER PROPERTIES

CTF's original steam tables, utilized when IPROPS = 0, are a mixture of several sources. They are the default option when running CTF. Their complete origins are somewhat unknown, but most property evaluations have been traced to existing documentation. This uncertainty prompted the inclusion of newer, better documented steam tables which could be verified by sources.

14.1.1 Saturated Liquid and Vapor

Saturated liquid and vapor enthalpies are calculated as a function of pressure based on expressions developed for the Electric Power Research Institute (EPRI) [127]. Other state properties, including density, saturation temperature, thermal conductivity, viscosity, specific heat, and surface tension, are interpolated from lookup tables that are indexed by the saturated liquid enthalpy. Both the correlations used for determining saturation enthalpies, as well as the other state property lookup tables, provide close agreement with the ASME Steam Tables [128] and the NBS/NRC Steam Tables [129].

Saturation enthalpies are calculated in $^{\mathrm{BTU}}/_{\mathrm{lbm}}$ as a function of pressure in psia. Liquid and vapor saturation enthalpies are calculated in the SAT subroutine. The polynomial expression for saturated liquid enthalpy is as follows:

$$H_f(P_{\mathrm{sat}}) = \Sigma_{n=1}^{9} A_n \left[\ln(P_{\mathrm{sat}})\right]^{n-1}, \quad \text{for } P_{\mathrm{sat}} < 2529.9\,\mathrm{psia} \tag{646a}$$

$$H_f(P_{\mathrm{sat}}) = \Sigma_{n=1}^{9} A_n \left[(3208.2 - P_{\mathrm{sat}})^{0.41}\right]^{n-1}, \quad \text{for } 2529.9\,\mathrm{psia} <= P_{\mathrm{sat}} < 3208.0\,\mathrm{psia} \tag{646b}$$

The constants for the polynomial expansion, A_n, are given in Table 6.

Table 6. Polynomial expansion constant for the saturated liquid enthalpy correlation

	Pressure		
A_n	$0.1 <= P < 898.7$	$898.7 <= P < 2529.9$	$2529.9 <= P < 3208$
1	$0.6970887859 \cdot 10^{+2}$	$0.8408618802 \cdot 10^{+6}$	$0.9060030436 \cdot 10^{+3}$
2	$0.3337529994 \cdot 10^{+2}$	$0.3637413208 \cdot 10^{+6}$	$0.1426813520 \cdot 10^{+2}$
3	$0.2318240735 \cdot 10^{+1}$	$-0.4634506669 \cdot 10^{+6}$	$0.1522233257 \cdot 10^{+1}$
4	$0.1840599513 \cdot 10^{+0}$	$0.1130306339 \cdot 10^{+6}$	$-0.6973992961 \cdot 10^{+0}$
5	$-0.5245502294 \cdot 10^{-2}$	$-0.4350217298 \cdot 10^{+3}$	$0.1743091663 \cdot 10^{+0}$
6	$0.2878007027 \cdot 10^{-2}$	$-0.3898988188 \cdot 10^{+4}$	$-0.2319717696 \cdot 10^{-1}$
7	$0.1753652324 \cdot 10^{-2}$	$0.6697399434 \cdot 10^{+3}$	$0.1694019149 \cdot 10^{-2}$
8	$-0.4334859620 \cdot 10^{-3}$	$-0.4730726377 \cdot 10^{+2}$	$-0.6454771710 \cdot 10^{-4}$
9	$0.3325699282 \cdot 10^{-4}$	$0.1265125057 \cdot 10^{+1}$	$0.1003003098 \cdot 10^{-5}$

The polynomial expression for vapor saturated enthalpy is given as follows:

$$H_g(P_{\text{sat}}) = \Sigma_{n=1}^{5} B_n \left[\ln(P_{\text{sat}})\right]^{n-1} + \Sigma_{n=6}^{9} B_n \left[\ln(P_{\text{sat}})\right]^{n+3}, \quad \text{for } 0.1 \text{ psia} <= P_{\text{sat}} < 1467.6 \text{ psia} \tag{647a}$$

$$H_g(P_{\text{sat}}) = \Sigma_{n=1}^{9} B_n \left[\ln(P_{\text{sat}})\right]^{n-1}, \quad \text{for } 1467.6 \text{ psia} <= P_{\text{sat}} < 2586.0 \text{ psia} \tag{647b}$$

$$H_g(P_{\text{sat}}) = \Sigma_{n=1}^{9} B_n \left[(3208.2 - P_{\text{sat}})^{0.41}\right]^{n-1}, \quad \text{for } 2586.0 \text{ psia} <= P_{\text{sat}} < 3208.0 \text{ psia} \tag{647c}$$

The polynomial expansion constants, B_n, are provided in Table 7.

Table 7. Polynomial expansion constant for the saturated vapor enthalpy correlation.

	Pressure		
B_n	$0.1 <= P < 1467.6$	$1467.6 <= P < 2586.0$	$2586.0 <= P < 3208$
1	$0.1105836875 \cdot 10^{+4}$	$0.5918671729 \cdot 10^{+6}$	$0.9059978254 \cdot 10^{+3}$
2	$0.1436943768 \cdot 10^{+2}$	$-0.2559433320 \cdot 10^{+6}$	$0.5561957539 \cdot 10^{+1}$
3	$0.8018288621 \cdot 10^{+0}$	$0.3032474387 \cdot 10^{+5}$	$0.3434189609 \cdot 10^{+1}$
4	$0.1617232913 \cdot 10^{-1}$	$0.4109051958 \cdot 10^{+1}$	$-0.6406390628 \cdot 10^{+0}$
5	$-0.1501147505 \cdot 10^{-2}$	$0.3475066877 \cdot 10^{+0}$	$0.5918579484 \cdot 10^{-1}$
6	$-0.1237675562 \cdot 10^{-4}$	$-0.3026047262 \cdot 10^{+0}$	$-0.2725378570 \cdot 10^{-2}$
7	$0.3004773304 \cdot 10^{-5}$	$-0.1022018012 \cdot 10^{+2}$	$0.5006336938 \cdot 10^{-4}$
8	$-0.2062390734 \cdot 10^{-6}$	$0.1591215116 \cdot 10^{+1}$	0.0
9	0.0	$-0.6768383759 \cdot 10^{-1}$	0.0

The lookup table for other state properties includes 90 entries for each property. Property data are shown in Table 8.

Table 8. Saturated water thermophysical properties

P_{sat} psia	T_{sat} °F	ρ_f lbm/ft³	ρ_g lbm/ft³	H_f BTU/lbm	H_g BTU/lbm	μ_f lbm/hr·ft	μ_g lbm/hr·ft	k_f BTU/hr·ft·°F	k_g BTU/hr·ft·°F	Cp_f BTU/lbm·°F	Cp_g BTU/lbm·°F	σ lbf/ft
0.1	41.97	62.42	0.000	10	1079.83	3.61570	0.02262	0.33023	0.01002	1.00440	0.44426	0.00513
0.2	51.93	62.40	0.001	20	1084.18	3.06850	0.02295	0.33627	0.01022	1.00320	0.44477	0.00508
0.3	61.91	62.36	0.001	30	1088.55	2.64160	0.02331	0.34218	0.01041	1.00140	0.44542	0.00502
0.4	71.90	62.29	0.001	40	1092.92	2.30190	0.02368	0.34791	0.01062	0.99975	0.44623	0.00496
0.5	81.91	62.20	0.002	50	1097.28	2.02710	0.02406	0.35338	0.01083	0.99851	0.44723	0.00491
0.7	91.93	62.09	0.002	60	1101.62	1.80170	0.02445	0.35848	0.01105	0.99776	0.44844	0.00484
1.0	101.95	61.97	0.003	70	1105.94	1.61440	0.02485	0.36334	0.01128	0.99743	0.44988	0.00478
1.4	111.98	61.83	0.004	80	1110.23	1.45700	0.02526	0.36765	0.01152	0.99745	0.45157	0.00472
1.8	122.00	61.68	0.005	90	1114.49	1.32340	0.02568	0.37183	0.01177	0.99774	0.45353	0.00465
2.3	132.02	61.52	0.007	100	1118.70	1.20900	0.02611	0.37530	0.01203	0.99823	0.45577	0.00459
3.0	142.04	61.34	0.009	110	1122.86	1.11020	0.02654	0.37863	0.01230	0.99888	0.45832	0.00452
3.9	152.04	61.15	0.011	120	1126.97	1.02440	0.02698	0.38146	0.01258	0.99965	0.46117	0.00445
5.0	162.04	60.95	0.014	130	1131.04	0.94915	0.02742	0.38403	0.01287	1.00050	0.46435	0.00438
6.3	172.02	60.75	0.017	140	1135.03	0.88297	0.02787	0.38624	0.01318	1.00150	0.46786	0.00432
7.9	182.01	60.53	0.021	150	1138.98	0.82425	0.02832	0.38814	0.01349	1.00270	0.47172	0.00424
9.7	191.96	60.31	0.025	160	1142.85	0.77208	0.02877	0.38984	0.01381	1.00390	0.47591	0.00417
12.0	201.92	60.07	0.031	170	1146.66	0.72533	0.02923	0.39115	0.01415	1.00530	0.48047	0.00410
14.7	211.84	59.83	0.037	180	1150.39	0.68345	0.02969	0.39236	0.01449	1.00690	0.48538	0.00403
17.8	221.78	59.58	0.045	190	1154.05	0.64561	0.03015	0.39320	0.01486	1.00860	0.49067	0.00396
21.4	231.66	59.32	0.053	200	1157.62	0.61149	0.03061	0.39397	0.01523	1.01050	0.49633	0.00388
25.7	241.55	59.05	0.063	210	1161.12	0.58043	0.03107	0.39444	0.01561	1.01260	0.50239	0.00381
30.6	251.39	58.78	0.074	220	1164.50	0.55228	0.03153	0.39481	0.01601	1.01490	0.50882	0.00373
36.2	261.22	58.50	0.087	230	1167.79	0.52655	0.03199	0.39496	0.01642	1.01740	0.51569	0.00366
42.5	271.02	58.21	0.101	240	1170.98	0.50302	0.03245	0.39498	0.01684	1.02010	0.52299	0.00358
49.8	280.80	57.92	0.117	250	1174.05	0.48145	0.03291	0.39485	0.01727	1.02300	0.53075	0.00351
58.0	290.54	57.61	0.135	260	1177.01	0.46163	0.03337	0.39456	0.01772	1.02610	0.53899	0.00343
67.2	300.26	57.30	0.155	270	1179.84	0.44339	0.03383	0.39418	0.01817	1.02940	0.54775	0.00335
77.6	309.93	56.99	0.177	280	1182.54	0.42656	0.03429	0.39358	0.01864	1.03290	0.55706	0.00327
89.1	319.58	56.66	0.202	290	1185.10	0.41101	0.03474	0.39293	0.01912	1.03670	0.56696	0.00320
101.8	329.19	56.34	0.229	300	1187.53	0.39661	0.03520	0.39205	0.01962	1.04060	0.57748	0.00312

P_{sat} psia	T_{sat} °F	ρ_f lbm/ft^3	ρ_g lbm/ft^3	H_f BTU/lbm	H_g BTU/lbm	μ_f lbm/hr·ft	μ_g lbm/hr·ft	k_f BTU/hr·ft·°F	k_g BTU/hr·ft·°F	Cp_f BTU/lbm·°F	Cp_g BTU/lbm·°F	σ lbf/ft
116.0	338.76	56.00	0.260	310	1189.82	0.38325	0.03565	0.39113	0.02012	1.04470	0.58869	0.00304
131.6	348.28	55.66	0.293	320	1191.95	0.37083	0.03610	0.39000	0.02064	1.04910	0.60063	0.00296
148.6	357.77	55.31	0.329	330	1193.94	0.35927	0.03655	0.38882	0.02116	1.05380	0.61336	0.00288
167.4	367.21	54.95	0.368	340	1195.77	0.34849	0.03699	0.38743	0.02170	1.05870	0.62693	0.00280
187.8	376.61	54.59	0.411	350	1197.44	0.33842	0.03744	0.38597	0.02225	1.06390	0.64141	0.00272
210.0	385.96	54.22	0.458	360	1198.96	0.32898	0.03788	0.38435	0.02281	1.06940	0.65687	0.00264
234.0	395.26	53.85	0.508	370	1200.30	0.32014	0.03832	0.38265	0.02338	1.07530	0.67338	0.00256
260.0	404.50	53.47	0.563	380	1201.48	0.31182	0.03876	0.38078	0.02396	1.08150	0.69101	0.00248
288.0	413.69	53.08	0.622	390	1202.49	0.30399	0.03920	0.37881	0.02455	1.08820	0.70984	0.00240
318.1	422.83	52.69	0.686	400	1203.32	0.29660	0.03964	0.37667	0.02516	1.09540	0.72995	0.00232
350.4	431.90	52.29	0.755	410	1203.97	0.28961	0.04008	0.37441	0.02578	1.10300	0.75144	0.00224
384.9	440.91	51.88	0.828	420	1204.44	0.28299	0.04052	0.37199	0.02642	1.11130	0.77439	0.00216
421.6	449.86	51.47	0.907	430	1204.71	0.27670	0.04095	0.36946	0.02707	1.12010	0.79891	0.00208
460.7	458.73	51.05	0.992	440	1204.79	0.27072	0.04139	0.36679	0.02773	1.12970	0.82510	0.00200
502.1	467.53	50.62	1.082	450	1204.67	0.26501	0.04183	0.36401	0.02841	1.13990	0.85307	0.00192
546.0	476.26	50.18	1.178	460	1204.34	0.25954	0.04227	0.36106	0.02912	1.15100	0.88295	0.00185
592.2	484.91	49.74	1.281	470	1203.79	0.25431	0.04271	0.35800	0.02984	1.16290	0.91488	0.00177
641.2	493.51	49.29	1.391	480	1203.02	0.24926	0.04315	0.35472	0.03059	1.17590	0.94916	0.00169
692.1	501.94	48.84	1.507	490	1202.04	0.24444	0.04359	0.35138	0.03136	1.18980	0.98549	0.00161
745.9	510.35	48.37	1.631	500	1200.81	0.23976	0.04404	0.34782	0.03218	1.20490	1.02460	0.00154
802.0	518.65	47.90	1.762	510	1199.35	0.23524	0.04450	0.34426	0.03300	1.22130	1.06650	0.00146
860.5	526.84	47.42	1.901	520	1197.64	0.23086	0.04495	0.34043	0.03390	1.23890	1.11140	0.00139
921.3	534.91	46.93	2.048	530	1195.69	0.22662	0.04541	0.33660	0.03480	1.25800	1.15940	0.00132
984.4	542.86	46.44	2.204	540	1193.50	0.22250	0.04588	0.33255	0.03581	1.27870	1.21100	0.00124
1050.0	550.72	45.93	2.368	550	1191.03	0.21846	0.04636	0.32846	0.03684	1.30120	1.26690	0.00117
1117.8	558.47	45.42	2.543	560	1188.31	0.21452	0.04685	0.32427	0.03795	1.32560	1.32710	0.00111
1187.8	566.10	44.89	2.727	570	1185.33	0.21067	0.04734	0.31999	0.03915	1.35220	1.39240	0.00104
1259.9	573.61	44.36	2.922	580	1182.08	0.20689	0.04785	0.31571	0.04038	1.38120	1.46330	0.00097
1334.0	580.98	43.82	3.127	590	1178.57	0.20318	0.04837	0.31134	0.04174	1.41290	1.54050	0.00091
1410.0	588.22	43.27	3.344	600	1174.80	0.19953	0.04891	0.30694	0.04324	1.44770	1.62510	0.00084
1487.8	595.33	42.71	3.574	610	1170.75	0.19594	0.04946	0.30255	0.04486	1.48590	1.71800	0.00078
1567.2	602.29	42.14	3.816	620	1166.42	0.19239	0.05004	0.29817	0.04663	1.52810	1.82060	0.00073

P_{sat} psia	T_{sat} °F	ρ_f lbm/ft^3	ρ_g lbm/ft^3	H_f BTU/lbm	H_g BTU/lbm	μ_f lbm/hr·ft	μ_g lbm/hr·ft	k_f BTU/hr·ft·°F	k_g BTU/hr·ft·°F	Cp_f BTU/lbm·°F	Cp_g BTU/lbm·°F	σ lbf/ft
1648.2	609.11	41.56	4.072	630	1161.76	0.18889	0.05063	0.29382	0.04854	1.57490	1.93450	0.00067
1730.4	615.77	40.96	4.343	640	1156.76	0.18543	0.05125	0.28954	0.05069	1.62710	2.06150	0.00061
1813.8	622.28	40.36	4.629	650	1151.40	0.18200	0.05190	0.28531	0.05307	1.68570	2.20410	0.00056
1898.2	628.62	39.74	4.931	660	1145.66	0.17859	0.05258	0.28115	0.05565	1.75180	2.36520	0.00051
1983.9	634.84	39.11	5.253	670	1139.49	0.17518	0.05330	0.27709	0.05848	1.82770	2.55010	0.00046
2069.5	640.84	38.47	5.593	680	1132.96	0.17181	0.05405	0.27314	0.06173	1.91440	2.76120	0.00042
2155.4	646.65	37.81	5.953	690	1126.01	0.16845	0.05485	0.26926	0.06527	2.01490	3.00550	0.00037
2241.1	652.28	37.14	6.335	700	1118.63	0.16509	0.05570	0.26545	0.06919	2.13280	3.29110	0.00033
2326.3	657.69	36.46	6.740	710	1110.82	0.16173	0.05661	0.26186	0.07374	2.27250	3.62830	0.00029
2410.6	662.89	35.76	7.170	720	1102.59	0.15837	0.05758	0.25836	0.07854	2.44030	4.03110	0.00025
2494.0	667.89	35.03	7.630	730	1093.91	0.15497	0.05863	0.25520	0.08401	2.64650	4.52210	0.00025
2575.2	672.62	34.29	8.117	740	1084.90	0.15156	0.05975	0.25212	0.08983	2.90110	5.12290	0.00022
2653.8	677.08	33.53	8.635	750	1075.52	0.14813	0.06096	0.24935	0.09704	3.22290	5.87350	0.00019
2729.8	681.29	32.75	9.190	760	1065.74	0.14464	0.06228	0.24673	0.10465	3.64070	6.14500	0.00016
2801.8	685.18	31.95	9.777	770	1055.59	0.14113	0.06371	0.24493	0.11447	4.19150	6.14500	0.00013
2869.6	688.77	31.12	10.403	780	1045.00	0.13755	0.06526	0.24313	0.12429	4.94400	6.14500	0.00011
2931.9	692.01	30.27	11.066	790	1034.06	0.13393	0.06694	0.24418	0.13890	5.99630	6.14500	0.00008
2988.5	694.90	29.39	11.771	800	1022.75	0.13024	0.06878	0.24576	0.15442	6.14500	6.14500	0.00007
3038.4	697.40	28.48	12.513	810	1011.17	0.12649	0.07076	0.24734	0.16993	6.14500	6.14500	0.00005
3081.4	699.53	27.55	13.293	820	999.32	0.12268	0.07291	0.25288	0.19158	6.14500	6.14500	0.00004
3116.7	701.26	26.60	14.101	830	987.40	0.11885	0.07520	0.26470	0.22270	6.14500	6.14500	0.00002
3144.7	702.62	25.63	14.927	840	975.50	0.11500	0.07761	0.29237	0.27220	6.14500	6.14500	0.00002
3165.7	703.63	24.65	15.750	850	963.98	0.11119	0.08008	0.81017	0.80644	6.14500	6.14500	0.00001
3180.5	704.34	23.68	16.541	860	953.38	0.10744	0.08253	2.55507	2.55265	6.14500	6.14500	0.00000
3190.3	704.81	22.72	17.243	870	944.22	0.10382	0.08475	4.29997	4.29886	6.14500	6.14500	0.00000
3196.0	705.08	21.78	17.759	880	937.47	0.10034	0.08642	10.00000	10.00000	6.14500	6.14500	0.00000
3198.3	705.19	20.87	17.987	890	934.25	0.09704	0.08717	50.00000	50.00000	6.14500	6.14500	0.00000
3206.4	705.39	20.16	19.244	900	917.46	0.09704	0.08717	100.00000	100.00000	6.14500	6.14500	0.00000

14.1.2 Superheated Vapor

14.1.2.1 Enthalpy

Enthalpy is calculated as a function of pressure and temperature using the expression developed by Keenan and Keys [130]. Pressure is provided in atmospheres, and Eq. (648) gives enthalpy in units of J/g.

$$H_v = 0.43\left[0.10129\left(F_0 P + \frac{F_1}{2}P^2 + \frac{F_3}{4}P^4 + \frac{F_{12}}{13}P^{13}\right) + F^1\right] \tag{648}$$

The F coefficients are defined as follows:

$$F_k = \frac{\partial}{\partial\tau}(B_k\tau), \text{ for } k = 0, 1, 3, 12 \tag{649}$$

where: τ = the inverse of the temperature (°K), $1/T$
B_k = coefficients

The B_k coefficients are defined as follows:

$$B_0 = 1.89 - 2641.62\tau \cdot 10^{80870\tau^2} \tag{650}$$
$$B_1 = B_0^2\left(82.546\tau^2 - 1.6246 \cdot 10^5\tau^3\right) \tag{651}$$
$$B_3 = B_0^4\left(0.21828\tau^3 - 1.2697 \cdot 10^5\tau^5\right) \tag{652}$$
$$B_{12} = -B_0^{13}\left(3.635 \cdot 10^{-4}\tau^{12} - 6.768 \cdot 10^{64}\tau^{36}\right) \tag{653}$$

The F^1 term of Eq. (648) is defined as

$$F^1 = 2502.36 + \int_{273.16}^{T}\left(1.472 + 0.00075566T + \frac{47.8365}{T}\right)dT. \tag{654}$$

14.1.2.2 Density

Superheated vapor density is calculated in HGAS. The specific volume is first calculated.

$$v = 4.55504\frac{T}{P} + B_0 + \left[(B_0\tau)^2 G_1 P + (B_0\tau)^4 G_2 P^3 - (B_0\tau)^{13} G_3 P^{12}\right]T, \tag{655}$$

where: T = temperature (°K)
P = pressure (atm)
B_0 = coefficient is defined as it was for enthalpy in Eq. (650)
τ = the inverse of the temperature (°K), $1/T$

The G terms are defined as follows:

$$G_1 = 82.546\tau - 1.6246 \cdot 10^5\tau^2 \tag{656}$$
$$G_2 = 0.21828 - 1.2697 \cdot 10^5\tau^2 \tag{657}$$
$$G_3 = 3.635 \cdot 10^{-4} - 6.768 \cdot 10^{64}\tau^{24} \tag{658}$$

The density is calculated as follows:

$$\rho = \frac{62.428}{\nu} \tag{659}$$

where: ν = specific volume (cm^3/g)
ρ = density (lbm/ft^3)

14.1.2.3 Temperature

Superheated vapor temperature is calculated directly from enthalpy and pressure by the method outlined by Wagner and Kruse [131] in Industrial Standard IAPWS-IF97. One of three possible correlations is used to calculate temperature, depending on the region in which the pressure falls. The pressure regions are Regions 2a, 2b, and 2c. The division between Regions 2a and 2b is 4 MPa. The division between Regions 2b and 2c is calculated by the following equation:

$$P_{\text{2b threshold}} = 10\left(905.843 - 0.679558 h_{\text{norm}} + 0.000128090 h_{\text{norm}}^2\right) \tag{660}$$

where: h_{norm} = normalized enthalpy to 2,000 kJ/kg prior to inputting it into the above equation

For Region 2a, the temperature is then calculated as follows:

$$T = \Sigma_{i=1}^{34} n_1(i) P_{\text{norm}}^{l_1(i)} (h_{\text{norm}} - 2.1)^{j_1(i)} \tag{661}$$

where: h_{norm} = normalized enthalpy to 2,000 kJ/kg prior to inputting it into the above equation.
P_{norm} = normalized pressure to 10 bar
n_1, l_1, j_1 = the coefficients given in Table 9

The Region 2b temperature calculation is performed as follows:

$$T = \Sigma_{i=1}^{38} n_2(i) (P_{\text{norm}} - 2)^{l_2(i)} (h_{\text{norm}} - 2.6)^{j_2(i)} \tag{662}$$

where: n_2, l_2, j_2 = the coefficients given in Table 10

The Region 2c temperature calculation is performed as follows:

$$T = \Sigma_{i=1}^{23} n_3(i) (P_{\text{norm}} + 25)^{l_3(i)} (h_{\text{norm}} - 1.8)^{j_3(i)} \tag{663}$$

where: n_3, l_3, j_3 = the coefficients given in Table 11

Table 9. Coefficients for the temperature calculation in Region 2a

n_1	l_1	j_1
$0.108990 \cdot 10^{+04}$	0	0
$0.849517 \cdot 10^{+03}$	0	1
$-0.107817 \cdot 10^{+03}$	0	2
$0.331537 \cdot 10^{+02}$	0	3
$-0.742320 \cdot 10^{+01}$	0	7
$0.117650 \cdot 10^{+02}$	0	20
$0.184457 \cdot 10^{+01}$	1	0
$-0.417927 \cdot 10^{+01}$	1	1
$0.624782 \cdot 10^{+01}$	1	2
$-0.173446 \cdot 10^{+02}$	1	3
$-0.200582 \cdot 10^{+03}$	1	7
$0.271961 \cdot 10^{+03}$	1	9
$-0.455113 \cdot 10^{+03}$	1	11
$0.309197 \cdot 10^{+04}$	1	18
$0.252266 \cdot 10^{+06}$	1	44
$-0.617074 \cdot 10^{-02}$	2	0
$-0.310780 \cdot 10^{+00}$	2	2
$0.116709 \cdot 10^{+02}$	2	7
$0.128128 \cdot 10^{+09}$	2	36
$-0.985549 \cdot 10^{+09}$	2	38
$0.282245 \cdot 10^{+10}$	2	40
$-0.359490 \cdot 10^{+10}$	2	42
$0.172273 \cdot 10^{+10}$	2	44
$-0.135513 \cdot 10^{+05}$	3	24
$0.128487 \cdot 10^{+08}$	3	44
$0.138657 \cdot 10^{+01}$	4	12
$0.235988 \cdot 10^{+06}$	4	32
$-0.131052 \cdot 10^{+08}$	4	44
$0.739998 \cdot 10^{+04}$	5	32
$-0.551967 \cdot 10^{+06}$	5	36
$0.371541 \cdot 10^{+07}$	5	42
$0.191277 \cdot 10^{+05}$	6	34
$-0.415352 \cdot 10^{+06}$	6	44
$-0.624599 \cdot 10^{+02}$	7	28

Table 10. Coefficients for the temperature calculation in Region 2b

n_2	l_2	j_2
$0.148950 \cdot 10^{+04}$	0	0
$0.743078 \cdot 10^{+03}$	0	1
$-0.977083 \cdot 10^{+02}$	0	2
$0.247425 \cdot 10^{+01}$	0	12
$-0.632813 \cdot 10^{+00}$	0	18
$0.113860 \cdot 10^{+01}$	0	24
$-0.478119 \cdot 10^{+00}$	0	28
$0.852081 \cdot 10^{-02}$	0	40
$0.937471 \cdot 10^{+00}$	1	0
$0.335931 \cdot 10^{+01}$	1	2
$0.338094 \cdot 10^{+01}$	1	6
$0.168445 \cdot 10^{+00}$	1	12
$0.738757 \cdot 10^{+00}$	1	18
$-0.471287 \cdot 10^{+00}$	1	24
$0.150203 \cdot 10^{+00}$	1	28
$-0.217641 \cdot 10^{-02}$	1	40
$-0.218108 \cdot 10^{-01}$	2	2
$-0.108298 \cdot 10^{+00}$	2	8
$-0.463333 \cdot 10^{-01}$	2	18
$0.712804 \cdot 10^{-04}$	2	40
$0.110328 \cdot 10^{-03}$	3	1
$0.189552 \cdot 10^{-03}$	3	2
$0.308915 \cdot 10^{-02}$	3	12
$0.135555 \cdot 10^{-02}$	3	24
$0.286402 \cdot 10^{-06}$	4	2
$-0.107799 \cdot 10^{-04}$	4	12
$-0.764627 \cdot 10^{-04}$	4	18
$0.140524 \cdot 10^{-04}$	4	24
$-0.310838 \cdot 10^{-04}$	4	28
$-0.103027 \cdot 10^{-05}$	4	40
$0.282173 \cdot 10^{-06}$	5	18
$0.127049 \cdot 10^{-05}$	5	24
$0.738034 \cdot 10^{-07}$	5	40
$-0.110301 \cdot 10^{-07}$	6	28
$-0.814564 \cdot 10^{-13}$	7	2
$-0.251805 \cdot 10^{-10}$	7	28
$-0.175652 \cdot 10^{-17}$	9	1
$0.869342 \cdot 10^{-14}$	9	40

Table 11. Coefficients for the temperature calculation in Region 2c

n_3	l_3	j_3
$-0.323684 \cdot 10^{+13}$	-7	0
$0.732634 \cdot 10^{+13}$	-7	4
$0.358251 \cdot 10^{+12}$	-6	0
$-0.583401 \cdot 10^{+12}$	-6	2
$-0.107831 \cdot 10^{+11}$	-5	0
$0.208255 \cdot 10^{+11}$	-5	2
$0.610748 \cdot 10^{+06}$	-2	0
$0.859777 \cdot 10^{+06}$	-2	1
$-0.257457 \cdot 10^{+05}$	-1	0
$0.310811 \cdot 10^{+05}$	-1	2
$0.120823 \cdot 10^{+04}$	0	0
$0.482198 \cdot 10^{+03}$	0	1
$0.379660 \cdot 10^{+01}$	1	4
$-0.108430 \cdot 10^{+02}$	1	8
$-0.453642 \cdot 10^{-01}$	2	4
$0.145591 \cdot 10^{-12}$	6	0
$0.112616 \cdot 10^{-11}$	6	1
$-0.178050 \cdot 10^{-10}$	6	4
$0.123246 \cdot 10^{-06}$	6	10
$-0.116069 \cdot 10^{-05}$	6	12
$0.278464 \cdot 10^{-04}$	6	16
$-0.592700 \cdot 10^{-03}$	6	20
$0.129186 \cdot 10^{-02}$	6	22

14.1.2.4 Specific heat

The specific heat is calculated as a function of the superheated vapor temperature and pressure using the method outlined by Wagner and Kruse [131] in Industrial Standard IAPWS-IF97. Pressure is normalized to 10 bar. Temperature is first normalized by 1/540 K, as follows:

$$T_{\text{norm}} = \frac{540}{T} \tag{664}$$

where: T = temperature (°K)

The specific heat is calculated in units of $^{\text{kJ}}/_{\text{kg}^\circ\text{K}}$ as follows:

$$Cp = -R_{H_2O} T_{\text{norm}}^2 (\gamma_0 + \gamma_r) \tag{665}$$

where: $R_{H_2O} = 0.461526$, the specific gas constant for water

γ_0 is defined as follows:

$$\gamma_0 = \Sigma_{i=1}^{9} n_0(i) j_0(i)(j_0(i) - 1) T_{\text{norm}}^{j_0(i)-2} \tag{666}$$

where: n_0, j_0 = terms are given in Table 12

γ_r is defined as follows:

$$\gamma_r = \Sigma_{i=1}^{43} \text{nr}(i) P_{\text{norm}}^{\text{ir}(i)} \text{jr}(i)(\text{jr}(i) - 1)(T_{\text{norm}} - 0.5)^{\text{jr}(i)-2} \tag{667}$$

where: nr, ir, jr = coefficient terms given in Table 13

Table 12. Coefficients for the calculation of γ_0

n_0	j_0
-9.6927686500217	0
10.086655968018	1
-0.0056087911283020	-5
0.071452738081455	-4
-0.40710498223928	-3
1.4240819171444	-2
-4.3839511319450	-1
-0.28408632460772	2
0.021268463753307	3

Table 13. Coefficients for the calculation of γ_r.

nr	*jr*	*ir*
-0.177 317 424 732 13·10^{-02}	0	1
-0.178 348 622 923 58·10^{-01}	1	1
-0.459 960 136 963 65·10^{-01}	2	1
-0.575 812 590 834 32·10^{-01}	3	1
-0.503 252 787 279 30·10^{-01}	6	1
-0.330 326 416 702 03·10^{-04}	1	2
-0.189 489 875 163 15·10^{-03}	2	2
-0.393 927 772 433 55·10^{-02}	4	2
-0.437 972 956 505 73·10^{-01}	7	2
-0.266 745 479 140 87·10^{-04}	36	2
0.204 817 376 923 09·10^{-07}	0	3
0.438 706 672 844 35·10^{-06}	1	3
-0.322 766 772 385 70·10^{-04}	3	3
-0.150 339 245 421 48·10^{-02}	6	3
-0.406 682 535 626 49·10^{-01}	35	3
-0.788 473 095 593 67·10^{-09}	1	4
0.127 907 178 522 85·10^{-07}	2	4
0.482 253 727 185 07·10^{-06}	3	4
0.229 220 763 376 61·10^{-05}	7	5
-0.167 147 664 510 61·10^{-10}	3	6
-0.211 714 723 213 55·10^{-02}	16	6
-0.238 957 419 341 04·10^{+02}	35	6
-0.590 595 643 242 70·10^{-17}	0	7
-0.126 218 088 991 01·10^{-05}	11	7
-0.389 468 424 357 39·10^{-01}	25	7
0.112 562 113 604 59·10^{-10}	8	8
-0.823 113 408 979 98·10^{+01}	36	8
0.198 097 128 020 88·10^{-07}	13	9
0.104 069 652 101 74·10^{-18}	4	10
-0.102 347 470 959 29·10^{-12}	10	10
-0.100 181 793 795 11·10^{-08}	14	10
-0.808 829 086 469 85·10^{-10}	29	16
0.106 830 318 794 09·10^{+00}	50	16
-0.336 622 505 741 71·10^{+00}	57	18
0.891 858 453 554 21·10^{-24}	20	20
0.306 293 168 762 32·10^{-12}	35	20
-0.420 024 676 982 08·10^{-05}	48	20
-0.590 560 296 856 39·10^{-25}	21	21
0.378 269 476 134 57·10^{-05}	53	22
-0.127 686 089 346 81·10^{-14}	39	23
0.730 876 105 950 61·10^{-28}	26	24
0.554 147 153 507 78·10^{-16}	40	24
-0.943 697 072 412 10·10^{-06}	58	24

14.1.2.5 Thermal conductivity

The thermal conductivity of vapor is calculated in the TRANSP subroutine as a function of temperature and density. It is calculated using equations given in the ASME Steam Tables [128]. The expression for thermal conductivity is given as

$$k_v = k_1 + \left[103.51 + 0.4198T - 2.771 \cdot 10^{-5}T^2\right]\rho_v + 2.1482 \cdot 10^{14}\frac{\rho_v^2}{T^{4.2}}, \tag{668}$$

with

$$k_1 = 17.6 + 5.87 \cdot 10^{-2}T + 1.04 \cdot 10^{-4}T^2 - 4.51 \cdot 10^{-8}T^3, \tag{669}$$

where: k_v, k_1 = thermal conductivity (W/m-K)
ρ_v = density (g/cm^3)
T = temperature (°C)

14.1.2.6 Viscosity

Like thermal conductivity, viscosity is determined in the TRANSP subroutine using equations given by the ASME Steam Tables [128].

$$\mu_v = \begin{cases} \mu_1 - \rho(1858 - 5.9T), \text{ if } T < 340\,^\circ\text{C} \\ \mu_1 + 353\rho + 676.5\rho^2 + 102.1\rho^3, \text{ if } T > 365\,^\circ\text{C} \end{cases} \tag{670}$$

with

$$\mu_1 = 0.407T + 80.4 \tag{671}$$

where: ρ_v = density (g/cm^3)
T = temperature (°C)

For temperatures between 340 °C and 365 °C, the viscosity is linearly interpolated between values given by the two components of Eq. (670). Viscosity is given in units of micropoise by Eq. (670).

14.1.3 Subcooled liquid

Subcooled liquid properties are found as a function of liquid enthalpy using the saturated liquid properties given in Table 8. Dependence on pressure is neglected because it is very small for subcooled liquids. Density is the only term not obtained from Table 8. Specific volume is obtained using the following equation:

$$v_l = \exp\left[\Sigma_{i=1}^{5}\left(\Sigma_{j=1}^{3}C_{CXij}P^{j-1}\right)H_l^{i-1}\right] \tag{672}$$

where: C_{CXij} = the coefficient based on the indices i and j from Table 14

The Prandtl number for subcooled water is calculated as follows:

$$\text{Pr}_l = \frac{\mu_f C p_f}{k_f} \tag{673}$$

Table 14. Subcooled water density constants, C_{CXij}

i=	1	2	3
j=1	$-0.413450\cdot10^{1}$	$0.13252\cdot10^{-4}$	$0.15812\cdot10^{-5}$
j=2	$-0.59428\cdot10^{-5}$	$0.63377\cdot10^{-7}$	$-0.39974\cdot10^{-9}$
j=3	$0.15681\cdot10^{-8}$	$-0.40711\cdot10^{-10}$	$0.25401\cdot10^{-12}$
i=	4	5	
j=1	$-0.21959\cdot10^{-8}$	$0.21683\cdot10^{-11}$	
j=2	$0.69391\cdot10^{-12}$	$-0.36159\cdot10^{-15}$	
j=3	$-0.52372\cdot10^{-15}$	$0.32503\cdot10^{-18}$	

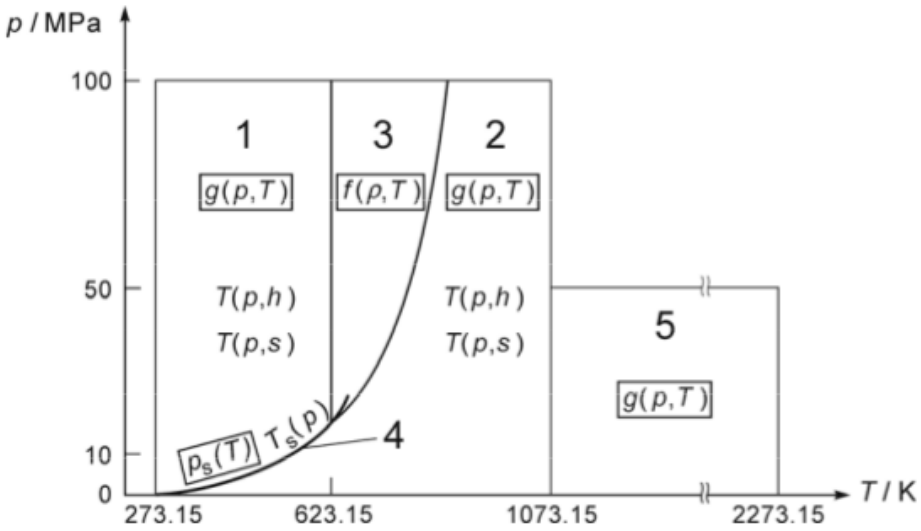

Figure 34. IAPWS-IF97 Fluid Regions.

14.2 IAPWS WATER PROPERTIES

The International Association for the Properties of Water and Steam (IAPWS) defines a consistent set of correlations to calculate the properties of water and steam that has been integrated into the code as an alternative to the calculations presented above. The correlations in IAPWS-IF97 [132] divide the fluid domain into several distinct regions with pressures reaching up to 100 MPa and temperatures up to 1,073 K for specific enthalpy, specific volume, and specific heat capacity.

Region 1 can be considered as a subcooled liquid. Region 2 can be considered as a superheated vapor. Region 3 can be considered as a supercritical fluid. Region 5 can be considered as an extreme superheated vapor add-on. The correlations for enthalpy, specific heat, and specific volume for Regions 1, 2,and 5 are based on the derivatives for the correlation of the dimensionless Gibbs free energy as a function of dimensionless pressure and temperature. However, Region 3 calculates these values based on the derivatives for the correlations of the dimensionless Helmholtz free energy as a function of dimensionless density and temperature. The IAPWS correlations for thermal conductivity [133], dynamic viscosity [134], and surface tension [135] are not based on dimensionless free energy.

14.3 MOLTEN SALT PROPERTIES

Thermophysical properties for LiF-BeF_2 (FLiBe) liquid salt are available in CTF. The properties are based on a mixture of 67 molar percent LiF and 33 molar percent BeF_2. The implemented correlations are shown in Table 15.

The liquid enthalpy relationship is defined using the assumption that the enthalpy is equal to zero at the melting temperature:

$$h = c_p(T - T_{melt}) \tag{674}$$

Standard convention would dictate that the internal energy, not the enthalpy, be set to zero at the melting temperature. The enthalpy at the melting temperature would then be calculated using the general formula:

$$h = u + p/\rho \tag{675}$$

Equation 674 effectively ignores the contribution of the p/ρ term to avoid introducing a pressure dependence into the enthalpy-temperature relationship, which (like the other correlations given in Table 15) is otherwise independent of pressure. The effect of this simplification is negligible, especially at the relatively low pressures typical of molten salt applications. Furthermore, only the *change* in enthalpy along a flow channel is of real interest, so the selection of a reference enthalpy value is only a matter of convention.

Note that CTF requires that property values be available for both the liquid and vapor phases of the working fluid; therefore, dummy values were used for the "vapor" phase of the molten salt fluid. However, the molten salt properties are intended for use only in the subcooled liquid regime because the vapor properties are not physically realistic.

Table 15. FLiBe salt thermophysical properties [136]

Quantity	Equation	Units	Uncertainty
Melting Point (T_{melt})	731.15	T_{melt} in [°K]	unknown
Boiling Point (T_{boil})	1673.15	T_{boil} in [°K]	unknown
Density (ρ)	$-0.4884T + 2413.$	T in [°K]	±0.05%
		ρ in [kg/m^3]	±0.05%
Dynamic Viscosity (μ)	$(1.16 \cdot 10^{-4})e^{3755./T}$	T in [°K]	±20%
		μ in [Pa-s]	±20%
Thermal Conductivity (k)	$0.0005T + 0.63$	T in [°K]	±15%
		k in [W/m-K]	±15%
Specific Heat (c_p)	2.416	c_p in [kJ/kg-K]	±2%

15. SOLID PROPERTIES

The primary purpose of this chapter is to provide a complete list of thermophysical solid properties available to CTF. Section 15.1 provides properties of LWR oxide fuels, Section 15.2 provides properties of fuel clad materials, and Section 15.3 provides properties used for fuel rod fill gases. The material properties correlations for the nuclear fuel rod are mostly included from recent versions of MATPRO nuclear material library handbook.

15.1 FUEL PELLET MATERIAL PROPERTIES

The properties are temperature dependent, so they were implemented into CTF as state functions with conversion from SI to English units. The user may model other fuel types using materials besides UO_2 and Zircaloy by giving CTF the thermal conductivity and specific heat as a function of material temperature in lookup tables.

15.1.1 Fuel Emissivity

The UO_2 emissivity ϵ_{UO_2} is used for calculating the radiative heat transfer between clad and gap. The spectral emissivity from Luscher et al. [137] is given by

$$\epsilon_{UO_2} = 0.78557 + 1.5263 \cdot 10^{-5} T \tag{676}$$

where: T = fuel temperature (°K)

Figure 35 shows the spectral emissivity of UO_2 fuel as a function of temperature with the hemispherical spectral data of Held and Wilder (1969) [138], as well as the emissivity data of Cabannes (1967) [139] and Claudson (1958) [140].

15.1.2 Fuel Specific Heat Capacity

The specific heat capacity is needed for temperature calculations in transient calculations as a result of the calculated stored energy/enthalpy being calculated via the specific heat capacity. The specific heat of UO_2 from MATPRO-11 [141] is calculated as follows:

$$Cp = \left\{ \frac{K_1 \theta^2 \exp(\theta/T)}{T^2 (\exp(\theta/T) - 1)^2} + K_2 T + \frac{\mathrm{OM}}{2} \frac{K_3 E_D}{RT^2} \exp\left(\frac{-E_D}{RT}\right) \right\}. \tag{677}$$

where: Cp = specific heat capacity of UO_2 fuel ($J/kg\text{-}°K$)
T = the temperature °K
OM = the oxygen to metal ratio, which is taken to be 2
R = 8.3143 $J/mol\text{-}K$
θ = the Einstein temperature

Figure 36 shows the fuel specific heat of UO_2 fuel as a function of temperature.

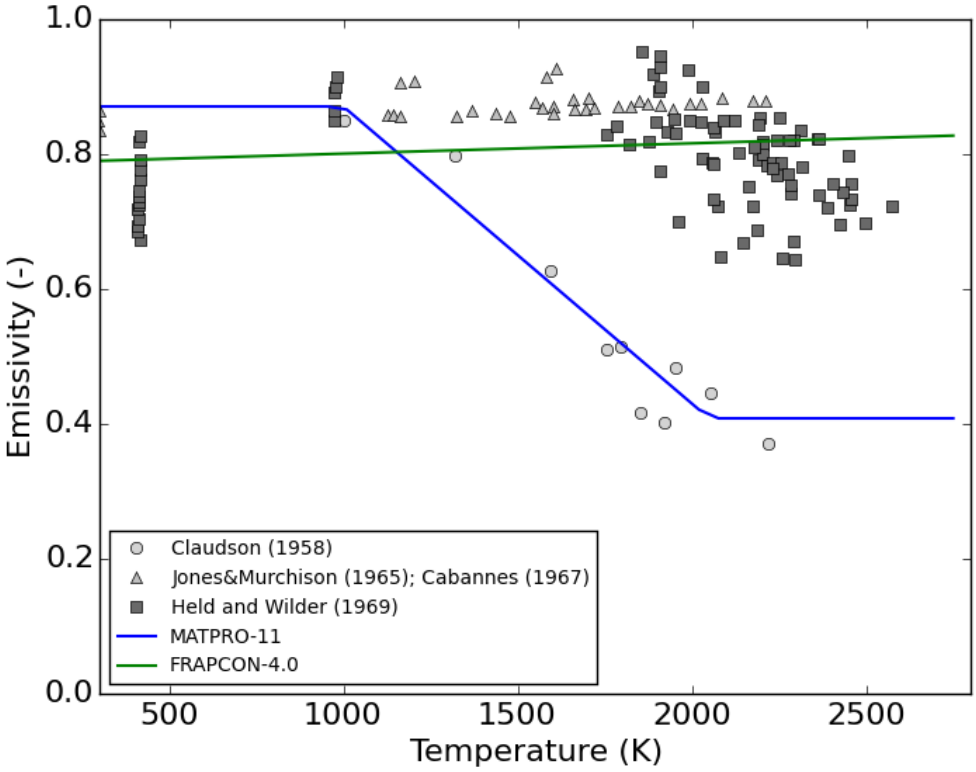

Figure 35. UO_2 fuel emissivity.

Table 16. Empirical coefficients in Eq. (677).

Fuel type	K_1 (J/kg-°K)	K_2 (J/kg-°K)	K_3 (J/kg-°K)	θ (°K)	E_D (J/mol)
UO_2	296.7	$2.43 \cdot 10^{-2}$	$8.745 \cdot 10^{7}$	535.285	$1.577 \cdot 10^{5}$

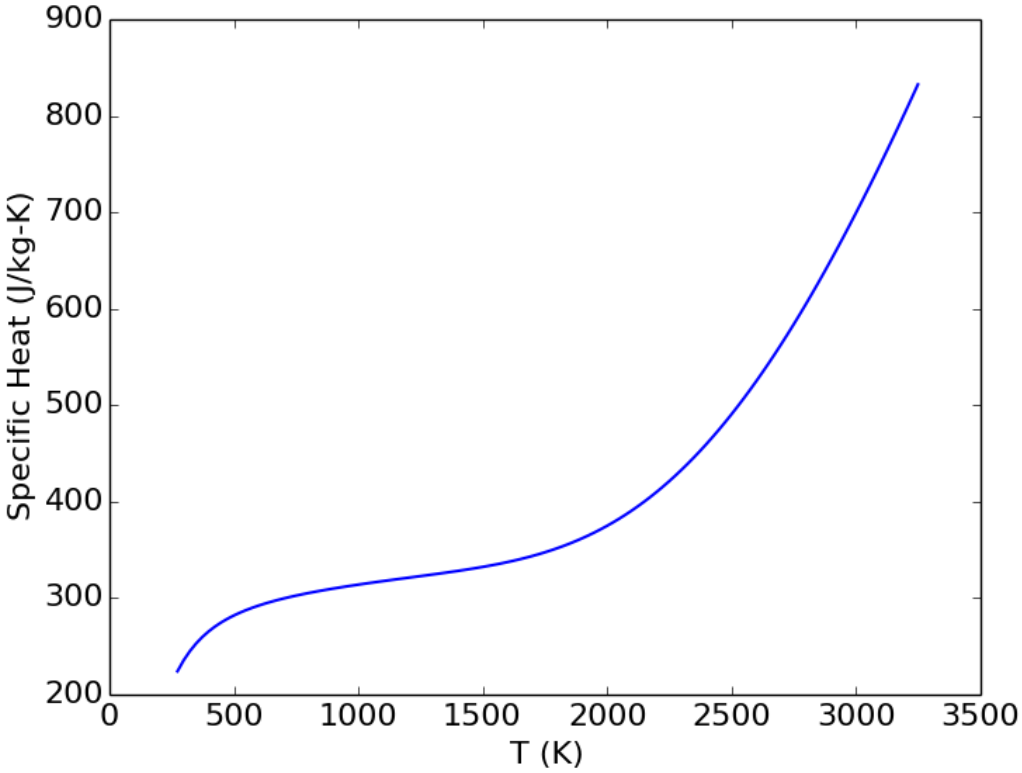

Figure 36. UO_2 fuel specific heat.

15.1.3 Fuel Thermal Conductivity

15.1.3.1 Uranium dioxide

The cold-state density of UO_2 density is 684.86 $^{lbm}/_{ft^3}$. The thermal conductivity of UO_2 is calculated in three different ways, as shown below:

- **MATPRO correlation** [142], with an expected operating range of 500–3,000°K, is only a function of temperature. The thermal conductivity is given in units of $^{BTU}/_{hr\text{-}ft\text{-}F}$ by

$$\begin{aligned} K_{UO_2} &= C\Big\{\max\left(\frac{2335}{464 + T_{\circ C}}, 1.1038\right) \\ &\quad + 7.027 \cdot 10^{-3} \exp\left(1.867 \cdot 10^{-3} \cdot T_{\circ C}\right)\Big\} \\ C &= \frac{1 - \beta \cdot (1 - TD)}{1 - 0.05 \cdot \beta} \\ \beta &= 2.58 - \left(5.8 \cdot 10^{-4}\right) T_{\circ C} \end{aligned} \tag{678}$$

where: T_C = the temperature (°C)
TD = the theoretical density (-)
C, β = the empirical coefficients

This model is set to CTF's default fuel thermal conductivity model. Figure 37 shows the thermal conductivity of UO_2 as a function of temperature.

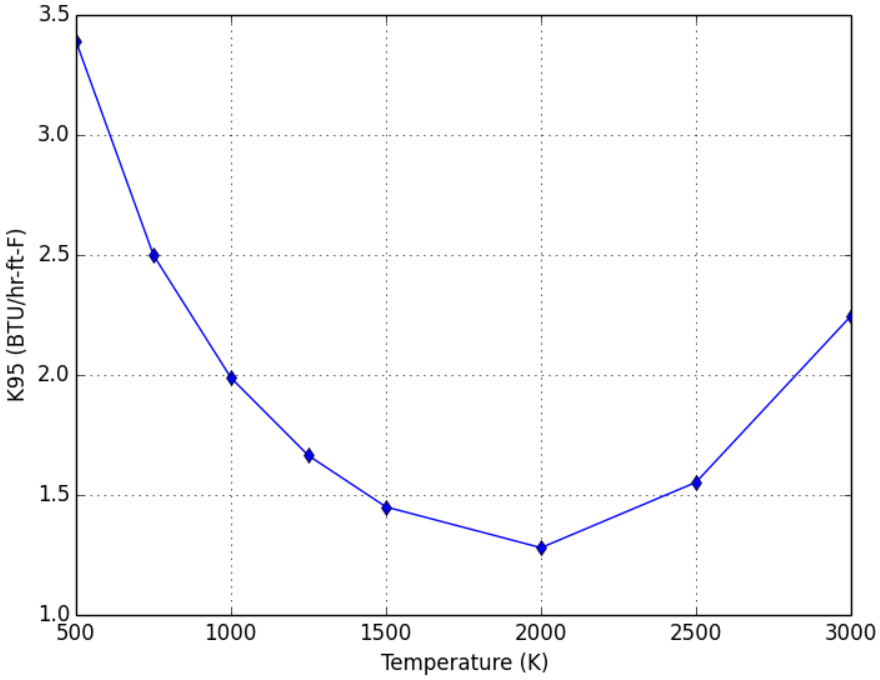

Figure 37. MATPRO-11 model for the thermal conductivity of 95% TD UO_2.

- **Modified NFI correlation** [143], the thermal conductivity (W/m-K) for the unirradiated 95% TD UO_2 fuel is represented as the summation of a lattice vibration (phonon) term K_{phonon} and electronic (electron hole pair effect) term $K_{electronic}$.

$$\begin{aligned} K_{UO_2,95} &= K_{phonon} + K_{electronic} \\ K_{phonon} &= 1/(0.0452 + 0.000246T_K + 0.00187Bu + 1.1599Gad \\ &\quad + [1.0 - 0.9\exp(-0.04Bu)]0.038hBu^{0.28}) \\ K_{electronic} &= \frac{3.50 \cdot 10^9}{T_K^2}\exp\left(-\frac{16361}{T_K}\right) \\ h &= 1/\left\{1.0 + 396.0\exp\left(-\frac{6380.0}{T_K}\right)\right\} \end{aligned} \tag{679}$$

where: T_K = the temperature (°K)
Bu = the burnup in MWD/kgU
Gad = is the gadolinia content in wt.%
h = the empirical function

The model is valid over

$$\begin{aligned} 300 \leq & T(K) \leq 3000 \\ 0 \leq & Bu \leq 62\text{MWd/kgU} \\ 0.92 \leq & TD \leq 0.97 \\ 0 \leq & Gad \leq 10\text{wt.\%} \end{aligned}$$

Figure 38 shows the thermal conductivity of 95% TD UO_2 as a function of temperature, burnup, and gadolinia content.

- **Halden correlation** [144], the thermal conductivity (W/m-K) for the unirradiated 95% TD UO_2 fuel, is estimated as

$$\begin{aligned} K_{UO_2,95} &= K_{phonon} + K_{electronic} \\ K_{phonon} &= 1/(0.1148 + 1.1599Gad + 1.1599f_x + 4 \cdot 10^{-3}Bu_{UO_2} \\ &\quad + 2.475 \cdot 10^{-4}[1.0 - 0.00333Bu_{UO_2}]T_o) \\ K_{electronic} &= 1.32 \cdot 10^{-2}\exp(0.00188T_C) \\ T_o &= \min(1650.0, T_C) \end{aligned} \quad . \tag{680}$$

where: T_C = the temperature (°C)
Bu = the burnup in MWD/kgU
Bu_{UO_2} = Bu/1.1366, the burnup in MWd/kgU
OM = oxygen-to-metal ratio (i.e., represents the deviation from stoichiometry, 2)
Gad = is the gadolinia content in wt.%
h = the empirical function

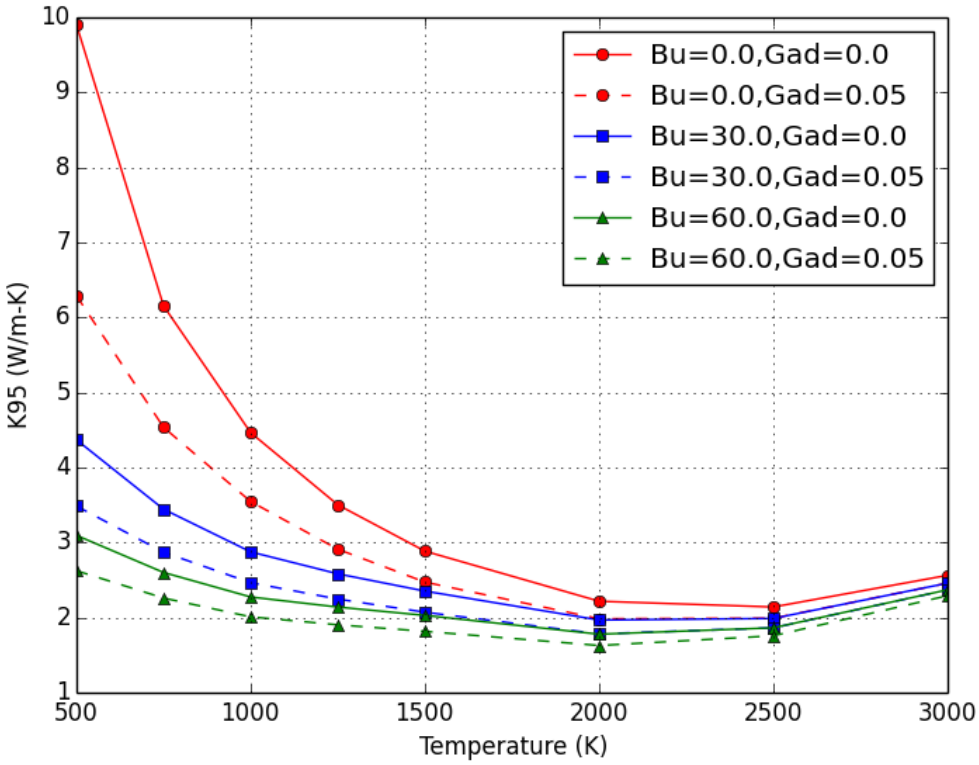

Figure 38. Modified NFI model for the thermal conductivity of 95% TD UO_2.

The model is valid over

$$\begin{aligned} 300 \leq & T(K) \leq 3000 \\ 0 \leq & Bu \leq 62\text{MWd/kgU} \\ 0.92 \leq & TD \leq 0.97 \\ 0 \leq & Gad \leq 10\text{wt.\%} \end{aligned}$$

Figure 39 shows the thermal conductivity of 95% TD UO_2 as a function of temperature, burnup and the gadolinia content.

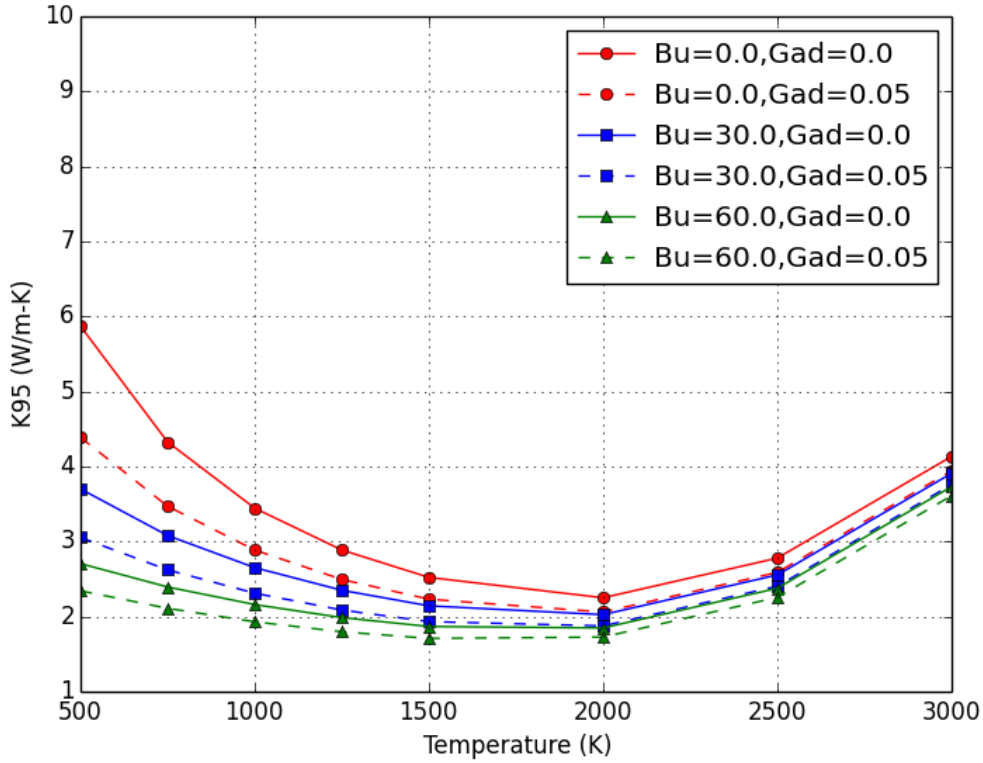

Figure 39. Halden model for the thermal conductivity of 95% TD UO_2.

The thermal conductivity model is adjusted for as fabricated fuel density using Lucuta's recommendation for spherical-shaped pores [145, 146, 144].

$$K_{UO_2} = K_{UO_2,95}\left(\frac{1.0789TD}{1.0 + 0.5\,(1.0 - TD)}\right) \tag{681}$$

15.1.3.2 MOX

The thermal conductivity is represented as the summation of a lattice vibration (phonon) term K_{phonon} and an electronic (electron hole pair effect) term $K_{electronic}$. For unirradiated 95% *TD* MOX fuel, the thermal conductivity $K_{MOX,95}$ is calculated by using the three models presented below.

- **The Duriez/Modified NFI correlation** is developed combining the Duriez stoichiometry-dependent correlation and a modified NFI correlation that includes the burnup degradation effects. For 95% *TD* MOX fuel, the thermal conductivity is given in units of W/m-K by

$$\begin{aligned} K_{MOX,95} &= K_{phonon} + K_{electronic} \\ K_{phonon} &= 1/(a_{OM} + c_{OM}T_K + 0.00187Bu + 1.1599Gad \\ &\quad + [1.0 - 0.9\exp(-0.04Bu)]0.038hBu^{0.28}) \\ K_{electronic} &= \frac{1.50 \cdot 10^9}{T_K^2}\exp\left(-\frac{13520}{T_K}\right) \\ h &= 1/\left\{1.0 + 396.0\exp\left(\frac{-6380.0}{T_K}\right)\right\} \\ a_{OM} &= 2.85OM + 0.035 \\ c_{OM} &= (2.86 - 7.15OM)\,1.0 \cdot 10^{-4} \end{aligned} \tag{682}$$

where: a_{OM}, b_{OM}, h = the empirical coefficients
OM = oxygen-to-metal ratio
Bu = the burnup (MWD/kgU)
T_K = the temperature in (°K)
Gad = the gadolinia content (wt.%)

Figure 40 shows the thermal conductivity of 95% TD MOX as a function of temperature, burnup, and the gadolinia content.

- **In the Halden correlation** [144], the thermal conductivity for 95% *TD* MOX fuel, is calculated as given in Eq. (680) except for the K_{phonon} term that is multiplied by 0.92 to account for reduction in thermal conductivity because of the presence of mixed oxides, and the $K_{electronic}$ term remains unchanged.

$$K_{MOX,95} = 0.92K_{phonon} + K_{electronic} \tag{683}$$

The model is valid over

$$\begin{aligned} 300 \leq & T(K) \leq 3000 \\ 0 \leq & Bu \leq 62\text{MWd/kgU} \\ 0.92 \leq & TD \leq 0.97 \\ 0 \leq & \text{plutonia content} \leq 7wt.\% \\ & \text{plutonia particle size} < 2\mu m \end{aligned} \quad .$$

Figure 41 shows the thermal conductivity of 95% TD MOX as a function of temperature, burnup, and the gadolinia content.

- **The Amaya correlation** [147] provides a dependency on plutonium concentration by applying corrections for the UO_2 thermal conductivity. CTF uses the MATPRO model to compute unirradiated UO_2 thermal conductivity. The MOX thermal conductivity (W/m-K) is given by

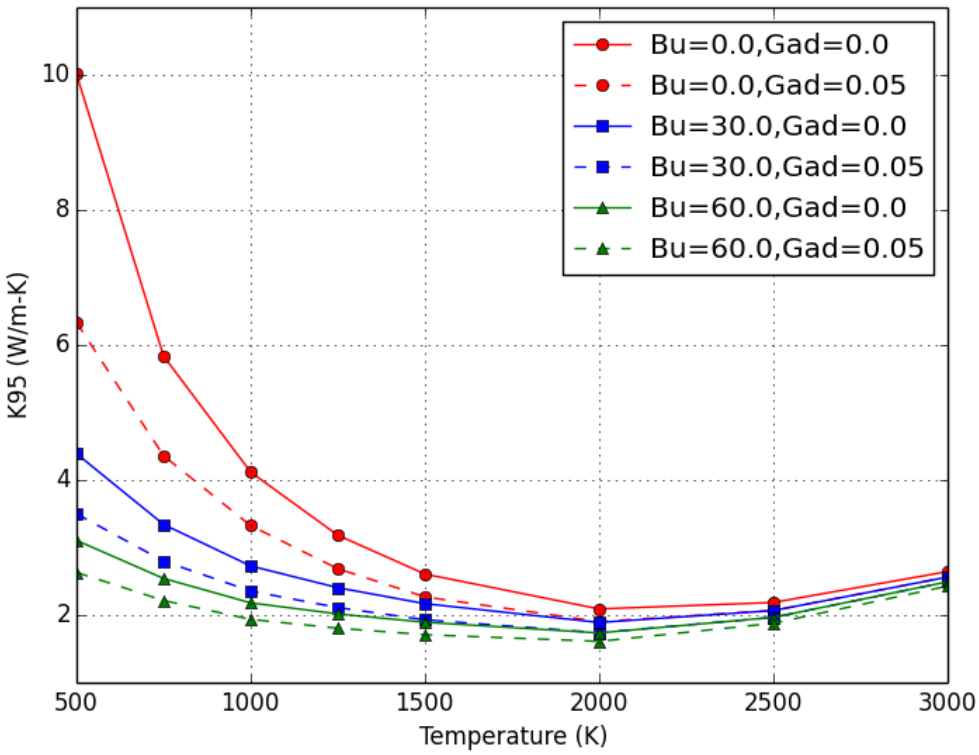

Figure 40. Duriez/Modified NFI model for the thermal conductivity of 95% TD MOX.

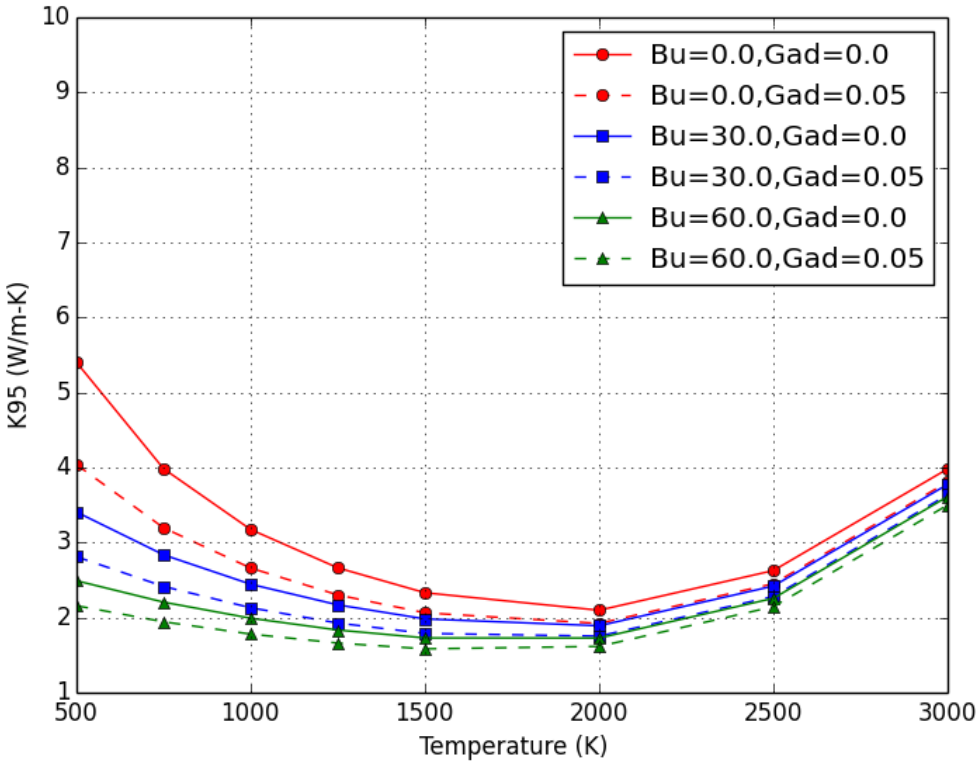

Figure 41. Halden model for the thermal conductivity of 95% TD MOX.

$$K_{MOX,95} = \sqrt{\frac{K_{UO_2,95}}{D_{0,Pu}\exp(D_{1,Pu}T)y}} \cdot \frac{}{\arctan(\sqrt{D_{0,Pu}\exp(D_{1,Pu}T)yK_{UO_2,95}})} \tag{684}$$

where: $K_{UO_2,95}$ = the unirradiated UO_2 thermal conductivity (W/m-K)
T = the temperature (K)
y = the plutonium concentration (wt.%)
$D_{0,Pu}, D_{1,Pu}$ = the empirical coefficients

The empirical coefficients are as follows:

$$\begin{aligned} D_{0,Pu} &= 0.209\text{m-W/K} \\ D_{1,Pu} &= 1.09 \cdot 10^{-3} K^{-1} \end{aligned} \tag{685}$$

CTF uses the MATPRO model for the thermal conductivity of 95% TD UO_2. This model will be adapted to use any UO_2 thermal conductivity in CTF. The MATPRO model is set for simplicity. Figure 42 shows the thermal conductivity of 95% TD MOX as a function of temperature, burnup, and the gadolinia content.

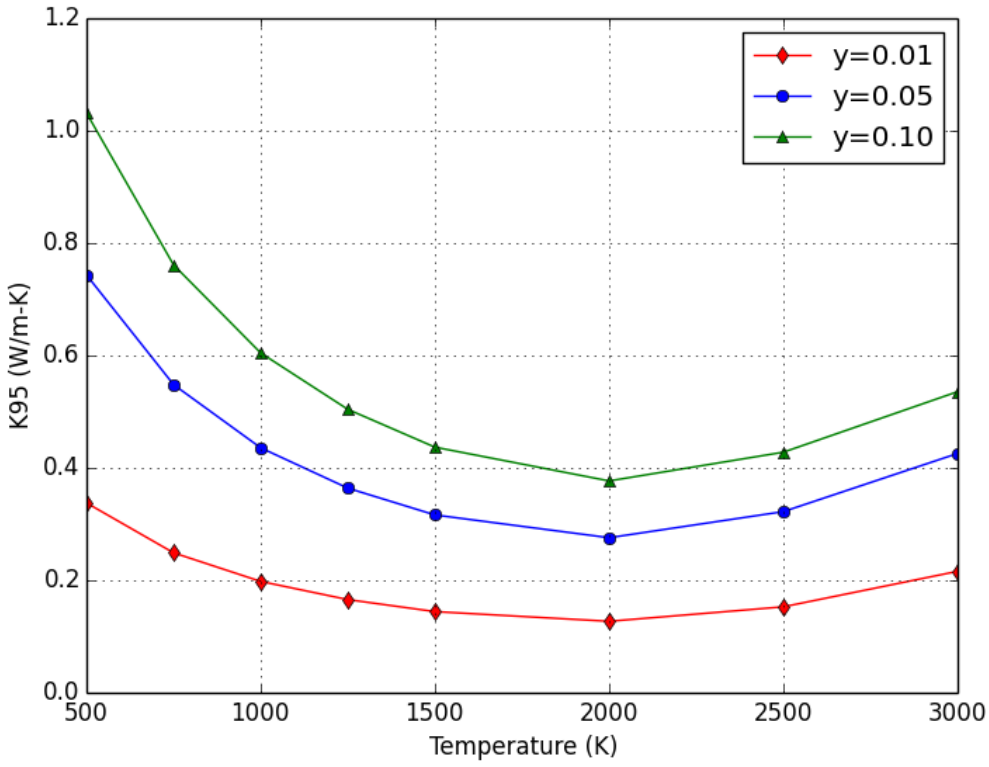

Figure 42. Amaya model for the thermal conductivity of 95% TD MOX.

The thermal conductivity of 100% *TD* is obtained by multiplying by the density correction factor to be representative of the material of interest. The thermal conductivity of MOX fuel is obtained in a manner similar to that used for UO_2, as follows:

$$K_{MOX} = K_{MOX,95}\left(\frac{1.0789TD}{1.0 + 0.5\,(1.0 - TD)}\right) \tag{686}$$

15.1.4 Fuel Melting Temperature

The fuel melting temperature is used to calculate the temperature of the liquid phase (solidus) and the last solid phase (liquidus) of UO_2 and MOX fuels as a function of burnup, gadolinia content, and plutonia content [141, 137].

$$\begin{aligned} T_{sldus} &= 3113.15 - 5.41395X_{Pu} + 7.46839 \cdot 10^{-3}X_{Pu}^2 \\ T_{liqdus} &= 3113.15 - 3.21860X_{Pu} + 1.448518 \cdot 10^{-2}X_{Pu}^2 \end{aligned} \tag{687}$$

where: T = fuel local temperature (°K)
X_{Pu} = the content of plutonia [wt.%]

The melting temperature is calculated as follows:

- for $X_{Pu} = 0$:

$$T_m = 3113.15 - 5.0 \cdot 10^{-4}Bu \tag{688}$$

- for $X_{Pu} \neq 0$:

$$\begin{aligned} T_m &= T_{sldus} - 5.0 \cdot 10^{-4}Bu \\ \Delta T_m &= T_{liqdus} - T_{sldus} - 5.0 \cdot 10^{-4}Bu \end{aligned} \tag{689}$$

- for Gd-doped urania:

$$T_m = 3115 - 4.8X_{Gd_2O_3} \tag{690}$$

where: Bu = fuel burnup [MWd/MTU]
$X_{Gd_2O_3}$ = the concentration of gadolinia [wt.%]
T_{sldus} = solidus temperature [K]
T_{liqdus} = liquidus temperature [K]
T_m = fuel melting temperature [K]
ΔT_m = temperature range between the solidus and liquidus [K]

Figure 43 shows the solidus and liquidus boundaries of the melting temperature of UO_2 and MOX, as well as the calculated fuel melting temperature.

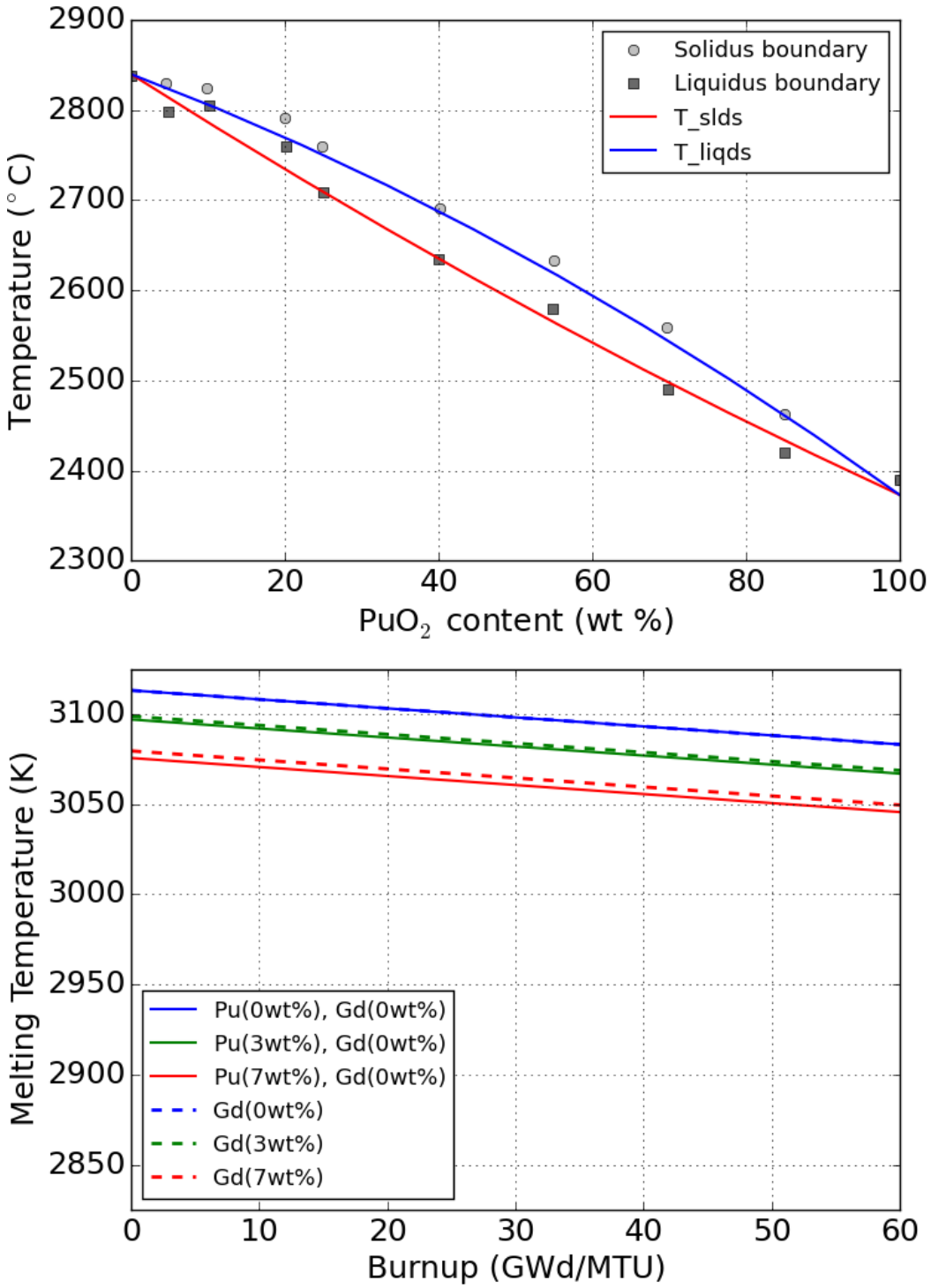

Figure 43. Solidus and liquidus boundaries of the melting temperature (top) and melting temperature (bottom).

15.1.5 Fuel Thermal Expansion

The FTHEXP subroutine to calculate the fuel thermal expansion is used in CTF [141, 137]. Linear strain caused by fuel thermal expansion (equal to zero at 300K) is given in a generic form of

$$\left(\frac{\Delta L}{L}\right) = K_1 T - K_2 + K_3 \exp\left(-E_D/kT\right). \tag{691}$$

- During melting, an expansion equal to a linear strain of 0.043 occurs.
- For the fuel is partially molten:

$$\left(\frac{\Delta L}{L}\right) = \left(\frac{\Delta L}{L}\right)_{T_m} + 0.043 \cdot R_{molten}. \tag{692}$$

- For the entirely molten fuel:

$$\left(\frac{\Delta L}{L}\right) = \left(\frac{\Delta L}{L}\right)_{T_m} + 0.043 + 3.5 \cdot 10^{-5}\left[T - (T_m + \Delta T_m)\right]. \tag{693}$$

where: $(\Delta L/L)_{T_m}$ = thermal expansion of solid fuel with $T = T_m$ [-]
E_D = energy of formation of a defect [J]
k = Boltzmann's constant [$1.38 \cdot 10^{-23}$ J/K]
R_{molten} = fraction of the molten fuel [-] (solid 0.0; molten 1.0)
T = temperature [K]
T_m = fuel melting temperature [K]

The empirical constants for UO_2 and PuO_2 to be used in Eq. (691) are tabulated in Table 17.

Table 17. The empirical constants for UO_2 and PuO_2, as shown in Eq. (691)

Constant	MATPRO UO_2	FRAP UO_2	PuO_2
K_1 [K^{-1}]	$1.0 \cdot 10^{-5}$	$9.80 \cdot 10^{-6}$	$9.0 \cdot 10^{-6}$
K_2 [-]	$3.0 \cdot 10^{-3}$	$2.61 \cdot 10^{-3}$	$2.7 \cdot 10^{-3}$
K_3 [-]	$4.0 \cdot 10^{-2}$	$3.16 \cdot 10^{-1}$	$7.0 \cdot 10^{-2}$
E_D [J]	$6.9 \cdot 10^{-20}$	$1.32 \cdot 10^{-19}$	$7.0 \cdot 10^{-20}$

Figure 44 and Figure 45 show the linear strain caused by the thermal expansion of UO_2 and PuO_2 fuels, respectively, as a function of fuel temperature.

15.2 CLADDING MATERIAL PROPERTIES

15.2.1 Cladding Thermal Conductivity

The cold-state density of Zircaloy is 409 $^{lbm}/_{ft^3}$. The thermal conductivity of Zr2/4 is calculated using the model from MATPRO-11 [141] as follows:

$$K_Z = 7.51 + 0.0209T - 1.45 \cdot 10^{-5}T^2 + 7.67 \cdot 10^{-9}T^3 \tag{694}$$

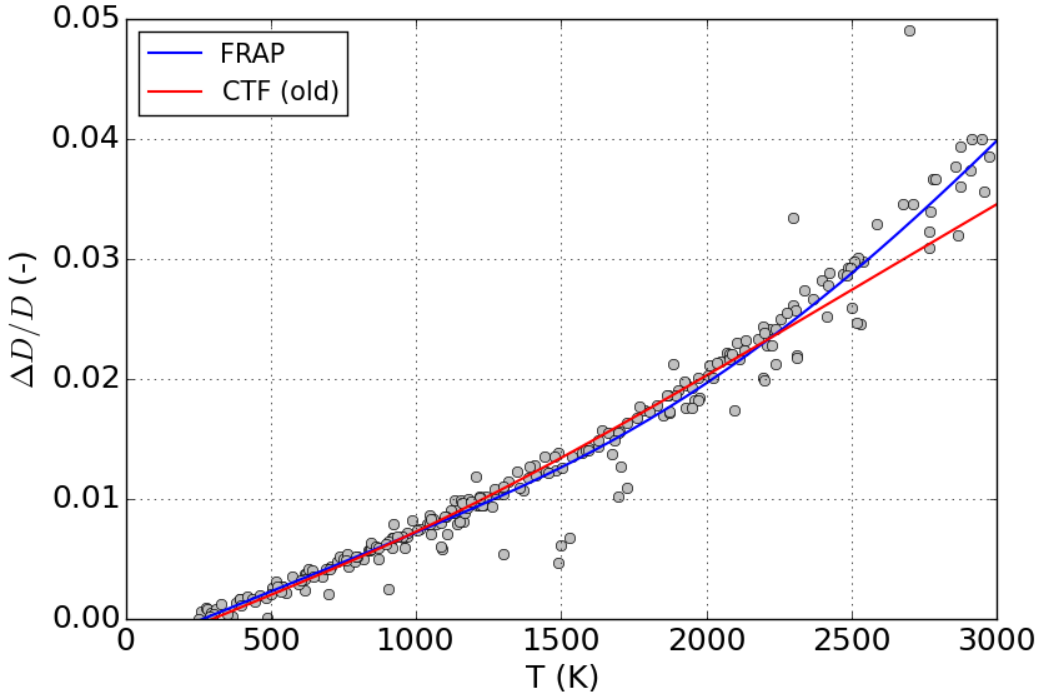

Figure 44. UO_2 fuel thermal expansion.

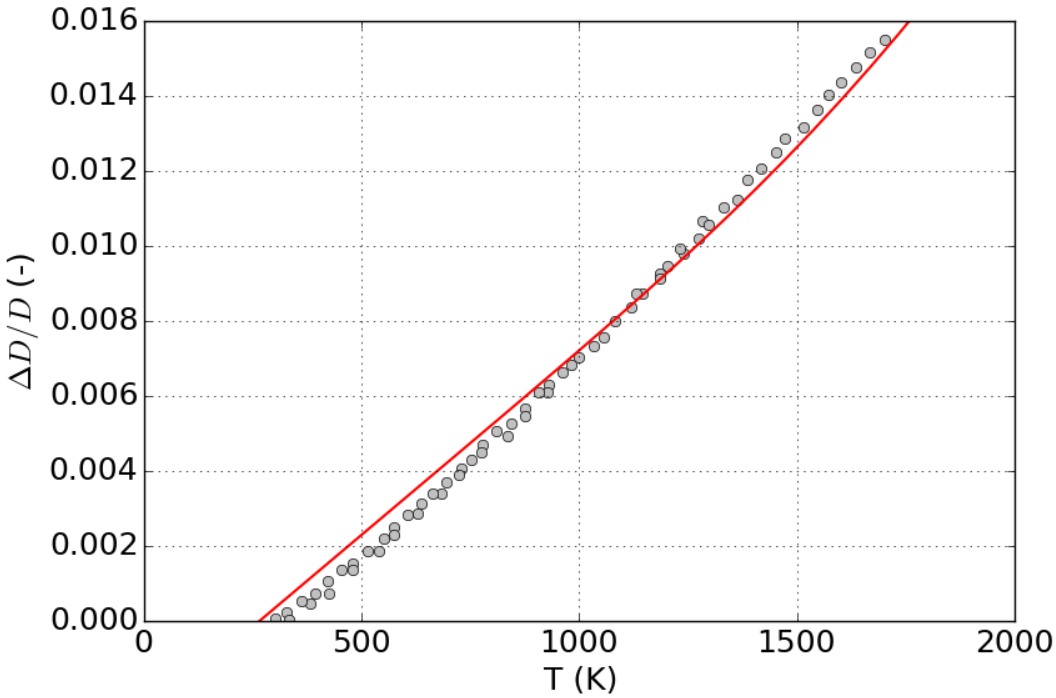

Figure 45. PuO_2 fuel thermal expansion.

where: K_Z = thermal conductivity (W/m-K)
T = fuel temperature (°K)

Thermal conductivity of Zircaloy, K_Z (W/m-K) from FRAPCON [137] is given as

$$K_Z = \begin{cases} 7.51 + 0.0209T - 1.45 \cdot 10^{-5}T^2 + 7.67 \cdot 10^{-9}T^3 & \text{for} \quad T < 2098°K \\ 36 & \text{for} \quad T \geq 2098°K \end{cases} \tag{695}$$

Thermal conductivity of Zircaloy, K_Z (W/m-K), from IAEA report [148], is given as

$$K_Z = 12.767 - 5.4348 \cdot 10^{-4}T + 8.9818 \cdot 10^{-6}T^2 \tag{696}$$

Figure 46 shows the thermal conductivity of Zircaloy as a function of temperature.

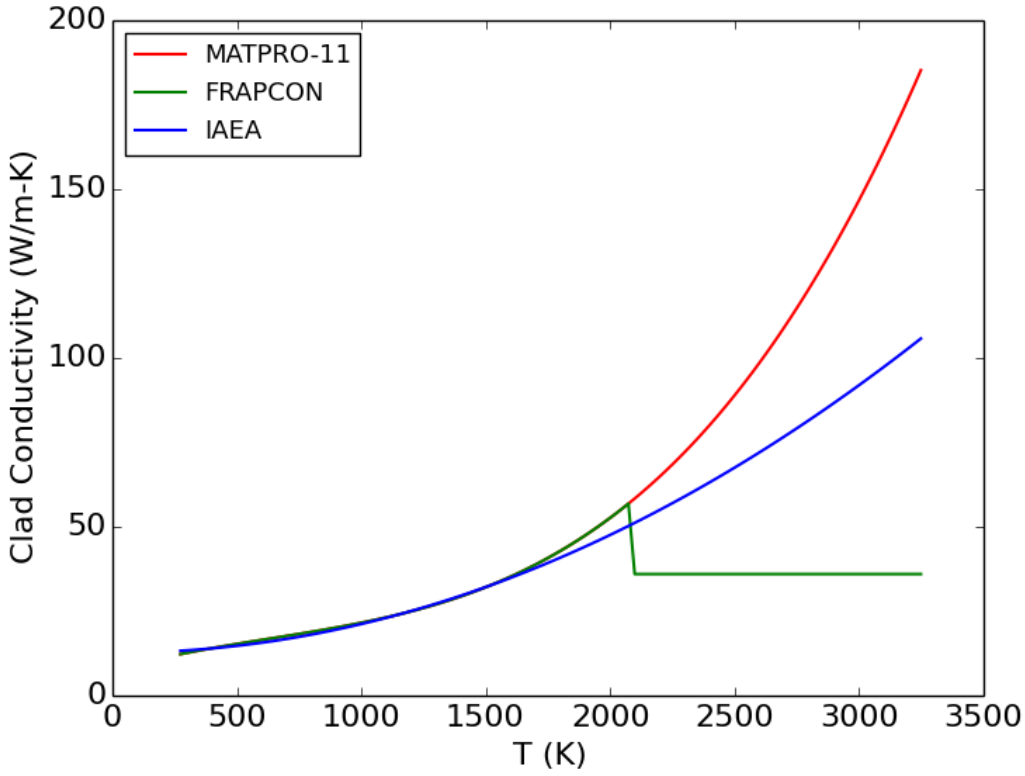

Figure 46. Thermal conductivity of Zircaloy.

15.2.2 Cladding Oxide Thermal Conductivity

The cold-state density of ZrO_2 is 409 lbm/ft³, and the specific heat capacity of ZrO_2 is set to 0.0785. The thermal conductivity, K_{ZrO_2} (W/m-K) as a function of temperature T (°K) from [141, 137] is given as

$$K_{ZrO_2} = 1.96 - 2.41 \cdot 10^{-4}T + 6.43 \cdot 10^{-7}T^2 - 1.95 \cdot 10^{-10}T^3 \tag{697}$$

where: K_{ZrO_2} = thermal conductivity (W/m-K)
T = fuel temperature (°K)

Figure 47 shows the thermal conductivity of ZrO_2 as a function of temperature.

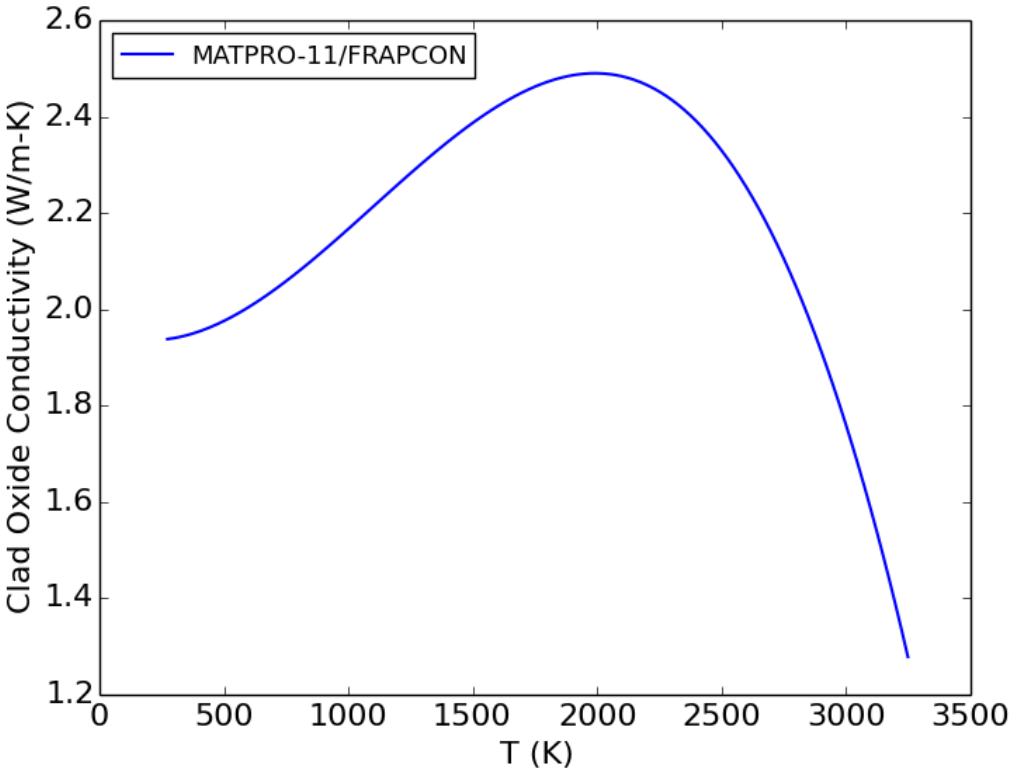

Figure 47. Thermal conductivity of ZrO_2.

15.2.3 Cladding Specific Heat

The specific heat of Zircaloy is obtained from a lookup table taken from MATPRO-11 (Revision 1)[75], as shown in Table 18. Figure 48 shows the tabulated data of cladding specific heat as a function of temperature, with α-phase data of Brooks and Stansbury (1966) [149] and β-phase data of Deem and Eldridge (1967) [150] and Coughlin and King (1950) [151]. The data of cladding-specific heat are applicable for Zircaloy-2, Zircaloy-4, ZIRLO, Optimized ZIRLO, and M5.

15.2.4 Cladding Surface Emissivity

The emissivity of the zirconium cladding with thin oxide coatings was taken from the ZOEMIS subroutine of MATPRO-11 (Revision 2) [141], which is given as

$$\epsilon_{Z,1} = \begin{cases} 0.325 + 0.1246 \cdot 10^6 d & \text{for} \quad d < 3.88x10^{-6} \\ 0.808642 - 50d & \text{for} \quad d \geq 3.88x10^{-6} \end{cases} \tag{698}$$

where: d = the oxide thickness (m)
T = the maximum cladding temperature (°K)

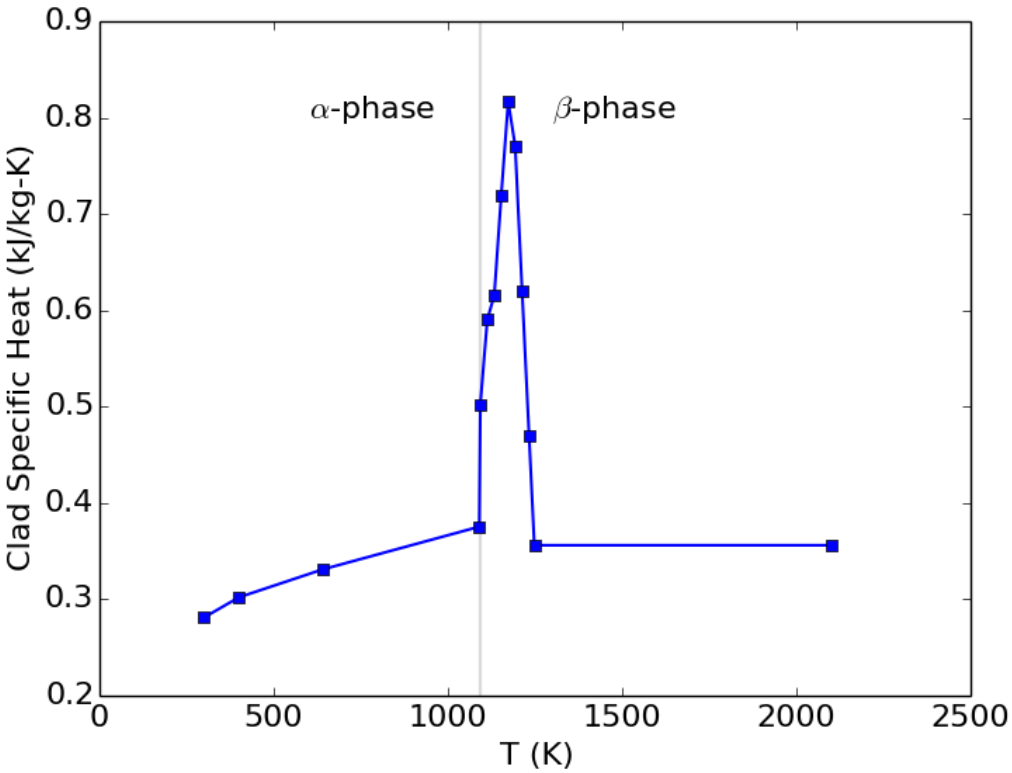

Figure 48. Cladding-specific heat capacity.

Table 18. Lookup table for calculating the specific heat of Zircaloy

T(K)	Cp (J/kg-K)	Source
300	281	Brooks and Stansbury [149]
400	302	
640	331	
1090	375	
1093	502	Deem and Eldridge [150]
1113	590	
1133	615	
1153	719	
1173	816	
1193	770	
1213	619	
1233	469	
1248	356	
2098	356	Coughlin and King [151]
2099	356	

When the maximum cladding temperature exceeds 1,500°K, the emissivity is assumed to be greater than 0.325. Equation (698) relates the emissivity $\epsilon_{Z,2}$ (unitless) above 1,500 K to $\epsilon_{Z,1}$ and T (K) as follows:

$$\epsilon_{Z,2} = \epsilon_{Z,1} \exp\left(\frac{[1500 - T]}{300}\right). \tag{699}$$

Figure 49 shows the cladding spectral emissivity of zirconium as a function of temperature and oxide thickness.

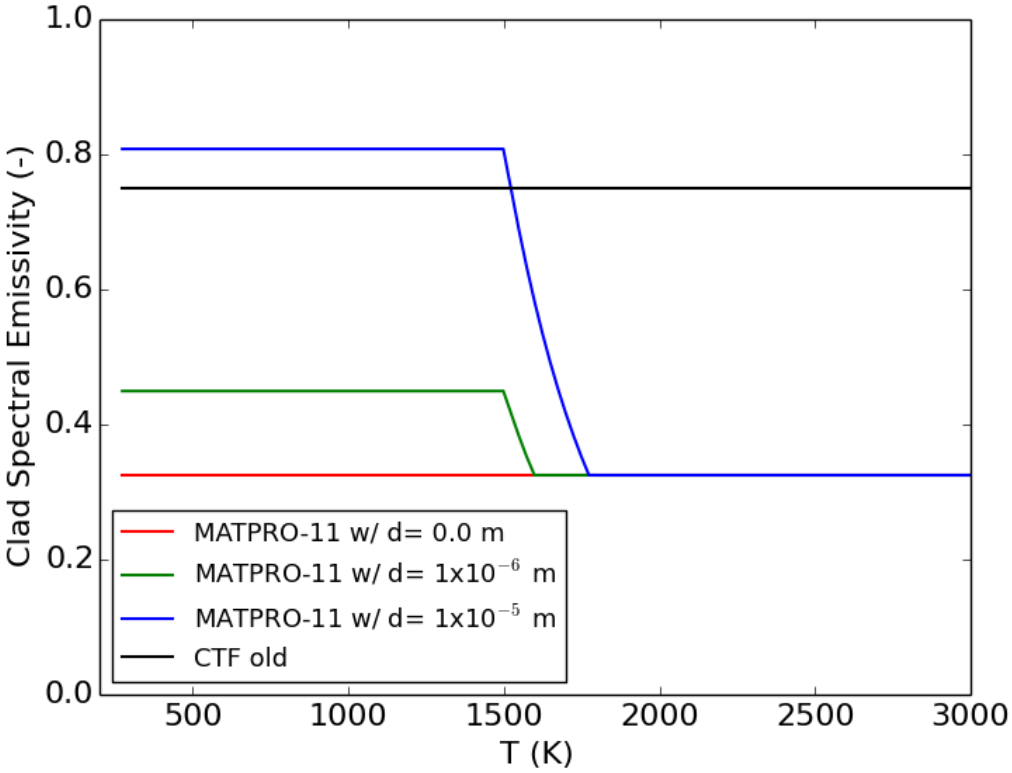

Figure 49. Zirconium cladding emissivity (Eq. (698)).

15.2.5 Cladding Meyer Hardness

For the case in which the gap closes as a result of fuel pellet expansion, there will be fuel/cladding contact. In this case, it is necessary to know the hardness of the cladding to determine the heat transfer caused by pellet/clad contact. Meyer hardness as a function of temperature, T (°K), H_Z (N/m^2), is implemented to CTF from the CMHARD subroutine of MATPRO-11 manual [141] and is given as

$$H_Z = \exp\left(26.03 - 0.02639T + 4.3502 \cdot 10^{-5}T^2 - 2.5621 \cdot 10^{-8}T^3\right) \tag{700}$$

where: T = temperature (°K).

Figure 50 shows the cladding's Meyer hardness as a function of temperature with the data of Peggs and Godin (1975) [152].

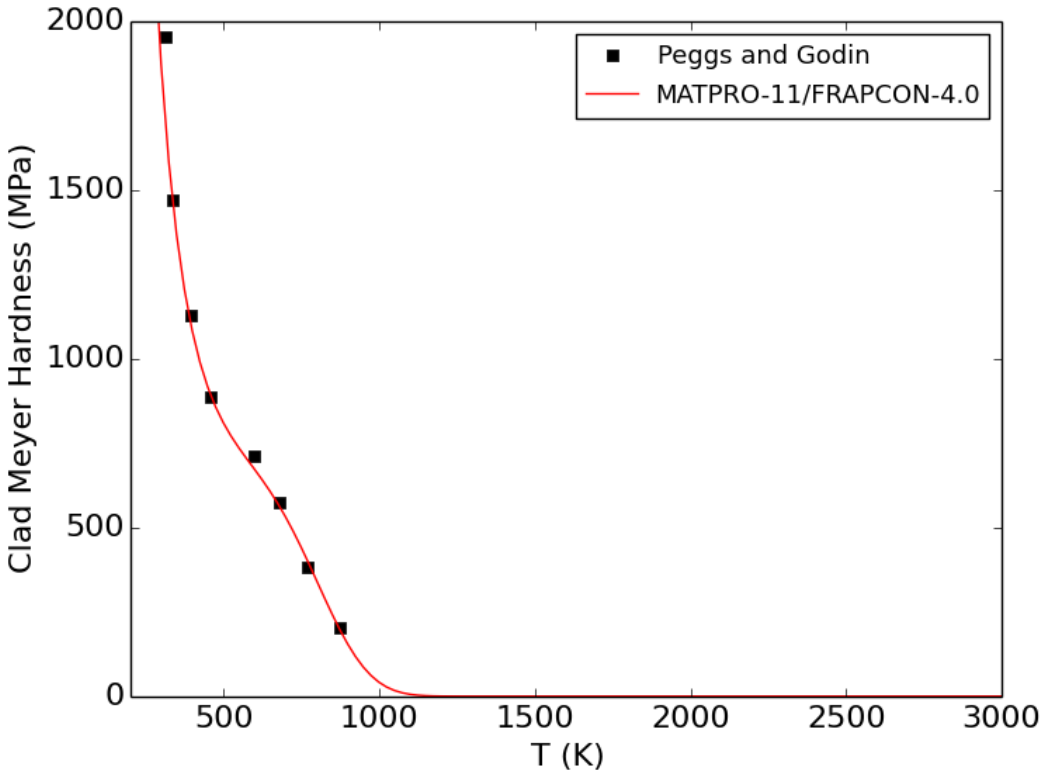

Figure 50. Meyer hardness of cladding.

15.2.6 Cladding Thermal Expansion

When determining cladding deformation caused by thermal expansion, it is important to know the cladding strain and stress. The cladding strain is calculated in axial and radial directions.

For the α-phase runs with temperatures between 300 K and 1,073 K:

$$\begin{aligned} \epsilon_{\text{Z,axial}} &= 4.44 \cdot 10^{-6} T - 1.24 \cdot 10^{-3} \\ \epsilon_{\text{Z,radial}} &= 6.72 \cdot 10^{-6} T - 2.07 \cdot 10^{-3} \end{aligned} \tag{701}$$

and for the β-phase with temperatures between 1,273 K and the melting point:

$$\begin{aligned} \epsilon_{\text{Z,axial}} &= 9.7 \cdot 10^{-6} T - 1.1 \cdot 10^{-2} \\ \epsilon_{\text{Z,radial}} &= 9.7 \cdot 10^{-6} T - 9.45 \cdot 10^{-3} \end{aligned} \tag{702}$$

where: T = temperature (°K)

Very little data are available for the α-phase to β-phase transition zone, which exists for temperatures from 1,073 K to 1,273 K. A lookup table was entered into CTF for this range; the data were taken from Scott's

data[153] as presented in MATPRO-11 (Revision 1)[75]. Axial and radial strain data for Zircaloy are given in Table 19. Figure 51 shows the cladding's axial and radial thermal expansion as a function of temperature.

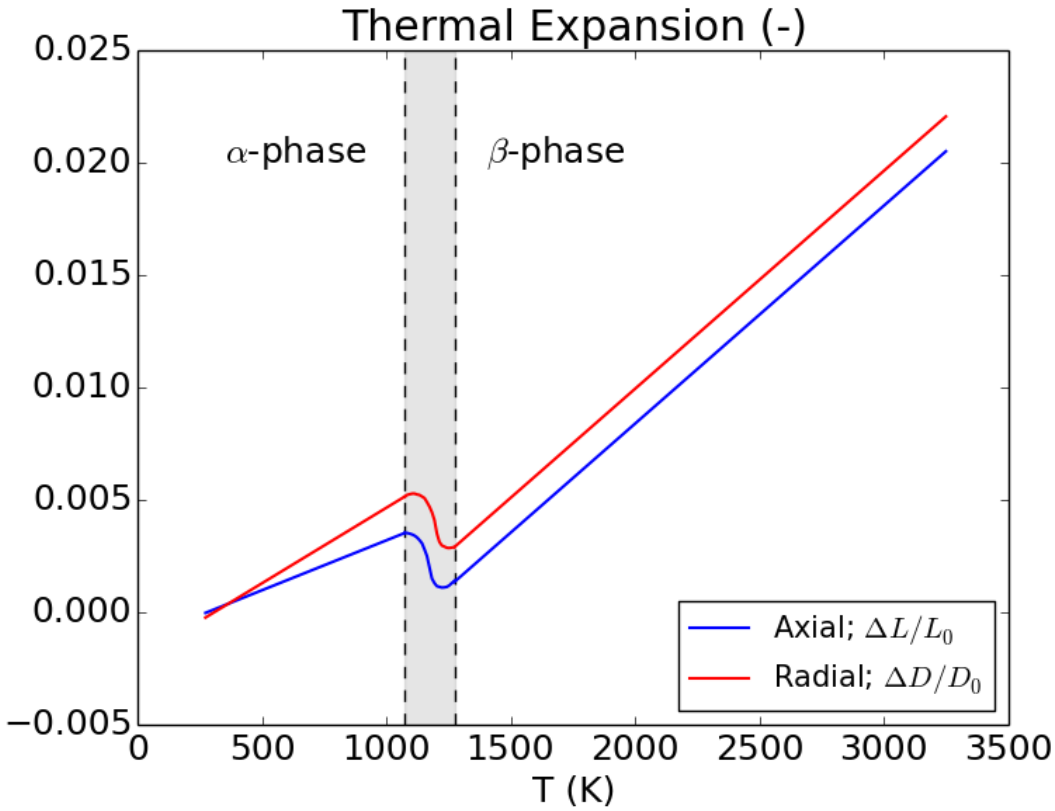

Figure 51. Cladding axial and radial thermal expansion.

15.2.7 Cladding Elastic Modulus and Shear Modulus

Stress in the cladding is calculated using Young's modulus. The shear modulus for Zircaloy is calculated as in the CELMOD and CSHEAR subroutines of MATPRO-11. Effects of oxidation (K_1), cold work (K_2), and fast neutron fluence (K_3) are neglected.

For the α-phase wtih $T < 1,093$ K:

$$\begin{aligned} E_Z &= 1.088 \cdot 10^{11} - 5.475 \cdot 10^{7} T \\ G_Z &= 4.04 \cdot 10^{10} - 2.168 \cdot 10^{7} T \end{aligned} \tag{703}$$

and for the β-phase with $T > 1,239$ K:

$$\begin{aligned} E_Z &= 9.21 \cdot 10^{10} - 4.05 \cdot 10^{7} T \\ G_Z &= 3.48 \cdot 10^{10} - 1.66 \cdot 10^{7} T \end{aligned} \tag{704}$$

where: T = temperature (°K)
E_Z = Young's modulus (Pa)
G_Z = shear modulus (Pa)

Table 19. Zircaloy axial strain data for the α-phase to β-phase transition zone

T (°K)	$\epsilon_{Z,axial}$ (ft/ft)·10^3	$\epsilon_{Z,radial}$ (ft/ft)·10^3
1073.15	3.52774	5.1395
1083.15	3.53	5.22
1093.15	3.50	5.25
1103.95	3.46	5.28
1113.15	3.41	5.28
1123.15	3.33	5.24
1133.15	3.21	5.22
1143.15	3.07	5.15
1153.15	2.80	5.08
1163.15	2.50	4.90
1173.15	2.00	4.70
1183.15	1.50	4.45
1193.15	1.30	4.10
1203.15	1.16	3.50
1213.15	1.13	3.13
1223.15	1.10	2.97
1233.15	1.11	2.92
1243.15	1.13	2.87
1253.15	1.20	2.86
1263.15	1.30	2.88
1273.15	1.40	2.90

Linear interpolation is used for calculating E_Z and G_Z in the α-phase to β-phase transition region. Poisson's ratio is obtained as follows:

$$\nu = \frac{E}{2G} - 1 \tag{705}$$

where: ν = Poisson's ratio (unitless)
E = Young's modulus (Pa)
G = shear modulus (Pa)

Figure 52 shows the cladding elastic moduli for the isotropic material as a function of temperature.

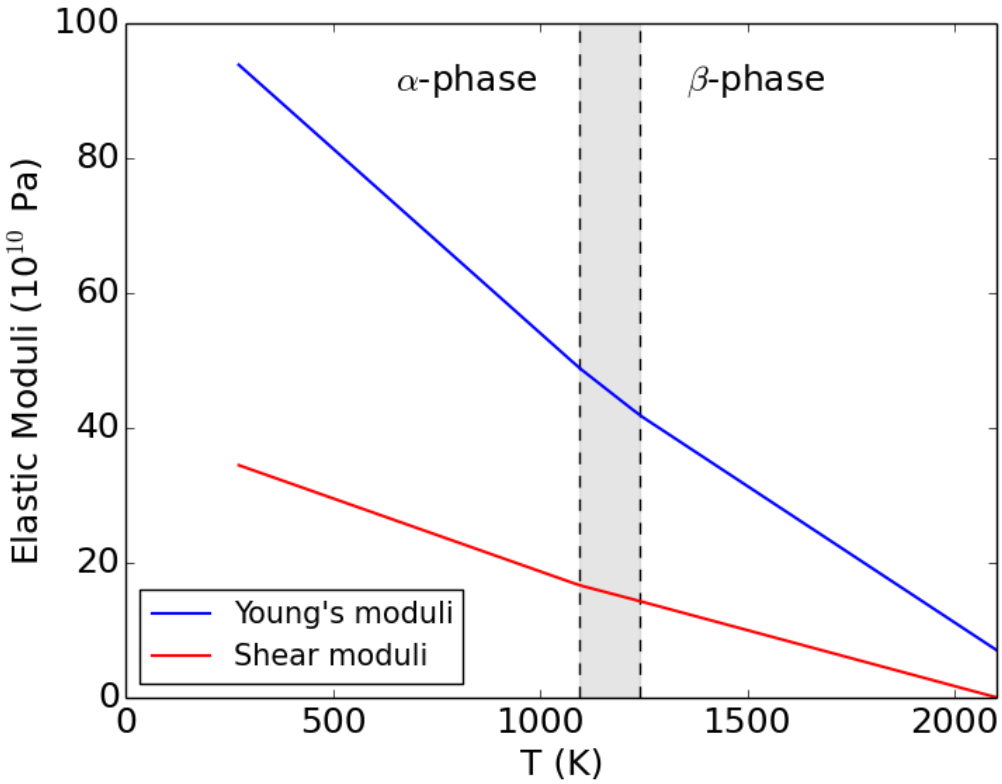

Figure 52. Cladding elastic moduli for isotropic material.

15.3 GAS PROPERTIES

CTF includes capabilities to model several noncondensable gases in the simulation, including air, argon, helium, hydrogen, krypton, nitrogen, oxygen, and xenon. This necessitates including a means of calculating gas properties for different system conditions. Noncondensable gases are modeled by the user providing information on the gases present in the system, their concentrations, and the reference enthalpy of the gas mixture. CTF includes specific heat and gas constant data for the gases to enable the calculation of the gas mixture's enthalpy and density.

15.3.1 Gas Conductivity

Properties are available for six different types of nuclear fuel rod fill gases. The gas conductivity and the gas molecular weight (M_i) is needed to determine the mixture gas conductivity. The fill gas conductivity

(BTU/hr-ft-F) is given by

$$K = a * T_{\circ R}^{b} \tag{706}$$

where: K = thermal conductivity (BTU/hr-ft-F)
a, b = the empirical coefficients
T = temperature (°R)

The temperature-dependent conductivities and gas molecular weights are given in Table 20.

Table 20. Fill gas conductivity relations

	Gas	a	b	M_i
1	Helium	$1.314 \cdot 10^{-3}$	0.668	4.003
2	Xenon	$1.395 \cdot 10^{-5}$	0.872	131.3
3	Argon	$1.31 \cdot 10^{-3}$	0.701	39.944
4	Krypton	$1.588 \cdot 10^{-5}$	0.92331	83.8
5	Hydrogen	$5.834 \cdot 10^{-4}$	0.8213	2.016
6	Nitrogen	$7.35 \cdot 10^{-5}$	0.846	28.8

Figure 53 shows the fill gas thermal conductivity as a function of temperature for helium, xenon, argon, krypton, hydrogen, and nitrogen.

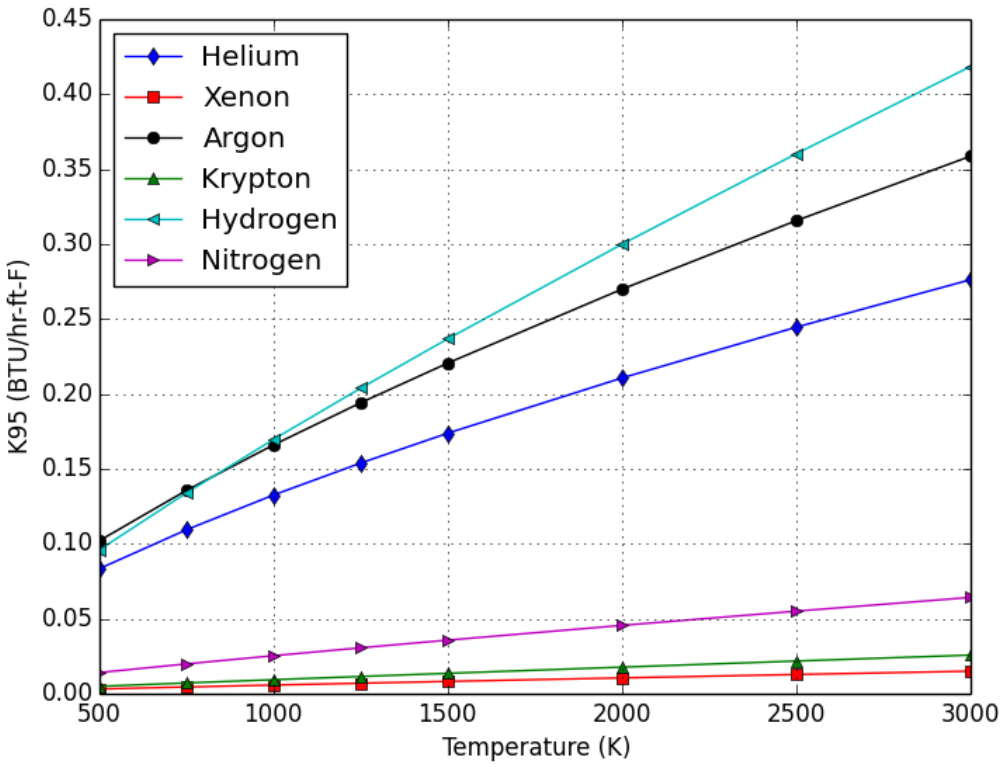

Figure 53. Fill gas thermal conductivity.

15.3.2 Molecular Weight

The molecular weight of the gases supported by CTF are given in Table 21.

Table 21. Molecular weights and specific gas constants of gases used in CTF

Gas	Molecular Weight	Specific gas constant ($^{psf}/_{^\circ R(lbm/ft^3)}$)
Air	28.96	53.34
Argon	39.94	38.66
Helium	4.003	386.0
Hydrogen	2.016	766.4
Krypton	83.70	18.459
Nitrogen	28.016	55.15
Oxygen	32.0	48.28
Xenon	131.3	11.767

15.3.3 Gas-Specific Heat

Specific heat is determined in the GASP subroutine. The specific heat for the gas mixture is calculated by summing the specific heats of individual constituent gases times their mass fraction.

$$Cp = \Sigma_{i=1}^{\text{ngas}} \text{mf}_i \text{Cp}_i \tag{707}$$

where: mf = the mass fraction of the gas

The mass fraction of the gas is found by dividing the gas molecular weight by the total molecular weight of the gas mixture.

$$\text{mf}_i = \frac{\alpha_i \text{mw}_i}{\Sigma_{i=1}^{\text{ngas}} \alpha_i \text{mw}_i} \tag{708}$$

where: α_i = the fraction of the individual gas in the mixture
mw_i = the molecular weight of the gas

The specific heats of the individual gases are found by correlation. For air, the correlation to be used depends on the gas temperature. Note that the gas mixture temperature is considered to be in thermoequilibrium with the vapor temperature, so they are equal in CTF. The air-specific heat, in units of $^{BTU}/_{lbm^\circ F}$, is:

$$\text{Cp}_{\text{air}} = 0.244388 - 4.20419 \cdot 10^{-5} T + 9.61128 \cdot 10^{-8} T^2 - 1.16383 \cdot 10^{-11} T^3, \text{ for } T <= 600\,\text{K} \tag{709a}$$

$$\text{Cp}_{\text{air}} = 0.208831 + 7.71027 \cdot 10^{-5} T - 8.56726 \cdot 10^{-9} T^2 - 4.75772 \cdot 10^{-12} T^3, \text{ for } T > 600\,\text{K} \tag{709b}$$

Argon-specific heat is set to a constant of 0.12428 $^{BTU}/_{lbm^\circ F}$. Helium-specific heat is set to a constant of 1.2404 $^{BTU}/_{lbm^\circ F}$. The hydrogen-specific heat is temperature-dependent.

$$\mathrm{Cp_H} = 1.46910 + 1.60057 \cdot 10^{-2} T - 4.44048 \cdot 10^{-5} T^2 + 4.21220 \cdot 10^{-8} T^3, \text{ for } T <= 400\,\mathrm{K} \quad (710a)$$

$$\mathrm{Cp_H} = 3.56903 - 4.8959 \cdot 10^{-4} T + 6.22549 \cdot 10^{-6} T^2 - 1.19686 \cdot 10^{-10} T^3, \text{ for } T > 400\,\mathrm{K} \quad (710b)$$

The krypton specific heat is set to $0\,^{\mathrm{BTU}}/_{\mathrm{lbm}^\circ\mathrm{F}}$. Nitrogen specific heat is temperature dependent.

$$\mathrm{Cp}_N = 0.259934 - 8.42119 \cdot 10^{-5} T + 1.72117 \cdot 10^{-7} T^2 - 6.7294 \cdot 10^{-11} T^3, \text{ for } T <= 775\,\mathrm{K} \quad (711a)$$

$$\mathrm{Cp}_N = 0.201678 + 1.08013 \cdot 10^{-4} T - 3.32212 \cdot 10^{-8} T^2 + 2.45228 \cdot 10^{-12} T^3, \text{ for } T > 775\,\mathrm{K} \quad (711b)$$

The oxygen specific heat is temperature dependent.

$$\mathrm{Cp}_O = 0.222081 - 7.6923 \cdot 10^{-5} T + 2.78765 \cdot 10^{-7} T^2 - 1.70107 \cdot 10^{-10} T^3, \text{ for } T <= 760\,\mathrm{K} \quad (712a)$$

$$\mathrm{Cp}_O = 0.1771 + 1.49509 \cdot 10^{-4} - 8.4494 \cdot 10^{-8} T^2 + 1.83236 \cdot 10^{-11} T^3, \text{ for } T > 760\,\mathrm{K} \quad (712b)$$

The xenon-specific heat is set to $0\,^{\mathrm{BTU}}/_{\mathrm{lbm}^\circ\mathrm{F}}$.

Figure 54 shows the specific heat of air, nitrogen, hydrogen, and oxygen as a function of temperature.

15.3.4 Gas Density

The gas mixture density is found using the ideal gas law.

$$\rho_{\mathrm{mix}} = \frac{P}{R_{\mathrm{mix}}\,(T + 459.6)} \quad (713)$$

where: T = the temperature (°F)
R = the gas constant ($^{\mathrm{psi}}/_{^\circ\mathrm{R(lbm/ft^3)}}$)

The gas constant for a mixture is calculated by summing the products of individual gas mass fractions and their individual gas constants.

$$R_{\mathrm{mix}} = \Sigma_{i=1}^{\mathrm{ngas}} \mathrm{mf}_i R_i \quad (714)$$

The individual specific gas constants are given in Table 21. Units are in pounds per square foot (psf) in the table, so those values are converted to psi before being used to calculate density. Gas mixture density is calculated in various locations of the source code as needed.

15.3.5 Gas Enthalpy

The enthalpy of the gas mixture is calculated using the specific heat of the mixture. The temperature change from the reference temperature, T_{ref}, is multiplied by Cp and added to the reference enthalpy, h_{ref}.

$$H_{\mathrm{mix}} = \mathrm{Cp_{mix}} \left(T_v - T_v^{ref} \right) + H_{\mathrm{ref}} \quad (715)$$

If the solution is in the middle of a transient, then the previous time step temperature and enthalpy are used in place of the reference values.

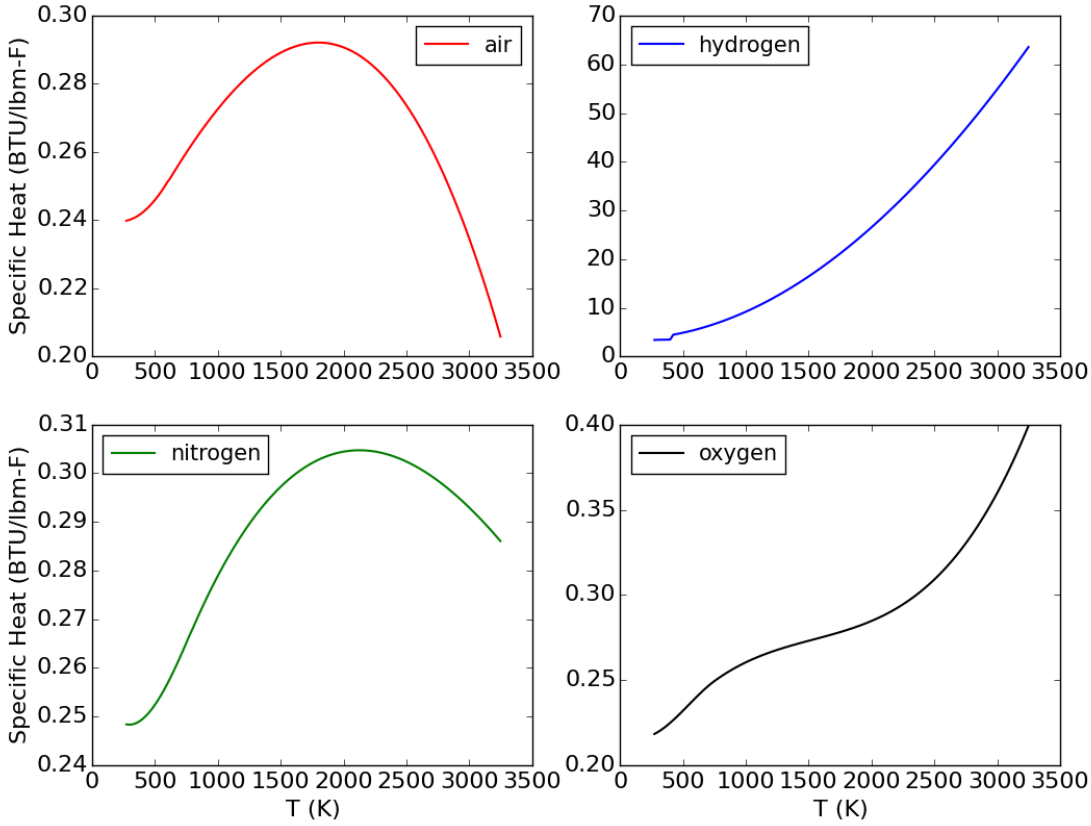

Figure 54. Specific heat of air, nitrogen, hydrogen and oxygen.

REFERENCES

[1] M.J. Thurgood et al. "COBRA-TF Development". In: *8th Water Reactor Safety Information Meeting*. 1980.

[2] David J. Kropaczek et al. "Advanced two-phase subchannel method via non-linear iteration". In: *Nuclear Engineering and Design* 408 (2023), p. 112328. ISSN: 0029-5493. DOI: https://doi.org/10.1016/j.nucengdes.2023.112328. URL: https://www.sciencedirect.com/science/article/pii/S0029549323001772.

[3] M.N. Avramova. *CTF—A Thermal-Hydraulic Subchannel Code for LWR Transient Analyses: Theory Manual: Volume II Linearization of Mass and Energy Equations*. Tech. rep. Pennsylvania State University, 2009.

[4] S.V. Patankar. *Numerical Heat Transfer and Fluid Flow*. McGraw-Hill, 1980.

[5] M.N. Avramova. *CTF—A Thermal-Hydraulic Subchannel Code for LWR Transient Analyses: Theory Manual: Volume I Momentum Equations*. Tech. rep. Pennsylvania State University, 2009.

[6] M.N. Avramova. *CTF: A Thermal Hydraulic Sub-Channel Code for LWR Transient Analyses, User's Manual*. Feb. 2009.

[7] E. Ozdemir. "Multidimensional Boron Transport Modeling in a Subchannel Approach". PhD thesis. The Pennsylvania State University, 2012.

[8] S. Kliem et al. "Experiments at the mixing test facility ROCOM for benchmarking of CFD codes". In: *Nuclear Engineering and Design* 238 (2008), pp. 566–576.

[9] J. Tuunanen et al. "Long-term emergency cooling experiments with aqueous boric acid solution with the REWET-II and VEERA facilities." In: *Proc. Int. ENS/ANS Conf. On Thermal Reactor Safety*. 1988.

[10] J. Tuunanen, H. Tuomisito, and P. Raussi. "Experimental and analytical studies of boric acid concentrations in a VVER-440 reactor during long-term cooling period of loss-of-coolant accidents". In: *Nuclear Engineering and Design* 148 (1994), pp. 217–231.

[11] J. Freixa, R. Francesc, and C. Pretel. "Boron Transport Model with Physical Diffusion for RELAP5". In: *Nuclear Technology* 160 (2007), pp. 205–215.

[12] E. Ozdemir, M. N. Avramova, and K. Sato. "Multi-dimensional boron transport modeling in subchannel approach: Part I. Model selection, implementation and verification of COBRA-TF boron tracking model". In: *Nuclear* 278 (2014), pp. 701–712.

[13] E. Ozdemir and M. N. Avramova. "Multi-dimensional boron transport modeling in subchannel approach: Part II. Validation of CTF boron tracking model and adding boron precipitation model". In: *Nuclear E* 278 (2014), pp. 713–722.

[14] P. L. Roe. "Some Contributions to the Modeling of Discontinuous Flow". In: *Lectures of Applied Mathematics*. Vol. 22. 163. 1975.

[15] H. C. Yee and R. F. Warming. "Implicit Total Variation Dismishing (TVD) Schemes for Steady-State Calculations". In: *Computational Physics* 57 (1985), p. 327.

[16] A. Einstein. "On the Movement of Small Particles Suspended in Stationary Liquids Required by the Molecular -Kinetic Theory of Heat". In: *Annals of Physics* 17 (1905), p. 549.

[17] P. Zanetti. "Pollution Modelling: Theories, Computational Methods and Available Software". In: *Computational Mechanics Publications, Southhamption, United Kingdom* (1990).

[18] Numerical diffusion and Part 1. One-dimensional flows the tracking of solute fields in system codes. "R. Macian-Juan and J. Mahaffy". In: *Nuclear Engineering and Design* 179 (1998), pp. 297–319.

[19] S. Y. Kim et al. "High temperature boric acid solubility during post-LOCA long-term cooling period". In: *Transactions of the American Nuclear Society* 99 (2008), pp. 489–490.

[20] GEH. *GEH Licensing Topical Report NEDO-32176, Revision 4,TRACG Model Description*. 2008.

[21] G. B. Wallis. *One-dimensional Two-phase Flow*. New York: McGraw-Hill, 1972.
[22] Belgacem Hizoum, Vineet Kuma, and Robert Salko. "CTF Improved Drag Model and Flow Regime Transition Criteria". In: *The 19th International Topical Meeting on Nuclear Reactor Thermal Hydraulics (NURETH-19) Log nr.: 19001* (March 6, 2022.).
[23] M. Ishii. *One-Dimensional Drift-Flux Model and Constitutive Equations for Relative Motion between Phases in Various Two-Phase Flow Regimes*. Tech. rep. ANL-77-47. Argonne National Laboratory, Sept. 1977.
[24] P. Griffith and G.B. Wallis. "Two-Phase Slug Flow". In: *J. Heat Transfer* 83 (1961), pp. 307–320.
[25] P.A. Griffith and G.A. Snyder. *The Bubbly-Slug Transition in High Velocity Two-Phase Flow*. Tech. rep. TID-20947. MIT, July 1964.
[26] K. Mishima and M. Ishii. "Theoretical Prediction on Onset of Horizontal Slug Flow". In: *J. Fluids Eng.* 102 (1980), pp. 441–445.
[27] N.A. Radovich and R. Moissis. *The Transition from Two-Phase Bubble Flow to Slug Flow*. Tech. rep. 7-7673-22. MIT, 1962.
[28] Y. Taitel, D. Bornea, and A.E. Dukler. "Modeling flow pattern transitions for steady upward gas-liquid flow in vertical tubes". In: *AIChE Journal* 26.3 (1980), pp. 345–354.
[29] M. Ishii and K. Mishima. *Study of Two-Fluid Model and Interfacial Area*. Tech. rep. NUREG/CR-1873, ANL-80-111. Argonne National Laboratory, Dec. 1980.
[30] G.B. Wallis. *One-Dimensional Two-Phase Flow*. McGraw-Hill, 1969.
[31] N.E. Todreas and M.S. Kazimi. *Nuclear Systems II Elements of Thermal Hydraulic Design*. Hemisphere Publishing Corporation, 1990.
[32] R.W. Lockhart and R.C. Martinelli. "Proposed Correlation of Data for Isothermal Two-Phase, Two-Component Flow in Pipes". In: *Chemical Engineering Progress* 45.1 (1949), pp. 39–48.
[33] D. Chisholm. "Pressure Gradients Due to Friction during the Flow of Evaporating Two-Phase Mixtures in Smooth Tubes and Channels". In: *Int J Heat and Mass Transfer* 16 (1973), pp. 347–358.
[34] W. H. McAdams. *Heat Transmission*. First. McGraw-Hill, New York, 1933.
[35] D. J. Zigrang and N. D. Sylvester. "Explicit Approximations to the Solution of Colebrook's Friction Factor Equation". In: *AICHE J* 28.3 (May 1982), pp. 514–515.
[36] S. W. Churchill. "Friction Factor Equation Spans All Fluid-Flow Regimes". In: *Chemical Engineering* 7 (Nov. 1977), pp. 94–95.
[37] M. Ishii and T.C. Chawla. *Local Drag Laws in Dispersed Two-Phase Flow*. Tech. rep. NUREG/CR-1230. Argonne National Laboratory, Dec. 1979.
[38] R. Salko et al. *CTF Void Drift Validation*. Tech. rep. CASL-U-2015-0320-002. Consrotium for Advanced Simulation of Light Water Reactors, 2015.
[39] Xingang Zhao et al. "Assessment of the Subchannel Code CTF for Single- and Two-Phase Flows". In: *Nuclear Technology* 205.1–2 (2019), pp. 338–351.
[40] A. Wysocki and R. Salko. *Validation of CTF Droplet Entrainment and Annular/Mist Closure Models using Riso Steam/Water Experiments*. Tech. rep. CASL-U-2016-1080-000. Consortium for Advanced Simulation of Light Water Reactors, 2016.
[41] Nathan W. Porter, Maria N. Avramova, and Vincent A. Mousseau. "Uncertainty Quantification Study of CTF for the OECD/NEA LWR Uncertainty Analysis in Modeling Benchmark". In: *Nuclear Science and Engineering* 190.3 (2018), pp. 271–286. DOI: 10.1080/00295639.2018.1435135.
[42] JO. Shaug JGM. Andersen KH. Chu. "Development Basic Models for the BWR Version of TRACG". In: *NUREG/CR-2573* (1983).
[43] S. Bajorek et al. *TRACE V5.1051 Theory Manual*. US NRC. 2016.
[44] J. E. Kelly, S. P. Kao, and M. S. Kazimi. *THERMIT-2: A Two-Fluid Model for Light Water Reactor Subchannel Transient Analysis*. Tech. rep. MIT-EL-81-014. MIT Energy Laboratory Electric Utility Program, 1981.

[45] Isoa Kataoka and Mamoru Ishii. “Drift Flux Model for Large Diameter Pipe and New Correlation for Pool Void Fraction”. In: *Inf. J. Hear Mass Transfer. Vol. 30, No. 9, pp. 1927-1939* (1987).
[46] W.H. Henstock and T.J. Hanratty. “The Interfacial Drag and the Height of the Wall Layer in Annular Flows”. In: *AIChE Journal* 22.6 (1976), pp. 990–1000.
[47] A.E. Dukler et al. *Two-Phase Interactions in Countercurrent Flow Studies of the Flooding Mechanism*. Tech. rep. NUREG/CR-0617. Nuclear Regulatory Commission, 1979.
[48] P.N. Rowe, K.T. Claxton, and J.B. Lewis. “Heat and Mass Transfer from a Single Sphere in an Extensive Flowing Fluid”. In: *Trans. Instn. Chem. Engrs.* Vol. 43. 1965, T14–T31.
[49] M. J. Boussinesq. “Calcul du Pouvoir Refroidissant des Courants Fluids (Calculation of the Cooling power of a Fluid Stream)”. In: *Journal de Mathématiques Pures et Appliquées* 1 (1905), p. 310.
[50] K. Lee and D.J. Ryley. “The Evaporation of Water Droplets in Superheated Steam”. In: *Trans. ASME J. Heat Transfer* 90 (1968), pp. 445–451.
[51] A.P. Colburn. “A Method of Correlating Forced Convection Heat Transfer Data and a Comparison with Fluid Friction”. In: *Trans Am Inst Chem Eng*. Vol. 29. 1933, pp. 174–210.
[52] M. Ishii and M.A. Grolmes. “Inception Criteria for Droplet Entrainment in Two-Phase Concurrent Film Flow”. In: *AIChE Journal* 21.2 (1975), p. 308.
[53] G.A. Hughmark. “Film Thickness Entrainment and Pressure Drop in Upward Annular and Dispersed Flow”. In: *AICHE J* 19 (1973), pp. 1062–1065.
[54] J. G. M. Andersen. *REMI/HEAT COOL, A Model for Evaluation of Core Heat-Up and Emergency Core Spray Cooling System Performance for Light-Water-Cooled Nuclear Power Reactors*. Tech. rep. 296. RISO National Laboratory, Sept. 1973.
[55] N. Frössling. “The Evaporation of Falling Drops”. In: *Gerlands Beitrage zur Geophysik* 52 (1938), pp. 107–216.
[56] M.C. Yuen and L.W. Chen. “Heat-Transfer Measurements of Evaporating Liquid Droplets”. In: *Int J Heat and Mass Transfer* 21 (1978), pp. 537–542.
[57] R.T. Lahey and F.J. Moody. *The Thermal-Hydraulics of a Boiling Water Nuclear Reactor*. Tech. rep. ANS Monograph, 1977.
[58] J.T. Rogers and R.G. Rosehart. “Mixing by Turbulent Interchange in Fuel Bundles. Correlations and Influences”. In: *ASME*. Paper 75-HT-31. 1972, pp. 1–12.
[59] S.G. Beus. *A Two-Phase Turbulent Mixing Model for Flow in Rod Bundles*. Tech. rep. WAPD-TM-2438. Bettis Atomic Power Laboratory, 1971.
[60] A. Faya, L. Wolf, and N.E. Todreas. *Canal Users Manual*. MIT-EL-79-028. 1979.
[61] P.B. Whalley. *Experimental Wave and Entrainment Measurements in Vertical Annular Two-Phase Flow*. Tech. rep. AERE-R7521. Atomic Energy Research Establishment, 1973.
[62] J. Wurtz. *An Experimental and Theoretical Investigation of Annular Steam-Water flow in Tubes and Annuli at 30 to 90 Bar*. Tech. rep. 372. RISO National Laboratory, Denmark, 1978.
[63] I.I. Paleev and B.A. Filippovich. “Phenomena of Liquid Transfer in Two-Phase Dispersed Annular Flow”. In: *International Journal of Heat and Mass Transfer* 9 (1966), pp. 1089–1093.
[64] L.B. Cousins. “Liquid Mass Transfer in Annular Two-Phase Flow”. In: *Symposium on Two-Phase Flow, Volume 2*. 1965, pp. 401–430.
[65] P.B. Whalley. “The Calculation of Dryout in a Rod Bundle”. In: *International Journal of Multiphase Flow* 13 (1977), pp. 501–515.
[66] I. Kataoka. “Generation and Size Distribution of Droplet in Annular Two-Phase Flow”. In: *Journal of Fluids Engineering* 105 (1983).
[67] J.E. Adams and A.J. Clare. *A Preliminary Study of Droplet Breakup at PWR Spacer Grids*. Tech. rep. Central Electric Generating Board, PWR/HTWS/P, 1983.
[68] S.L. Lee et al. *Reentrainment of Droplets from Grid Spacers in Mist Flow Portion of a LOCA Reflood of a PWR*. Tech. rep. NUREG-CR-0043. Nuclear Regulatory Commisson, 1982.

[69] S.C. Yao et al. “Dynamics of Droplets Impacting on Thin Heated Strips”. In: *National Heat Transfer Conference*. 1985.
[70] L.H.J. Wachters and N.A.J. Westerling. “The Heat Transfer from a Hot Wall to Impinging Water Drops in a Spheroidal State”. In: *Chem. Eng. Sci.* 21 (1966), pp. 1047–1056.
[71] L.H.J. Wachters et al. “The Heat Transfer from a Hot Wall to Impinging Mist Droplets in the Spheroidal State”. In: *Chem. Eng. Sci.* 21 (1966), pp. 1231–1238.
[72] K. Takeuchi et al. “Experimental Studies on the Behavior of a Small Droplet Impinging upon a Hot Surface”. In: *Proceedings of the Second International Conference on Liquid Atomization and Spray Systems*. 1982, pp. 397–404.
[73] D.S. Trent and J.R. Welty. *A Summary of Numerical Methods for Solving Transient Heat Conduction Problems*. Tech. rep. Bulletin No. 49. Engineering Experimental Station, Oregon State University, 1974.
[74] G.E. Kendall and W.M. Rohsenow. *Heat Transfer to Impacting Drops and Post Critical Heat Flux Dispersed Flow*. Tech. rep. 85694-100. MIT, 1978.
[75] D.L. Hagrman, G.A. Reymann, and R.E. Manson. *MATPRO-Version 11: A Handbook of Material Properties for Use in the Analysis of Light Water Reactor Fuel Rod Behavior*. Tech. rep. NUREG/CR-0497. US Nuclear Regulatory Commission, 1980.
[76] G.A. Berna et al. *FRAPCON-2: A Computer Code for the Calculation of Steady-State Thermal-Mechanical Behavior of Oxide Fuel Rods*. Tech. rep. NUREG/CR-1845. US Nuclear Regulatory Commission, 1981.
[77] D.R. Coleman and E.T. Laats. *FRAP-T3, A Computer Code for the Transient Analysis of Oxide Fuel Rods—Model Assessment Report*. Tech. rep. NUREG/CR-0555, TREE-1320. U.S. Nuclear Regulatory Commission, 1979.
[78] J. Hales et al. *BISON Theory Manual*. Tech. rep. INL/EXT-13-29930 Rev. 3. Idaho National Laboratory, 2016.
[79] S. Yagnik. *Fuel Analysis and Licensing Code: FALCON MOD01 (Vol 1: Theoretical and Numcerical Bases)*. 2004.
[80] D. Franklin. “Zircaloy-4 Cladding Deformation During Power Reactor Irradiation”. In: *Zirconium in the Nuclear Industry: Fifth Conference, ASTM STP 754, American Society for Testing and Materials*. 1982.
[81] C. M. Allison et al. *SCDAP/RELAP5/MOD3.1 Code Manual, Volume IV: MATPRO—A Library of Materials Properties for Light-Water-Reactor Accident Analysis.* Tech. rep. NUREG/CR-6150, EGG-2720. Idaho National Engineering Laboratory, 1993.
[82] K. J. Geelhood et al. *FRAPCON-4.0: A Computer Code for the Calculation of Steady-State, Thermal-Mechanical Behavior of Oxide Fuel Rods for High Burnup*. Tech. rep. PNNL-19418, Vol. 1 Rev. 2. Pacific Northwest National Laboratory, 2015.
[83] J. Hu et al. *Prepare CTFFuel for Core Follow Applications*. Tech. rep. CASL-U-2019-1854-000. 2019.
[84] D.D. Lanning and C.R. Hann. *Review of Methods Applicable to the Calculation of Gap Conductance in Zircaloy-Clad UO_2 Fuel Rods*. Tech. rep. BNWL-1894. Pacific Northwest Laboratory, 1975.
[85] W.R. Lloyd et al. “Heat Transfer in Multicomponent Monatomic Gases in the Low, Intermediate, and High Pressure Regime”. In: *Nuclear Thermionics Conference*. 1973.
[86] A. Ullman, R. Acharya, and D.R. Olander. “Thermal Accommodation Coefficients of Inert Gases on Stainless Steel and UO_2”. In: *Journal of Nuclear Materials* 51 (1974), pp. 277–279.
[87] L.B. Thomas. *Fundamentals of Gas-Surfacing Interactions*. Academic Press, New York, 1967.
[88] M.G. Cooper, B.B. Mikic, and M.M. Yavonovich. “Thermal Contact Conductance”. In: *Journal of Heat and Mass Transfer* 12 (1969).

[89] N. Todreas and G. Jacobs. “Thermal Contact Conductance of Reactor Fuel Elements”. In: *Nuclear Science and Engineering* 50 (1973), p. 283.
[90] J.V. Cathcart et al. *Zirconium Metal-Water Oxidation Kinetics IV, Reaction Rate Studies*. Tech. rep. ORNL/NUREG-17, 1977.
[91] R.E. Henry. “A Correlation for the Minimum Film Boiling Temperature”. In: *AICHE Symposium Series*. Vol. 138. 1974, pp. 81–90.
[92] J.C. Chen. “A Correlation for Boiling Heat Transfer to Saturated Fluids in Convective Flow”. In: *ASME 63-HT-34*. 1963.
[93] J.R.S. Thom et al. “Boiling in Subcooled Water During Flow Up Heated Tubes for Annuli”. In: *Symposium on Boiling Heat Transfer in Steam Generating Units and Heat Exchangers, Manchester, London*. 1965.
[94] F.W. Dittus and L.M.K. Boelter. “Heat Transfer in Automobile Radiators fo the Tubular Type”. In: *Publications in Engineering 2*. University of California, Berkeley, 1930, pp. 443–461.
[95] S. Wong and L.E. Hochreiter. *Analysis of the FLECHT-SEASET Unblocked Bundle Steam Cooling and Boiloff Tests*. Tech. rep. NRC/EPRI/Westinghouse, 1981.
[96] E.M. Sparrow et al. “Heat Transfer to Longitudinal Laminar Flow Between Cylinders”. In: *J. Heat Transfer* 83 (1961), p. 415.
[97] W.T. Hancox and W.B. Nicoll. “A General Technique for the Prediction of Void Distributions in Nonsteady Two-Phase Forced Convection”. In: *Int. J. Heat and Mass Transfer* 14 (1971).
[98] N. Basu, G.R. Warrier, and V.K. Dhir. “Onset of Nucleate Boiling and Active Nucleation Site Density During Subcooled Flow Boiling”. In: *J Heat Transfer* 124 (2002), pp. 717–728.
[99] A.E. Bergles and W.M. Rohsenow. “The Determination of Forced-Convection Surface-Boiling Heat Transfer”. In: *J Heat Transfer* 86 (1964), pp. 365–372.
[100] P. Saha and N. Zuber. “Point of Net Vapor Generation and Vapor Void Fraction in Subcooled Boiling”. In: *Proceedings of the 5th International Heat Transfer Conference*, pp. 175–179.
[101] R.T. Lahey. “A Mechanistic Subcooled Boiling Model.” In: *Proc. Sixth Int. Heat Transfer Conference*. Vol. 1. 1978, pp. 293–297.
[102] H.K. Forster and N. Zuber. “Bubble Dynamics and Boiling Heat Transfer”. In: *AICHE J* 1 (1955), pp. 532–535.
[103] D. Gorenflo and D. Kenning. *VDI Heat Atlas*. 2nd. VD-Verlag GmbH, Springer, Dusseldorf, 1993. Chap. Pool Boiling, pp. 757–792.
[104] D. Steiner and J. Taborek. “Flow Boiling Heat Transfer in Vertical Tubes Correlated by an Asymptotic Model”. In: *Heat transfer engineering* 13 (1992), pp. 43–69.
[105] R.W. Bjorge, G.R. Hall, and W.M. Rohsenow. “Correlation of Forced Convection Boiling Heat Transfer Data”. In: *Int J Heat and Mass Transfer* 25 (1982), pp. 753–757.
[106] Z. Karoutas and other. *Subcooled Boiling Data From Rod Bundles*. Tech. rep. 1003383. The Electric Power Research Institute (EPRI), Palo Alto, CA, 2002.
[107] N. Zuber, M. Tribus, and J.W. Westwater. “The Hydrodynamic Crisis in Pool Boiling of Saturated and Subcooled Liquids”. In: *International Development in Heat Transfer: Proceedings of 1961–62 International Heat Transfer Conference*. 1961, pp. 230–236.
[108] T.A. Bjornard and P. Griffith. “PWR Blowdown Heat Transfer”. In: *Thermal and Hydraulic Aspects of Nuclear Reactor Safety*. Vol. 1. ASME. 1977, pp. 17–41.
[109] J.H. Lienhard and V.K. Dhir. “Hydrodynamic Prediction of Peak Pool-Boiling Heat Fluxes from Finite Bodies”. In: *J. Heat Transfer* 95.2 (1973), pp. 152–158.
[110] L. Sardh and K.M. Becker. *Assessments of CHF Correlations Based on Full-Scale Rod Bundle Experiments*. Tech. rep. KTH-NEL-36. Royal Institute of Technology (KTH), 1986.
[111] L. Biasi et al. “Studies on Burnout, Part 3”. In: *Energia Nucleare* 14.9 (1967), pp. 530–536.

[112] L.S. Tong. "Prediction of Departure from Nucleate Boiling for an Axially Non-Uniform Heat Flux Distribution". In: *Journal of Nuclear Energy* 21 (1967), pp. 241–248.
[113] L.S. Tong. *Boiling Crisis and Critical Heat Flux*. Tech. rep. TID-25887. US Atomic Energy Commission, 1972.
[114] N.E. Todreas and M.S. Kazimi. *Nuclear Systems I: Thermal Hydraulic Fundamentals*. Hemisphere Publishing Corporation, 1993.
[115] R.W. Bowring. *A Simple but Accurate Round Tube, Uniform Heat Flux Dryout Correlation over the Pressure Range 0.7 to 17 MPa*. Tech. rep. AEE Winfrith, 1972.
[116] D.C. Groeneveld et al. *The 2006 CHF look-up table*. Tech. rep. Nuclear Engineering and Design, 2007.
[117] R. Salko et al. *CTF Validation and Verification*. The Pennsylvania State University. 2015.
[118] D.C. Groeneveld et al. *Look-Up Tables for Predicting CHF and Film Boiling Heat Transfer - Past, Present and Future (NURETH)*. Tech. rep. Chalk River Lab, AECL, 2003.
[119] Tae-Hyun Chun et al. *Assessment of a tube-based bundle chf prediction method using a subchannel code*. Tech. rep. KAERI, 1998.
[120] S.C. Yao, L.E. Hochreiter, and W.J. Leech. "Heat-Transfer Augmentation in Rod Bundles Near Grid Spacers". In: *Journal of Heat Transfer* 104 (1982), pp. 76–81.
[121] E.N. Ganic and W.M. Rohsenow. "Dispersed Flow Heat Transfer". In: *Int. J. Heat and Mass Transfer* 20 (1977), pp. 855–866.
[122] L.A. Bromley. "Heat Transfer in Stable Film Boiling". In: *Chemical Engineering Progress* 46.5 (1950), pp. 221–226.
[123] K.H. Sun, J.M. Gonzalez-Santalo, and C.L. Tien. "Calculations of Combined Radiation and Convection Heat Transfer in Rod Bundles Under Emergency Cooling Conditions". In: *ASME Journal of Heat Transfer* (1976).
[124] E.M. Sparrow and R.D. Cess. *Radiation Heat Transfer*. McGraw-Hill, 1977, p. 231.
[125] C.Y. Paik et al. *Analysis of FLECHT-SEASET 163-Rod Blocked Bundle Data using COBRA-TF*. Tech. rep. NUREG/CR-3046. United States Nuclear Regulatory Commission, 1985.
[126] A. Yamanouchi. "Effect of Core Spray Cooling in Transient State after Loss-of-Cooling Accident". In: *J. Nucl. Science and Technology* 5 (1968), pp. 547–558.
[127] J.H. McFadden et al. *RETRAN-02 A Program for Transient Thermal-Hydraulic Analysis of Complex Fluid Flow Systems, Volume 1: Equations and Numbers*. Tech. rep. NP-1850. Electric Power Research Institute, 1980.
[128] American Society of Mechanical Engineers. *ASME Steam Tables*. 1968.
[129] L. Haar, J.S. Gallagher, and G.S. Kell. *NBS/NRC Steam Tables*. Hemisphere Publishing Corporation, New York, 1984.
[130] J.H. Keenan and F.G. Keyes. *Thermodynamic Properties of Steam*. John Wiley & Sons, New York, 1936.
[131] W. Wagner and A. Kruse. *Properties of Water and Steam*. The Industrial Standard IAPWS-IF97. Springer, 1998.
[132] IAPWS. *Revised Release on the IAPWS Industrial Formulation 1997 for the Thermodynamic Properties of Water and Steam*. Tech. rep. The International Association for the Properties of Water and Steam , Lucerne, Switzerland, 2007.
[133] IAPWS. *Release on the IAPWS Formulation 2011 for the Thermal Conductivity of Ordinary Water Substance*. Tech. rep. The International Association for the Properties of Water and Steam , Czech Republic, 2011.
[134] IAPWS. *Release on the IAPWS Formulation 2008 for the Viscosity of Ordinary Water Substance*. Tech. rep. The International Association for the Properties of Water and Steam , Berlin, Germany, 2008.

[135] IAPWS. *IAPWS Release on Surface Tension of Ordinary Water Substance*. Tech. rep. The International Association for the Properties of Water and Steam, 1994.
[136] D. F. Williams, L. M. Toth, and K. T. Clarno. *Assessment of Candidate Molten Salt Coolants for the Advanced High-Temperature Reactor (AHTR)*. Tech. rep. ORNL/TM-2006/69. Oak Ridge National Laboratory, 2006.
[137] W.G. Luscher, K.J. Geelhood, and I.E. Porter. *Material Property Correlations: Comparisons between FRAPCON-4.0, FRAPTRAN-2.0, and MATPRO*. PNNL-19417 Rev. 2. Pacific Northwest National Laboratory. Sept. 2015.
[138] Held P.C. and D.R. Wilder. "High temperature hemispherical spectral emittance of uranium oxides at 0.65 and 0.70 mircometers". In: *Journal of the American Ceramic Society* 52.4 (Apr. 1969), pp. 182–185.
[139] Cabannes MMF, JP Stora, and J Tsakiris. "Facteurs de reflexion et d'emission de UO2 a haute temperature". In: *C. R. Acad. Sc.* 264B (1967), pp. 45–48.
[140] T. T. Claudson. *Emissivity Data of Uranium Dioxide*. Report AW-55414. Nov. 1958.
[141] D.L. Hagrman, G.A. Reymann, and R.E. Mason. *MATPRO — Version 11 (Revision 2): A Handbook of Materials Properties for Use in the Analysis of Light Water Reactor Fuel Rod Behavior*. Tech. rep. NUREG/CR-0497, TREE-1280, Revision 2. U.S. Nuclear Regulatory Commission, 1981.
[142] P.E. MacDonald et al. *MATPRO - Version 9: A Handbook of Materials Properties for Use in the Analysis of Light Water Reactor Fuel Rod Behavior*. Tech. rep. TREE-NUREG-1005. Idaho National Engineering Laboratories, 1976.
[143] *Thermal Conductivity Measurements of High Burnup UO2 Pellet and a Benchmark Calculation of Fuel Center Temperature*. ANS International Topical Meeting on LWR Fuel Performance. Portland, Oregon, Mar. 1979.
[144] Lanning et al. *FRAPCON-3 Updates, Including Mixed-Oxide Fuel Properties*. Tech. rep. NUREG/CR-6354, Vol.4, PNNL-11513. U.S. Nuclear Regulatory Commission, 2005.
[145] Geelhood K.J. Lusher W.G. *Material Property Correlations: Comparisons between FRAPCON-3.4, FRAPTRAN 1.4, and MATPRO*. Technical Report NUREG/CR-7024. Richland, Washington: Pacific Northwest Laboratory, 2011.
[146] Lanning et al. *FRAPCON-3: Modifications to Fuel Rod Material Properties and Performance Models for High-Burnup Application*. Technical Report NUREG/CR-6534, Vol.1. U.S. Nuclear Regulatory Commission, 1997.
[147] M. Amaya et al. "Thermal conductivity evaluation of high burnup mixed- oxide (MOX) fuel pellet". In: *Journal of Nuclear Materials* 404 (2011), pp. 303–308.
[148] *Thermophysical properties database of materials for light water reactors and heavy water reactors*. Final report of a coordinated research project: 1999–2005 IAEA-TECDOC-1496. IAEA, June 2006.
[149] Brooks CR and EE Stansbury. "The specific heat of Zircaloy-2 from 50 to 700 °C". In: *Journal of Nuclear Materials* 18 (1966), p. 223.
[150] Deem HW and EA Eldridge. *Specific Heats of Transformation of Zirclaoy-2 and Low Nickel Zircaloy-2*. Tech. rep. USAEC BM1-1803. Columbus, Ohio: Battelle Memorial Institute, 1967.
[151] Coughlin JP and EG King. "High-temperature heat contents of some zirconium-containing aubstances". In: *Journal for the American Chemical Society* 72 (1950), p. 2262.
[152] Peggs ID and DP Godin. "The yield strength-hot hardness relationship of zircaloy-4." In: *Journal of Nuclear Materials* 57 (1975), pp. 246–248.
[153] D.B. Scott. *Physical and Mechanical Properties of Zircaloy-2 and -4*. Tech. rep. WCAP-3269-41. Idaho National Engineering Laboratories, 1965.